

REPORT DOCUMENTATION PAGE			Form Approved OMB No. 0704-0188	
Public reporting burden for this collection of information is estimated to average 1 hour per response, including the time for reviewing instructions, searching existing data sources, gathering and maintaining the data needed, and completing and reviewing the collection of information. Send comments regarding this burden estimate or any other aspect of this collection of information, including suggestions for reducing this burden, to Washington Headquarters Services, Directorate for Information Operations and Reports, 1215 Jefferson Davis Highway, Suite 1204, Arlington, VA 22202-4302, and to the Office of Management and Budget, Paperwork Reduction Project (0704-0188), Washington, DC 20503.				
1. AGENCY USE ONLY (Leave blank)		2. REPORT DATE 7 Jan. 99		3. REPORT TYPE AND DATES COVERED DISSERTATION
4. TITLE AND SUBTITLE CYCLE-BY-CYCLE VARIATION IN SPARK IGNITION INTERNAL COMBUSTION ENGINES			5. FUNDING NUMBERS	
6. AUTHOR(S) MAJ BALL JEFFREY K				
7. PERFORMING ORGANIZATION NAME(S) AND ADDRESS(ES) UNIVERSITY OF OXFORD AT MERTON COLLEGE			8. PERFORMING ORGANIZATION REPORT NUMBER	
9. SPONSORING/MONITORING AGENCY NAME(S) AND ADDRESS(ES) THE DEPARTMENT OF THE AIR FORCE AFIT/CIA, BLDG 125 2950 P STREET WPAFB OH 45433			10. SPONSORING/MONITORING AGENCY REPORT NUMBER  FY99-3	
11. SUPPLEMENTARY NOTES				
12a. DISTRIBUTION AVAILABILITY STATEMENT Unlimited distribution In Accordance With AFI 35-205/AFIT Sup 1			12b. DISTRIBUTION CODE	
13. ABSTRACT (Maximum 200 words)				
14. SUBJECT TERMS			15. NUMBER OF PAGES	
			16. PRICE CODE	
17. SECURITY CLASSIFICATION OF REPORT	18. SECURITY CLASSIFICATION OF THIS PAGE	19. SECURITY CLASSIFICATION OF ABSTRACT	20. LIMITATION OF ABSTRACT	

***Cycle-by-cycle variation in spark ignition internal  
combustion engines***



**Jeffrey K. Ball  
Merton College  
Oxford**

**19990120 002**

A thesis submitted to the University of Oxford for the degree of Doctor of Philosophy

Department of Engineering Science  
University of Oxford

Hilary Term 1998

## Cycle-by-cycle variation in spark ignition internal combustion engines

Jeffrey K. Ball

Department of Engineering Science

Doctor of Philosophy

Merton College, Oxford

A thesis submitted in partial fulfilment of the requirements of the Degree of Doctor of Philosophy at the University of Oxford, Hilary Term 1998.

### **Abstract**

The primary objective of this work was to extend the engine cycle simulation used by the Oxford Internal Combustion Engine Group to enable it to perform cycle-by-cycle modelling. A literature review concluded that the most appropriate metric for quantifying the cyclic variation was the coefficient of variation of the indicated mean effective pressure, and that for zero dimensional computer simulations, the most sensible parameter to perturb for cycle-by-cycle modelling was the burn rate.

Modelling attempts using burn rate information alone resulted in an under-prediction of the cyclic variability exhibited by the engine. The work then examined a two-zone polytropic process model in an attempt to improve burn rate estimation. The model proved unreliable for burn rate calculations. The Rassweiler and Withrow method was then modified to include both the compression and expansion indices throughout the combustion period. The technique proved viable, but was not used because the slow burn up of the significant crevice mass in the experimental engine made calculation of an accurate expansion index doubtful.

A further cause of the under-prediction in cyclic variability was postulated to be incomplete combustion, which is not detected by the burn rate model. A completeness of combustion parameter was derived from information contained in the Rassweiler and Withrow analysis. This parameter was used along with burn rate variations to perturb the cycle simulation and resulted in good cycle-by-cycle agreement between the experimental data and the modelled data in terms of mean effective pressure, maximum pressure, and the phasing of maximum pressure. Cyclic measurements of NO showed that the technique did not predict the cyclic variability in NO formation, and this was attributed to the sensitivity of NO formation to parameters that were not allowed to vary on a cyclic basis within the model (such as residuals). It was concluded that variations in combustion completeness and burn rate were sufficient to enable the simulation to perform cycle-by-cycle modelling of the engine output, but further modifications are required to model the cyclic NO formation.

The second objective of this work was to examine the feasibility of using measurements of the angular acceleration of the engine block as a means of estimating misfires. A model was constructed that assumed that the engine block behaved as a rigid body, single degree of freedom torsional oscillator, and was used to estimate the gas pressure torque produced by each cylinder. Torque estimation was good under low speed conditions, but was less accurate at high speed and load due to a coupling of the block rolling and pitching motion. Misfire metrics were developed in both the temporal and spatial frequency domains. The metrics based on low frequency information were most reliable. However, their accuracy was degraded at high engine speeds, and this was thought to be due to structural vibration of the block and the variable inertial properties of the engine, neither of which were incorporated into the model. It was concluded that the measurements of the angular acceleration of the block could be used to detect misfires, and that the most significant advantage of this method was the fact that the load torque through the drivetrain did not affect the calculations.

## Acknowledgements

I would like to express my sincere gratitude to my supervisor, Dr. Richard Stone, for his guidance, instruction, and support throughout this project. He truly treated me as a colleague and gave me far more credit for my background and experience than was warranted.

I am indebted to the U.S. Air Force Institute of Technology for their financial and administrative support, and to the U.S. Air Force Academy Department of Engineering Mechanics for sponsoring my studies.

I would also like to thank Dr. Robert Raine of the University of Auckland for his advice and collaboration during his sabbatical in Oxford, Dr. Mario Cortina-Borja of the Department of Statistics for his assistance with Pearson distributions, and Dr. Peter McFadden of the Department of Engineering Science for his advice on vibration analysis, the use of his accelerometers, and his willingness to proofread the final portion of this manuscript. I am also indebted to Dr. Chris Mace of the Ministry of Defence for making time in his busy schedule to proofread this manuscript.

Thanks also go to my office mates Dr. Nick Pashley, Stef Simonini, and Rick Lim for creating a positive working environment. I am grateful to the following people within the department for their assistance with electronics and equipment: Anthony Cooper, Brian Busby, Dominic Harris, John Hastings, Ken Dunford, Harry Fearnley, and Geoff Jones. A special mention to John Gills, whose encyclopaedic knowledge of the English countryside added immensely to the richness of my family's time in England.

I must thank my children Austin, Audra, Annalise, and Amber for their constant ability to lift my spirits after long days.

And most importantly, I want to thank my wife, Patricia, for everything – for taking an interest in thermodynamics and engine research, for caring for me, for teaching our children, and most of all for her undying love and support. Without you, none of this would have been possible.

*Gloria in excelsis Deo.*



## Table of Contents

Abstract .....	ii
Acknowledgements .....	iii
Table of Contents .....	iv
Nomenclature .....	viii
<b>CHAPTER 1 INTRODUCTION .....</b>	<b>1</b>
1.1 ORIGINAL AIMS.....	1
1.2 DEFINITION AND RELEVANCE OF CYCLE-BY-CYCLE VARIATION.....	1
<b>CHAPTER 2 LITERATURE SURVEY .....</b>	<b>5</b>
2.1 INTRODUCTION .....	5
2.2 MEASURES OF CYCLE-BY-CYCLE VARIATION .....	5
2.3 CAUSES AND INFLUENCES OF CCV.....	11
2.3.1 Mixture composition factors .....	12
2.3.2 Physical factors .....	18
2.3.3 Cylinder charging.....	20
2.3.4 Ignition Factors .....	22
2.3.5 In-cylinder motion .....	26
2.3.6 Prior cycle effects .....	33
2.4 COMPUTER MODELLING OF CYCLE-BY-CYCLE VARIATION .....	34
2.4.1 Introduction.....	34
2.4.2 Flame kernel displacement models .....	35
2.4.3 Turbulent propagation models .....	37
2.4.4 General thermodynamic models .....	40
2.5 SUMMARY.....	42
<b>CHAPTER 3 EXPERIMENTAL APPARATUS .....</b>	<b>45</b>
3.1 INTRODUCTION .....	45
3.2 TEST FACILITY DESCRIPTION .....	45
3.3 QUASI-STEADY MEASUREMENTS .....	47
3.3.1 Engine Speed and Torque Measurement and Control.....	47
3.3.2 Air Flow Measurement and Control .....	49
3.3.3 Fuel Flow Measurement and Control.....	49
3.3.4 Blow-by Gas Measurement.....	50
3.3.5 Temperature Measurement and Control.....	50
3.3.6 Exhaust Pressure Measurement .....	50

3.4	<i>EXHAUST GAS ANALYSERS</i> .....	51
3.4.1	OTC AutoGas4 .....	51
3.4.2	Flame Ionisation Detection .....	52
3.4.3	Thermo-Electron Chemiluminescence NO/NO <sub>x</sub> Analyser .....	53
3.4.4	Cussons Lamdascan .....	53
3.5	<i>EXHAUST ANALYSER CALIBRATION</i> .....	56
3.5.1	OTC AutoGas4 .....	56
3.5.2	Flame Ionisation Detector.....	56
3.5.3	Thermo-Electron Chemiluminescent Analyser.....	57
3.5.4	Cussons Lamdascan .....	57
3.5.5	AFR and $\lambda$ Calculation for Calibration Gas.....	58
3.6	<i>CYCLIC MEASUREMENTS</i> .....	59
3.6.1	Crankshaft Encoder.....	59
3.6.2	High-speed data acquisition .....	60
3.6.3	Cylinder Pressure Measurement .....	60
3.7	<i>CYLINDER PRESSURE TRANSDUCER CALIBRATION</i> .....	66
3.8	<i>SUMMARY</i> .....	67
<b>CHAPTER 4 COMPUTER MODELS AND INITIAL RESULTS OF CYCLE-BY-CYCLE MODELLING</b> .....		<b>68</b>
4.1	<i>INTRODUCTION</i> .....	68
4.2	<i>COBRA</i> .....	68
4.3	<i>THE RASSWEILER AND WITHROW METHOD</i> .....	71
4.4	<i>ISIS</i> .....	74
4.5	<i>RESULTS OF INITIAL CYCLE-BY-CYCLE MODELLING</i> .....	76
4.6	<i>SUMMARY</i> .....	83
<b>CHAPTER 5 EVALUATION OF COMBUSTION ANALYSIS ROUTINES</b> .....		<b>84</b>
5.1	<i>INTRODUCTION</i> .....	84
5.2	<i>TWO ZONE POLYTROPIC PROCESS MODEL</i> .....	85
5.2.1	Combustion modelling.....	85
5.2.2	Results.....	88
5.2.3	Conclusion .....	98
5.3	<i>MODIFICATION TO THE RASSWEILER AND WITHROW METHOD</i> .....	99
5.3.1	Derivation of equations.....	99
5.3.2	Use of alternative MFB analysis method .....	101
5.4	<i>SLOW BURN UP OF CREVICE HYDROCARBONS</i> .....	104

5.5	SUMMARY.....	109
<b>CHAPTER 6 COMPLETENESS OF COMBUSTION .....</b>		<b>111</b>
6.1	INTRODUCTION .....	111
6.2	THEORETICAL BASIS FOR CALCULATING COMPLETENESS OF COMBUSTION.....	111
6.3	DEVELOPMENT OF THE COMPLETENESS OF COMBUSTION PARAMETER .....	114
6.4	IMPLEMENTATION OF COMPLETENESS OF COMBUSTION INTO CYCLE-BY-CYCLE MODELLING.....	125
6.5	SUMMARY AND INTRODUCTION TO NEXT STAGE OF WORK .....	132
<b>CHAPTER 7 CYCLE-BY-CYCLE MODELLING OF NO .....</b>		<b>134</b>
7.1	INTRODUCTION .....	134
7.2	EXPERIMENTAL FACILITY.....	136
7.3	FAST NO MEASUREMENTS.....	138
7.4	MODEL RESULTS .....	141
7.5	CONCLUDING REMARKS .....	151
<b>CHAPTER 8 TORQUE ESTIMATION AND MISFIRE DETECTION USING BLOCK ANGULAR ACCELERATION .....</b>		<b>152</b>
8.1	INTRODUCTION .....	152
8.2	LITERATURE REVIEW .....	153
8.2.1	Complexity of system model .....	153
8.2.2	Metrics of misfire detection .....	154
8.2.3	Methods of analysis .....	154
8.2.4	Common assumptions .....	155
8.2.5	Review of relevant literature.....	156
8.2.6	Summary .....	159
8.3	SYSTEM MODEL .....	160
8.4	EXPERIMENTAL APPARATUS.....	163
8.5	EXPERIMENTAL RESULTS – TORQUE ESTIMATION.....	169
8.6	EXPERIMENTAL RESULTS – FREQUENCY DOMAIN ANALYSIS.....	176
8.7	CONCLUDING REMARKS .....	187
<b>CHAPTER 9 CONCLUSIONS AND SUGGESTIONS FOR FURTHER WORK.....</b>		<b>189</b>
9.1	CYCLE-BY-CYCLE MODELLING.....	189
9.2	TORQUE ESTIMATION AND MISFIRE DETECTION .....	190
9.3	SUGGESTIONS FOR FURTHER WORK.....	191
9.3.1	Cycle-by-cycle modelling.....	191

9.3.2 Torque estimation and misfire detection.....	192
REFERENCES.....	194
APPENDIX A DERIVATION OF RASSWEILER AND WITHROW RELATIONSHIP WITH VARIABLE POLYTROPIC INDICES .....	204
APPENDIX B MODIFICATION OF THE WIEBE MASS FRACTION BURNED RELATION TO ALLOW FOR INCOMPLETE COMBUSTION.....	208
APPENDIX C EXPERIMENTAL AND MODELLED IMEP DISTRIBUTION PLOTS.	211
APPENDIX D SUMMARY OF ISIS INPUTS FOR CYCLE-BY-CYCLE MODELLING OF NO.....	215
APPENDIX E RESULTS OF NO MODELLING .....	219
APPENDIX F DERIVATION OF COMPOSITE TORQUE USING ENGINE BLOCK ANGULAR ACCELERATION.....	227
APPENDIX G MISFIRE METRIC RESULTS .....	235

## Nomenclature

ABDC	after bottom dead centre
AFR	air-fuel ratio
ATDC	after top dead centre
B	bore diameter
BBDC	before bottom dead centre
BDC	bottom dead centre
BMEP	brake mean effective pressure
BTDC	before top dead centre
CCV	cycle-by-cycle variation
CLD	chemiluminescent detector
COV	coefficient of variation (COV = standard deviation/mean)
$C_t$	torsional damping coefficient
DFT	discrete Fourier transform
EGR	exhaust gas recirculation
EOC	end of combustion
EVC	exhaust valve closing
EVO	exhaust valve opening
FID	flame ionisation detector
IMEP	indicated mean effective pressure
IVC	inlet valve closing
IVO	inlet valve opening
J	polar moment of inertia
$K_t$	torsional stiffness
<i>kurt</i>	kurtosis
m	mass
MBT	minimum advance for best torque
MFB	mass fraction burned
$n_c$ $n_e$	polytropic index for compression and expansion
P	pressure
R	correlation coefficient
R	gas constant
s	spark timing
<i>sk</i>	statistical skewness

$T$	temperature
TDC	top dead centre
tmf	trapped mass fraction
$V$	volume
$v_p$	mean piston speed
$x$	mass fraction burned
$\chi$	completeness of combustion
$\Psi$	normalised pressure rise due to combustion
$\eta_{HC}$	hydrocarbon efficiency
$\gamma$	ratio of specific heats
$\lambda$	relative air-fuel ratio
$\lambda$	spatial frequency
$\theta$	crank angle
$\sigma$	standard deviation
$\zeta$	damping ratio

#### subscripts

b	burned mixture
c	combustion
cr	crevice
exh	exhaust
f	end of combustion
in	intake
m	statistical maximum indicating complete combustion
max	maximum
u	unburned mixture

## Chapter 1 Introduction

### *1.1 Original aims*

The objectives of this work were two-fold. The first, and primary, objective was to extend the engine cycle simulation currently used by the Oxford Internal Combustion Engine Group to enable it to perform cycle-by-cycle modelling. Conventionally, a simulation is used to model a mean cycle, which is derived from an ensemble averaged pressure trace for a given engine at a given operating point. An attempt at cycle-by-cycle modelling using this simulation was done by Raine et al. (1995). This attempt used variations in burn rate to achieve cyclic perturbations in the combustion calculations. Specifically, experimental burn rates were used as inputs, and the model results were compared to the experimental data on a cycle-by-cycle basis. These results indicated that the variations in burn rate were not sufficient to model the cycle-by-cycle variations in maximum pressure or indicated mean effective pressure (IMEP).

The second objective was to examine the feasibility of using measurements of the angular acceleration of the engine block as a means of identifying misfires. Current work in this area has used measurements of flywheel angular velocity to detect misfires. However, this technique is currently hampered by the effects of the load torque induced by the drivetrain and the assumption of a rigid crankshaft.

### *1.2 Definition and relevance of cycle-by-cycle variation*

Before delving into the main body of the current work, it is perhaps prudent to define cycle-by-cycle variation, and to discuss its importance in the context of engine development. Cycle-by-cycle variation (CCV) may be defined as the non-repeatability of the combustion process on a cycle resolved basis. This means that when a reciprocating internal combustion engine is operating, the combustion within a given cylinder is different each time the cylinder fires. This has several important effects on the engine, and these effects can be best explained with reference to Figure 1.1.

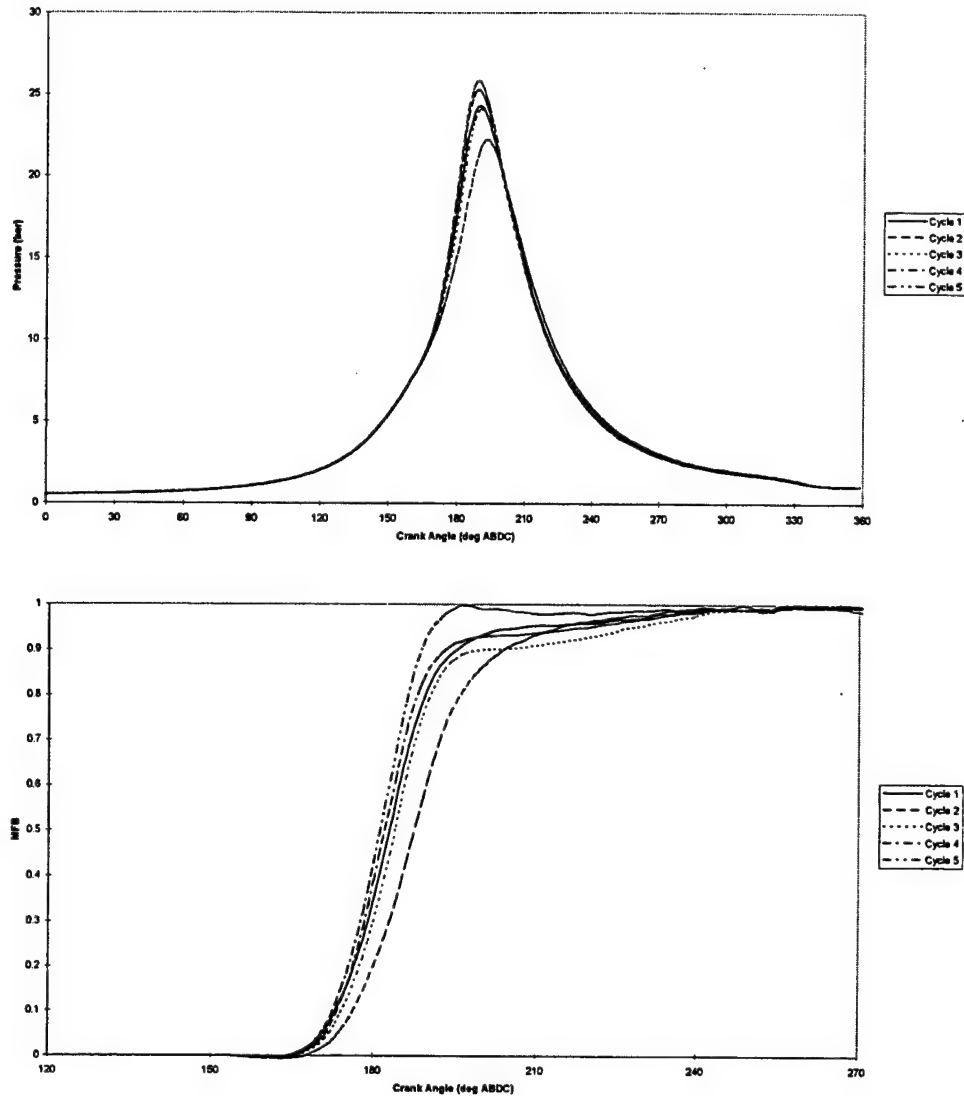


**Figure 1.1. Pressure-crank angle traces and mass fraction burned curves showing cycle-by-cycle variation.**

Figure 1.1 shows the pressure-time and mass fraction burned (MFB) curves for 5 consecutive cycles of data taken from a Rover K4 engine operating on a stoichiometric mixture of methane at 1000 RPM and with an ignition timing of 25 degrees BTDC. Referring to Figure 1.1, it is clear that the maximum pressure for each cycle is different. Also, the maximum pressure occurs at a slightly different point in each cycle. The reason for this occurrence is shown by the lower portion of Figure 1.1, where it can be seen that the fuel in the cylinder is not burning at the same rate every time.

So why is this important? On a subjective level, it is important to the user of the engine since different pressures at different times translates into different work outputs for



each cycle. If the difference in work output between cycles becomes too large, the user experiences subjective problems such as engine roughness. To the engineer, cycle-by-cycle variations are important because they imply that not all cycles are optimum. Soltau (1960) suggested that if cyclic dispersion could be eliminated, there would be a 10 per cent increase in the power output for the same fuel consumption with weak mixtures. Similar conclusions were drawn by Lyon (1986), who indicated that a 6 per cent improvement in fuel economy could be achieved if all cycles burned at the optimum rate. Early work in understanding the causes of CCV was driven by the improvement in engine performance and fuel economy wrought by reducing CCV. Adequate understanding of these causes, and the means of controlling them, eventually led to the lean burn engine. This engine offered high levels of economy, provided the high levels of CCV normally produced by lean combustion were adequately reduced. However, the lean burn engine was also found to generate high levels of emissions. Thus, it has been forced aside by increasingly stringent emissions legislation. Far from eliminating the motive for studying CCV, these emission regulations have sparked a renewed interest in it. The fact that all cycles are not optimum also means that some cycles pollute more than others. Furthermore, the use of exhaust gas recirculation (EGR) to reduce the formation of oxides of nitrogen also induces increased levels of CCV. EGR has also been used to reduce an engine's output without having to throttle the engine (thus reducing its volumetric efficiency). Hence, work continues into the causes of CCV and the means of eliminating it.

Recent advances in computing power have allowed more research into engine processes to be done analytically. The models used in these investigations range from the modelling of individual processes, such as in-cylinder flow or combustion, to the prediction of engine output. However, the processes occurring in an internal combustion engine are complex and inter-related, and many of them are not well understood at a fundamental level (Heywood, 1988). Thus, current models rely on empirical correlations to provide the requisite agreement with experimental results. Furthermore, most computer simulations only attempt to model a mean cycle at any given operating point. The models produce good results, but all information concerning the CCV of the engine is lost in the process. Recently, several researchers have attempted to model the CCV of an engine. Because of the number of factors giving rise to CCV, the primary focus of the models has been to allow just a few parameters to vary. In each case, the study focused on whether the chosen parameters were sufficient to account for the overall CCV.

In summary, emission legislation is forcing an examination of the causes and effects of CCV, whilst computer simulation offers the possibility of time and cost savings in developing an engine. Thus, it is highly desirable to have a computer simulation that can model an engine's performance on a cycle by cycle basis. Such a model would permit the

analysis or prediction of cyclic engine performance and its effect on emissions, fuel economy, or performance (work output). This is the motivation for the primary objective of this work.

A misfire can be considered to be the most extreme case of CCV. In a misfired cycle, combustion has failed to occur at all. This results in a degradation of engine performance, high hydrocarbon emissions, and driveability problems for the user (Lee and Rizzoni, 1995). In addition to the increase in hydrocarbon emissions, a misfired cycle sends a large quantity of unburned fuel through the catalytic converters. This reduces the service life of the converter due to high temperature excursions (Klenk, et al., 1993). Concern over these effects has led the California Air Resources Board (CARB) on-board diagnostic regulations for 1994 model vehicles to require the vehicle's diagnostic system to monitor misfire continuously. This is the motivation behind the secondary objective of this work.

Since the two objectives of this work are unrelated in their experimental and analytical approaches, the work treats each objective separately. Chapters 2-7 comprise the work done on cycle-by-cycle modelling, whilst Chapter 8 is devoted exclusively to misfire detection through measurements of the angular acceleration of the engine block. The primary section begins with a review of the relevant literature regarding the measurement of CCV, the causes of CCV, and recent attempts at cycle-by-cycle modelling. The goals of this review were to

- a) define a metric for measuring CCV,
- b) understand the causes of CCV,
- c) identify those parameters which can be most profitably perturbed to induce cyclic variation in the computer simulation, and
- d) understand the current state of cycle-by-cycle modelling.

## Chapter 2 Literature Survey

### 2.1 *Introduction*

Since the primary objective of this work is to incorporate cycle-by-cycle modelling into a current engine simulation, an understanding of the causes of cycle-by-cycle variation (CCV) is required. However, any effort to outline the causes of CCV, and the response of the engine to those causes, is dependent to a large degree on the choice of parameter used to quantify CCV. Hence, the first issue that will be reviewed here is the measurement and quantification of CCV. Section 2.3 is devoted to a review of the factors that cause or influence CCV. The causes will be examined so as to determine which factors can be perturbed within a computer simulation to provide accurate modelling of the CCV of the engine, "accuracy" being defined by the metric chosen after the review described in Section 2.2. Section 2.4 provides an overview of the cycle-by-cycle modelling of spark ignition engines. Since the work at hand involves extending an existing model rather than developing a new one, the review of current models is undertaken in an effort to understand the current state of the art in cycle-by-cycle modelling.

### 2.2 *Measures of Cycle-by-Cycle Variation*

In general, four categories of CCV measurement have been used (Ozdor et al., 1994):

- a) exhaust gas related parameters
- b) flame front related parameters
- c) combustion related parameters
- d) pressure related parameters.

When one speaks of a measurement that characterises CCV, it is generally meant that the measure is used to quantify the effect of some factor on the CCV of an engine. Hence, it is used as a basis of comparison, either for the same engine at different operating points or for different engine geometries at a single operating point.

The exhaust gas related parameters are not widely used to characterise CCV, but are used more often to gain insight into various factors influencing CCV (Ozdor et al., 1994), and these will not be addressed here. The flame front related parameters have been examined in

some detail by several researchers (Pischinger and Heywood, 1988, Shen, et al., 1994, Lee and Foster, 1995). These studies resulted in models of initial flame kernel growth, and were very useful in examining the causes of CCV. However, the variations in flame front parameters were always compared to variations in pressure or indicated mean effective pressure (IMEP). Because the flame front parameters were viewed as a cause of CCV, and the CCV itself was still characterised by other parameters, flame front related parameters are not considered to be measures of CCV here.

The combustion related parameters comprise factors such as maximum rate of heat release, ignition delay, burn duration, etc. These parameters are derived from pressure traces, and could be considered as a subset of the pressure related parameters. Nonetheless, rates of heat release or of mass fraction burned have not been found to be used to quantify CCV. The burn duration, while providing information about variations in combustion, is affected by the ignition delay and is not widely used. The ignition delay has been a convenient factor, but its use is somewhat questionable since its magnitude is greatly affected by noise in the pressure signal. Since the calculated burn rate is a function of the pressure, any errors in the pressure signal lead to large variations in the computed level of CCV with this parameter, and its use will not be considered either.

This leaves pressure related parameters as the primary means of quantifying CCV. Pressure related parameters would seem a natural choice since the required data can be easily obtained with a transducer. Assuming the data obtained are reasonably accurate, the following parameters may be used to quantify CCV:

- a) in-cylinder peak pressure, ( $P_{\max}$ ), and the crank angle at which it occurs,  $\theta_{P_{\max}}$
- b) maximum rate of pressure rise,  $(dP/d\theta)_{\max}$ , and the crank angle at which it occurs,  $(\theta_{(dP/d\theta)_{\max}})$
- c) IMEP of individual cycles.

By far, peak cylinder pressure is the most commonly used measure of CCV, primarily due to the presumed association of high burn rates with high peak pressures and low burn rates with low peak pressures (Matekunas, 1983). Also, the relationship between peak pressure and the crank angle at which it occurs can be shown graphically as in Figure 2.1.

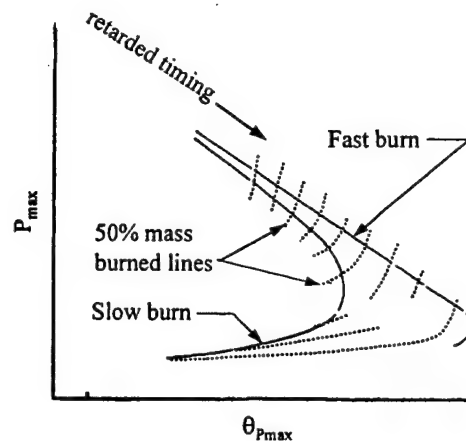


**Figure 2.1. Generalised plot of peak pressure versus crank angle of peak pressure (adapted from Matekunas (1983)).**

This plot shows two extremes of burning rates, one fast and the other slow, the speed being based on the mass fraction burnt at the point of peak pressure. The dashed lines indicate constant 50% mass burnt fractions, which correspond to varying ignition timings. As one moves down the curve, ignition timing has been retarded. One can see that the relationship between peak pressure and the angle at which it occurs is nearly linear for fast burning cycles, whilst for slow burning cycles, there is a hook back region when timing is retarded beyond a certain point. This region corresponds to a low level of peak pressure occurring closer to top dead centre (TDC), or in other words, the pressure rise due to combustion is being overcome by the pressure drop due to expansion.

The advantage of using peak pressure to quantify CCV, besides ease of measurement, is that it does respond to variations in phasing of the burn (Matekunas, 1983). Also, variations in peak pressure respond to cyclic variation in peak burning rate. However, peak pressure is affected by variations in cylinder charging, and care must be taken in relating the cyclic variation in peak pressure to flame propagation. The angle of peak pressure, however, is independent of charging variations and only weakly dependent on mass burning rate, provided the engine is operating in the linear region of Figure 2.1 (Matekunas, 1983). The maximum rate of pressure rise and the angle at which it occurs are less acceptable measures, due in part to the inherent noise in the pressure signal (Matekunas, 1983).

It has been argued that IMEP is a better indicator of CCV than the maximum pressure (Heywood, 1988, Stone, 1992, Hoard and Rehagen, 1997). From a practical standpoint, the impact of CCV is on the driveability of the vehicle. Since IMEP is a measure of the work done which gets transmitted to the flywheel (minus frictional losses), it is IMEP that the

driver “feels” whether driving down the motorway or sitting at idle. Heywood (1988) has noted that when the coefficient of variation ( $COV = \text{standard deviation}/\text{mean}$ ) in IMEP exceeds about 10%, there are driveability problems with the vehicle.

Studies have compared the use of IMEP to maximum pressure as a measure of CCV. Brown (1991) and Stone et al. (1992) found that CCV in IMEP was minimised as ignition timing approached MBT. Brown et al. (1996) confirmed this finding, and also found that the CCV in peak pressure and the angle at which it occurs decreased as timing was advanced. They concluded that the reduction in CCV of maximum pressure was a consequence of the pressure rise being due in part to piston motion. In the limiting case, timing could be so far advanced that combustion was always completed before TDC (assuming knock does not become a factor). This would result in smaller differences in peak pressure. At the other end of this spectrum, if timing were retarded and/or the burning rate was significantly slowed, the maximum pressure in the cycle would occur slightly before TDC, and would be due solely to piston motion during compression (as in the hook back region in Figure 2.1). In either case, the COV of maximum pressure would be small, yet in the case of retarded timing, the work output of the engine would vary widely. Furthermore, IMEP and maximum pressure may respond in opposite ways to any variation in the cycle. For example, suppose an engine is operating at MBT timing. If a particular cycle burns faster than the average cycle, this has the same effect as a slight advancement in timing. The IMEP in this case would fall due to more work being done on the charge during compression, whilst maximum pressure would rise since more of the charge burns before TDC.

Further adding to the confusion is the question of whether the parameter used to quantify CCV is an absolute or relative measure. Absolute measures include the “cyclic spread” of IMEP or maximum pressure, whilst relative measures would include things like the COV of IMEP or maximum pressure.

The foregoing discussion can best be clarified with an example similar to that given by Patterson (1966). Figure 2.2 shows the pressure-crank angle and pressure-volume traces for 6 cycles taken from the Oxford K4 engine operating at 1000 RPM at part load with an ignition timing of 15 degrees BTDC (details of this engine are given in Chapter 3). The three cycles on the left were taken under a fast burning condition whilst those on the right were taken under a slow burning condition. (These conditions were produced by varying the air-fuel ratio, i.e., the fast burning cases correspond to a stoichiometric mixture whilst the slow burning cases are very lean.)

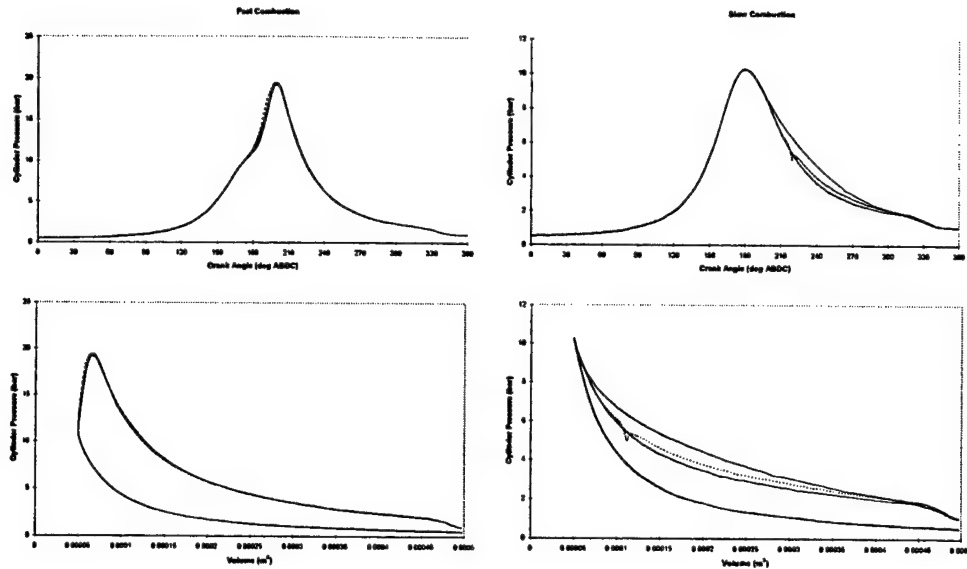


**Figure 2.2. Pressure-crank angle and pressure volume diagrams for fast (left) and slow (right) combustion taken from K4 engine.**

Each case in Figure 2.2 contains 3 cycles, and whilst these would not constitute a statistically valid sample from which to draw any conclusions, they do illustrate the care which must be taken in quantifying CCV. The cycles have been selected such that in the fast burning case, the maximum rate of pressure rise is twice as large as the maximum rate of pressure rise in the slow case. Specifically, the highest cycle in the fast case has a maximum rate of pressure rise of 0.66 bar/degree whilst in the slow case it is 0.33 bar/degree. Furthermore, the spread in the rate of pressure rise in the fast case is from 0.56 bar/deg to 0.66 bar/deg whilst in the slow case it is from 0.23 bar/deg to 0.33 bar/deg. Hence, the cyclic spread in these two cases is equal for this parameter, and if the spread in the maximum rate of pressure rise were being used to quantify the CCV, these cases would be judged to have equal cycle-by-cycle variation. However, if one were using a relative measure of maximum rate of pressure rise, the COV in the fast burning case is 8.2% whilst in the slow case it is 20.65%. On this basis, the fast case looks over twice as good.

If maximum pressure is used as the measure, the fast case has a spread of 0.19 bar whilst the slow case has a spread of 0.02 bar, an order of magnitude improvement for the slow burning case. On a relative basis, the COV of maximum pressure for the fast case is 0.51% and for the slow case 0.10%. Again, the slow burning case looks significantly more stable. However, the spread in IMEP for the fast case is 0.06 bar whilst in the slow case it is 0.52 bar. Converting this to relative measures, the COV of IMEP is 0.84% in the fast case and 16.47% in the slow case. These results are seen intuitively in Figure 2.2 where the areas enclosed by

the pressure-volume curves in the fast case have insignificant differences whilst in the slow cases the areas vary markedly. A summary of this discussion is contained in Table 2.1.

**Table 2.1. Comparison of CCV metrics for data shown in Figure 2.2.**

Factor	Fast Burn	Slow Burn	Minimum CCV
$\Delta dP/d\theta$	0.1 bar/degree	0.1 bar/degree	-----
COV of $dP/d\theta$	8.2%	20.65%	Fast Burn
$\Delta P_{max}$	0.19 bar	0.02 bar	Slow Burn
COV of $P_{max}$	0.51%	0.10%	Slow Burn
$\Delta IMEP$	0.06 bar	0.52 bar	Fast Burn
COV of IMEP	0.84%	16.47%	Fast Burn

The main point to be made from this discussion is that the conclusions which are drawn as to what does or does not affect CCV depend largely on the parameter used to measure the variation, and due care must be taken when analysing the results of a particular study. Furthermore, a particular measure may be more suited to a specific study because of the focus of that study. Patterson (1966) states that combustion rate is dependent on flame front area, and since pressure rise is strongly related to combustion rate, maximum rate of pressure rise should be used to quantify CCV. Matekunas (1983) notes that IMEP is not as closely related to flame propagation as the other measures, and that maximum pressure responds to cyclic variations in cylinder charging. Hence, his study uses maximum pressure to quantify CCV. In both of these studies, the primary focus was on combustion stability rather than overall engine stability. In the study by Brown, et al. (1996), the focus was on overall engine stability and the authors used COV of IMEP as their measure of CCV. Finally, there are studies such as Young (1980) which attempt to link combustion variations to variations in engine stability (IMEP). As would be expected, Young used several measures of CCV in that study.

It must be emphasised that the choice of measurement parameter is neither right nor wrong when viewed in isolation. The correctness of the parameter is found in the conclusions drawn from the study. For example, using peak pressure to quantify CCV when the study focused on engine stability would be questionable. The previous discussion highlights this since the slow burn case had stable peak pressures, but the engine output was not stable.

Since the work presented here is concerned with modelling engine performance, COV of IMEP will be used as the primary measure of CCV. Other parameters (maximum pressure, phasing of maximum pressure, and NO) will be referenced when validating the model. However, the IMEP will be the primary target parameter of the modelling.



### 2.3 Causes and influences of CCV

Over the years, several good reviews of CCV have been published (Patterson, 1966, Matsuoka et al., 1971, Young, 1981, Ozdor, et al., 1994). As the body of knowledge in this area has grown, it has become more challenging to establish some sort of taxonomy for organising the various factors surrounding CCV. One approach is to group the factors under general headings of the phase of the combustion process that they affect. It is generally agreed (Heywood, 1988) that the combustion process may be divided into the following stages:

- a) sparking and flame initiation,
- b) initial flame kernel development,
- c) turbulent flame propagation, and
- d) flame termination.

At any stage, there are many governing factors, and effects in one phase may carry over to the succeeding phase. Rather than trying to discern the causes of CCV at each stage, this work will follow the strategies adopted by Young (1981) and Ozdor, et al., (1994) in which general causes and influences are grouped under broader factors which may influence one or more of the combustion stages. These factors are:

- a) mixture composition: including air-fuel ratio, fuel type, mixture inhomogeneity, and residual fraction,
- b) physical factors: chamber geometry and compression ratio,
- c) cylinder charging,
- d) ignition factors: which may be further broken down into
  - ignition system factors such as type of system, spark jitter, ignition timing, and discharge characteristics
  - spark plug factors such as electrode shape, electrode orientation, and number and location of spark plugs,
- e) in-cylinder flow factors: turbulence intensity and scales, mean flow in plug gap, and overall flow pattern, and
- f) prior cycle effects.

There is some overlap between these categories. For example, the in-cylinder motion will affect the local mixture composition, which in turn affects the spark characteristics (Pashley, 1997). Furthermore, it is necessary to differentiate between a cause and an influencing factor. Causes refer to those factors from which CCV can arise such as variations in trapped mass, flame kernel development, spark discharge, turbulence, etc. Influencing factors consist of parameters such as spark plug location and orientation, fuel characteristics, etc. These parameters do not cause CCV in themselves, but rather affect the engine's susceptibility to variations in the causal factors. Even with these distinctions, there is some room for discussion as to which category a factor belongs. For example, although Ozdor treats relative air-fuel ratio ( $\lambda$ ) as an influence, the fact that CCV rises dramatically as the engine operation becomes leaner, primarily due to the decreased flame speeds associated with lean combustion, would lend support to placing this factor under causes. Nevertheless, the following work will utilise this distinction as it seems a logical method of providing some organisation to a large quantity of information.

### 2.3.1 Mixture composition factors

The air-fuel ratio exhibits a strong influence on CCV, and most research has indicated that this is a result of the changes in flame speed as the air-fuel ratio changes. Young (1981) noted that pressure variations are not as severe for fast burning cycles. He attributed this to the fact that in fast burning cycles, a large portion of the energy release occurs near TDC where volume changes slowly. Thus, the variations are primarily due to variations in combustion. On the other hand, slow burning cycles release more energy late in the cycle where combustion variations are accentuated by the rapidly changing cylinder volume. He thus identified a basic principle of CCV: any factor which increases the burn rate will decrease the level of CCV. This is one reason as to why the air-fuel ratio exhibits such a strong effect. Kuo (1990) noted that with decreasing equivalence ratio (leaner mixtures) the flame speed decreased. His study was based on two computer simulations, one a quasi-dimensional model and the other a multi-dimensional model. His results indicated that the laminar burning velocity and the flame propagation speed, defined as the time derivative of the flame radius, decreased at leaner mixtures. He attributed this decrease to the lower burned-gas temperature in lean mixtures. Shen and Jiang (1992) also reported that CCV decreased with a richer mixture, and attributed this to the fact that a richer mixture is easier to burn due to its higher minimum flame speed. Because of the relationship between air-fuel ratio and burning speed, air-fuel ratio can be considered as a cause of CCV.

Several researchers have noted a relationship between fuel type and CCV. Young (1981) focused on the reaction front speeds for various fuels as shown in Figure 2.3.

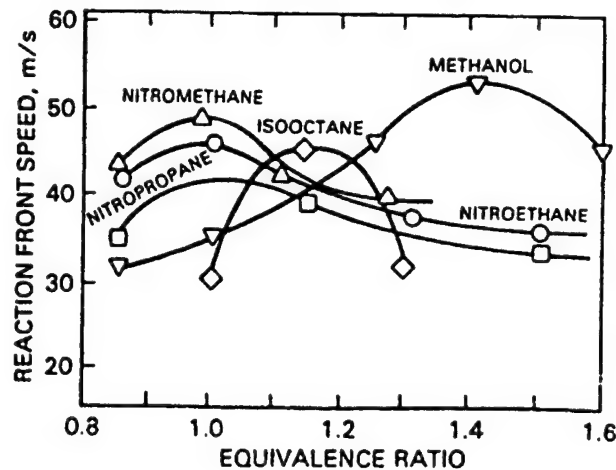


Figure 2.3. Reaction front speeds for various fuels (from Young, 1981).

Young noted that CCV should be minimised by faster burning fuels, and that the equivalence ratio at which this maximum speed occurred was different for each fuel. Hence, one would suspect that fuel type would have a strong influence on CCV at a specific air-fuel ratio. However, Lyon (1986) found that the relationship between fuel type and CCV was very minor, and different fuels produced a change in burn duration of roughly 2% at any given operating point. He conducted his study using fifty different blends of gasolines, some of which contained heavy aromatic compounds at much higher levels than commercial fuels over a range of equivalence ratios and ignition timings. Brown et al. (1996) performed tests on a Ricardo E6 engine utilising iso-octane, methanol, and toluene. They varied the ignition timing, compression ratio, equivalence ratio, and throttle setting, and found that the differences in COV of IMEP between the different fuels were largest at lean mixtures and retarded timings. They also noted that the slowest burning fuel (iso-octane) had the highest COV of IMEP, and that a change of 0.1 in relative air-fuel ratio ( $\lambda$ ) produced a greater change in CCV than did changing the fuel type. One further point of interest was that the CCV in IMEP was a minimum near the minimum ignition timing for best torque (MBT). They attributed this to a trade-off between: late ignition, which induced a higher laminar burning velocity since the additional compression prior to ignition resulted in a higher initial unburned gas temperature, and earlier ignition, which would lead to a decrease in turbulence during compression. Ellison, et al. (1968) studied the effect of tetraethyl-lead (TEL) on CCV. While TEL is effective in reducing knock, its effect was found to be due to a reduction in end gas

temperature rather than an increase in flame speed. Thus, once enough TEL has been added to a fuel to eliminate knock, further additions would have no effect on the extent of CCV.

Several studies have been done which examined the effect of in-cylinder mixing on CCV, however, these studies have produced conflicting results. Patterson (1966) noted that a gaseous propane-air charge produced lower levels of CCV than a normally carbureted mixture using liquid indolene. However, Soltau (1960) found no difference between a gaseous fuel and a liquid fuel sprayed into the intake manifold.

More recent work has been undertaken in this area by Grunefeld, et al. (1994) and Lee and Foster (1995). Grunefeld, et al. used Raman scattering to measure the bulk equivalence ratio on a cycle-by-cycle basis. A schematic of their experimental set-up is shown in Figure 2.4.

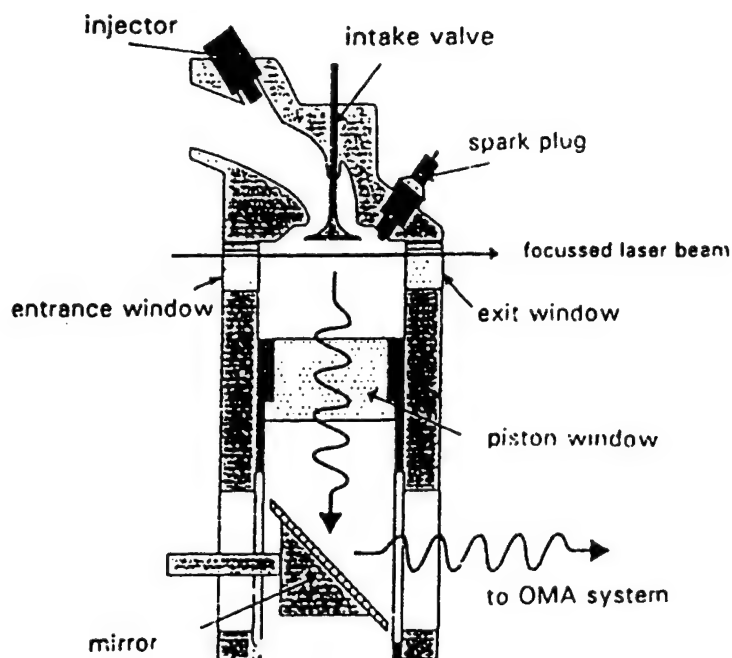


**Figure 2.4. Section of cylinder modified for Raman measurements (from Grunefeld, et al., 1994).**

The Raman technique provided information about the bulk equivalence ratio and the residual fraction in each cycle. Their results indicated a large variation in equivalence ratio and a correlation between the standard deviation of equivalence ratio and the standard deviation of the IMEP, as shown in Figure 2.5.

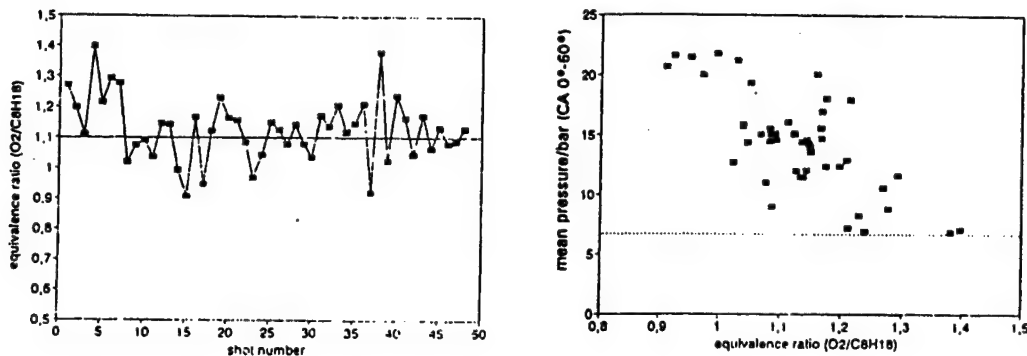


Figure 2.5. Cycle variations of equivalence ratio and scatter plot of equivalence ratio and mean pressure (from Grunefeld, et al., 1994).

Interestingly, Grunefeld et al. chose variations in IMEP to characterise the CCV. However, they defined IMEP as “the in-cylinder pressure averaged over the range 0°-60° CA after TDC”, and while admitting that this was not actually the IMEP for a cycle, they contended that it was a measure of IMEP. In fact, this correlates much better to maximum pressure than to IMEP as shown in Figure 2.6.

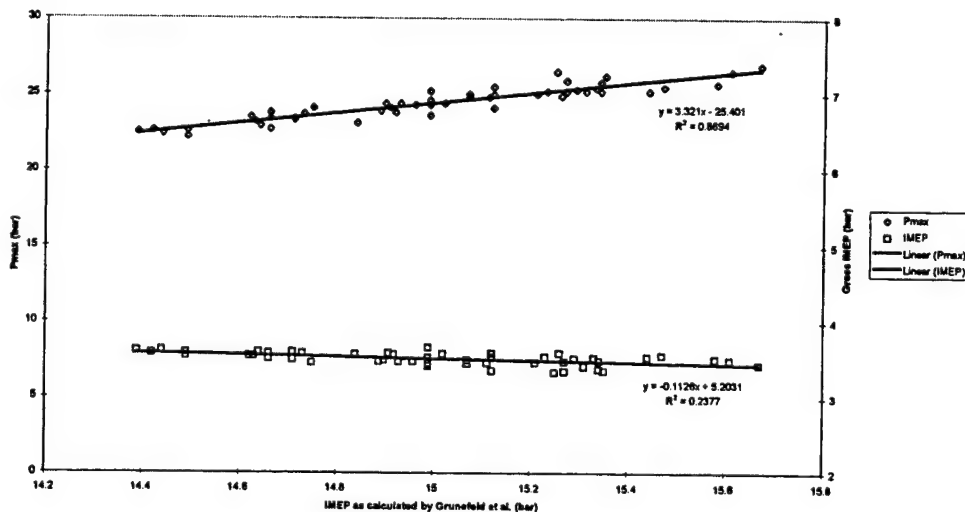


Figure 2.6. Comparison of IMEP and maximum pressure to Grunefeld IMEP.

Figure 2.6 was derived from 50 consecutive cycles of pressure data obtained from the Oxford K4 engine. The IMEP as defined by Grunefeld et al., along the x-axis, is plotted against maximum pressure, plotted along the left y-axis, and the gross IMEP, plotted along the right y-axis. A linear least squares fit is superimposed on the scatter plot in each case, and

indicates that the IMEP as computed by Grunefeld, et al. is a much more effective measure of maximum pressure. Peak pressure is a widely used measure of CCV, however, this case illustrates the care which must be taken by researchers in interpreting measures and results of CCV studies.

The study by Lee and Foster (1995) used Rayleigh scattering to measure variations in the air-fuel ratio in the vicinity of the spark plug gap. They performed their experiments on a single-cylinder optical-access engine, and looked at cases involving a homogeneous charge mixture and port injection. They also utilised a fibre-optic spark plug to measure flame arrival times, and from them to determine flame front expansion rate, convection direction and velocity, and flame kernel growth rate. Their results indicated that variations in the local equivalence ratio near the spark gap had no correlation with CCV.

In contrast to the Lee and Foster study, Berckmuller et al. (1997) used laser induced fluorescence (LIF) to measure the local fuel concentration in the vicinity of the spark plug. They performed their measurements on a lean burn, stratified charge engine. Their results indicated a strong correlation between variations in the fuel concentration near the spark plug and variations in pressure development.

It would appear that the three studies just reviewed provide conflicting information. However, the differences may be explained. First, Grunefeld et al. (1994) studied variations in the bulk equivalence ratio. A study by Shen et al., (1994) found that the initial spark-generated kernel size and mean temperature are completely determined by the breakdown energy and heat conduction from the burned region to the unburned gas. This would seem to imply that as long as the local mixture at the gap was ignitable, combustion would commence, and any variations in local equivalence ratio would have no effect until the flame kernel grew to sufficient size that inhomogeneities in the bulk mixture caused variations in flame propagation.

The difference in the results presented by Lee and Foster (1995) and Berckmuller et al. (1997) may be explained by noting the type of engine used for each study. Berckmuller et al. used a lean burn, stratified charge engine. Since this engine operates at very lean air-fuel ratios and is dependent on proper charge stratification for combustion, it would also be expected to be very sensitive to the initial flame development. Thus, their conclusion that variations in mixture strength near the spark plug strongly influence CCV might be expected given the unique operating characteristics of their research engine. On the other hand, Lee and Foster used a homogeneous charge engine with a disc-shaped combustion chamber. A disc-shaped combustion chamber generally produces slower rates of combustion due to quenching of the flame, especially at higher compression ratios (see Section 2.3.2). Thus, the cyclic variation in combustion in a disc-shaped chamber is more strongly effected by the

flame growth late in the cycle, and one could reasonably assume that initial flame growth would have a secondary impact.

Furthermore, whilst Lee and Foster examined the relationship between various metrics of CCV, they used variations in burn rate to quantify the CCV induced by variations in fuel concentration in the spark plug gap. Specifically, they used variations in the 1%, 10%, and 90% burn times (in degrees crank angle after ignition) which were calculated from a heat release computation. Several researchers (Douglas et al., 1997, Brunt and Pond, 1997, Brunt and Emtage, 1997) have highlighted the effects of errors and noise in the pressure measurements on calculated MFB. The noise in particular affects the MFB calculations, and whilst smoothing of the pressure data can help eliminate the noise, care is required to avoid introducing further errors due to the smoothing (Douglas, 1997). One can infer that these errors would make the short burn durations (1% and 10%) a dubious metric for quantifying CCV. On the other hand, Berckmuller et al. used variations in peak pressure as a metric. Noise in the pressure signal would tend to have a lesser effect on peak pressure since the signal-to-noise ratio is improved when the in-cylinder pressure is high. The point to be made here is that the studies used different metrics to quantify the effects of the same variable on CCV, and this also contributes to the different conclusions reached by these studies.

Early studies (Patterson, 1966) indicated that increasing the levels of residual gas had no effect on the CCV of an engine. This conflicts with the results of more recent studies (Young, 1981, Ozdor, et al., 1994, Pashley, 1997) which have indicated that increasing the level of residuals in the cylinder also results in increased levels of CCV. This anomaly is explained by the techniques which Patterson used whilst varying the residual level. As the residual level was increased, Patterson altered the throttle setting of the engine in order to maintain a constant IMEP. This would have the effect of maintaining a constant residual mass fraction, i.e., as the residual level rose, more air and fuel were inducted to maintain the IMEP.

Furthermore, increased CCV with increased residuals would seem to follow when the reasons for increasing residual levels are examined. The level of residuals may be increased either by increased exhaust gas recirculation (EGR) or by part-load (throttled) operation. EGR is used to reduce NO<sub>x</sub> formation and/or reduce throttling losses by lowering peak temperatures. Hence, in the light of Kuo's findings (1990), the lowered burned gas temperatures result in a slower flame propagation speed, and higher levels of CCV.

In addition to the CCV induced by high residuals due to the slower flame speed, there is evidence that there are cyclic variations in the level of residuals which influence CCV as well. Sztenderowicz and Heywood (1990a) operated a single-cylinder engine under skip-firing conditions. The purpose of skip-firing was to eliminate any residual gas nonuniformity. The results indicated that eliminating this nonuniformity had no detectable impact on flame

development, yet reduced IMEP fluctuations by roughly 50% under light load conditions. This led to a further study which examined the sources of IMEP fluctuations and reasons for their decrease under skip-firing conditions, and this will be addressed in the next section.

### 2.3.2 Physical factors

The shape of the combustion chamber has been shown to influence CCV. Young (1980) compared three different chamber shapes as shown in Figure 2.7.

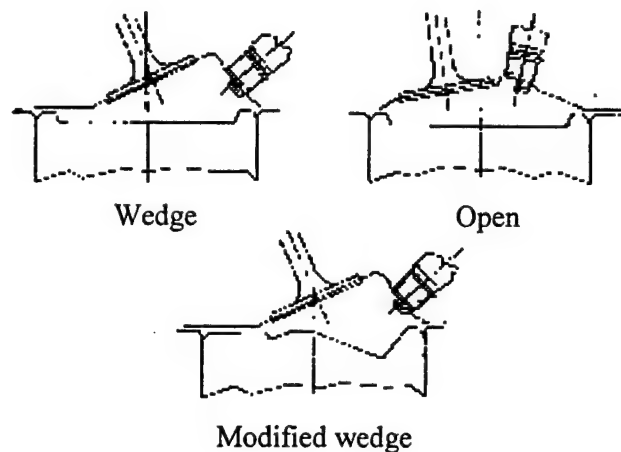


Figure 2.7. Combustion chamber geometries (adapted from Young (1980)).

He defined a chamber “openness” parameter, which was based on fitting Wiebe functions to plots of volume-burned fraction versus normalised flame radius. The chamber openness was then defined as the ratio of the parameters ‘a’ to ‘m’ of the Wiebe function, with a larger number indicating a more open chamber. He defined “squish” as the percentage of the total bore area for which the clearance between the piston and cylinder head at TDC was equal to the gasket thickness. His study showed that the more open a chamber was, the less CCV was evident. He attributed this to the fact that in an open chamber, the flame could propagate spherically with a minimum of interference and/or quenching from the chamber surfaces. This, he reasoned, led to a higher flame speed which results in more energy being released near TDC and better combustion-volume phasing. While squish contributed to a lower combustion duration, he found it to slightly increase the variation in combustion duration. Since increasing squish generates more turbulence, this would lead to faster flame propagation. However, this turbulence is random and would explain the increase in duration



variation despite the overall quicker burn. Again, since the squish generally decreased the burn duration, and hence improved the combustion-volume phasing, the increased variation may not have been seen in terms of engine stability since these variations would have occurred in a region of small piston motion.

Lucas and Brunt (1982) performed a similar comparison between a disc shaped chamber, a bowl-in-piston design, and the May Fireball chamber which was incorporated into the Jaguar V-12. The May chamber is shown in Figure 2.8.

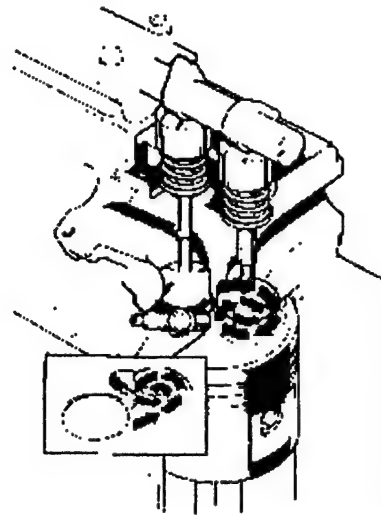


**Figure 2.8. May “Fireball” combustion chamber (from Stone (1992)). Inset shows underside view of swirl pattern.**

This chamber has a disc-shaped recess around the inlet valve, and a connecting, tangential passage to a larger disc around the exhaust valve. The tangential passage generates a high degree of swirl, whilst the flat-topped piston generates squish. These features were intended to ensure rapid and controlled combustion. Lucas and Brunt found that the May chamber decreased the burn duration by over 20% as compared to a disc chamber with the same compression ratio, and produced a 47% reduction in CCV. It is worth noting that peak pressure was used to quantify the CCV, hence, one can only conclude that the faster combustion chamber shape enhanced combustion stability. No data were presented for its effect on overall engine stability, although the inference is that more stable combustion will necessarily result in more stable operation.

Studies of the effect of compression ratio on CCV have proved inconclusive. Young (1981) notes a weak relation between increasing compression ratio and decreasing CCV in peak pressure. He noted that an increased compression ratio appeared to increase the

variation in flame speed, but also increased the average flame speed. These two effects would tend to hold the relative variations constant over a large range of compression ratio. Chanchaona et al. (1990) also found conflicting evidence of the effect of compression ratio. In this study, they compared a disc-shaped chamber to a bowl-in-piston design over a range of compression ratios. Their results are shown in Figure 2.9.

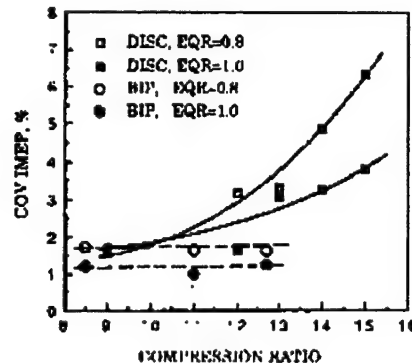


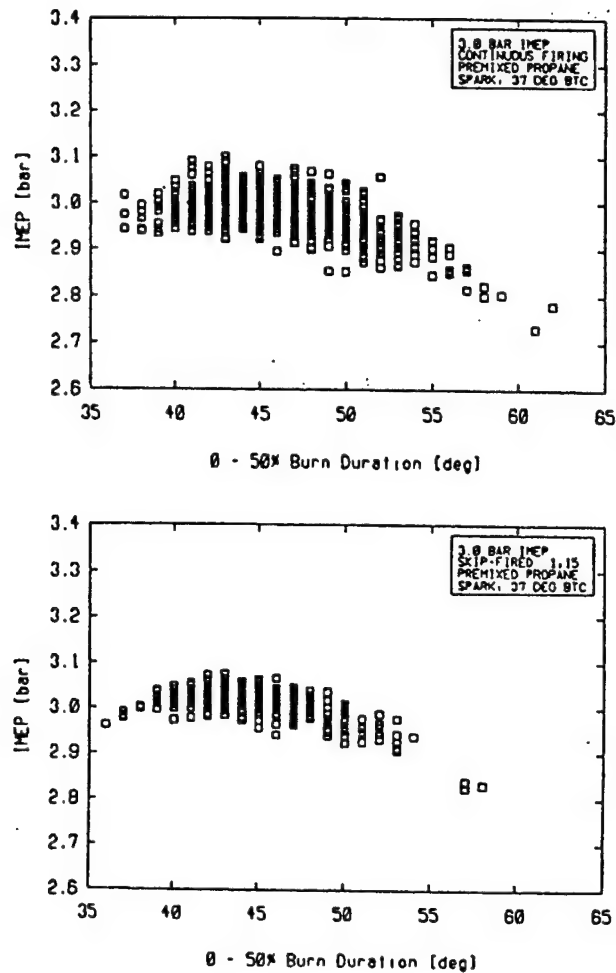
Figure 2.9. COV of IMEP versus compression ratio for disc and bowl-in-piston (BIP) combustion chambers (from Chanchaona, et al. (1990)).

Figure 2.9 seems to imply that increasing the compression ratio of a disc-shaped combustion chamber reduces the clearance height, and results in more quenching of the flame front and a longer combustion duration. However, the bowl-in-piston chamber shows no sensitivity to compression ratio in this study, and they concluded that the real effect was due to chamber shape and was not a function of compression ratio.

### 2.3.3 Cylinder charging

Variations in the efficiency with which a cylinder draws in a fresh charge is a cause of CCV. However, there are many factors which affect the charging process, and any variation in these factors results in a variation of the charge. A study by Sztenderowicz and Heywood (1990b) examined the impact of charging variations, and grew out of the work mentioned in the previous section. Their experiment involved operating a Ricardo Hydra single-cylinder engine at MBT with a stoichiometric mixture which was varied among premixed iso-octane, injected indolene, and premixed propane whilst continuously fired, and premixed propane whilst skip-fired. They then plotted the IMEP for individual cycles versus

the 0-50% burn duration, as that parameter gives an indication of the phasing of the burn. An example of their results is shown in Figure 2.10.



**Figure 2.10.** Scatter plots of IMEP versus 0-50% burn duration for continuous and skip-fired operation (from Sztenderowicz and Heywood, 1990).

The results clearly show a reduction in the variation of IMEP under skip-fired conditions, and the authors attributed this to a reduction in the variation of the trapped mass. They then concluded that for optimally phased cycles, roughly one-half to three-quarters of the IMEP fluctuations could be attributed to variations in the amount of trapped fuel. They also listed several factors which would contribute to variations in trapped fuel mass, none of which appear to dominate:

- a) Variations in the amount of fuel left in the cylinder from the previous cycle due primarily to variations in the oxidation of crevice masses late in the cycle. The variation in oxidation is thought to be caused by differences in flame geometry and its interaction with the crevice volumes.
- b) Fresh charge displacement due to variations in residual temperature. Specifically, by using a computer simulation, they determined that a change of 150 K in residual temperature induced a 2-3% change in volumetric efficiency. This, in turn, produces an equal variation in the mass of the fresh charge inducted.
- c) Variations in the fluid dynamics of the intake process due to the nature of the intake flow, in that it is unsteady, compressible, and separated. Furthermore, the processes of vaporisation and mixing in the inlet port of a fuel injected engine contribute to CCV.
- d) Variations in mass leakage past the valves and piston rings due to the non-repeatability of the valves and rings to seat in the same positions cycle-by-cycle.

They also took measurements of the residual mass fraction in the cylinder and found that the residual mass fraction showed little fluctuation cycle-by-cycle. Hence, displacement of the fresh charge by residuals was concluded to have little to no effect on CCV, the primary influence being due to the temperature of the residuals as mentioned previously. This conclusion has since been refuted by Berckmuller et al. (1997) who found that the residuals were not homogeneous. They also found significant fluctuation in the mixing of fresh mixture with the residuals on a cycle-by-cycle basis. Since these fluctuations can influence the local mixture composition in the vicinity of the spark plug, they can also induce cyclic variations in the initial kernel growth and subsequent variations in combustion.

### 2.3.4 Ignition Factors

Several factors involving the ignition system and spark plugs influence CCV. A study by Hamai et al. (1986) utilised three different ignition systems; a conventional spark ignitor (CSI) with a transistorised coil, a long duration spark ignitor (LDSI), and a pulsed plasma ignitor (PPI). They determined that CCV in the spark duration was due to fluctuations in spark path length which were caused by variations in the gas flow velocity at the gap. The LDSI system produced longer duration sparks, which helped to minimise CCV by shortening the heat release delay, defined as the time from spark initiation to the beginning of heat release.

Spark “jitter”, or CCV in spark timing, was examined by Young (1981) and found to be an insignificant factor. Furthermore, the advent of electronic breakerless ignition systems has virtually eliminated jitter as a source of CCV (Ozdor et al., 1994).

Whilst ignition timing is not a cause of CCV, it does influence the sensitivity of the engine to other factors. Several studies (Young, 1981; Pischinger and Heywood, 1988; Stone et al., 1992) have determined that CCV of IMEP is minimised when ignition timing is kept close to the minimum advance for best torque (MBT). This can be explained by reference to Figure 2.11.

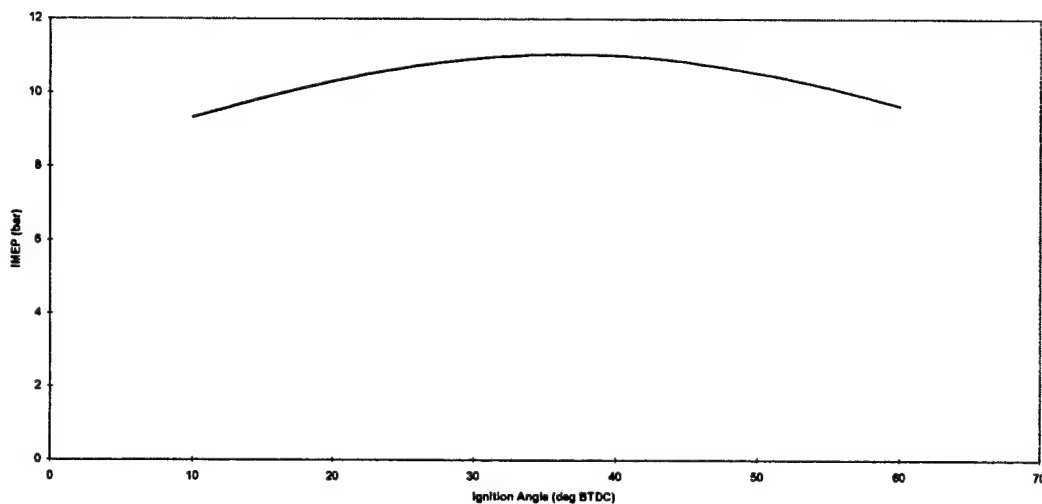


**Figure 2.11. Variation in IMEP as a function of ignition timing. Computer simulation of Rover K16 engine.**

Figure 2.11 was developed from a computer simulation of a Rover K16 engine operating at wide open throttle at 2000 RPM on a stoichiometric mixture of gasoline. As the figure shows, IMEP varies very little within a band of ignition timings within  $\pm 10$  degrees of MBT. Thus, when an engine is run at MBT, any apparent cyclic variation in timing due to fast or slow burning cycles has a small effect on IMEP. However, variations in burn rate at MBT do affect the maximum pressure to a greater degree, and highlights the need to specify which measure of CCV is being used.

The spark discharge characteristics also influence CCV. In general, a spark discharge can be broken into three phases (Heywood, 1988, Pashley, 1997):

- a) the breakdown phase: characterised by very short duration, low energy dissipation, but high power level
- b) the arc phase: caused by the discharge of the capacitance of the high voltage leads and coil and characterised by longer duration and higher energy dissipation
- c) the glow phase: which, depending on the type of circuit, deposits up to 90% of the energy into the circuit, yet due to the length of time (on the order of milliseconds) has very low power.

A study by Shen and Jiang (1992) concluded that maximising the breakdown energy results in a faster initial flame growth rate, and a resulting lowering of CCV. They achieved their increase in breakdown energy by increasing the spark plug gap, thus increasing the breakdown voltage, and found that for the non-resistor plugs used in this study, the increase in energy was directly proportional to the increase in plug gap. Increasing the energy deposited during breakdown did not produce higher temperatures. However, it did produce a larger plasma volume which then accounts for a reduced combustion initiation period (Heywood, 1988).

The number, location, orientation, and design of the spark plugs also influence CCV. Young (1981), while failing to find any relation between type of ignition system, spark duration, or spark energy and CCV, did find that the number and location of spark plugs had a large influence. This effect primarily manifests itself by reducing the flame travel times. For example, he noted that in the absence of in-cylinder motion, a centrally located plug would minimise CCV since it provides the minimum distance for the flame to travel in any direction.

Pischinger and Heywood (1990) performed a systematic examination of spark plug geometry effects. They defined a contact area fraction, which is the ratio of the electrode contact area to the instantaneous flame surface area, and calculated this from digitally enhanced Schlieren photos and assumptions about the flame shape and volume. They performed this analysis for standard plugs and thin electrode plugs. The cycle averaged results from 6 cycles are shown in Figure 2.12.

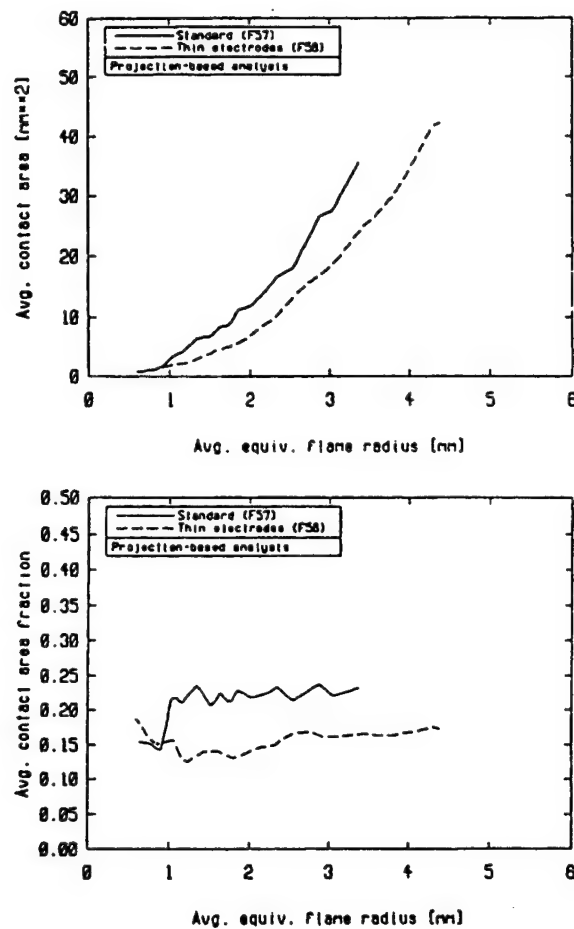


**Figure 2.12. Cycle-averaged contact area and contact area fraction for standard and thin electrodes spark plugs (from Pischinger and Heywood, 1990).**

Since the thin electrode plugs had less contact with the developing flame, the heat transfer to the electrodes was lessened. This produced faster initial flame growth, a faster overall burn, and a decrease in CCV. This study also found that the thin electrode plugs were more likely to operate in the arc discharge mode, which produced a longer discharge duration with a higher release rate of useful energy towards the end of the discharge. The effect of flame kernel displacement in the early stages of combustion was also examined in this study, and this topic will be discussed in the next section.

### 2.3.5 In-cylinder motion

In-cylinder motion is a very important factor governing CCV as it interacts with and influences several of the previously discussed factors, for example, the mixture composition and convection of the flame kernel. Turbulence may be defined (Lancaster et al., 1976) as “the fluctuating velocity component superimposed on the mean velocity of viscous fluid flow”. Turbulence is generally described by its scale and intensity: scale referring to a representative eddy size and intensity referring to the rms value of the velocity fluctuations at a point. Early work by Cole and Mirsky (1968) studied the effect of disturbing the combustion in a constant volume bomb with a laminar jet. Variations in turbulence were accomplished by varying the jet size (which alters the scale) and the jet velocity (which alters the intensity). They discovered that by disturbing the combustion with the jet, the rate of combustion rose, and they attributed 60% of this rise to an increase in flame area due to wrinkling. The remainder was attributed to increased mixture density and burning velocity. In fact, all studies reviewed by Young (1981) and by Ozdor et al. (1994) agreed that turbulence increased the rate of combustion primarily by increasing the area of the flame front, hence, turbulence would be expected to lower CCV.

However, there is a limit to the amount of turbulence which can be beneficially generated. LeCoz (1992) found two main processes affecting the initial stages of combustion: convection of the flame kernel by the large scale velocity field, and flame wrinkling by the small scale turbulence. Flame kernel convection results in the flame contacting the plug electrodes or, depending on plug location, the chamber walls. Discussion of the effects of flame kernel displacement will be deferred to the next section.

Once the kernel has grown larger than the turbulence length scale, the predominant factor becomes the turbulence intensity. This induces wrinkling of the flame front and increased flame speed. However, as turbulence increases, the increased speed due to wrinkling begins to be offset by an increase in flame stretch. Bradley et al. (1992) analysed the effect of flame stretch on turbulent burning. Their study assumed a turbulent flame front propagating in a Cartesian co-ordinate system as shown in Figure 2.13.



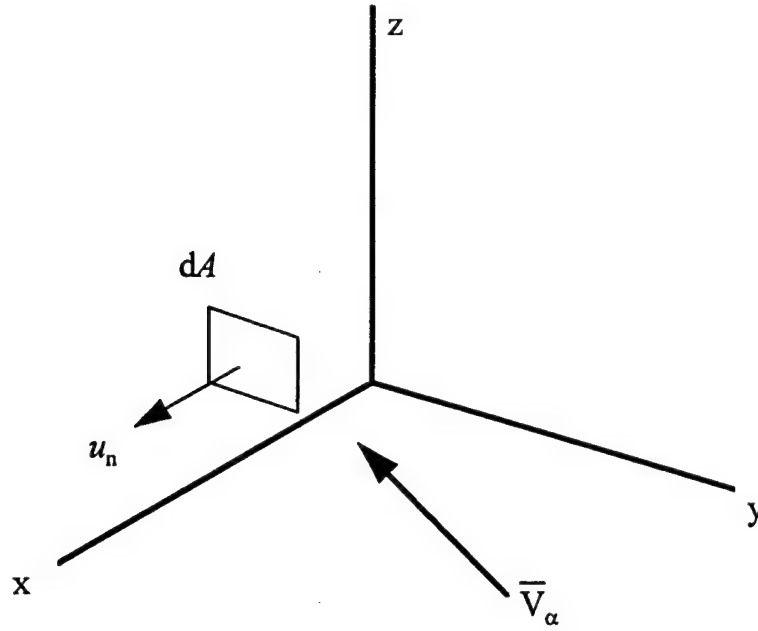


**Figure 2.13. Turbulent flame front propagation within fluid velocity field.**

The velocity of the flame surface normal to itself is the burning velocity,  $u_n$ , and the fluid velocity components may be described as  $\bar{V}_\alpha = (V_x, V_y, V_z)$ . Hence, the velocity components of the flame front are

$$U_x = u_n + V_x, U_y = V_y, \text{ and } U_z = V_z.$$

The flame stretch may then be given by

$$\frac{1}{A} \frac{dA}{dt} = \frac{u_n}{R} + \left( \frac{V_x}{R} + \nabla_t \bar{V}_\alpha \right),$$

where  $R$  is the radius of flame curvature. The bracketed terms in this equation represent the flow field contribution to flame stretch whilst the first term represents flame propagation and curvature contributions to flame stretch. As turbulence velocities increase, the bracketed terms increase relative to the first term, hence, the flame stretch is governed primarily by the flow field ahead of the flame. In other words, if turbulence increases beyond a certain point, the flame will stretch rather than propagate. This is due to the thinning of the flame front, and eventually it will lead to partial quenching of the flame.

As mentioned previously, a further effect of turbulence is to displace the flame kernel during its initial growth. Pischinger and Heywood (1990) found that, by varying the position of the flame kernel relative to the electrodes, the local flow field strongly influenced the heat loss from the developing flame as shown in Figure 2.14.

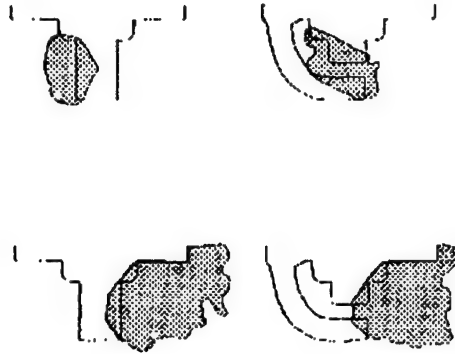


**Figure 2.14.** Flame boundaries traced 0.93 ms after spark onset (adapted from Pischinger and Heywood (1990)).

Figure 2.14 shows that, in the first case (top of figure), the kernel remained attached to the electrodes which resulted in a large contact area, increased heat loss, and slower flame initiation. In the second case, the kernel was convected away from the electrodes which lengthened the discharge channel, reduced heat loss, and resulted in faster flame initiation. These results were confirmed by Hacoheh et al. (1992) with a theoretical thermodynamic model of early flame growth. This model analysed the flame growth from the onset of the arc discharge, and included the input of electrical energy, combustion energy release, and heat transfer to the plug. Whilst many studies have been done on this topic in recent years, the conclusion of all of them is that variations in kernel motion give rise to variations in flame development and consequent variations in combustion.

While some turbulence results naturally from the intake process, this turbulence is of a random, or uncontrolled, nature and thus gives rise to CCV in combustion. As a result, many studies have been done on the means of generating long-lasting, large scale flow structures within the cylinder which will minimise variations in turbulence, while at the same time producing combustion enhancing turbulence.

Swirl is an axial motion generated about an axis parallel to the piston line of motion as shown in Figure 2.15.

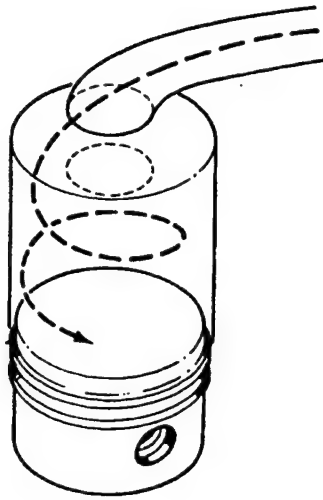


**Figure 2.15.** Swirl generation from tangential inlet passage (from Stone (1992)).

In this figure, the tangential inlet passage generates swirl which is less likely to vary. Other techniques include using a helical inlet port (Brandstatter et al., 1985) as shown in Figure 2.16.

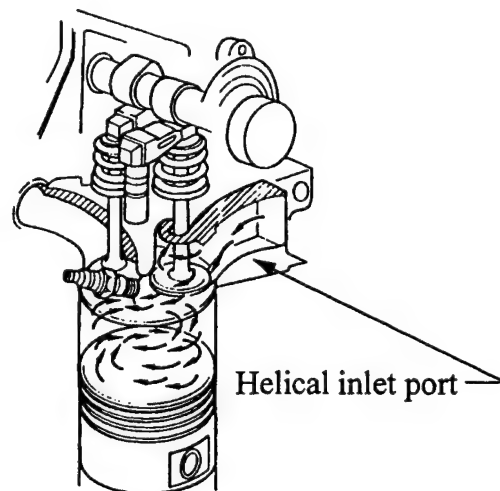


**Figure 2.16.** Swirl generation from helical port (adapted from Erjavec and Scharff (1992)).

In this arrangement, the helical geometry located directly above the valve seat imparts a swirling motion to the charge as it leaves the port. One advantage of swirl is that it generates turbulence later into the cycle (Belmont et al., 1994). The largest disadvantage to generating

swirl is that the kinetic energy required induces losses and reduces volumetric efficiency (Stone, 1992). This has led to the generation of barrel swirl, or tumble, which is motion about an axis perpendicular to the piston travel as shown in Figure 2.17.

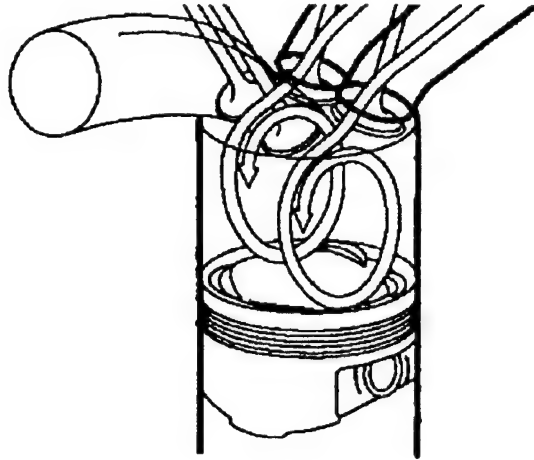


**Figure 2.17. Tumble generation in a pentroof chamber.**

Tumble also reduces the volumetric efficiency. However, by using a pentroof combustion chamber with two inlet valves, some of the lost volumetric efficiency can be regained (Stone et al., 1993). As the piston moves upward on the compression stroke, the swirl ratio increases due to conservation of angular momentum. Then, as the volume continues to decrease, the swirl breaks up into turbulence, ideally during the important early stages of combustion (Belmont et al., 1994). It has been suggested (Belmont et al., 1994) that the optimum situation is a combination of tumble and swirl which will produce a larger turbulence intensity throughout the cycle.

Matekunas (1983) studied the effect of three different swirl configurations on combustion. The three cases examined were: a conventional inlet port/valve, a conventional valve with a swirl port, and a shrouded valve with a conventional port. These three cases were designed to generate increasing levels of swirl. The swirl port imparted a rotational motion to the charge in the port. The shrouded valve directed the intake flow to produce a strong tangential component relative to the chamber wall. Because it partially masked the inlet flow area, the shrouded valve produced a higher velocity swirl but at a cost of reduced volumetric efficiency. The study also examined two spark plug locations at each swirl condition: one centrally mounted and the other mounted near the periphery of the wall. A plot of the standard deviation in the location of peak pressure is plotted against air-fuel ratio in Figure 2.18

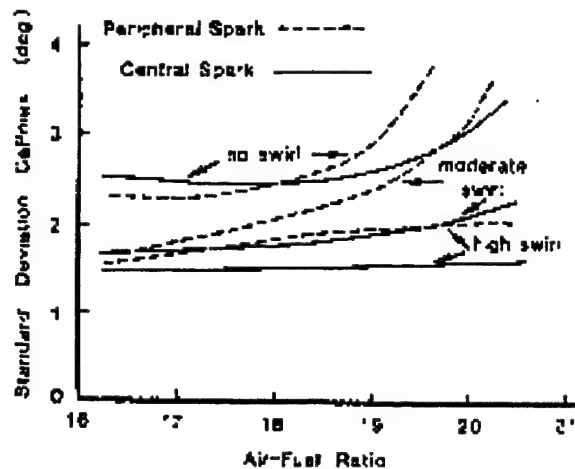


Figure 2.18. Standard deviation of crank angle of maximum pressure versus air-fuel ratio (from Matekunas, 1983).

Several points were made from these results. First, increasing swirl from zero to a moderate level resulted in a marked reduction in the CCV of pressure phasing. This would indicate less variation in combustion initiation and duration. Increasing the swirl to the high level brought little additional benefit when the mixture was near stoichiometric. However, the high swirl condition showed less sensitivity to increasingly lean mixtures. The central plug location was also found to have less variation in combustion phasing than the peripheral plug, since a central plug location minimises flame travel distance and shortens combustion duration. Furthermore, even when the flame kernel has grown large enough to avoid displacement by the flow, the large scale flow does impart a preferential burn direction to the flame. If this situation is not considered by a designer, the swirl could well induce the flame to grow into a chamber wall with detrimental effects on both combustion stability and unburned hydrocarbon emissions.

Stone et al. (1993) examined the effect of disabling one inlet valve of a 4 valve, pentroof combustion chamber. The engine used for the tests had the specifications shown in Table 2.2.

**Table 2.2. Engine specifications (Stone, et al., (1993))**

Bore	84.5 mm
Stroke	89.0 mm
Compression ratio	10:1
Inlet valve opening	18° BTDC
Inlet valve closing	46° ABDC
Exhaust valve opening	52° BBDC
Exhaust valve closing	12° ATDC

Initially, steady flow tests were performed on cylinder number 4 with the disabled valve fixed open at 1 mm. This was done in anticipation of actual engine tests in which the inlet valve was disabled by grinding down the appropriate cam lobe to 1 mm above its base circle. This allowed 1 mm of lift on the disabled valve to preclude fuel puddling, as the engine was port fuel injected. The flow rig consisted of a centrifugal fan with an inlet throttle to control flow, and the flow rate was measured by the pressure drop across an orifice plate. The results of the steady flow measurements are shown in Table 2.3.

**Table 2.3. Steady flow rig measurements (from Stone, et al., 1993).**

Valve operation	Mean flow coefficient	Ricardo swirl ratio	
		Barrel	Axial
Both	0.53	0.45	0.02
Inner	0.33	0.85	1.40
Outer	0.32	0.81	1.21

When both valves were operated, there was virtually no axial swirl whilst valve disablement induced a large increase. Inlet valve disablement also induced a large increase in barrel swirl (tumble). A swirl torque meter was used to measure the swirl axis inclination, and it was concluded that the two types of swirl could be considered to be a single vortex rotating about an inclined axis.

Engine testing was performed over a range of load-speed conditions, and the results indicated that inlet valve disablement led to:

- a) a 23% reduction in burn duration,
- b) an average of a 5.6% reduction in brake specific fuel consumption, and

- c) a reduction of up to 3 percentage points in the COV of IMEP.

To summarise, turbulence can be considered as statistical fluctuations of the flow about some mean flow velocity. The fact that turbulence is itself of a random nature tends to cause some level of variation in combustion. However, turbulence also tends to reduce CCV through an increased flame speed and reduced combustion duration. When the turbulence is combined with an ordered mean flow, e.g., tumble or swirl, the combustion variations induced by turbulence variations are further reduced.

### 2.3.6 Prior cycle effects

Prior cycle effects do influence CCV by impacting several of the aforementioned factors. Belmont et al. (1986) first noted that CCV exhibited a “memory” element, and misfired cycles tended to break this memory chain. Martin et al. (1988) studied burn modes and prior cycle effects on CCV. They noted that at stoichiometric conditions, prior cycles had little effect on CCV. However, as the mixture became leaner, prior cycle effects increased. Specifically, misfires tended to be followed by cycles with high IMEP, and low IMEP cycles tended to be followed by strong cycles. They explained this by noting that a cycle which follows a misfire will have residuals with a higher concentration of unburned fuel than a cycle which follows a normal cycle. This was also noted by Sztenderowicz and Heywood (1990), and they concluded that the “memory” element was due to the composition of the residual mass from the previous cycles. By breaking the memory chain by skip firing, Sztenderowicz and Heywood also demonstrated a reduction in CCV.

This phenomenon has led to work on predicting next-cycle combustion with the aim of reducing CCV (Stevens et al., 1992). In this work, 500 cycles of pressure data were recorded and divided into two groups. The first group was the “library” group, and patterns were developed within this group by differencing various parameters cycle-by-cycle. The differences in parameters in the second set of 250 cycles were then predicted based on the patterns established in the library group. It was found that the Work Mean Effective Pressure (WMEP), which has historically been referred to as the gross IMEP because it is calculated only over the compression and expansion strokes, was found to yield the best predictions. Results were most promising at very lean conditions, where the variations in residual mass characteristics dominated the CCV. The lack of any published work in this area since 1992 would seem to indicate that implementing this strategy was impractical.

## 2.4 Computer modelling of cycle-by-cycle variation

### 2.4.1 Introduction

Recent advances in computer power have made computer simulation, or modelling, of engine processes much more attractive. There are obvious benefits in being able to simulate engine performance instead of having to build, instrument, test, and analyse an actual engine. Hence, computer modelling offers savings in both time and money. However, the processes occurring in an internal combustion engine are extremely complex. For example, considering a fuel injected spark ignition engine, the processes which might have to be modelled include:

- a) unsteady flow in the induction system,
- b) flow through the inlet valve(s),
- c) dynamics of the injection system,
- d) combustion,
- e) emissions including NO, unburned hydrocarbons, CO, and CO<sub>2</sub>,
- f) heat transfer within the combustion chamber and to the cooling media, and
- g) unsteady flow in the exhaust system.

Furthermore, in many areas, understanding of these processes at a fundamental level is inadequate (Heywood, 1988). As a result, most models require empirical relations or approximations in order to provide good agreement with actual engine performance. Attempts to fully model all engine processes would tend to diminish the time and cost savings inherent in computer simulations. Hence, current computer models tend to focus on one aspect of engine performance, and either model that aspect in isolation in order to gain insight into the underlying fundamentals, or couple it to simplified models of other processes in order to maintain computational efficiency. An example is the use of computational fluid dynamics (CFD) to model the three-dimensional flow details within the cylinder. These are often coupled to simple combustion models, and the focus of the models is on turbulent flow details rather than overall engine performance.

The vast majority of engine performance models can be classified as mean-cycle models. These models attempt to predict engine performance on the basis of a mean cycle, which is generally computed by ensemble averaging the pressure-crank angle histories of numerous engine cycles. There are obvious time savings in this method since only one cycle



need be modelled, namely the mean cycle. However, such models are completely incapable of providing any insight into the origins or consequences of cyclic variation in the engine. Hence, there has been recent interest in cycle-by-cycle modelling, in which the variability inherent in engine performance can be studied in detail.

In light of the aim of the current work, models have been selected for review which attempt to model the cyclic variation in combustion and relate these variations to the experimental variations derived from actual engine data. Because of the many causes and influences of CCV discussed in the preceding section, the challenge in modelling CCV is to select model parameters which will encompass a majority of these causes. Again, any attempt to incorporate all causes at a fundamental level would result in such a computationally complex model that the time and cost savings would be dissipated. Recent studies have generally selected one or more parameters which were allowed to vary cycle by cycle. It was hoped that the selected parameters would enable the model to reproduce the level of CCV experienced by the target engine. Since the researchers currently reviewed took several different approaches to this challenge, it seems expedient to organise the following discussion on the basis of the fundamental phenomena which were selected to model the CCV. They fall into three broad categories:

- a) flame kernel displacement models,
- b) turbulent propagation models, and
- c) general thermodynamic models

#### **2.4.2 Flame kernel displacement models**

The models in this category proceeded on the assumption that variation in the position of the initial flame kernel would account for the majority of the CCV in engine performance parameters (IMEP, peak pressure, crank angle of peak pressure, etc.). All of the models in this section and the next utilised a turbulent-entrainment, or eddy burn-up model, based on the work of Blizard and Keck (1974) and Tabaczynski, et al. (1980). Due to the popularity of this combustion model, a brief discussion of its basic form is in order.

The model is based on two zones within the combustion chamber, one containing unburned charge and the other containing the burned gas. The model is a phenomenological, thermodynamic, quasi-dimensional model which accounts for the effect of intake generated turbulence (swirl and tumble) and chamber geometry (by assuming a spherical flame front) on burning rate. Being a phenomenological model, each researcher in this review made slight modifications to the basic model in order to adapt it to the particular focus of their study, and

these modifications will be highlighted as required. The burn rate is determined from the following differential equations:

$$\frac{dm_e}{dt} = \rho_u A_f \left( \alpha \sqrt{\frac{\rho_u}{\rho_b}} u' \left( 1 - e^{-\frac{r_f}{\tau_c}} \right) + S_L \right) \quad (2.1)$$

$$\frac{dm_b}{dt} = \frac{m_e - m_b}{\tau_c} + \rho_u A_f S_L \quad (2.2)$$

where

$m_e$  is the total mass entrained by the flame

$m_b$  is the total burned mass

$\rho_u, \rho_b$  are the densities of the unburned and burned gases, respectively

$A_f, r_f$  are the area and radius of a spherical flame front required to entrain  $m_e$

$\tau_c$  is on the order of the integral length scale

$u'$  is the turbulence intensity

$S_L$  is the laminar flame speed

$\tau_c$  is the chemical time for eddy burn-up

$\alpha$  is a constant.

The model employed by Stone et al. (1996) modified the combustion model by allowing for variations in the ignition site (spark location), which they reasoned was a good representation of the flame kernel displacement. The engine used in the study was a Ricardo E6, and the combustion chamber was modelled as a simple disc. Since the researchers had no data on the actual movement of the flame kernel, the spark location was assumed to have a distribution as shown in Figure 2.19.

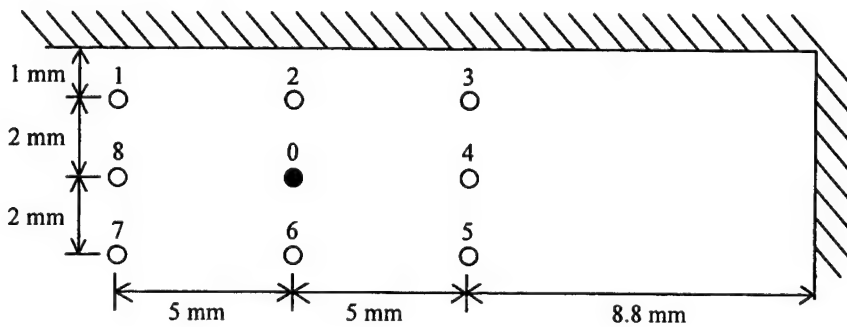


Figure 2.19. Assumed distribution of ignition sites (from Stone et al., 1996).

They evaluated the effectiveness of the model by comparing predicted and experimental values of the COV of the following parameters: IMEP, peak pressure, crank angle of peak pressure, 0-10% burn duration, 0-50% burn duration, and 0-90% burn duration. They found good qualitative agreement between the model and the engine in the response of the CCV to variations in ignition timing, air-fuel ratio, and throttle setting. Certain cases produced good quantitative agreement, but the tendency was for the model to underpredict the CCV. This underprediction was attributed to the fixed schedule of kernel displacement necessitated by the lack of actual data, and was most significant in cases where the laminar burning velocity was low (weak mixtures and throttled operation). When the laminar burning velocity is low, the flame kernel will be displaced further before it reaches a size at which it is no longer convected by the flow. Nonetheless, the study did show that flame kernel displacement was a significant contributor to CCV.

A similar study by Holmstrom and Denbratt (1996) also modelled the effects of flame displacement. The combustion model in this case was modified by incorporating random motion of the flame kernel centre. This was accomplished by using a method which produced a uniform distribution of a point on a sphere. If the point was outside the co-ordinates of the chamber boundaries, the calculation was performed again until the point remained within the combustion chamber. Then, the mean flow velocity was superimposed on the flame centre causing it to move downstream. This was done as a result of in-cylinder flow measurements on the engine involved. The flame centre was again constrained from leaving the combustion chamber. If the centre position hit the wall, it was allowed to move downwards (towards the piston crown). Once the flame kernel grew to the size of the turbulence integral length scale, its position was fixed for the remainder of combustion.

They characterised the CCV with the COV of the same parameters used by Stone et al. (1996). This study found that the random walk of the flame centre had the same effect on combustion in both stoichiometric and lean operation since heat losses to the electrode were not accounted for. Furthermore, they concluded that the flame kernel displacement accounted for approximately 20-30% of the variation in the standard deviation of the experimental parameters. They purposely did not allow any other combustion factors to vary cycle-by-cycle so as to estimate the magnitude of kernel displacement effects.

### 2.4.3 Turbulent propagation models

Whilst the models in this category do allow for displacement of the flame kernel, they are more extensive models in that they allow more factors to vary on a cyclic basis. Both

models reviewed here have modified the basic turbulent entrainment model to allow the residuals calculated on one cycle to be used as input for the next cycle.

Brehob and Newman (1992) used the General Engine Simulation (GESIM) program for their investigation. Normally, the model is a steady-state model. In other words, the model simulates several successive cycles until the results from one cycle suitably approximate the results of the previous cycle. The converged results are the ones used in comparison with engine measurements. Hence, the measured parameters used for comparison are usually the average of a large number (200-500) of cycles. The model, as normally implemented, gives no information about the cyclic variation of the measured parameters. This was overcome in the present study by limiting the number of cycles GESIM is to run with any given set of input data to one cycle, and ignoring the convergence criteria. Experimental data was taken from a single cylinder Ricardo Hydra engine at two operating points.

In order to induce the cyclic variation in the model, the following parameters from Equations 2.1 and 2.2 were varied randomly:

- a)  $r_c$ , the turbulence integral length scale,
- b) flame kernel offset from the spark plug, and
- c)  $\alpha$ , the constant in equation 2.1.

These factors were chosen for the following reasons. The integral length scale influences the early burn period as it defines the point at which the kernel position becomes fixed and wrinkling of the flame front begins. The flame kernel offset primarily effects the later stages of burning since the point at which the advancing flame front contacts the chamber wall is determined by its initial position within the chamber. The parameter  $\alpha$  affects both early and late stages of the burn, and this can be explained with reference to equation 2.1. The quantity in brackets in equation 2.1 is the total flame speed. The exponential term in this expression is based on the premise that the early flame growth should not be significantly affected by the turbulence until the flame kernel grows to a size on the order of the integral length scale. Once at that stage, the value of  $\alpha$  influences the rate of turbulent flame propagation, and hence the burn parameters used to quantify the CCV. This parameter was chosen as a means of allowing the turbulence to vary cycle-by-cycle.

The CCV computed by the model was quantified by the IMEP, peak pressure, crank angle of peak pressure, and the burn durations for 0-2%, 0-10%, 10-90%, and 0-90%. The unique feature of this study was that the comparison was not done with a single measure such as the COV. Instead, the simulation was used to generate frequency distributions of the

parameters of interest, and these distributions were compared to the experimental distributions in terms of magnitude (mean), spread (standard deviation), and shape (skewness).

Determining the variation in the model parameters was achieved through various means. The variation in integral length scale ( $r_c$ ) was determined by performing a series of GESIM runs over a range of  $r_c$  values. Based on these runs, a relationship was determined between  $r_c$  and the crank angle of peak pressure. A frequency distribution was then developed for  $r_c$  and was used as an input to GESIM. The frequency distribution for flame kernel offset was chosen to match the frequency distribution of the experimental 10-90% burn duration, due to the effect of flame kernel offset on later stages of combustion. The frequency distribution for  $\alpha$  was determined in a manner similar to the one employed to determine the distribution for  $r_c$ . Initial tests were performed by allowing one of the three input parameters to vary according to its frequency distribution whilst holding the other two constant. A final test was performed in which all three parameters were allowed to vary.

By perturbing  $r_c$ , the frequency distribution of the early burn parameters (0-2% and 0-10%) could be closely matched with experimental distributions. However, the main burn period (0-90%) was relatively unaffected, and they concluded that variations in  $r_c$  alone could not be used to model CCV. Variations in spark kernel offset alone were also found to be incapable of modelling the CCV, although good matching was achieved in the frequency of the 10-90% burn duration. Likewise,  $\alpha$  alone did not give proper distributions of all parameters. By perturbing all three parameters simultaneously, the model was able to match the frequency distributions of both the burn rate parameters and the pressure parameters.

The study by Shen et al. (1996) expanded the turbulent entrainment model and incorporated some good features from the previously reviewed models. First, they incorporated a previous model of initial flame kernel size and temperature (Shen, et al., 1994) which varied from cycle to cycle. Also, the flame shape was not constrained to spherical propagation, but an ellipsoidal flame front could be assumed depending on the magnitude of the convection velocity and flame growth rate. The flame centre shift was not varied randomly as was done in the previous studies. Instead, an empirical relation based on the work of Beretta et al. (1983) was used, and accounts for kernel displacement based on in-cylinder flow measurements. Turbulence intensity was also varied cycle to cycle. Pressure data from the engine being modelled was used to determine the values of  $\alpha$  and  $r_c$  in equation 2.1, and the model used gas convection velocities measured with a fibre-optic plug as an input.

This study again quantified the CCV with the same parameters as the previous studies, and used frequency distributions to compare the model to experimental results. The study found that variations in turbulence intensity were the dominant effect. The turbulence

variations in the small region near the plug gap varied more cycle-by-cycle than did the average turbulence in the cylinder. Hence, as flame size increased, combustion variations decreased as the flame grew out of the region of highest variability since the local variations tended to be integrated over the larger flame front.

#### 2.4.4 General thermodynamic models

The models in this category are based on an application of the first law of thermodynamics solved on a crank-angle basis. They do not model flame propagation or the geometric features of the combustion chamber. Nonetheless, this type of model can produce good results if good empirical correlations are available.

The model developed by Daw et al. (1996) inputs variations in air-fuel ratio, residual fraction, and combustion efficiency. The air-fuel ratio is perturbed by assuming a Gaussian distribution about the as-fed mean value. The combustion efficiency is defined as a function of the air-fuel ratio, hence, its cyclic variation is a direct result of the perturbations in air-fuel ratio. Finally, the residual fraction level was also perturbed randomly. The authors assumed this would account for prior-cycle effects, however, no indication was given that the residual levels from one cycle were fed forward into the next.

Since the combustion efficiency was a non-linear function of air-fuel ratio, this induced non-linearities in the model output, and caused bifurcation of the heat release diagrams. The CCV was quantified by the cyclic heat release and was compared to experimental heat release histograms. The authors stated that the experimental heat release was calculated in a manner “similar to Rassweiler and Withrow”. However, they gave no indication of how this calculation was performed. Their results indicated good agreement between the model and experiment in a statistical analysis of the cycle-by-cycle heat release.

The model proposed by Roberts et al. (1997a) and Peyton Jones et al. (1997a) is also based on the Rassweiler and Withrow method of computing mass fraction burned (MFB). Using the Rassweiler and Withrow method, the mass fraction burned is computed from the pressure trace and is given by

$$x = \frac{\sum_0^i \Delta p_c^*}{\sum_0^N \Delta p_c^*} \quad (2.3)$$

$$\text{where } \Delta p_c^* = \left( p_{i+1} - p_i \left( \frac{V_i}{V_{i+1}} \right)^n \right) \frac{V_i}{V_{TDC}} \quad (2.4)$$

A complete discussion of this method is given in Chapter 4. In this case, the authors use the method in reverse, i.e., instead of analysing a pressure trace to compute mass fraction burned, they input a computed mass fraction burned and use the method to build the pressure-crank angle history. To generate the MFB curves used as model inputs, the study calculated an ensemble mean pressure trace from 500 cycles of engine data. The conventional Rassweiler and Withrow analysis was used to calculate the beginning and end of combustion, and the burn duration ( $\Delta\theta$ ). Two models were used to generate the MFB curves. First, a Wiebe function was employed, and this has the form (Heywood, 1988)

$$x_b = 1 - \exp \left[ -a \left( \frac{\theta - \theta_o}{\Delta\theta} \right)^{m+1} \right] \quad (2.5)$$

where

$\theta_o$  is the beginning of combustion,

$\Delta\theta$  is the combustion duration, and

$a$  and  $m$  are adjustable parameters which govern the shape of the curve.

The second method was a logistical model, and has the form

$$x_b = \frac{1}{1 + \exp[-B_j(\theta_i - (M_j + \theta_{SOB}))]} \quad (2.6)$$

where

$\theta_{SOB}$  is the crank angle at ignition, and

$B_j$  and  $M_j$  are adjustable parameters governing the shape of the curve.

The parameter  $M_j$  is the inflection point in the MFB curve, and also corresponds to the point of maximum slope and 50% mass fraction burned. The adjustable parameters ( $a$  and  $m$  for the Wiebe function,  $B_j$  and  $M_j$  for the logistical model) and the normalised pressure rise due to combustion (which is the term in the denominator of equation (2.3)) were then calculated for each cycle of data. This calculation was done by minimising the least squares error between the actual pressure trace and the pressure calculated by running Rassweiler and Withrow in

reverse. Having fitted the parameters to each cycle, the model was run to recreate the actual series of pressure traces from the experiment. Their results showed good agreement between the model and experiment. This exercise demonstrated that a majority of the CCV in pressure related parameters (on the order of 80% according to the study) could be modelled by varying the shape parameters and the normalised pressure rise due to combustion.

Having demonstrated that the majority of the CCV could be modelled by varying the shape parameters and the normalised pressure rise due to combustion, this study was continued (Roberts et al., 1997b, Peyton Jones et al., 1997b). In this case, the adjustable parameters were assumed to have a Gaussian distribution, and these distributions were used to perturb the generated MFB curves. These curves were then used in the reversed Rassweiler and Withrow model to generate pressure traces which were compared on a statistical basis to experimental data. The results showed good agreement in the mean and standard distribution of the pressure curves.

Of great interest to the work here was a study conducted by Raine et al. (1995). In this study, Raine proposed a modification to the cycle simulation used by the Oxford Internal Combustion Engine Group to enable it to perform cycle-by-cycle modelling. The details of this simulation are given in Chapter 4. His hypothesis was that variations in burn rate would allow the simulation to model the cyclic variation in IMEP, maximum pressure, and phasing of maximum pressure. The experimental data in the study were taken from a gas-fuelled, in-line 6-cylinder engine described by Mendis et al. (1993). His results showed that the simulation tended to under predict the CCV in the experimental data, and he concluded that burn rate information alone was insufficient to encompass the many causes of CCV.

## 2.5 *Summary*

This section has reviewed the measurement of CCV, the causes and influences of CCV, and recent methods of modelling CCV. Several conclusions can be reached from this review. First, since this study is concerned with modelling overall engine performance, as opposed to combustion performance, the COV of IMEP will be used as the primary metric in quantifying the CCV of the experimental engine. Second, due to the large number of factors causing CCV, it is impractical to attempt to perturb each factor at a fundamental level within a computer model. Instead, factors must be identified which can capture the effects of several fundamental causes. In all modelling cases reviewed, the authors selected certain model inputs to be perturbed. The perturbations generally were assumed to have a Gaussian distribution, and as such were easily implemented into the models. Since the objective of this work is to modify the current simulation used by the Oxford Internal Combustion Engine



Group, and this simulation is in the category of a general thermodynamic model, the factors which may be considered for perturbation are limited.

Finally, within a thermodynamic model, the most sensible parameter to perturb is the burn rate. However, the results of the studies by Raine et al. (1995), Roberts et al. (1997b), and Peyton Jones et al. (1997b) indicate that burn rate information alone is not sufficient to adequately model the CCV in combustion or engine performance. Burn rate would be expected to encompass the effects of mixture composition (especially air-fuel ratio), initial flame kernel development, and to some degree, the effects of turbulence. It cannot be expected to account for phenomenon such as variations in cylinder charging (the mass of fuel burned). Flame kernel displacement also influences the quenching of the flame in the latter stages of combustion, and as this would result in incomplete combustion, the burn rate information would not capture this effect either. This is due to the fact that the Rassweiler and Withrow method normalises the MFB to 100% in all cases.

These conclusions have led to two hypothesis, and two courses of investigation. First, the Rassweiler and Withrow method of burn rate analysis may not be robust enough to accurately reflect the true variations in combustion, particularly during the late stages of combustion. Thus, the work will examine two alternative methods of burn rate analysis. The first method examined will be based on a two-zone combustion model that assumes combustion can be modelled as a polytropic process. The second alternative is a modification to the Rassweiler and Withrow method that incorporates both the expansion and compression indices throughout the combustion period. The examination of these methods is contained in Chapter 5.

The second hypothesis is that combustion is not complete on each cycle. Since the Rassweiler and Withrow method normalises the MFB curve to 100%, this effect is not captured by the analysis. However, the information concerning completeness of combustion is postulated to be contained within the Rassweiler and Withrow analysis. Thus, Chapter 6 of this work is devoted to deriving a completeness of combustion parameter based on the Rassweiler and Withrow method.

Before delving into the examinations in Chapters 5 and 6, the groundwork will be laid for the experimental data taken and the models used for analysis. Chapter 3 is a discussion of the experimental apparatus used throughout this portion of the work. Chapter 4 comprises two sections. The first section is a description of the models used in this work. The first model is a combustion analysis program that was used to analyse the experimental pressure data. This program was written specifically to support the work being done. The next section is a derivation of the Rassweiler and Withrow method as it is normally implemented on a personal computer. Finally, the cycle simulation used to model the experimental data is described. Chapter 4 also describes a repeat of the experiment performed by Raine et al.

(1995). This was done for two reasons: first, to validate the conclusion reached by Raine in his study, and second, to establish a baseline of performance for the experimental engine used in this work.

## Chapter 3 Experimental Apparatus

### 3.1 Introduction

This chapter describes the experimental apparatus used in this portion of the work to include the Rover K4 optical access engine, and the instrumentation and control equipment. Due to the K4 being fitted with two pressure transducers, it was possible to examine the effects of the charge amplifier time constant on pressure data and pressure derived parameters. This chapter also includes a discussion of that investigation.

### 3.2 Test Facility Description

An engine test facility was installed and commissioned to carry out the experimental work. The engine used for the experiments was the Oxford University Rover K4 single-cylinder, optical access research engine. The technical specifications for this engine are contained in Table 3.1, and a diagram of the engine test cell and associated instrumentation is shown in Figure 3.1.

**Table 3.1. Rover K4 Specification.**

Main Specification	
Bore	80.0 mm
Stroke	89.0 mm
Conrod length (ctr-to-ctr)	160.0 mm
Compression ratio	10:1
Cam Timing	
IVO	12° BTDC
IVC	52° ABDC
Peak lift inlet	8.8 mm @ 70° BBDC
EVO	52° BBDC
EVC	12° ATDC
Peak lift exhaust	8.8 mm @ 70° ABDC
Cylinder head	
Type	Rover K16 1.4 MPI

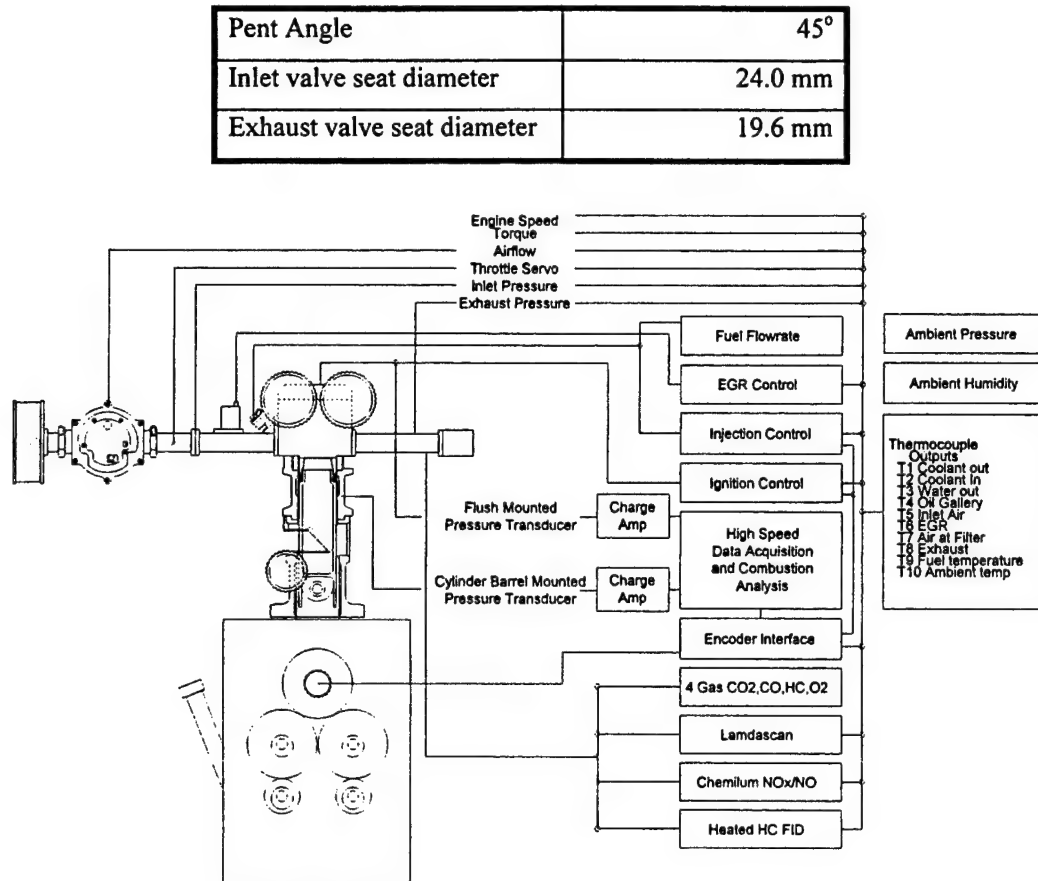


Figure 3.1. Sketch of the Oxford Optical Access Engine.

Based upon the Rover K series 1400cc four cylinder automotive engine, the K4 represents modern designs of combustion and gas exchange systems. The engine is composed of a purpose built crankcase with primary and secondary balance shafts to minimise vibration whilst using optical combustion analysis methods such as high speed photography and laser diagnostics. The single water cooled cylinder has the facility for the use of a synthetic quartz annulus just below the combustion face for viewing the early stages of combustion. The aluminium alloy piston is of an extended variety with open slots in the skirt. An angled mirror is placed through the slots and bolted to the upper cylinder block, and this is used to view the combustion process through a synthetic quartz piston crown. The quartz window is held in position by an aluminium collar which screws onto the extended piston, sealing is achieved using Viton rings. The optical components, in the piston crown and the annulus at the top of the barrel, were replaced with aluminium components, and the mirror removed, to reduce the risk of damage during extended test periods when optical access was not required. Three piston rings were used, the middle ring used was made from Zircon Z43, a modified crystalline polyether, the outer two, used to maintain the location of the piston, were made from Luytex C324, a fibre glass impregnated composite

material. The cylinder head had been adapted from the multi-cylinder Rover K16 engine. The cylinder head had been reduced by two and a half cylinders from the opposite end to the cam drive, to leave two cam journal pairs, and the head was then sealed at the severed end by a 20mm alloy plate. The cam journals were lubricated by a grease nipple since there is no oil provision in the upper cylinder. Initially valve springs of lower rate than the production engine were used, but these were later changed as part of a study to maximise repeatability (Pashley 1997). The intake manifold was fitted with two separate fuel injectors: one connected to a plenum for gaseous fuel supply, the other connected to a piped liquid fuel supply. This arrangement, through the use of solenoid valves, allowed quick and easy switching between liquid and gaseous fuels.

Provision was made for measuring and controlling the load and speed of the engine. Controls were also constructed which governed parameters such as injector pulse width, exhaust gas recirculation level, throttle position, ignition timing, etc. These controls will be explained in due course.

Samples drawn from the intake manifold, cylinder, and exhaust were analysed with four types of exhaust gas analysers. Combustion analysis was performed on data gathered by a piezo-electric cylinder pressure transducer and a high speed data acquisition and combustion analysis software package.

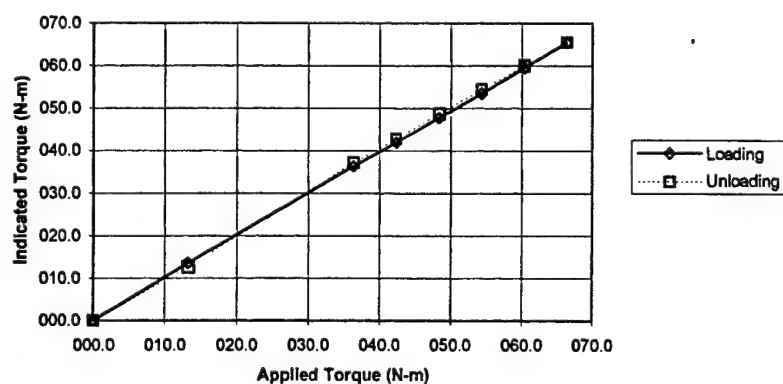
### **3.3 *Quasi-steady measurements***

#### **3.3.1 Engine Speed and Torque Measurement and Control**

The engine was connected to a DC dynamometer provided by Dynamometer Services. The physical connection was made via a flexible coupling which was used to absorb any vibrations and misalignment of the engine with respect to the dynamometer. The package contained a Mawdsley dynamometer with a 40 kW, 3600 RPM capability and an external load cell utilising strain gauges. The analogue output from the load cell was displayed on a digital display meter. The load cell was calibrated using a fixed moment arm bolted to the dynamometer shaft with known masses applied. The fixed arm provided a moment arm of 611.83 mm, and loads were applied as shown in Table 3.2. The calibration curve for loading and unloading is shown in Figure 3.2.

**Table 3.2. Dynamometer load cell calibration**

Applied Load (N)	Applied Torque (N-m)	Indicated Torque (N-m) Loading	Indicated Torque (N-m) Unloading
000.0	000.0	000.0	
021.5	013.2	013.6	
059.5	036.4	036.4	
069.3	042.4	042.0	
079.1	048.4	047.8	
088.9	054.4	053.6	
098.7	060.4	059.6	
108.5	066.4	065.5	065.5
098.7	060.4		060.2
088.9	054.4		054.6
079.1	048.4		048.8
069.3	042.4		042.8
059.5	036.4		037.3
021.5	013.2		012.7
000.0	000.0		000.0

**Figure 3.2. Load cell calibration curve.**

The discrepancies in the unloading curve were traced to binding between the lever arm and the dynamometer shaft. Attempts to rectify this problem were unsuccessful, and as the error in

measured torque was within 2%, the load cell was deemed to be accurate. In any case, the IMEP is more important than absolute values of BMEP.

Speed and load control was provided by a Control Techniques M155R four quadrant controller. The manufacturer claims a loss of less than 0.28 kW over the operating range of the drive. Speed measurement was provided by means of a 60 tooth wheel which fed into a frequency meter, and the speed is displayed on a digital display.

### **3.3.2 Air Flow Measurement and Control**

The air flow was measured by a Roots type positive displacement air flow meter which was installed directly downstream of the air filter. This generated a digital output which was sent to a frequency meter with internal scaling and was displayed in L/sec. A positive displacement type of air flow meter is capable of an accuracy of 1% over a turn down ratio of 10 (Stone, 1992). However, there are several drawbacks. First, these meters do cause a small pressure drop in the flow. Since air/fuel ratio was to be calculated primarily by exhaust gas samples, this was deemed to be acceptable. Also, the inertia of the rotors lead to a poor transient response, but transient response is not an objective of this study. Air flow control was achieved with a servo-controlled butterfly valve which provided a digital readout of the throttle position from 0-100% open. Finally, the pressure in the inlet manifold was measured by a Druck PCDR 810 pressure transducer with a digital pressure indicator. This pressure transducer and indicator were calibrated against a mercury manometer using a vacuum pump connected to a T-fitting.

### **3.3.3 Fuel Flow Measurement and Control**

As stated previously, the engine was equipped with two separate fuel injectors. The first was connected to a methane source which was regulated to a pressure of 6 bar gauge. The flow rate of the methane was measured by two Rotameters, for low and high flow, mounted near the gas supply bottle. The air/fuel ratio (for a given throttle plate setting) was controlled by varying the injector pulse width. The control circuit for varying this width was produced in-house. In addition to a calibrated potentiometer dial, the pulse signal was routed to an oscilloscope for verification. Ultimately, the air/fuel ratio was fine tuned through exhaust gas measurements. The liquid fuel supply (initially toluene) was pressurised to 3.5 bar. Again, the air/fuel ratio was controlled by varying the injector pulse width.

### **3.3.4 Blow-by Gas Measurement**

The blow-by flow was measured under conditions of 1000 RPM, WOT, and  $\lambda=1.00$ . A plate with a rubber gasket and a tube fitting was mounted to the cylinder barrel opposite to the mirror mounting, which was also sealed with a rubber gasket. The blow-by gas flowrate was measured in cubic feet per minute using a positive displacement gas flowmeter and a stopwatch. Initial blow-by was of the order of 6% of the inlet air flow. However, once the engine had reached normal operating temperatures, the blow-by reduced to less than 1% of the air flow. It was concluded that blow-by would be negligible.

### **3.3.5 Temperature Measurement and Control**

Thermocouples were used extensively for monitoring a wide range of operating temperatures (see Figure 3.1). All readings from the thermocouples were routed to the control room, where by use of a rotary switch, individual temperatures could be monitored.

Engine cooling was provided by two circuits. A coolant circuit provided cooling for the head, and was then routed to an oil heater. There was no provision made for measuring coolant flow rate as energy balance type calculations were not required. The lower cylinder barrel was the critical component requiring cooling due to the extended piston skirt. This was cooled by a total loss system fed by mains water. This circuit also provided the cooling water for the cylinder pressure transducer, a sampling valve (when used and installed in place of the pressure transducer), and the exhaust pressure transducer.

### **3.3.6 Exhaust Pressure Measurement**

The exhaust manifold pressure was measured with a Kistler model 4075A10 piezo-resistive pressure transducer in a water cooled adapter. The excitation current for the transducer was adjusted to yield an amplifier output of 1 bar/Volt. The transducer/amplifier combination was calibrated under positive pressure on a dead weight tester, and under negative (below atmospheric) pressure using the same vacuum pump/mercury manometer fitting as the inlet pressure transducer. The calibration curve is shown in Figure 3.3. Atmospheric pressure at the time of the calibration was 1.013 bar, hence the calibration curve reflects absolute pressure.



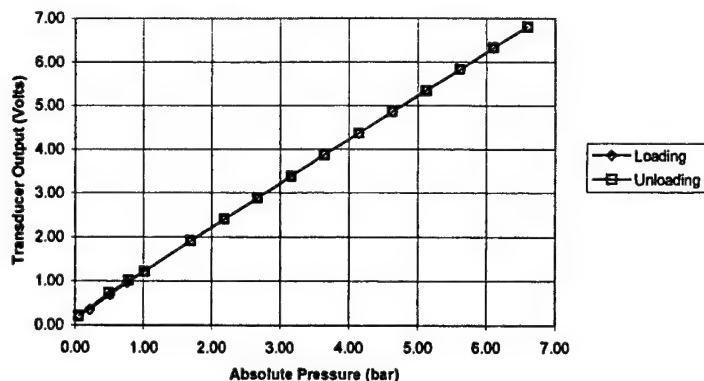


Figure 3.3. Exhaust pressure transducer calibration

### 3.4 Exhaust Gas Analysers

The test facility was equipped with four separate exhaust gas analysers: an OTC model VLC 6202 AutoGas4 four gas analyser, an Analysis Automation flame ionisation detection (FID) analyser, a Thermo-Electron chemiluminescence NO/NO<sub>x</sub> analyser, and a Cussons Lamdascan. Initially, a system was devised which would allow two analysers (one 4 gas analyser and one NO<sub>x</sub> analyser) to cycle among the various samples (intake, in-cylinder, and exhaust). However, the delay involved with the sample travelling through the tubing coupled with the analysers own response times made this option unfeasible, and in the end, the OTC and NO<sub>x</sub> analysers were used to analyse the exhaust gas only.

#### 3.4.1 OTC AutoGas4

This analyser is capable of measuring CO, CO<sub>2</sub>, HC, and O<sub>2</sub>. The O<sub>2</sub> is measured independently by a Teledyne Oxygen sensor, model R-21A, and the analyser automatically compensates the CO<sub>2</sub> reading for O<sub>2</sub> interference effects.

The analyser measures CO, CO<sub>2</sub>, and HC using non-dispersive infrared absorption (NDIR). An infrared beam is passed through the sample, and the amount of light absorbed by a fixed species is proportional to the concentration of that species for a fixed sample length. For a fixed concentration, the amount of light absorbed is also a function of wavelength. Each species has its own absorption spectrum, and certain wavelengths are absorbed more strongly than others. CO has absorption maxima at wavelengths of 4.62 and 4.70 microns whilst CO<sub>2</sub> has a maximum at 4.25 microns (Stone, 1992). The analyser contains three infrared detectors, and through the use

of narrow band filters, each detector is sensitive to a specific wavelength. As light of the specific wavelength strikes the detector, an analogue signal is generated which is digitally processed and displayed as the concentration of the target species. NDIR can be used to measure hydrocarbons. However, since different hydrocarbon species have different absorption spectra, this is not an entirely accurate method. In the case of the OTC analyser, the detector measures Hexane as it is claimed to be a good indicator of hydrocarbon content in gasoline fuelled engines. For other hydrocarbon species, the reading must be multiplied by a correction factor. Because of this, the OTC analyser was not used to provide quantitative hydrocarbon measurements.

### 3.4.2 Flame Ionisation Detection

When hydrocarbons are burned, ions and electrons are produced. If the hydrocarbons are burned in an electric field, a current flows in the analyser. In the flame ionisation detector (FID), the sample is mixed with air and fuel and burned. Since it is not desirable to add hydrocarbons to the sample, the fuel is a hydrogen/helium mixture. If the sample contains hydrocarbons consisting of only hydrogen and carbon atoms, the current produced is proportional to the mass of carbon in the compound. The manufacturer provides a list of response factors relative to methane. However, since the response factors vary with flowrate, the factors vary from instrument to instrument. This was accounted for by the manufacturer for this analyser in the following manner. First, the instrument was calibrated with hydrocarbon-free air, then with a known concentration of methane. Next, a known concentration of propane was sampled without changing the range. The new relative response factor (RRF) of propane to methane is the instrument reading divided by the actual concentration of propane, which for this analyser was 2.67. A correction factor is obtained by dividing the new RRF by the RRF given in the manufacturer's general table (2.7209):

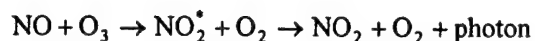
$$CF = \frac{RRF_{\text{test}}}{RRF_{\text{table}}} = \frac{2.67}{2.7209} = 0.9813$$

Relative response factors given by the manufacturer must be multiplied by this conversion factor to give relative response factors for this particular analyser.

The sampling system leading to the detector is heated to 200 °C to prevent heavier hydrocarbons and water from building up inside the analyser. Furthermore, the sample line from the engine is similarly heated to prevent deposition inside the line.

### 3.4.3 Thermo-Electron Chemiluminescence NO/NO<sub>x</sub> Analyser

This analyser utilises the chemiluminescent reaction of nitric oxide (NO) and ozone (O<sub>3</sub>). Nitric oxide reacts with ozone to produce oxygen and nitrogen dioxide in an electronically excited state. When the excited nitrogen dioxide converts to its normal state, it emits a photon. Specifically



The emitted light is passed through a narrow band filter and impinges on a photomultiplier. The output from the photomultiplier is proportional to the concentration of NO.

NO<sub>2</sub> may also be present in exhaust gas, and the sum of nitric oxide and nitrogen dioxide is called NO<sub>x</sub>. To measure NO<sub>x</sub>, the sample is diverted through an oven maintained at 650 °C to convert NO<sub>2</sub>-to-NO. The photomultiplier output is then linearly proportional to the NO<sub>x</sub> concentration entering the converter. Since the photomultiplier output must be amplified, any variation in this gain will adversely effect the instruments accuracy, and it is advisable to calibrate the analyser on a regular basis.

### 3.4.4 Cussons Lamdascan

The advent of three way catalysts has led to the use of a zirconia based oxygen sensor, or lambda sensor, in the exhaust of most current automobiles. The Lamdascan uses this principle, although instead of mounting the sensor in the exhaust flow, a sample is drawn off and fed into the analyser. Basically, the sensor consists of a solid electrolyte of yttria (Y<sub>2</sub>O<sub>3</sub>) stabilised zirconia (ZrO<sub>2</sub>) which is exposed to air on one side and the exhaust on the other. The difference in partial pressure of the oxygen on each side of the cell generates a current across the cell. The voltage of the cell is related to the oxygen partial pressures by the Nernst equation (Heywood, 1988):

$$V_o = \frac{RT}{4F} \ln \left( \frac{p''_{\text{O}_2}}{p'_{\text{O}_2}} \right)$$

where R is the gas constant, T is the zirconia cell temperature, F is Faraday's constant, and p''<sub>O<sub>2</sub></sub> and p'<sub>O<sub>2</sub></sub> are the oxygen partial pressures of the air and the exhaust gases. If the fuel

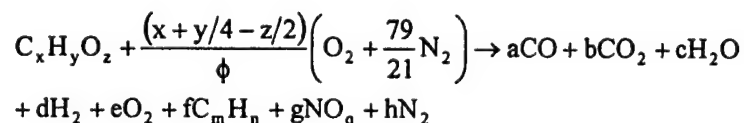
hydrogen/carbon/oxygen ratios are known as well as the level of dope air, the equivalence ratio and air/fuel ratio can be deduced (Stone, 1992).

The Lamdascan does not account for  $\text{NO}_x$  in the exhaust stream when deducing the equivalence ratio and air/fuel ratio. This error is negligible (Heywood, 1988) but a test case was examined to ensure the adequacy of this assumption. An engine simulation (ISIS: Integrated Spark Ignition engine Simulation, further explained in Chapter 4) was used to calculate the exhaust gas composition for an engine running on gasoline. A production 4 cylinder engine was chosen for the simulation since ISIS has previously demonstrated good agreement with experimental data for this engine (Raine et al., 1995). The exhaust gas composition resulting from the simulation for a range of air/fuel ratios is shown in Table 3.3.

**Table 3.3. Exhaust gas composition**

$\lambda$	AFR	$\text{CO}_2$ (%)	CO (%)	$\text{O}_2$ (%)
0.8	12.22	9.29	7.27	0.00
1.0	15.27	14.06	0.11	0.03
1.2	18.31	11.68	0.01	3.61
1.4	21.36	9.93	0.00	6.18
1.6	24.42	8.63	0.00	8.08
1.8	27.47	7.62	0.00	9.56
2.0	30.53	6.83	0.00	10.72
2.2	33.58	6.19	0.00	11.67
2.4	36.64	5.66	0.00	12.45
2.6	39.69	5.21	0.00	13.11

The air/fuel ratio was deduced in the following manner. The generalised equation for the combustion of an oxygenate fuel is (Stone, 1992):



Normal exhaust measurements are taken dry, and do not include hydrogen or nitrogen. If the fuel composition is known (the ratios of  $x:y$  and  $x:z$ ) the equations may be solved assuming there are enough reactants to form 100 kmols of dry products, since  $a$  is then the measured percentage of carbon dioxide, etc. Furthermore, it is generally assumed that the unburned hydrocarbons have

the same H/C ratio as the fuel, and some assumption must be made regarding the number of kmols of hydrogen. In this case, the water/gas equilibrium equation was used:



from which it follows

$$\frac{a \times c}{b \times d} = \text{const.}$$

A typical value for this constant is 3.5 (Stone, 1992, Heywood, 1988), and this was used for the calculation of the air/fuel ratio in this case. The air/fuel ratio was first calculated assuming no  $\text{NO}_x$  was present in the exhaust, then the ratio was calculated assuming a concentration of 2000 ppm  $\text{NO}_x$ . This value of  $\text{NO}_x$  was selected as an anticipated upper bound for the engine being used. The results of this test are shown in Figure 3.4.

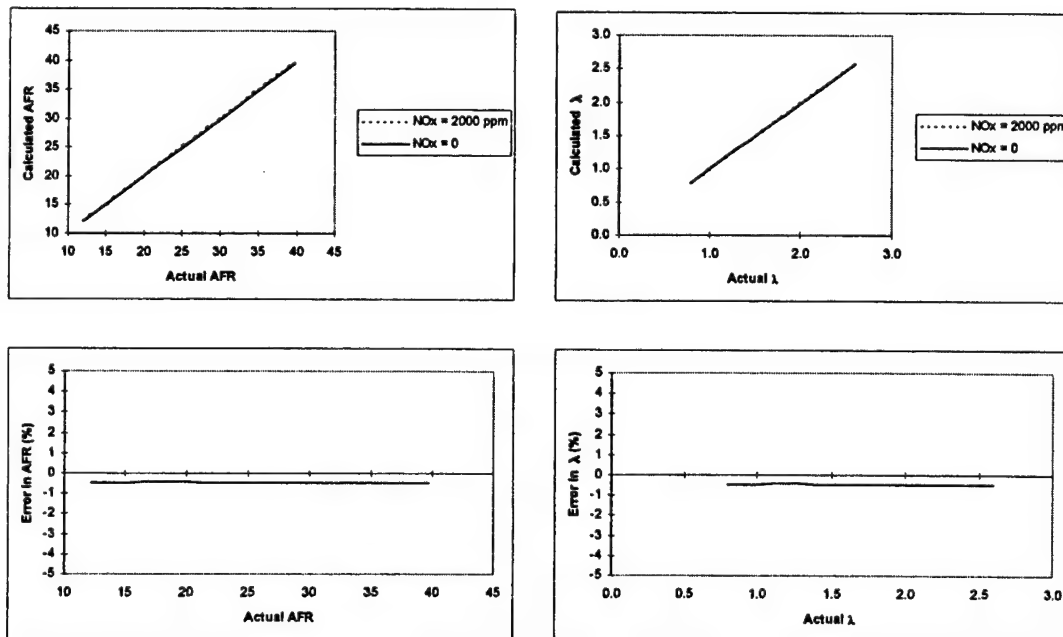


Figure 3.4. Comparison of calculated air/fuel ratio when  $\text{NO}_x$  is neglected.

As Figure 3.4 shows, when  $\text{NO}_x$  is neglected, the deduced air/fuel ratio is somewhat less, or in other words, the deduced air/fuel ratio is richer. This is as expected since once  $\text{NO}_x$  is introduced into the equation as an exhaust product, more air must be taken in as a reactant in order to produce the  $\text{NO}_x$ . This change is minimal primarily since 2000 ppm  $\text{NO}_x$  corresponds to 0.2%

of the 100 kmol of products produced, and the error in this case is a fairly consistent 0.4% change in the calculated air/fuel ratio. Thus, the assumption that neglecting  $\text{NO}_x$  when deducing air/fuel ratio is justifiable.

### 3.5 Exhaust Analyser Calibration

#### 3.5.1 OTC AutoGas4

The OTC analyser was calibrated by connecting a calibration gas bottle to the calibration port, adjusting the line pressure to between 0.3 and 1.0 bar, and selecting the 'CAL' option on the control menu. The cal option cannot be selected until a 30 minute warm-up period has elapsed. The calibration procedure requires the operator to enter the gas tag values, then the analyser self-calibrates based on these inputs. If the system calibrates within tolerances, the display directs the operator to disconnect the calibration gas, and the analyser then reverts to normal operating mode. The results of this calibration are shown in Table 3.4.

**Table 3.4. Results of four gas analyser calibration.**

		CO (%)	CO <sub>2</sub> (%)	HC (ppm)	O <sub>2</sub> (%)
Calibration Gas		3.50	14.06	2017 (propane)	0
OTC AutoGas4	Before	3.50	14.1	1036	0.03
	After	3.53	14.1	1035	0.02

The HC reading from this analyser is a "Hexane equivalent" reading, and must be converted to a propane reading using the manufacturer's conversion factor for the particular analyser in use. The inaccuracy in the measurement of unburned hydrocarbons is attributable to the previously discussed problems of using NDIR to measure HC levels. As a result, the HC levels were determined by FID.

#### 3.5.2 Flame Ionisation Detector

The FID analyser was powered up and allowed to warm-up for 60 minutes. During this time, the appropriate fuel, air, and span gas bottles were connected, and the supply pressures

regulated to the manufacturer's specifications. The analyser was zeroed with compressed air by adjusting the suppression potentiometer. A span gas calibrated at 1015 ppm Methane was input, and the reading was adjusted to match this concentration by adjusting the calibration potentiometer.

### **3.5.3 Thermo-Electron Chemiluminescent Analyser**

Calibration of the Thermo-Scan analyser began by setting the NO<sub>x</sub> converter to 650 °C. After turning on the main power, the bypass pump, and the NO<sub>x</sub> converter, the oxygen cylinder was connected and the pressure regulated to the manufacturer's recommendation ( $2.0 \pm 0.5$  psig). The system was allowed to warm-up for 20 minutes. The panel meter was checked for full scale deflection, and the background suppression potentiometer was adjusted fully anticlockwise. The digital panel meter reading was checked to ensure a reading of below 5 ppm, and the background suppression was adjusted to provide a zero reading. The sample inlet was then set to the calibration gas position, and the ozone generator switched on. The analyser was placed in the NO mode, and the reading checked against the calibration tag value of 2328 ppm. The reading was adjusted to agree with the tag value by adjusting the calibration potentiometer. Next, the analyser was placed in the NO<sub>x</sub> mode, and the reading rechecked.

### **3.5.4 Cussons Lamdascan**

The Lamdascan unit previously underwent a full calibration, and as such it was not deemed necessary to repeat the process. Hence, the procedure described was merely a check of the instrument's state of calibration. The procedure proceeded as follows:

- a) The AIR mode and O<sub>2</sub> display mode were selected, and the display read the ambient O<sub>2</sub>% concentration.
- b) DOPE ADD and DOPE RATIO 1 were selected, and the display checked to read less than 0.04% O<sub>2</sub>.
- c) DOPE ADD and each DOPE RATIO from 1 to 6 were selected. The display was checked to ensure: the oxygen reading was correct within  $\pm 0.04\%$ , the I value remained constant at  $1.000 \pm 0.005$ , and the AFR reading was stoichiometric for the calibration gas HC ratio ( $H/C = 1.45$ ,  $AFR_s = 13.95$ ).

Results of this check are shown in Table 3.5, and indicated that the instrument was within calibration tolerance.

**Table 3.5. Calibration check of Lamdascan analyser**

DOPE RATIO	O <sub>2</sub> Correct	O <sub>2</sub> Reading	$\lambda$	AFR
1	0.00	0.00	1.000	13.96
2	2.00	2.00	1.000	13.96
3	4.00	4.00	1.000	13.96
4	5.00	5.00	1.000	13.95
5	6.00	6.00	1.000	13.96
6	8.00	8.01	1.001	13.96

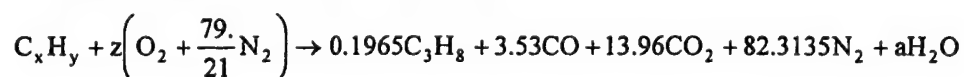
### 3.5.5 AFR and $\lambda$ Calculation for Calibration Gas

The method used for calculating the AFR and  $\lambda$  of the calibration gas is outlined below. The Lamdascan uses a similar method in its calculation of AFR and  $\lambda$ , the difference is that the user inputs the H/C ratio allowing the on-board processor to calculate AFR and  $\lambda$  with only the oxygen measurement (and the added quantity of dope air, if the mixture is rich).

The calibration gas bottle composition was:

CO - 3.53%  
 CO<sub>2</sub> - 13.96%  
 C<sub>3</sub>H<sub>8</sub> - 0.1965%  
 N<sub>2</sub> - balance (82.3135%)

For 100 kmole of dry products (molar masses taken from Stone, 1992):



C balance:  $x=3(0.1965)+3.53+13.96$ ;  $x=18.0795$

N<sub>2</sub> balance:  $z(79/21)=82.3135$ ;  $z=21.881$

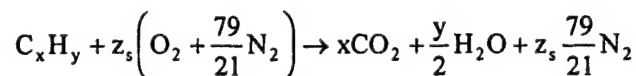
O<sub>2</sub> balance:  $21.881(2)=3.53+2(13.96)+a$ ;  $a=12.312$

H balance:  $y=8(.1965)+2(12.312)$ ;  $y=26.196$

H/C= $y/x=1.45$



For stoichiometric combustion:



From this it follows that

$$z_s = x + \frac{y}{4} = 18.0795 + \frac{26.192}{4}; z_s = 24.6275$$

$$\lambda = \frac{z}{z_s} = \frac{21.881}{24.6275}; \lambda = 0.8885$$

$$AFR_s = \frac{24.6275 \left( 31.99 + \frac{79}{21} 28.15 \right)}{18.0795(12.011) + 26.192(1.008)}; \underline{AFR_s = 13.95}$$

$$AFR = AFR_s(\lambda) = \underline{12.4}$$

Calibration of the Lamdascan could be easily checked with the use of two calibration gases, labelled CAL 1 and CAL 2. CAL 1 contained 5.86% oxygen in nitrogen, and CAL 2 had the composition illustrated in the calculations above. When CAL 1 was fed into the Lamdascan, the oxygen reading was checked to ensure it read  $5.86\% \pm 0.04\%$ . When CAL 2 was connected, the calculated air/fuel ratio and  $\lambda$  were checked to ensure they were within required tolerances.

### 3.6 Cyclic measurements

#### 3.6.1 Crankshaft Encoder

The engine was equipped with a Leine & Linde IS 632 incremental encoder. This encoder generates two series of pulses phased at  $90^\circ$  as well as a TDC marker flag. The encoder was connected to the shaft with a Heidenhain K17 diaphragm coupling on a 10 mm shaft. The encoder interface used the 'TDC' marker to generate a pulse of  $15^\circ$  crank angle duration, which was used to initiate the delay to satisfy the Dial-a-Time system. The encoder interface also generated user selectable pulses which enabled readings to be taken every 1,  $1/2$ , and  $1/4$  degree crank angle.

Piston TDC was determined using a dial indicator to set an initial estimate. The flywheel was then rotated approximately  $40^\circ$  beyond TDC, and the piston depression was recorded. The flywheel was rotated in the opposite direction until the dial indicator measured the same

depression, and the flywheel mark recorded. The bisection of the two flywheel readings was TDC. TDC was set to this mark, and the procedure repeated until accuracy was assured.

Ignition timing was controlled by a Lucas Logic Ltd. Dial-A-Time unit (Lucas, 1982). The unit provides variable ignition timing with a resolution of  $\frac{1}{2}$  degree crank angle over the range 79.5 degrees BTDC to 45.5 degrees ATDC. The ignition timing was adjusted with a multi-turn potentiometer, and the actual timing is displayed on a 3 digit display with reference to top dead centre. The unit also provides adjustments for coil off angle and coil on time. However, these features were not used for this study. The Dial-A-Time unit expects to see the falling edge of an encoder pulse at 80° BTDC. It uses this pulse to determine the coil on time required to produce the requested ignition timing, and this was supplied by the encoder interface. The encoder was synchronised so that the TDC pulse was generated 86° ABDC. The ensuing interface pulse had a falling edge 15° later, or 80° BTDC. The synchronisation was accomplished by connecting a timing strobe to the HT coil lead and setting the Dial-A-Time for 20° BTDC. With the engine motoring, the encoder was rotated relative to the crankshaft until the timing strobe indicated an ignition timing which agreed with the desired Dial-a-Time value.

### **3.6.2 High-speed data acquisition**

Data were collected using the RC Electronics, Inc. ComputerScope data acquisition system (RC Electronics, 1987). The system was designed for incorporation into an IBM compatible PC, and consists of a 16-channel analogue-to-digital (A/D) board, an external instrument interface, and driver software. The system is capable of logging data from up to 16 channels at an aggregate sampling rate of 1 MHz. Digital conversion is achieved with 12 bit accuracy over an input range of -10 to +10 volts.

### **3.6.3 Cylinder Pressure Measurement**

Cylinder pressure was primarily measured by an AVL QC32C-E water cooled piezoelectric transducer connected to a Kistler type 5006Y4 charge amplifier. In addition, a Kistler type 701A piezoelectric transducer in a water cooled jacket was mounted into an aluminium annulus which was used in place of the optical windows in the upper cylinder bore. The datum pressure for pressure measurements was determined by utilising a Kistler 4075A10 piezo-resistive pressure transducer mounted in the cylinder barrel. When the piston was within about 60° of TDC, the transducer was exposed to atmospheric pressure, whilst with the piston within about 60° of BDC, the transducer was exposed to in-cylinder pressure. Hence, knowing

atmospheric pressure allowed the datum to be set for the barrel transducer, which provided an accurate in-cylinder pressure at BDC. The barrel pressure from 20 to 45 degrees ABDC on the compression stroke was used to set the datum for the cylinder transducers. When this was done, pressure traces similar to those shown in Figure 3.5 were obtained.

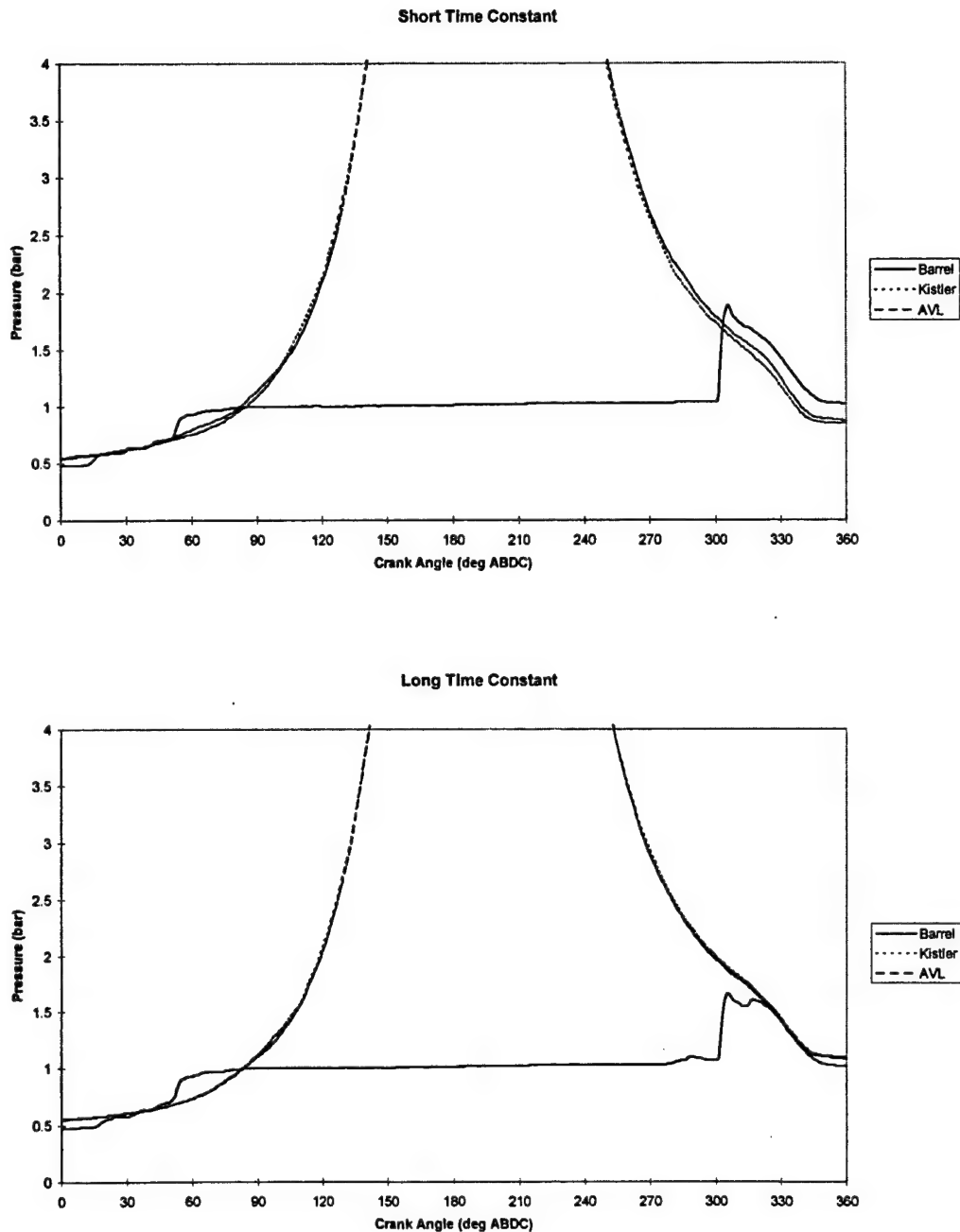


Figure 3.5. Pressure traces taken with short and long time constants.

The data obtained in Figure 3.5 was recorded with the engine running at 1000 RPM, near stoichiometric, and one-third throttle. Of note is the fact that, with the short time constant, there is a considerable amount of intra-cycle droop which results in the cylinder pressures being 200-300 millibar lower than the barrel transducer on the expansion stroke.

The cause of this intra-cycle droop whilst utilising the short time constant is explained by reference to Figure 3.6, which is a simplified circuit diagram of the integrating amplifier within the Kistler 5006 charge amplifier (Kistler, 1981).

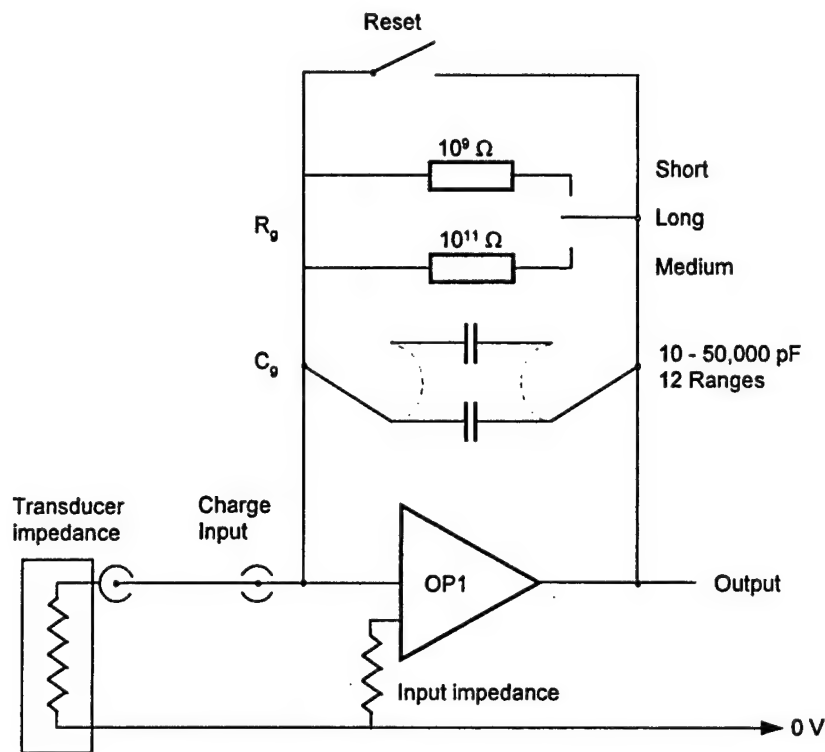


Figure 3.6. Simplified circuit diagram for Kistler 5006 charge amplifier, integrating op-amp portion (adapted from Kistler, 1981).

Suppose the pressure transducer produced a negative charge. The input to the op-amp (OP1) would be a voltage equal to the applied charge divided by the total capacitance of the input (transducer, cables, etc.). The output of the amplifier is an amplified voltage of opposite polarity which is then fed back through the feedback capacitor ( $C_f$ ) and produces a positive charge at the input which is equal in magnitude to the input. Hence, the input to the amplifier is held at a virtual zero whilst the feedback capacitor receives a charge equal to that produced by the transducer but of opposite polarity. However, due to spurious charges within the system, it is possible for the feedback capacitor to drift and over a period of minutes, it may saturate. This is compensated for by the system of resistors which are selected by the time constant switch. These

resistors ( $R_g$ ) provide a controlled discharge of the capacitor and prevent long term drift. If the system is reset, a short circuit is induced which rapidly discharges the capacitor and zeroes the system. The short and medium settings provide correspondingly slower discharge rates, whilst in the long setting, the discharge is governed by the input impedance of the op-amp, the transducer, and the cables. The long time constant, therefore, should be used for calibration only as the long term drift cannot be controlled.

The effect of these time constants on discharge rate were examined by applying a step input to a pressure transducer on a dead weight tester. The step input was applied by manually pressurising the dead weight tester, and zeroing the charge amplifier. A weight was then dropped onto the dead weight tester from a safe height. The resulting voltage traces for the short, medium, and long time constants are shown in Figure 3.7. Kistler calculates a time constant of 0.5 seconds for the amplifier on this scale with the short time constant, and an exponential fit to the short curve in Figure 3.7 yielded a time constant of 0.47 seconds. Since the expansion stroke requires 30 msecs at 1000 RPM, the decay resulting from using the short time constant can be bracketed. First, assuming a constant 20 bar pressure is applied to the transducer, the short time constant would yield a decay in pressure of 1165 mbar during this time. Likewise, a constant 1 bar pressure would decay 58 mbar over this time. Since the pressure is not remaining constant over the expansion stroke, it is reasonable to assume the decay should fall within these limits, which it does. Hence, the mismatch in the pressure traces on expansion can be attributed solely to the choice of the short time constant.

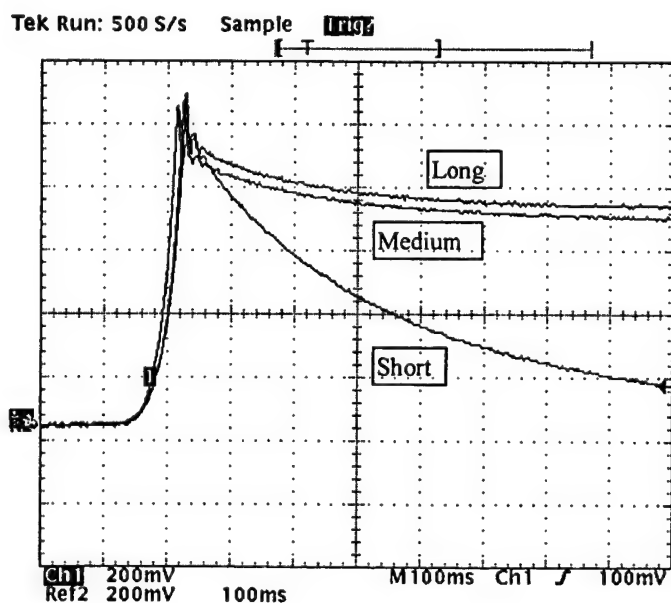


Figure 3.7. Response of Kistler 5006 charge amplifier to step load with varying time constants.

Of greater significance is the effect of the time constant on parameters derived from the pressure data. To examine this effect in more detail, data were collected at this operating point over a range of ignition timings. For each set of data, 180 continuous cycles were obtained and analysed with the charge amplifiers for each pressure transducer set to the same time constant. The IMEP, maximum pressure ( $P_{\max}$ ), crank angle of maximum pressure ( $\theta_{P_{\max}}$ ), and the 10% and 90% burn durations (in degrees crank angle after ignition) were obtained for each cycle and the results averaged (the cycle-by-cycle, or cbc, results). This analysis was performed utilising the specially written COmbustion Burn Rate Analysis (COBRA) program. This program reads in the data collected by the data collection system, converts the voltages to absolute pressure via the barrel pressure transducer, and utilises the Rassweiler and Withrow (1938) burn rate model in calculating burn rates. A full description of this program is given in Chapter 4. Next, an ensemble average pressure trace was derived for each operating point, and the same parameters were calculated for the mean pressure (the mean cycle results) utilising COBRA. The results of this analysis are summarised in Table 3.6.

Several inferences can be made from the results in Table 3.6. First, the calculated parameters showed no sensitivity to the method of calculation, and both the cycle-by-cycle calculations and the mean cycle calculations yielded nearly identical results. The exception was in  $P_{\max}$ , and the mean cycle calculation consistently yielded a lower value of  $P_{\max}$ . This is due to the smoothing effect of averaging the pressure traces in which  $P_{\max}$  occurs at different crank angles, thus resulting in a lowered maximum, although there was still a difference of only 1% between the two methods. The fact that both methods yield the same results is important when constructing mean cycle models, and indicates that a cycle-by-cycle average of burn rates will produce the same results as a burn rate derived from an ensemble average of the pressure traces; this agrees well with the results of recent studies (Brunt and Emtage, 1997).

Table 3.6. Results of pressure analysis comparing time constants.

Ignition (DBTDC)	Time Constant		Kistler		AVL	
			cbc	mean cycle	cbc	mean cycle
0	Short	IMEP	1.88	1.88	1.90	1.90
		Pmax	10.36	10.36	10.37	10.37
		CaPmax	179	179	179	179
		10% Burn	30.59	30	30.29	30
		90% Burn	69.24	69	70.12	70
	Long	IMEP	1.79	1.79	1.80	1.80
		Pmax	10.39	10.39	10.38	10.38
		CaPmax	179	179	179	179
		10% Burn	30.96	30	30.93	30
		90% Burn	76.01	75	75.88	76
25	Short	IMEP	2.76	2.76	2.83	2.83
		Pmax	23.21	23.08	23.10	22.98
		CaPmax	191	191	191	191
		10% Burn	19.69	19	19.54	19
		90% Burn	37.67	38	38.08	38
	Long	IMEP	2.87	2.87	2.85	2.85
		Pmax	22.63	22.41	22.48	22.28
		CaPmax	192	191	192	191
		10% Burn	21.12	20	20.27	20
		90% Burn	41.20	40	44.27	43
50	Short	IMEP	1.71	1.71	1.78	1.78
		Pmax	29.35	29.30	29.37	29.32
		CaPmax	179	179	179	179
		10% Burn	24.43	24	24.42	24
		90% Burn	41.49	42	41.34	41
	Long	IMEP	1.93	1.93	1.95	1.95
		Pmax	28.97	28.74	28.88	28.66
		CaPmax	179	180	179	179
		10% Burn	26.59	25	26.25	25
		90% Burn	42.73	43	42.63	43

Second, the effect of the time constants on the calculated parameters varies. There seems to be little effect on the 10% burn duration,  $P_{max}$ , or  $\theta_{Pmax}$ , but there is a larger effect on IMEP and 90% burn duration. Some of the differences in the above chart are attributable to performing the calculations on different sets of cycles. However, the two cylinder transducers show very good agreement at each operating point, and have produced nearly identical pressure traces throughout. More data was then collected at the same operating point with one transducer set to the short time constant and the other on the long constant. This allows the effects of the time constants to be separated from any cyclic variation in the data as the calculations are performed on the same cycles at the same time. The results of this test are shown in Table 3.7, and these results were obtained from the ensemble averaged pressure traces for the respective data sets.

**Table 3.7. Results of simultaneous calculations.**

Ignition Timing		Kistler Long	AVL Short	Kistler Short	AVL Long
25	IMEP	3.14	2.99	2.92	3.14
	$P_{max}$	24.48	24.32	24.94	24.91
	$\theta_{Pmax}$	191	190	190	190
	10% burn	20	19	19	19
	90% burn	42	37	35	41

Table 3.7 summarises two sets of 180 cycles, the difference between the two sets being the time constant used by each transducer. These results indicate that the choice of time constant has little effect on maximum pressure, the crank angle of maximum pressure, or the 10% burn duration. However, the short time constant produces a 5% decrease in IMEP, and approximately a 15% decrease in 90% burn duration. Since the pressure as measured by the transducer set to the short time constant is falling more rapidly, there is apparently less work performed by the gas, resulting in the lower calculated IMEP. The mass fraction burnt (MFB) was calculated by the Rassweiler and Withrow method, which normalises the burn rate hence indicating that 100% of the charge burns every cycle. As the transducer with the short time constant shows a more rapid drop off in pressure, the MFB model treats this as an earlier end to combustion. Yet since the model assumes 100% of the fuel is burnt, this translates into a decreased 90% burn duration.

The conclusion of this investigation is that the short time constant should not be used to obtain cylinder pressure data due to the adverse effects on IMEP and burn duration.

### **3.7 Cylinder Pressure Transducer Calibration**

The cylinder pressure transducers were paired with their respective charge amplifiers for the calibration. A dead weight tester was used for the calibration, and each transducer was calibrated over two ranges:

- With an output of 5 bar/volt, transducers were calibrated over a pressure change of 56 bar.
- With an output of 10 bar/volt, the transducers were calibrated over a pressure change of 105 bar.



These ranges are sufficient to ensure engine operation at all loads within the calibration range. An example calibration curve for the AVL transducer is shown in Figure 3.8.

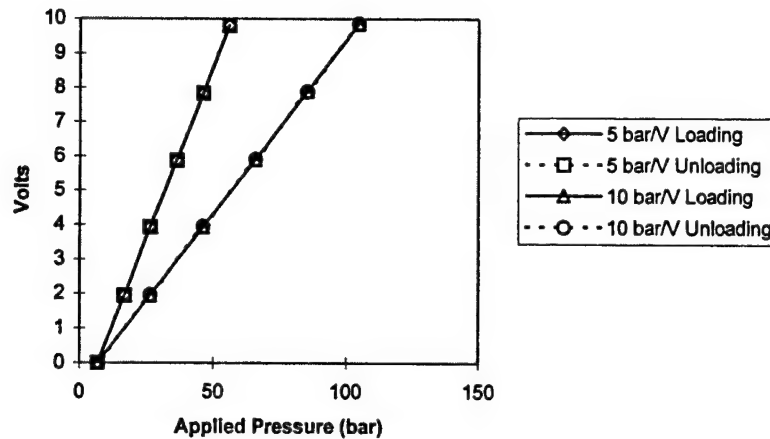


Figure 3.8. Calibration curve for AVL piezoelectric pressure transducer.

As shown by Figure 3.8, this particular transducer exhibits a very linear response with little charge leakage. The correlation coefficient for all cases shown in Figure 3.8 was 1. Furthermore, the transducer has integral water cooling to minimise the possibility of thermal drift.

### 3.8 Summary

This chapter outlined the equipment used for the duration of this portion of the work. It also examined the effects of the charge amplifier time constant on pressure data. The investigation concluded that the short time constant should not be used when recording pressure data. If the short time constant is used, it will cause a reduction in calculated IMEP of approximately 5% and a reduction in burn duration of approximately 15%. It is also known that the long time constant should only be used for static calibration of the pressure transducers (Kistler, 1981) because the long-term drift of the charge amplifier is not controlled with this time constant. Therefore, the medium time constant was used for all cylinder pressure measurements in this work.

## Chapter 4 Computer Models and Initial results of Cycle-by-Cycle Modelling

### 4.1 Introduction

The initial hypothesis to be tested is that variations in the burn rate will encapsulate the majority of the causes of CCV, and their incorporation into a cycle simulation will enable accurate modelling of the cyclic variation of an engine. Whilst this stage was a repeat of work previously accomplished by Raine et al. (1995), the work was performed for two reasons. First, this would validate the results presented by Raine et al. (1995), and second, the work would establish a baseline for the Rover K4 engine. The experimental data were analysed with the COmbustion Burn Rate Analysis (COBRA) program, and the burn rates for each cycle were calculated via the method outlined by Rassweiler and Withrow (1938). These results were used as input to the current engine simulation used by the Oxford Internal Combustion Engine Group: the Integrated Spark Ignition engine Simulation (ISIS).

This chapter will describe the theory and operation of COBRA and ISIS, and will also outline the Rassweiler and Withrow method of burn rate analysis as it is normally applied on a personal computer. The chapter will then report on the initial results of the cycle-by-cycle modelling and will draw conclusions as to whether burn rate data alone is sufficient to model the cyclic variation of an engine.

### 4.2 COBRA

COBRA was developed to perform combustion analysis calculations on cylinder pressure data. The data were obtained from the ComputerScope data acquisition system, and the COBRA output files were designed for importation to ISIS. As such, it is a single-purpose program, although the source code can be easily modified by anyone familiar with FORTRAN in order to adapt COBRA to the system in use.

COBRA requires several user inputs defining the engine geometry and operating point. The user inputs are entered first, usually from a configuration file. In any analysis of engine pressure data, two factors determine to a large degree the accuracy of the analysis: crank angle phasing and the pressure datum. An accurate knowledge of the former is required in order to determine the pressure-volume relationship, and hence, the IMEP. Whilst IMEP is completely insensitive to the latter, all other combustion related parameters are affected by

the accuracy of the pressure datum (Brunt and Pond, 1997, Douglas et al., 1997). Since the ComputerScope could not be relied upon to commence acquisition on the crank flag, the data files tended to start at random points within the first cycle. As a result, some processing was required to determine the phasing. First, COBRA read in the first 720 data points and searched the channel containing the crank flag for the first rising edge. This was a known point. However, it was not known whether the flag occurred during a compression or exhaust stroke. COBRA compared the cylinder pressure voltage at the flag location to that at TDC and deduced which stroke was operating at the first flag, i.e., whether the first flag occurred on a compression or exhaust stroke. COBRA then moved forward to BDC of the first compression stroke, and the data which was skipped was not used in any calculations.

COBRA then read in the data (from BDC compression) in 1 cycle (720 data point) sections. For each cycle, the following computations were performed:

1. The crank angles were identified.
2. The cylinder volume at each crank angle was computed.
3. The raw cylinder pressure voltage was scanned for saturation spikes, and the spikes were removed by replacing the noisy point by the average of the points on either side.
4. The pressure signal was smoothed with a 5 point smoothing algorithm.
5. The pressure datum was set as follows: the barrel transducer signal was corrected to atmospheric pressure over the applicable range. The barrel pressure from 20 to 45 degrees ABDC compression was then used to set the cylinder pressure datum.
6. The compression and expansion polytropic indices were calculated with a least squares fit to the logarithmic pressure-volume data. The compression index was calculated from a point halfway between IVC and ignition up to ignition. The expansion index was calculated over a user defined range of crank angle degrees between the end of combustion (as computed by the standard Rassweiler and Withrow method described in Section 4.3) and EVO. This feature was incorporated into COBRA because of the slow burn-up of the crevice mass in the K4 engine. (Chapter 5, Section 5.5 describes this phenomena.) Under lean operation with retarded ignition timing, it was discovered that combustion could continue up to EVO. In such cases, there was no crank angle range over which to calculate an expansion index, and the program would crash. Hence, the user could force a calculation over a small crank angle range. The calculated index in such cases was too low, and this induced errors in the mass fraction burned (MFB) calculations (Douglas, et al., 1997). These effects will be described in Chapter 5.

7. Maximum cylinder pressure and the crank angle at which it occurs were found.
8. Mass fraction burned was calculated with the Rassweiler and Withrow method.
9. The MFB profile generated by the Rassweiler and Withrow analysis was searched to find the burn time (in degrees crank angle) to the low and high MFB values input by the user. For the K4 engine, the time to 10% and 80% MFB was used. This choice was again due to the slow burn-up of crevice gases.
10. The ignition timing, relative air-fuel ratio ( $\lambda$ ), low MFB time, and high MFB time were output to an array.
11. Channel 4 was averaged over the desired range. Initially, this feature was used to calculate an average hydrocarbon reading from the FID over the entire data set.
12. Running averages were calculated for the IMEP (net), COV of IMEP (net), and Channel 4 readings. This allowed a plot to be produced of the parameter versus cycle number and gave an indication of the stability of the data collected.

At this stage, COBRA generated two output files. A summary file containing cyclic values of:

- a) compression and expansion indices,
- b) maximum cylinder pressure and the angle of its occurrence,
- c) net and gross IMEP,
- d) a running average of net IMEP and COV of net IMEP, and
- e) a running average of the Channel 4 reading.

The second file contained the ignition timing, relative air-fuel ratio, and low and high MFB times in a form that could be used as input to ISIS. COBRA also had a facility for generating individual cycle files in which the cylinder volume, cylinder pressure, and MFB were output on a crank angle basis.

A companion program was also written which contained the same front end and primary calculations as COBRA. However, this program generated an ensemble mean pressure trace and performed all combustion calculations on that mean cycle. Subsequently, COBRA was heavily modified, and these modifications will be explained in due course.

### 4.3 The Rassweiler and Withrow method

A popular technique for computing mass fraction burned (MFB) is the method developed by Rassweiler and Withrow (1938). In the original work, the authors develop two methods of calculating MFB. The first method is based on the assumption that once combustion commences, the change in pressure ( $\Delta p$ ) over a crank angle interval ( $\Delta\theta$ ) is the sum of two parts: the pressure rise due to piston motion ( $\Delta p_v$ ) and the pressure rise due to combustion ( $\Delta p_c$ ). Rassweiler and Withrow illustrated this method with a 'spread sheet' calculation procedure and the concept is shown graphically in Figure 4.1.

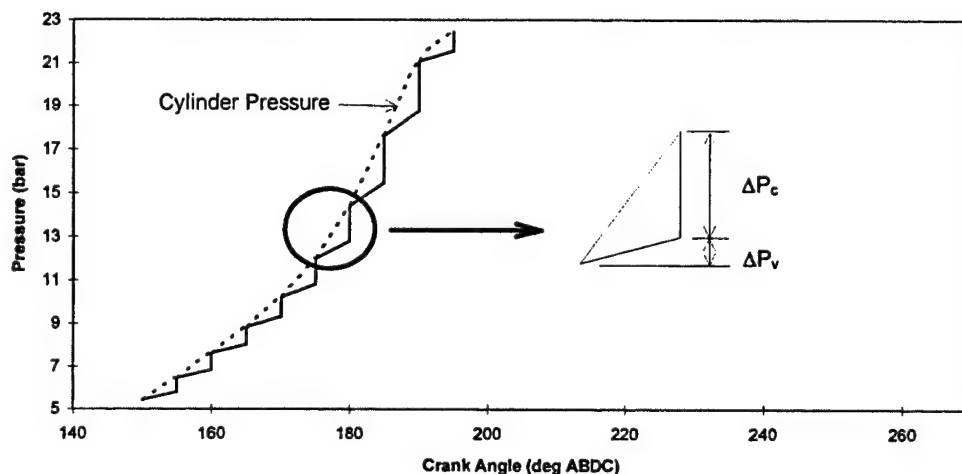


Figure 4.1. Measured pressure change as a sum of piston motion and combustion.

Rassweiler and Withrow approximated the combustion process with a series of small crank angle increments. First, the charge would be compressed polytropically by the piston, then a small amount of charge would burn. The pressure again changes polytropically, an increment of charge burns, and this continues throughout the combustion period. Since each increment of combustion occurs at a different volume, the pressure rises due to combustion must be normalised to some reference volume (Rassweiler and Withrow used the volume at ignition) in order to add the increments, and to calculate MFB. Several key observations were pointed out in the original work regarding this method:

- a) Since the piston motion and combustion are considered to progress in a stepwise fashion, small step sizes should be used to minimise errors.
- b) The effects of heat transfer are accounted for only in the choice of the polytropic index. The accuracy of the index thus influences the accuracy of the calculations.
- c) Blow-by will affect the results.
- d) In order to normalise the pressure rises due to combustion, it was assumed that pressure rise was inversely proportional to total volume.
- e) In order to calculate the pressure rise due to combustion, the polytropic indices for the burned and unburned regions were assumed to be equal.

The original work contained an example of this calculation, but was not mathematically expounded. Stone (1992) gives a mathematical derivation of this method, which will henceforth be referred to as the “standard” method. Since the total pressure rise over one crank interval is the sum of the pressure rise due to piston motion ( $\Delta p_v$ ) and the pressure rise due to combustion ( $\Delta p_c$ ),

$$\Delta p = \Delta p_c + \Delta p_v. \quad (4.1)$$

As the crank angle ( $\theta_i$ ) increments to the next value ( $\theta_{i+1}$ ), the volume changes from  $V_i$  to  $V_{i+1}$  and the pressure from  $p_i$  to  $p_{i+1}$ . It is assumed that the pressure change due to piston motion can be modelled by a polytropic process with an index  $n$ , hence:

$$p_i V_i^n = p_{v,i+1} V_{i+1}^n. \quad (4.2)$$

The pressure change due to piston motion can then be defined by

$$\Delta p_v = p_{v,i+1} - p_i = p_i \left[ \left( \frac{V_i}{V_{i+1}} \right)^n - 1 \right]. \quad (4.3)$$

Substituting equation (4.3) into equation (4.2) produces

$$p_{i+1} - p_i = \Delta p_c + p_i \left[ \left( \frac{V_i}{V_{i+1}} \right)^n - 1 \right], \quad (4.4)$$

from which the pressure rise due to combustion can be calculated

$$\Delta p_c = p_{i+1} - p_i \left( \frac{V_i}{V_{i+1}} \right)^n \quad (4.5)$$

Since combustion is not taking place at constant volume, equation (4.5) must be normalised to some reference volume, for example the cylinder volume at TDC, and this normalised pressure change is denoted by  $\Delta p_c^*$

$$\Delta p_c^* = \Delta p_c \left( \frac{V_i}{V_{TDC}} \right) \quad (4.6)$$

The end of combustion is indicated by the normalised pressure rise due to combustion becoming zero. Assuming that the normalised pressure rise is proportional to the mass fraction burned ( $x$ ), then for  $N$  total increments

$$x = \frac{\sum_0^i \Delta p_c^*}{\sum_0^N \Delta p_c^*} \quad (\text{standard method}) \quad (4.7)$$

One disadvantage of this method is its sensitivity to the selection of polytropic index. If the compression index is used throughout the calculation, it results in a characteristic fall in the mass fraction burned curve after the end of combustion. This is due to heat transfer and the presence of combustion products. An accurate index would produce a curve that rose to 1.0 and remained there through to the end of the cycle. Rassweiler and Withrow evaluated the index during compression and expansion, and used an appropriately averaged value during combustion. Shayler, et al. (1990) proposed switching from the compression index to the expansion index at a user defined point in the cycle, namely TDC. This technique did result in a curve that remained at 1.0 after the end of combustion for the cases reported by them.

Using the expansion index also poses problems as it may be difficult to accurately determine the end of combustion. Several methods have been used to define the end of combustion (Shayler, et al., 1990):

- a) the first negative method assumes combustion is complete when one negative combustion pressure is calculated

- b) the sum negative method requires three consecutive combustion pressures to be negative
- c) the standard error method which assumed the end of combustion when the combustion pressure had settled to within one standard error of zero.

Brunt and Emtage (1997) and Douglas et al. (1997) also investigate using the point at which  $PV^{1.15}$  is a maximum to determine the end of combustion. For cycles which are slow burning or in the case of retarded spark timing, the crank angle range over which the expansion index may be calculated can be very limited and is further limited by exhaust valve opening. In such cases, the index must be calculated close to EVO. On the other hand, if the crank angle range is too large, the index is calculated whilst combustion is continuing and will result in a low value of the index. Shayler et al. (1990) also noted the difficulty of dealing with late burn conditions and suggested that an arbitrary value of 1.25 be assigned to the expansion index for these cases.

Calculation of the compression index must also be done with care since the pressure rise at the beginning of the stroke is small and discretisation errors from the data acquisition system are more significant (Stone, 1992). This can be avoided by ignoring the initial part of compression, for example, by calculating the index from half way between inlet valve closure and ignition up to ignition.

Inherent in this method are several assumptions besides the constant index assumption (Heywood, 1988; Stone, 1992):

- a) it assumes that the referenced pressure rise is proportional to the mass of fuel burned rather than the amount of chemical energy released, and
- b) there is no allowance for heat transfer, dissociation, or change in composition beyond the fact that the polytropic index differs from the ratio of specific heats.

Despite these limitations, comparisons of mass fraction burned calculated using the Rassweiler and Withrow method with the results of other more complex thermodynamic models show remarkably close agreement (Stone and Green-Armytage, 1987; Brunt and Emtage, 1997).

#### 4.4 ISIS

The cycle simulation used was a development of the Integrated Spark Ignition engine Simulation (ISIS) (Raine et al., 1995). This simulation is based on routines developed by



Ferguson (1986) but with extensions including: nitric oxide kinetics, friction models, heat transfer correlations, and different burn rate models. The model was initially of the zero-dimensional two-zone thermodynamic type. The two zones constitute an unburned gas zone (a mixture of fuel, air, and residual gases) and a burned zone (a mixture of ten product species), and each zone is of uniform composition. The specified burn rate controls the rate at which material from the unburned zone is converted to the burned zone. However, the model has been extended to use multiple zones in the burned gas (Raine, et al., 1995). The model takes as input the following known data:

- a) engine geometry,
- b) operating conditions (ignition timing, air-fuel ratio, speed, etc.),
- c) ambient conditions (temperature, pressure, humidity),
- d) fuel type, and
- e) pressure at inlet valve closure.

In addition, several inputs must be calculated. First, the burn rate is calculated by fitting a Wiebe function to the measured 10% and 80% burn rates, the function having the form (Heywood, 1988)

$$x(\theta) = 1 - \exp\left(-a \left[\frac{\theta - \theta_o}{\theta_b}\right]^{m+1}\right) \quad (4.8)$$

where  $x(\theta)$  = mass fraction burned at crank angle  $\theta$ .

$\theta_o$  = crank angle at start of combustion

$\theta_b$  = duration of combustion

$a$  and  $m$  are adjustable parameters used to fit the curve to the data.

The residual mass fraction was estimated from the correlation of Fox et al. (1993), suitably modified for the 4-valve geometry of this engine and making allowance for the effects of spark timing. It was necessary to adjust this estimate slightly during the modelling to produce mean NO values that matched the mean experimental values.

Finally, ISIS requires the temperature at IVC as an input, and this is used to calculate an initial trapped mass. The temperature at IVC was not known. However, the airflow was measured, and the initial trapped mass can be estimated by

$$m_t = \frac{m_a + \frac{m_a}{AFR}}{(1 - r_f)} \quad (4.9)$$

from which the temperature at IVC was estimated by

$$T_{ivc} = \frac{P_{ivc} V_{ivc}}{m_t R} \quad (4.10)$$

Options exist in the program to select a heat transfer correlation and its weighting, and a blow-by factor. The Hohenberg (1979) correlation was used throughout. Measurements of the blow-by at this stage showed a negligible blow-by mass fraction. Nitric oxide chemistry was modelled in the burned gas zone using the well established extended Zeldovich mechanism (Heywood, 1988), and utilised reaction rates from Bowman (1975) which were recommended by Heywood (1988). More details are given on ISIS modelling of nitric oxide in Chapter 7.

The model has been validated against a range of experimental data, and these have shown that the original model was able to satisfactorily predict the power output and efficiency of the engine as mixture strength and ignition timing are varied. It also predicts the correct trends with changes in the compression ratio and the effects of a fast burn combustion system (Stone, et al., 1996).

ISIS was "tuned" to the ensemble pressure averaged mean cycle in each case. The targets for the tuning were the mean IMEP,  $P_{max}$ , phasing of  $P_{max}$ , and the mean NO level. The tuning process itself involved running ISIS for the mean cycle with the previously outlined inputs, and then adjusting the residual fraction and heat transfer as required to provide good matching with the target parameters.

For the cycle-by-cycle modelling, the parameters from the mean cycle tuning were left unchanged. The cyclic perturbations were achieved by inputting the cycle-by-cycle values for the 10% and 80% burn times into ISIS, and fitting an appropriate Wiebe function to those values for each cycle.

#### 4.5 Results of initial cycle-by-cycle modelling

Data was collected from the Rover K4 engine under conditions of part load and wide open throttle (WOT), and at a relative air-fuel ratio ( $\lambda$ ) of 1.0 and 1.5. Ignition timing was varied from 15 to 45 degrees BTDC in the part load case. However, due to the high cylinder

pressures obtained at WOT, the ignition timing was not advanced beyond 30 degrees BTDC. The data comprised 305 consecutive cycles at each operating point, and in light of recent studies (Brunt and Emtage, 1997) this number was deemed sufficient for the levels of cycle-by-cycle variation expected.

COBRA was used to analyse the experimental data, and identified maximum pressure ( $P_{\max}$ ) and the angle of its occurrence ( $CaP_{\max}$ ), calculated the mass fraction burned utilising the standard Rassweiler and Withrow method, and identified the times to 10% and 80% MFB from ignition. Finally, both the net and gross IMEP were calculated. Due to the previously mentioned difficulties in determining an accurate expansion index, the compression index alone was used in the Rassweiler and Withrow method. Besides being the more accurate of the two calculated indices, an accurate expansion index is of primary use in determining the late-burn characteristics. For the purposes at hand, only the initial 80% burn was of interest and it was assumed that the errors inherent in using only the compression index were no greater than those associated with a doubtful expansion index, and were at least consistent. The polytropic index used by the Rassweiler and Withrow method,  $P_{\max}$ , phasing of  $P_{\max}$ , IMEP, and the average hydrocarbon reading for that cycle were output to a summary file, whilst the 10% and 80% burn durations were output to a separate file for later use by ISIS. It must be emphasised that the hydrocarbon reading did not correlate to the unburned hydrocarbons for that particular cycle as the hydrocarbons were not measured with a fast FID. This was done merely since it was a convenient way to record hydrocarbon data and achieve an accurate average measurement over the entire set of data. COBRA also generated individual cycle files which output the cylinder volume, cylinder pressure, barrel pressure, and mass fraction burned on a crank angle basis. The mean cycle program was used to generate an ensemble mean pressure trace, and all mean cycle calculations were performed on this pressure-crank angle history. The results for the experimental data are shown in Table 4.1.

Table 4.1. Results of calculations for experimental data.

Load	$\lambda$	Ignition (DBTDC)		Cycle-by-Cycle	Mean Cycle
Part Load	1.0	15	IMEP	3.84	3.84
			Pmax	18.15	18.05
			CaPmax	200.2	200
			10% Burn	20.2	20
			80% Burn	43	43
		30	IMEP	3.27	3.27
			Pmax	26.08	25.92
			CaPmax	186.7	187
			10% Burn	20.5	20
			80% Burn	36.1	37
		45	IMEP	3.15	3.15
			Pmax	29.54	29.34
			CaPmax	182.0	182
			10% Burn	26.8	27
			80% Burn	41.9	42
	1.5	15	IMEP	1.46	1.46
			Pmax	10.25	10.23
			CaPmax	180.6	180
			10% Burn	36.1	34
			80% Burn	96.1	96
		30	IMEP	2.33	2.33
			Pmax	15.19	15.13
			CaPmax	191.6	192
			10% Burn	28.0	28
			80% Burn	59.3	59
		45	IMEP	2.25	2.25
			Pmax	21.71	21.44
			CaPmax	186.1	186
			10% Burn	30.7	29
			80% Burn	49.7	48

Load	$\lambda$	Ignition (DBTDC)		Cycle-by-Cycle	Mean Cycle
WOT	1.0	15	IMEP	6.14	6.14
			Pmax	33.35	33.02
			CaPmax	197.9	198
			10% Burn	18.1	18
			80% Burn	36.1	36
		30	IMEP	5.55	5.55
			Pmax	45.87	45.68
			CaPmax	185.3	185
			10% Burn	19.0	19
			80% Burn	33.2	33
	1.5	15	IMEP	3.83	3.83
			Pmax	17.99	17.33
			CaPmax	191.0	194
			10% Burn	27.6	26
			80% Burn	61.2	61
		30	IMEP	4.38	4.38
			Pmax	29.40	29.20
			CaPmax	192.5	192
			10% Burn	27.3	27
			80% Burn	51.6	52

The results in Table 4.1 confirm the results obtained earlier (Table 3.6), i.e., the calculated parameters showed no sensitivity to the method of calculation, and both the cycle-by-cycle calculations and the mean cycle calculations yielded nearly identical results

ISIS was then used to simulate a mean cycle for each case. The target for tuning ISIS was the gross IMEP, and secondary targets were the maximum pressure, crank angle of maximum pressure, mean NO, and torque. Once ISIS was tuned for the mean cycle, the tuning parameters were left unchanged, and the COBRA generated files of ignition angle,  $\lambda$ , and 10% and 80% burn durations were imported into ISIS for cycle-by-cycle modelling. The results of this modelling for both the mean cycle model (mcm) and cycle-by-cycle (cbc) modelling are shown in Table 4.2.

Table 4.2. ISIS results for mean cycle and cycle-by-cycle modelling.

Part Load								
$\lambda$	$\theta_{ign}$ (DBTDC)		IMEP- gross	IMEP- net	Pmax (bar)	CaPmax (DABDC)	NO (ppm)	Torque (N-m)
1.0	15	EXP (COV)	3.84 0.78	3.49 0.96	18.05 6.22	200	700	1.8
		ISIS-mcm	3.85	3.43	16.61	203	696	2.0
		ISIS-cbc (COV)	3.83 2.00	3.42 2.26	16.36 8.56	203	676	1.97
	30	EXP (COV)	3.27 2.31	2.90 2.71	25.92 3.58	187	1550	0.2
		ISIS-mcm	3.28	2.86	24.66	189	1494	0.0
		ISIS-cbc (COV)	3.28 0.625	2.85 0.72	24.66 6.03	189	1496	0.0
	45	EXP (COV)	3.15 4.13	2.79 4.72	29.34 3.23	182	1980	-1.0
		ISIS-mcm	3.16	2.74	28.62	183	2004	-1.0
		ISIS-cbc (COV)	3.15 2.15	2.73 2.48	28.52 2.64	183	2015	-1.07
1.5	15	EXP (COV)	1.46 23.69	1.08 31.88	10.23 1.48	180	7	-4.7
		ISIS-mcm	1.46	1.06	10.32	180	2	-5.0
		ISIS-cbc (COV)	1.47 17.18	1.07 23.30	10.36 0.91	180	2.95	-5.05
	30	EXP (COV)	2.33 5.59	1.98 6.55	15.13 10.24	192	15	-2.1
		ISIS-mcm	2.33	1.92	13.63	192	15	-2.0
		ISIS-cbc (COV)	2.30 5.84	1.89 7.05	14.17 12.52	191.5	20.7	-2.21
	45	EXP (COV)	2.25 5.92	1.90 7.19	21.44 8.98	186	75	-2.4
		ISIS-mcm	2.24	1.82	21.18	187	73	-2.0
		ISIS-cbc (COV)	2.22 2.50	1.80 3.08	21.22 10.97	187	97	-2.34

WOT								
$\lambda$	$\theta_{ign}$ (DBTDC)		IMEP- gross	IMEP- net	Pmax (bar)	CaPmax (DABDC)	NO (ppm)	Torque (N-m)
1.0	15	EXP	6.14	6.06	33.02	198	1750	10.8
		(COV)	0.85	0.89	6.68			
		ISIS-mcm	6.14	6.01	30.13	200	1786	11.0
	30	ISIS-cbc	6.16	6.03	30.22	200	1823	11.2
		(COV)	1.24	1.26	8.30			
		EXP	5.55	5.48	45.68	185	2560	8.5
1.5	15	(COV)	2.11	2.20	2.70			
		ISIS-mcm	5.56	5.43	43.56	187	2522	9.0
		ISIS-cbc	5.56	5.45	43.42	187	2503	9.0
	30	(COV)	0.82	0.83	4.02			
		EXP	3.83	3.73	17.33	190	10	3.3
		(COV)	8.77	8.99	11.35			
		ISIS-mcm	3.83	3.74	16.96	183	11	3.0
	30	ISIS-cbc	3.78	3.69	17.65	189	16.1	2.72
		(COV)	11.54	11.71	10.11			
		EXP	4.38	4.27	29.20	192	110	4.5
	30	(COV)	2.10	2.23	8.80			
		ISIS-mcm	4.37	4.29	26.01	195	117	5.0
		ISIS-cbc	4.37	4.29	26.35	195	137	4.88
		(COV)	2.01	2.04	12.46			

Several points need to be addressed in relation to these results. First, the net IMEP was included to assess the accuracy of the estimates of valve and throttling losses in ISIS. ISIS tends to overestimate the valve and throttling losses in the part load case, yet the agreement between the experimental data and the modelled data is reasonable.

Secondly, ISIS shows good agreement with gross IMEP since this was the primary target parameter. However, it consistently underestimates the maximum pressure, and there are some errors in the phasing of maximum pressure. This is attributed to the slow burn-up of the crevice gases which is not well modelled by a Wiebe function. (A discussion of this phenomenon is contained in Chapter 5.) One option to account for the crevice effects would be to modify ISIS to accept burn rate information on a crank angle basis directly from the

experimental data. This would certainly improve the accuracy of the model. However, for the case of engine development modelling, this would also require that an engine be built and run to get this information, which then defeats the purpose of having a predictive model. In any event, a production engine would not have crevice volumes of this order since the resulting unburned hydrocarbon emissions would make the engine commercially dubious. Hence, it was decided to accept the errors in maximum pressure caused by the Wiebe fit since the IMEP, NO, and torque results were in good agreement.

Thirdly, there has been some discussion in the literature as to which parameter should be used to characterise cycle-by-cycle variation. Whilst maximum pressure is often used, and is convenient, other researchers tend to advocate the use of COV of IMEP (Stone, 1992). The lean, part load case with retarded timing highlights the issue. In this case, the COV of maximum pressure was only 1.48% whilst the COV of IMEP was over 23%. The pressure did not vary much in this case because even with good combustion, cylinder pressure barely rose above the motoring maximum pressure of roughly 10 bar. On the other hand, it was obvious that the engine was not running smoothly, and to the operator of a vehicle, such engine performance would be totally unacceptable. Because the engine is a work producing device, COV of IMEP is favoured to characterise cyclic variation.

Finally, ISIS tended to under predict the COV of IMEP in most cases, the exception being the cases with retarded ignition timing (15 degrees BTDC). As has been discussed, the causes of CCV are numerous. It was assumed in the current modelling that these causes would manifest themselves in the varying burn rates. The fact that ISIS under-predicts the COV of IMEP indicates that not all of these factors are captured by the burn rate. It is most likely that the burn rate does account for variations in the initial kernel development and growth, and possibly the effects of turbulence on flame speed. It does not take into account sources of CCV such as variations in charging, residual temperatures, or in this case, the variations in the burn-up of the (significant) crevice mass. The cases in which ISIS over-predicted the COV of IMEP were all near MBT ignition timing. Since there were still variations in the burn rate in these cases, it must be assumed that other variations work to counteract the variation in burn rate and produce a more stable IMEP. This area remains open to further investigation as it would improve understanding of why COV of IMEP is at a minimum at MBT.



#### 4.6 Summary

The primary conclusion from this test is that burn rate data alone is insufficient to quantify the cyclic variation in an engine. In general, modelling variations in burn rate led towards an under-prediction of the actual variation in IMEP, although ISIS tended to over-predict the COV of IMEP near MBT ignition timing. The causes for this over-prediction are not understood at present. Furthermore, the results confirm the findings of Raine et al. (1995).

This test was successful in developing a baseline understanding of the Rover K4 operating and combustion characteristics, and the primary characteristic of this engine is its slow burn-up of crevice gas. This phenomenon was discovered whilst examining various burn-rate models in an attempt to improve the ability of ISIS to perform cycle-by-cycle modelling, and will be discussed in Chapter 5.

As a result of these findings, the work proceeded down two separate avenues. First, the possibility existed that the Rassweiler and Withrow method as implemented was not sufficiently accurate. This investigation is discussed in Chapter 5, and includes an investigation into a different burn rate model based on a two-zone polytropic process model, as well as a modification to the Rassweiler and Withrow method that incorporates the compression and expansion indices throughout the combustion period. The second avenue was directed towards deriving a completeness of combustion parameter that could be varied on a cyclic basis and would account for those causes that the variation in burn rate fails to capture. This investigation is discussed in Chapter 6.

## Chapter 5 Evaluation of Combustion Analysis Routines

### 5.1 Introduction

Since ISIS tended to under-predict the COV of IMEP in its cycle-by-cycle modelling, one possibility was that the Rassweiler and Withrow analysis used was not sufficiently sensitive to provide ISIS with accurate burn rate data upon which to model combustion. Cheung and Heywood (1993) review the limitations of the method, mentioning specifically the following:

- a) it is usually used with a constant polytropic index,
- b) the mass burn profile automatically goes to unity,
- c) the method does not account for crevices which are potentially a significant source of unburned hydrocarbons, and hence incomplete combustion, and
- d) heat transfer is not explicitly accounted for.

The focus of this part of the work was to evaluate methods of calculating burn rate from engine pressure data so as to overcome some of the limitations in the Rassweiler and Withrow method identified by Cheung et al. (1993). The first method developed was a two-zone polytropic process model. The goals set for this model were to: retain the simplicity of Rassweiler and Withrow, yield satisfactory results for mass fraction burned, and provide information about the temperatures of the burned and unburned zones. The development and evaluation of this model are described in the first part of this chapter.

In developing the two-zone model, pressure data from ISIS was used in order to evaluate its performance. The primary reason for this was that it was hoped that the two-zone model would provide temperature information as well as burn rate information, and this could be compared to the temperatures calculated by ISIS. The simulated engine for this part of the investigation was a production 4 cylinder engine, which was chosen since ISIS had already been validated against experimental data (Stone, et al., 1993) for this particular engine. ISIS used the burn rate from experimental measurements. The burn rates were stored in grids of 10% and 90% burn times (in degrees crank angle) for several combinations of air-fuel ratio and ignition timing. If the desired operating point did not correspond exactly to a point on the grid, ISIS interpolated between the data points.

The second method developed in this chapter was an extension of the Rassweiler and Withrow method. Many workers have considered modifications to the Rassweiler and Withrow method. For example, Shayler et al. (1990) suggest changing the value of the polytropic index during combustion in order to drive the pressure rise due to combustion to zero both prior to ignition and after the end of combustion. While this technique was demonstrated to improve mass fraction burned calculations, it requires a switch in the value of the polytropic index at an arbitrary, and user defined, crank angle. The method considered here incorporates both the compression and expansion indices throughout the calculation, and is described in the second part of the chapter.

During evaluation of the modified Rassweiler and Withrow method, it was discovered that the K4 engine exhibited a slow burn-up of a significant crevice mass. This phenomenon will be discussed in the last part of this chapter since it had a bearing on the decision as to whether to use the modified Rassweiler and Withrow method.

## **5.2 Two zone polytropic process model**

### **5.2.1 Combustion modelling**

The model under consideration is shown schematically in Figure 5.1. The primary assumptions in this model are as follows:

1. Two distinct zones are present during combustion, one containing unburned reactants and one containing burned products, separated by a thin flame front.
2. The pressure is constant across the combustion chamber at any instant.
3. There are two temperatures in the combustion chamber, one for the burned zone and one for the unburned zone. An abrupt transition between these two temperatures is assumed to occur at the flame front.
4. The charge undergoes polytropic compression and expansion. It is assumed that the polytropic index for the unburned gas remains constant during combustion at its value prior to ignition. The polytropic index for the burned gas is assumed to be equal to its value during expansion after the end of combustion.
5. The burned and unburned gases behave as semi-perfect gases.

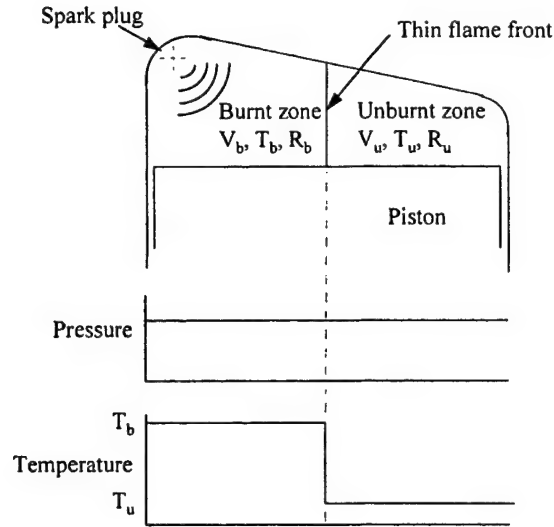


**Figure 5.1. Two zone combustion model.**

Under the two zone assumption, the total volume of the chamber is equal to the volumes of the burned and unburned zones

$$V = V_u + V_b. \quad (5.1)$$

If the mass fraction burned is described by  $x$ , and utilising the equation of state, the burned and unburned volumes may be expressed by

$$V_u = \frac{m(1-x)R_u T_u}{p} \quad (5.2)$$

$$V_b = \frac{mxR_b T_b}{p}. \quad (5.3)$$

By summing these two equations and rearranging, an expression for mass fraction burned is obtained

$$x = \frac{pV/m - R_u T_u}{R_b T_b - R_u T_u}. \quad (5.4)$$

Since ISIS calculates the mass in the cylinder at each instant, mass could be considered to be known. However, since the analysis was to be used on an actual engine, the mass was taken to be an average of the ISIS calculated mass at inlet valve closure and exhaust valve opening.

There are now three unknowns in the previous equation, namely  $x$ ,  $T_u$  and  $T_b$ . Since a polytropic process is assumed, the temperature at any point is related to the temperature at the previous point by

$$\frac{n-1}{n} = \frac{\ln\left(\frac{T_2}{T_1}\right)}{\ln\left(\frac{P_2}{P_1}\right)} \quad (5.5)$$

The temperature of the unburned zone can be calculated at ignition, whilst the temperature of the burned zone can be calculated at the end of combustion. For this study, the ISIS calculated temperatures at ignition and end of combustion were used. For experiments, the equation of state can be applied at exhaust valve opening to estimate the temperature, using a trapped mass that incorporates the blow-by and valve leakage loss. Since each zone is assumed to be undergoing a series of polytropic processes throughout combustion, calculation of the unburned zone temperature begins at ignition and proceeds forward through the combustion process. Calculation of the burned zone temperature begins at the end of the cycle and proceeds backwards through the combustion process. The polytropic index of the unburned zone is calculated from inlet valve closure to ignition, and is assumed constant during combustion. Likewise, the polytropic index for the burned zone is calculated from the end of combustion to exhaust valve opening and assumed constant. [As discussed later, the practical difficulties of determining the index for the burned zone are considerable.] Equation (5.5) is used for each zone to calculate the temperature in the next interval ( $T_2$ ). Once the burned and unburned temperatures have been calculated for each crank angle interval, equation (5.4) is used to determine the mass fraction burned as a function of crank angle.

The foregoing analysis was developed independently of the work of Al-Himyary and Karim (1988) who developed a very similar model. In their paper, a two zone model is assumed with each zone undergoing a polytropic process throughout combustion. However, Al-Himyary and Karim evaluated the heat transfer through the system walls, and thus a heat transfer coefficient. They then developed expressions by which the temperatures, specific heat capacities, and polytropic indices could be calculated for each step. (However, the method assumes that the heat transfer coefficient and the area it acts on remain constant during a time step, and the method also requires an estimate of wall temperature. This directly influences their calculation of the polytropic index.) The novelty in their approach was to use an iterative process to converge on a value for the polytropic index, which then

varied throughout combustion. Their results indicated some variation in the polytropic index, although the indicated variation tended to support the assumption of a constant value.

### 5.2.2 Results

The analysis was performed on simulations with operating conditions as shown in Table 5.1, and results of temperature calculations are shown in Figure 5.2.

**Table 5.1. Engine simulation operating conditions for the two zone model calculations.**

Test No	RPM	Compression ratio	Fuel	Ign Timing (deg BTDC)	$\lambda$
1	2000	10:1	Iso-octane	24	0.8
2	2000	10:1	Iso-octane	24	1.0
3	2000	10:1	Iso-octane	24	1.4

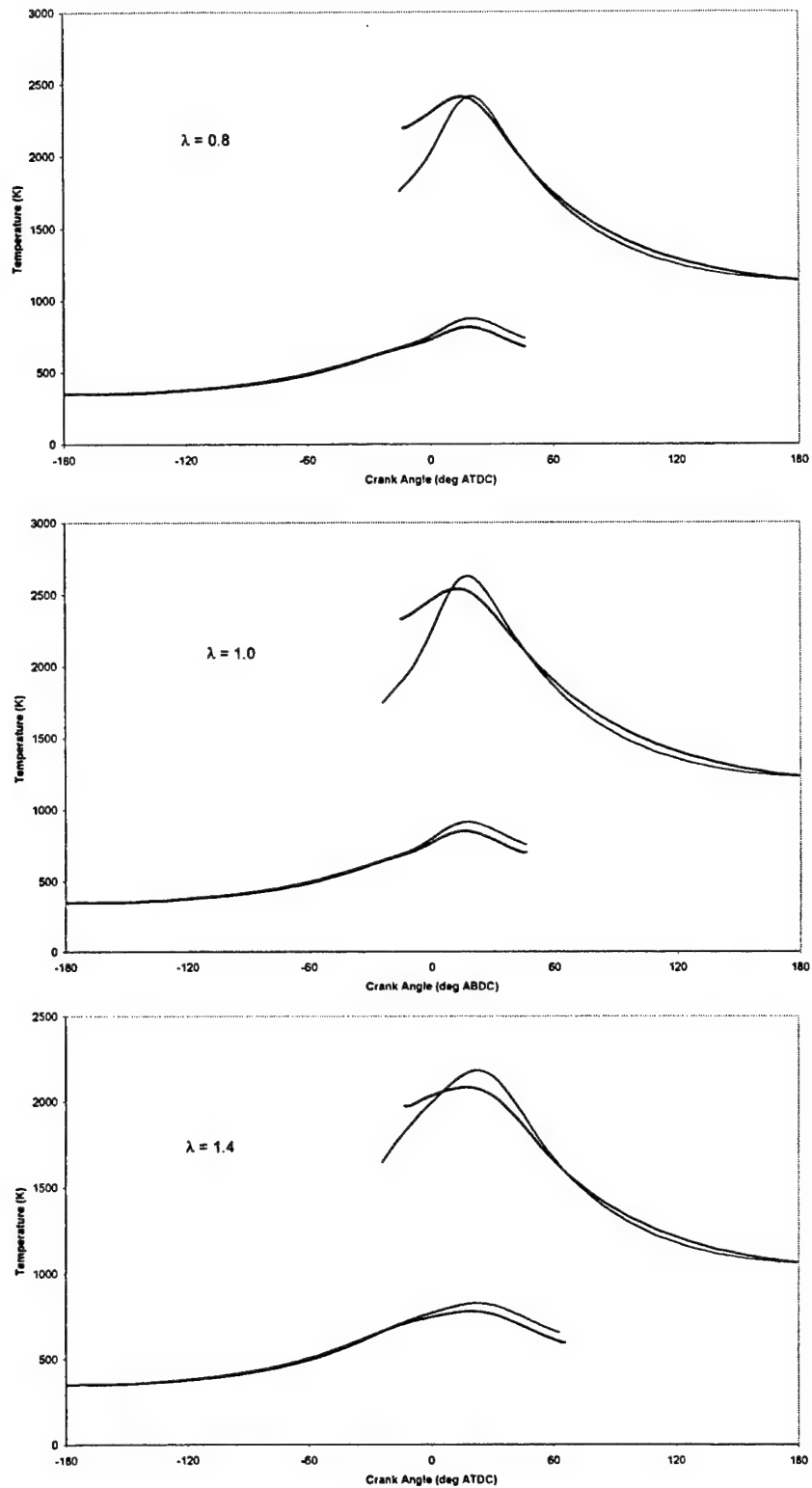


Figure 5.2. Temperatures of burned and unburned zones. ISIS calculated temperatures shown with heavy lines and two zone model calculated temperatures shown with thin lines.

As shown in Figure 5.2, the two zone model underestimates the temperature of the burned zone at the beginning of combustion, whilst overestimating the temperature of the unburned zone later on. The temperatures for the unburned zone could be improved with a better choice of polytropic index. However, this may not be the case for the burned zone. Heywood (1988) notes that a temperature gradient exists in the burned zone which may be as large as 400K between early and later burning elements. As a result, there is a disproportionately high rate of heat transfer in the early zones which is not accounted for by this model. Since the calculation of mass fraction burned is dependent on the temperature calculations, this calculation is also unreliable as shown in Figure 5.3. In this figure, the burn rate used as an input by ISIS (as described previously) is plotted, along with burn rates calculated by the two zone model and the method of Rassweiler and Withrow.



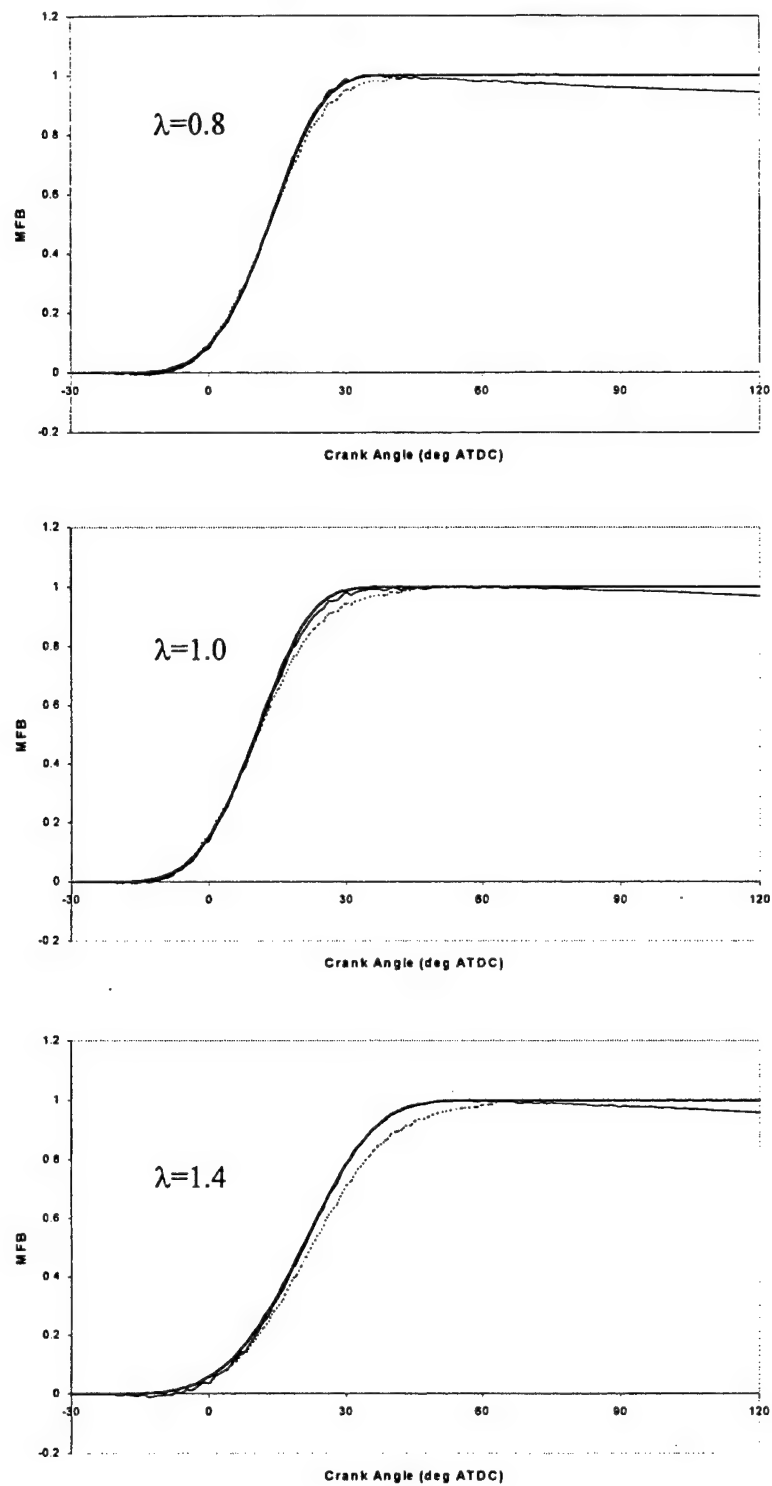


Figure 5.3. Comparison of mass fraction burned calculations. ISIS profile shown with heavy line, Rassweiler and Withrow with light line, and two zone model with dotted line.

Referring to Figure 5.3, the difference between the ISIS burn rate and that calculated by the Rassweiler and Withrow method appears insignificant. Furthermore, even the burn rate calculated by the two zone model seems adequate. However, the superior performance of the Rassweiler and Withrow method is emphasised by Figure 5.4, in which the data of Figure 5.3 have been re-plotted to show the error in the calculated mass fraction burned ( $X_{\text{ISIS}} - X$ ) plotted against the ISIS mass fraction burned.

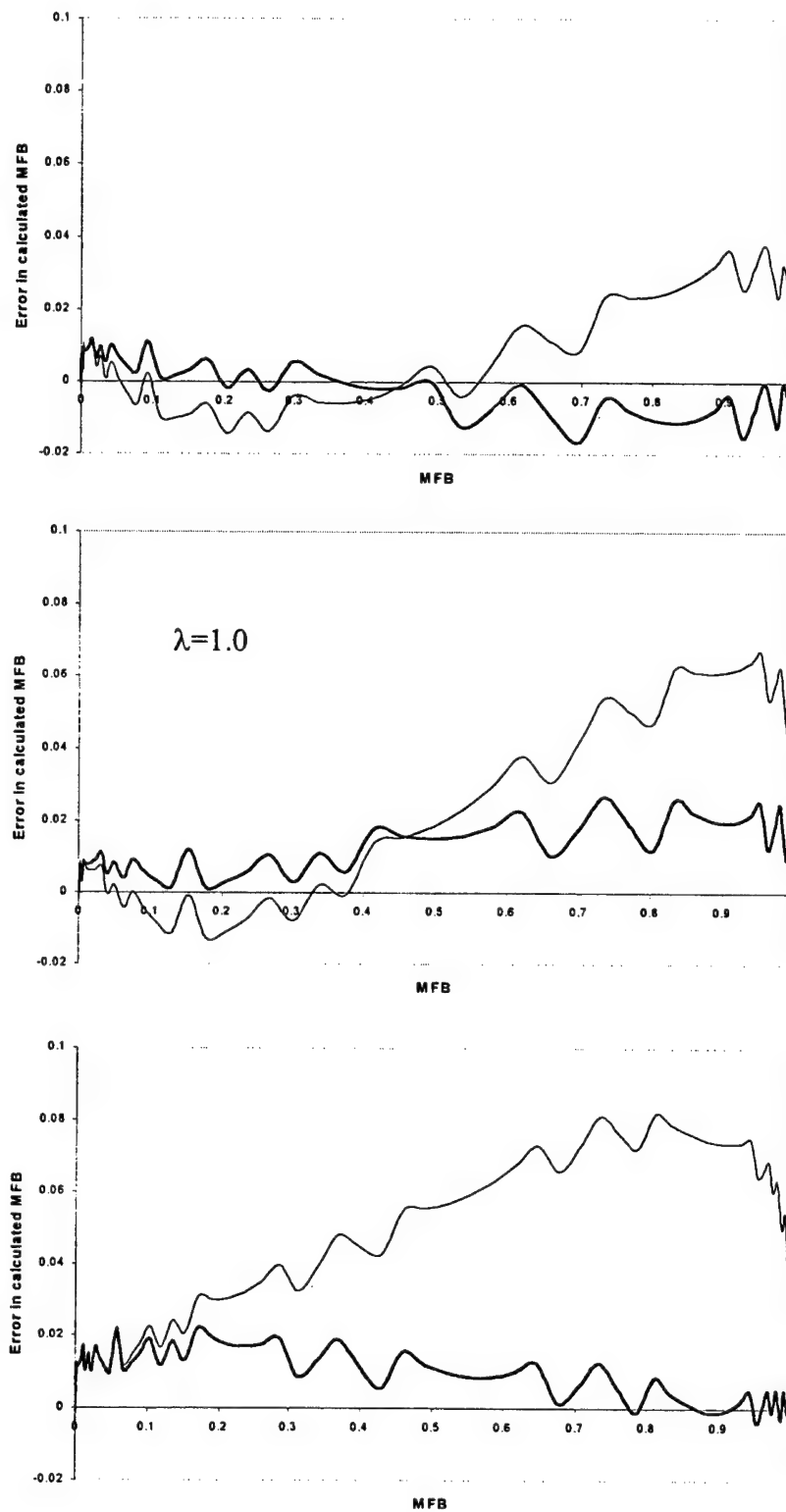


Figure 5.4. Error in calculated mass fraction burned: two zone model shown with light line, Rassweiler and Withrow with heavy line.

It can be seen in Figure 5.4 that the two zone model has a greater error than the Rassweiler and Withrow method in all cases. Since the two zone model assumes a constant value of the polytropic index for all points in the burned mixture at each time step, it underestimates the burn rate throughout the combustion process. This underestimation shows up in the mass fraction burned curve where this model indicates a slowing of the burn rate and subsequent increase in the burn time. The method of Rassweiler and Withrow is in better agreement with the simulation than the two zone model in all cases, and is significantly better for lean mixtures.

The unsatisfactory results for the estimation of burned temperature ( $T_b$ ), unburned temperature ( $T_u$ ), and mass fraction burned ( $x$ ) obtained from the two zone model led to a questioning of the assumptions about the polytropic indices. Since the simulation produced temperature data for each zone, the actual index could be calculated throughout the cycle. These results are shown in Figure 5.5 for an excess air ratio of  $\lambda = 0.8$ ; results for other ratios display the same trends. The gross polytropic index was calculated using the pressure and volume as outlined by Al-Himyary and Karim (1988), in which there is no distinction between products and reactants, while the indices for the burned and unburned zones were calculated using equation (5.5) with ISIS temperature and pressure data.

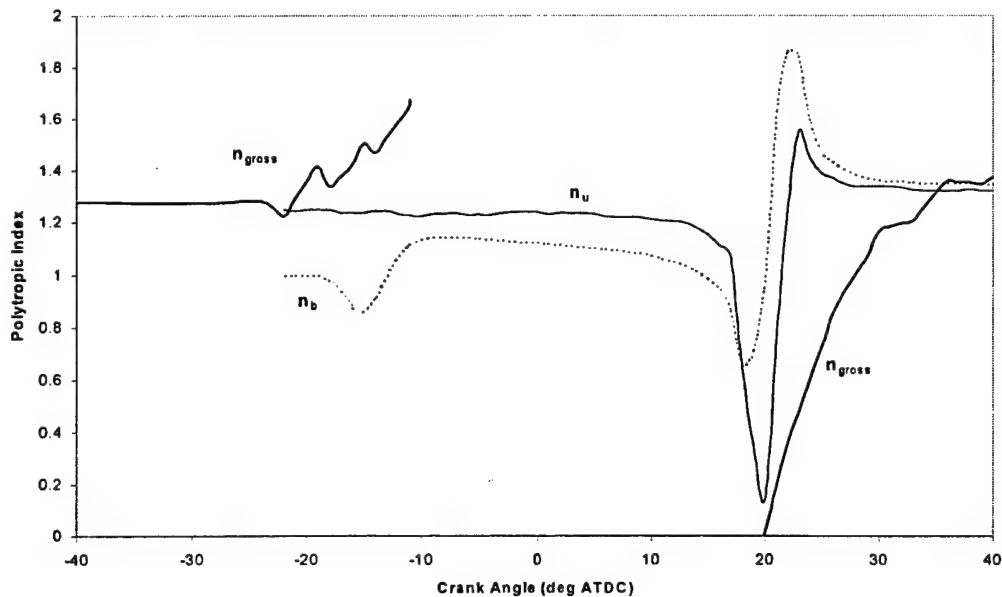


Figure 5.5. The gross polytropic index of the charge compared to the indices of the burned and unburned zones for a rich mixture ( $\lambda=0.8$ ).

These results do not agree very favourably with those of Al-Himyary and Karim (1988). The index for the unburned zone does indeed equal the gross index at ignition. However, at the point in the cycle of maximum pressure there is a singularity, so the index goes to infinity and returns to settle near the gross index for the burned gas, i.e., the gross index after combustion. Likewise, the index for the burned zone does in fact equal the gross index value at the end of combustion. It also exhibits similar behaviour at the point of maximum pressure. However, the index for the burned zone actually settles near to unity at the beginning of combustion, due to the previously mentioned high rate of heat transfer from the early combustion zones.

The simulation can be used to gain further insights into the shortcomings of assuming constant values of the polytropic indices for the burned and unburned gases. The simulation was used to study the following cases, all of which correspond to the same: burn rate, ignition timing, air-fuel ratio, etc.

- a) The burned gas divided into multiple zones, with all zones adiabatic.
- b) The burned gas in a single zone, with both zones treated as adiabatic.
- c) The burned gas divided into multiple zones, with all zones non-adiabatic.

When the polytropic index is evaluated for the multiple burned zones in case (a), it can be seen from Figure 5.6 that the polytropic indices are essentially constant. In this case, the polytropic indices are almost equal to the ratios of specific heat capacities ( $\gamma$ ), and the variations are solely due to the temperature and composition dependencies of the specific heat capacities and the limitation of a finite number of zones (10). Figure 5.6 also illustrates the wide variation in temperatures between the first burned zone and later burned zones in the adiabatic case.

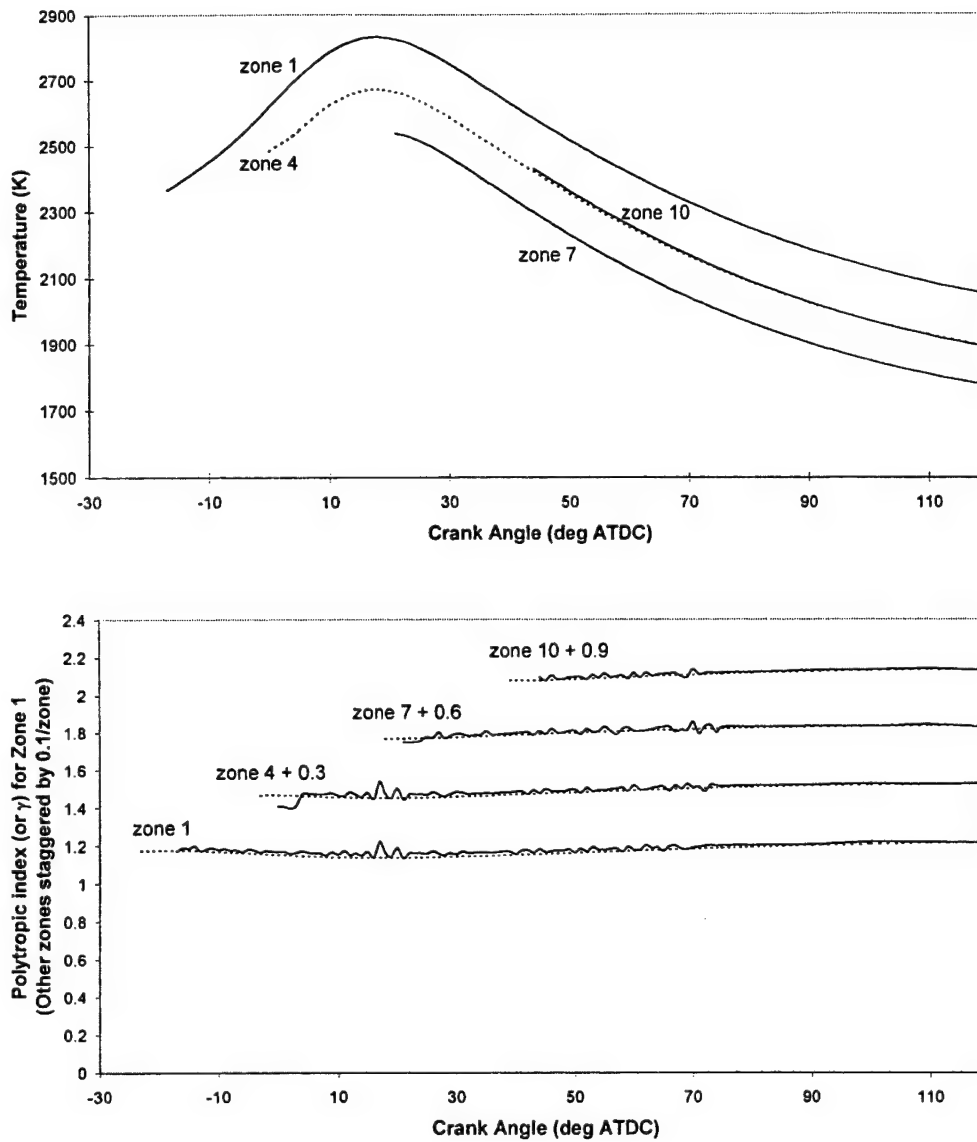


**Figure 5.6. Temperature, polytropic indices, and ratios of specific heat capacities for 10 zone model, adiabatic case. Zones 1,4,7, and 10 plotted. Plots staggered as indicated for clarity.**

Case (b) is also adiabatic, but when a single burned zone is modelled the temperature corresponds to an infinite number of zones (each at a different temperature) with perfect mixing. Figure 5.7 shows that there is now a significant variation in the polytropic index.

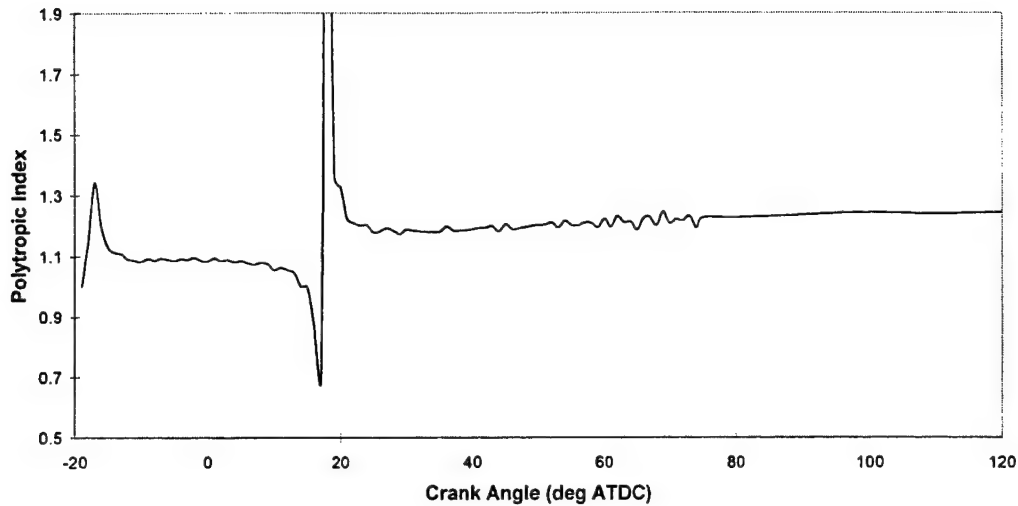


**Figure 5.7. Polytropic index for single burned zone model, adiabatic case.**

Finally, case (c) illustrates that even with multiple burned zones, there is a significant variation in the polytropic indices for each zone once heat transfer is present (Figure 5.8). This is because of the disproportionate amount of heat transfer from the zones burned first, and is due to the adverse volume-to-area ratio and the higher burned gas temperatures. Case (c) illustrates that even if an attempt was to be made at dividing the burned gas into a number of zones for combustion analysis, it would not be realistic to assume a constant value of the polytropic index for each zone. This illustrates another advantage of using a simulation, namely the ability to generate data for cases that could not be achieved with experimental data.

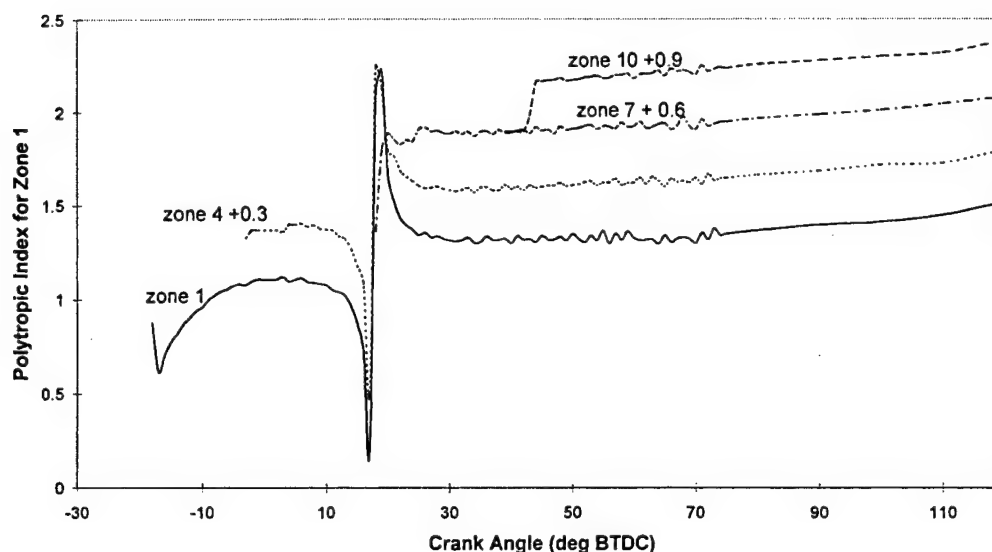


**Figure 5.8. Polytropic indices for 10 zone model, non-adiabatic case. Zones 1,4,7,and 10 plotted. Plots staggered as indicated for clarity.**

While an iterative scheme may allow the model to converge on the requisite indices, the approach outlined by Al-Himyary and Karim is dependent on the assumed wall temperature. This will affect the rate of heat transfer in the model and in turn affect the calculated polytropic index. The two zone model, by assuming a constant rate of heat transfer, is simply unable to calculate accurate temperatures in either zone.

### 5.2.3 Conclusion

This particular two zone combustion analysis model cannot be relied upon to calculate either the temperatures within the zones or the mass fraction burned. The error lies in the assumption of uniform temperature within each zone and a corresponding error in the rate of heat transfer throughout combustion. The model could be improved by considering conservation of energy as outlined by Heywood (1988). However, more accurate models require accurate estimations of the heat transfer to the cylinder walls and possibly crevice effects. Furthermore, results from a more sophisticated calculation would then be strongly dependent on the assumptions made in the analysis.



### 5.3 Modification to the Rassweiler and Withrow method

#### 5.3.1 Derivation of equations

Chapter 4 outlined the Rassweiler and Withrow method as it is usually implemented. As noted in that chapter, Rassweiler and Withrow do not present a mathematical formulation of this method, but only give a “spreadsheet” example of it, and a full derivation of the method is given in Stone (1992). This method will be referred to as the “standard” (ST) method for the remainder of this work to differentiate it from the other variations of Rassweiler and Withrow considered.

In their original work, Rassweiler and Withrow (1938) derive the following expression for the determination of mass fraction burned:

$$x = \frac{(V p^{1/n} - V_s p_s^{1/n})}{(V_f p_f^{1/n} - V_s p_s^{1/n})} \quad (\text{RW}) \quad (5.6)$$

where the subscripts ‘s’ and ‘f’ refer to conditions at the time of spark and the end of combustion, respectively. Since Rassweiler and Withrow used non-standard notation in their work, the derivation of equation (5.6) is contained in Appendix A with their original notation and equation numbering. The derivation of equation (5.6) is based upon the assumption that the polytropic index ( $n$ ) is the same for compression and expansion processes.

This formulation is not generally used in practice because of the difficulties in *a priori* determining the end of combustion. It is obvious that this expression will yield  $x=1$  for any selected value of  $V=V_f$  and corresponding  $p=p_f$ . In order to implement this method, it was initially assumed that combustion completed at EVO. Thus,  $p_f$  and  $V_f$  were set to those values. The denominator of equation (5.6) was then evaluated from ignition to EVO, and was found to achieve a maximum value at some point. This point was the desired end of combustion (EOC), and the appropriate corrected values of  $p_f$  and  $V_f$  were determined. Mass fraction burned (MFB) can then be computed using equation (5.6). It has been found that this method yields the same EOC as the standard method.

In the course of this investigation, use has been made of equation (5.6) to determine MFB, and this method will be referred to as RW. Numerical results for MFB are similar to

those obtained using the standard method, but no proof has been found that the two expressions can be related.

As a further development of the Rassweiler and Withrow approach, the derivation of equation (5.6) was followed with an allowance for different values of the polytropic index for compression and expansion ( $n_c$  and  $n_e$ ). The following expression for MFB is derived:

$$x = \frac{p^{1/n_e} (V p^{1/n_e} - V_s p_s^{1/n_e})}{(V_f p_f^{1/n_e} p^{1/n_e} - V_s p_s^{1/n_e} p^{1/n_e})} \quad (\text{RW2}) \quad (5.7)$$

An outline of the derivation is in Appendix A. This method will be referred to as RW2 in the remainder of this text.

Equation (5.7) provides no obvious method of determining EOC since the point at which the denominator achieves a maximum has no relation to EOC. However, by assuming initially that EOC occurs at EVO, the function will rise to 1.0 and remain there providing the value of the expansion index is correct. The key point is that the calculated expansion index must be correct. The effects of an incorrect expansion index are shown in Figure 5.9.

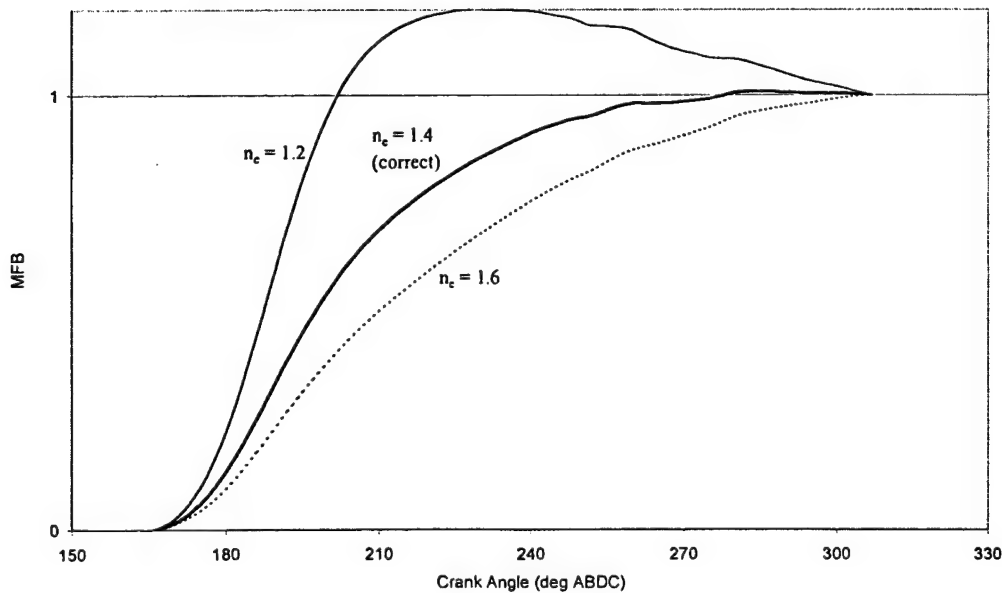


**Figure 5.9. Effects of incorrect expansion index on RW2 method of calculating mass fraction burned.**

Figure 5.9 shows the results of the RW2 method of calculating MFB on experimental data taken from the K4. The case presented in Figure 5.9 is for the lean, part load case with an ignition timing of 30 degrees BTDC. If the calculated expansion index is too low, the MFB curve will exceed 1.0 and return to 1.0 at EVO. Conversely, if the expansion index is too high, MFB will only reach 1.0 at EVO. In practice it was found that errors in the expansion index tended towards a low value, which may be due to the slow and long duration combustion exhibited by the K4 engine. The MFB curves in such cases did not exceed 1.1, often overshooting by only 0.02 to 0.03.

### 5.3.2 Use of alternative MFB analysis method

Pressure data generated by ISIS has been analysed using the standard method (equation (4.7)), Rassweiler and Withrow's original method (equation (5.6)), and the modified Rassweiler and Withrow method (equation (5.7)) presented above. The results from this analysis are shown in Figure 5.10 for stoichiometric operation with a 30 degree BTDC ignition timing. Figure 5.10 presents three variations of this operating point:

- a) adiabatic cycle with no blow-by
- b) heat transfer included with no blow-by
- c) heat transfer and blow-by included.

A Hohenberg (1979) heat transfer correlation was used to model the heat transfer within ISIS. To model blow-by, ISIS assumes an exponential mass loss throughout the cycle. The results of the three methods of calculating MFB are compared with the 'correct' mass fraction burned curve used as an input to ISIS. Figure 5.10 shows that all three analysis methods normalise the mass fraction burned to 1.0.

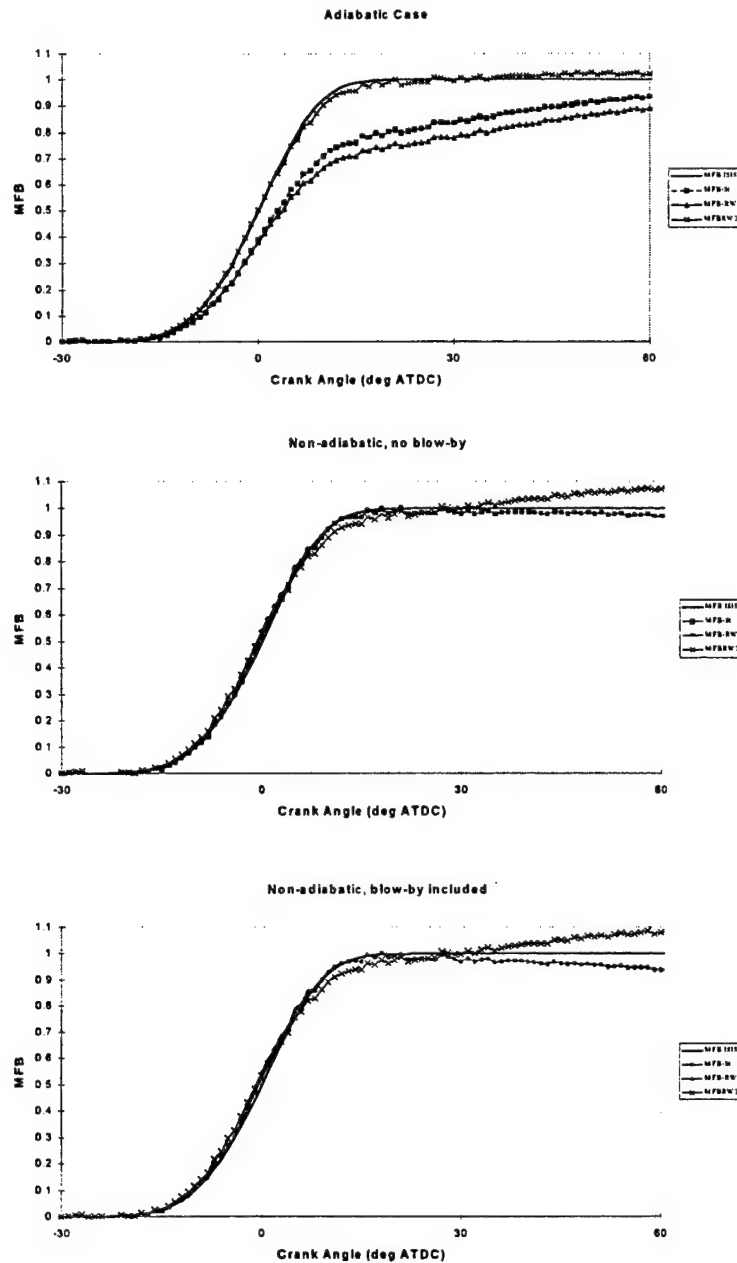


**Figure 5.10. Results of the different mass fraction burned analysis methods using pressure data from ISIS showing differences between the different methods.**

It should be noted that the standard analysis method (MFB-ST) and that based on Rassweiler and Withrow's original method (MFB-RW) give similar results. The main reason for the differences are in the polytropic indices used for the RW2 analysis. In the RW2 method, both the compression and expansion indices were used. The compression index was calculated from ISIS pressure-volume data from a point halfway between inlet valve closure

and ignition up to the ignition point. Since ISIS provides a definite end of combustion, the expansion index was calculated from that point up to the end of the cycle (ISIS does not model exhaust blowdown). In the other two methods, the compression polytropic index is used throughout the analysis. The method RW2 is in much better agreement with the actual MFB curve when compared with the other methods in case (a) because the expansion index is lower than the compression index. Since the first two methods (ST and RW) utilise the compression index throughout, the models underestimate the burn rate during the later stages of combustion.

In the last two cases, there is very little difference between the three methods even though the expansion index is on the order of 0.1 larger than the compression index. Hence, the ST method and RW method show the characteristic fall after the end of combustion whilst the modified method hovers near 1.0. It is concluded that the modified Rassweiler and Withrow method (RW2) is a viable method of calculating MFB provided an accurate expansion index can be calculated. It also removes the need to determine the end of combustion since EVO can be used as the final point and the MFB curve will rise to and remain at 1.0. Again, this assumes an accurate expansion index. However, the difficulties of calculating an accurate expansion index on experimental data taken from the K4 will be addressed, and may render the RW2 method as prone to errors as the first two.

#### 5.4 Slow burn up of crevice Hydrocarbons

Using both the standard analysis method and RW2, slow burning in the late stages of combustion for the Oxford optical access engine under certain engine operating conditions has been detected. This issue is being addressed here because it impacted the decision on whether to use the RW2 method outlined in the previous section. It is believed that the cause of these non-standard burn rate curves lies in crevice effects. The piston crown of the K4 engine is shown schematically in Figure 5.11.

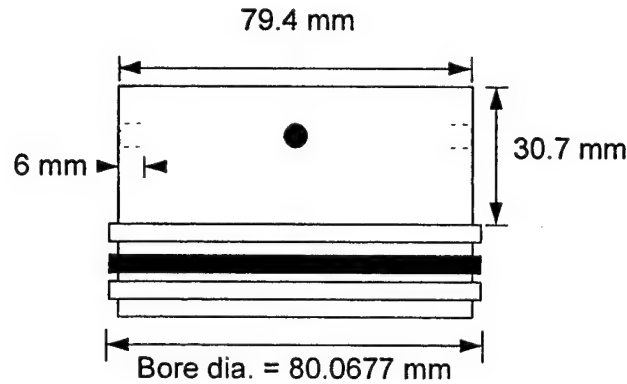


Figure 5.11: K4 piston crown.

Since the engine was designed for optical access, the highest sealing rings are very low in comparison to a production engine. In addition, there are four 6 mm holes bored around the circumference to facilitate tightening of the crown to the skirt. These features produce a crevice volume ( $V_{cr}$ ) of 3.25 cc. If it is assumed that the temperature of the mass trapped in the crevice volume during firing is approximately equal to the wall temperature (Heywood, 1988), the mass trapped in the crevice can be calculated at maximum pressure from

$$m_{tr} = \frac{p_{max} V_{cr}}{RT} \quad (5.8)$$

This can then be related to the initial trapped mass ( $m_{live}$  - calculated by ISIS) as a trapped mass fraction (tmf) as shown in Table 5.2. In Table 5.2, the maximum combustion pressure ( $P_{max}$ ) is the mean measured value, and wall temperature ( $T_{wall}$ ) is estimated from some limited measurements.

**Table 5.2. Calculated mass trapped in the crevice volume at maximum pressure.**

$\lambda$	ignition (°BTDC)	$m_{tvc}$ (grams)	$P_{max}$ (bar)	$T_{wall}$ (K)	R	$m_{tcr}$ (grams)	tmf
1.0	15	0.208	18.05	450	301.0	0.043	0.208
1.0	30	0.187	25.92	450	301.0	0.062	0.333
1.0	45	0.193	29.34	450	301.0	0.070	0.365
1.5	15	0.184	10.23	380	296.9	0.029	0.160
1.5	30	0.189	15.13	380	296.9	0.044	0.231
1.5	45	0.188	21.44	380	296.9	0.062	0.329

Table 5.2 indicates that between 16 and 36% of the initial charge can be forced into the crevice volume during compression and the initial burn period. Of even greater interest is when this trapped mass will flow from the crevice back into the main combustion volume. This flow will occur as the cylinder pressure reduces from the maximum value and will be enhanced by the movement of the piston down the cylinder. Figure 5.12 shows the MFB curves for 3 individual cycles for both the stoichiometric and lean cases based on the standard Rassweiler and Withrow analysis method. These curves indicate the crank angle of maximum pressure. From this point onward, flow will occur from the crevices into the main region of the combustion chamber.

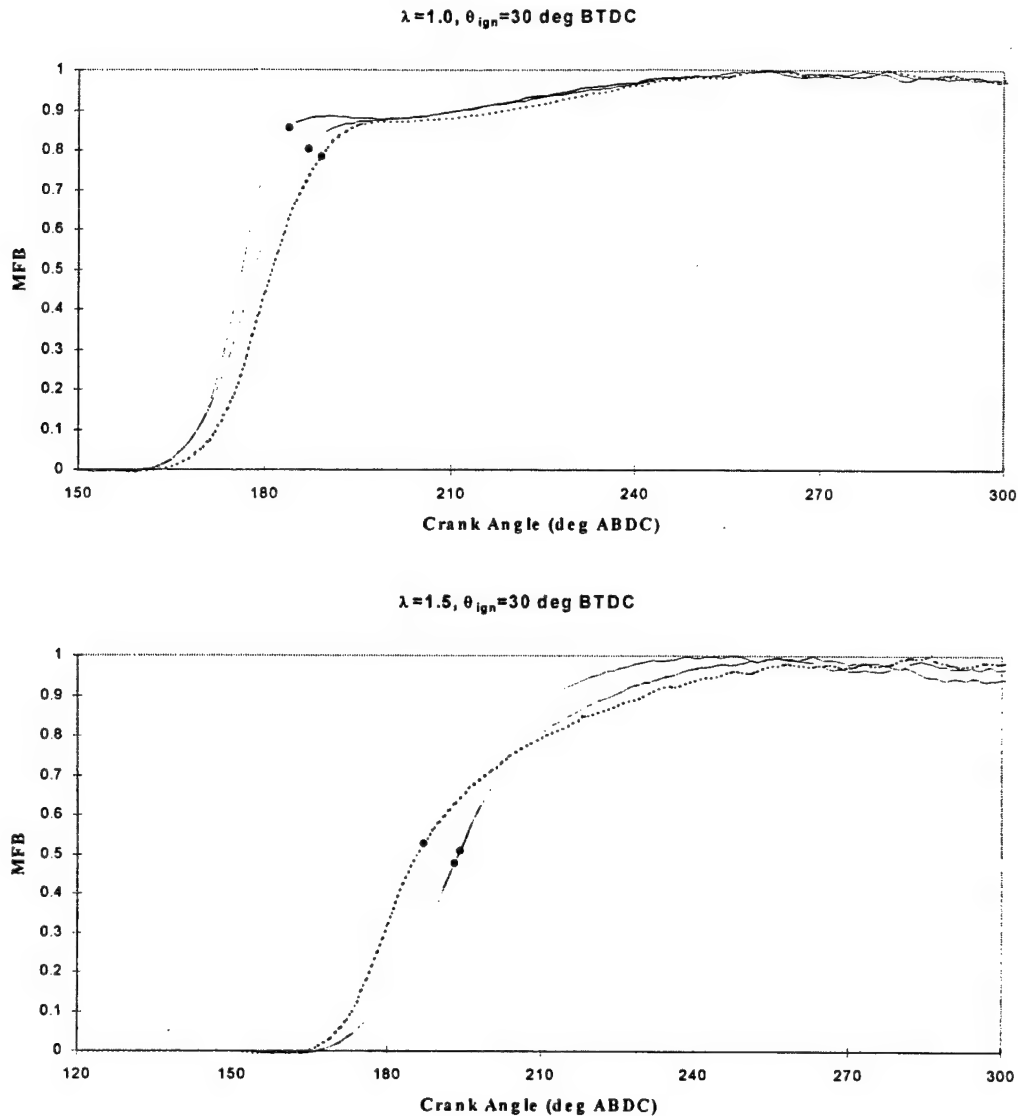


**Figure 5.12. Mass fraction burned curves for three consecutive cycles with the location of maximum pressure indicated by dark circles.**

In the stoichiometric case, the crevice mass would begin to flow out at approximately 80-90% mass fraction burned. It is reasonable to assume that at this point in the burn, the outflowing crevice mass enters a region of inflamed gas, or of high temperature burned mixture. This would result in certain oxidation of the crevice gases (Alkidas et al., 1995), and would explain the sharp change of slope in the MFB curve, i.e., that the bulk gas has completed combustion and the returning material is burning as it flows from the crevices.

In the lean case (Figure 5.12(b)), the crevice mass flows out prior to 50% of the charge being burned. Hence, in this case the crevice mass probably mixes with unburned mixture, and the result on the MFB curve is a gradual rounding of the last 50% MFB.



Figure 5.13 shows results of MFB analysis using the standard method and RW2 method applied to the mean cycles for the experimental conditions in Figure 5.12. The amount of mixture which appears to be participating in the slow burn phase is significantly different according to the standard analysis and the RW2 analysis, especially in the case of the stoichiometric operating condition. This is due to the expansion polytropic index used in each analysis. Specifically, the standard analysis uses  $n_c = n_e$ , whereas the RW2 analysis uses a different index for compression and expansion. By using an index which is based on the properties of the combustion products and heat transfer after combustion, more detail about the processes occurring in the late stages of combustion can be obtained.

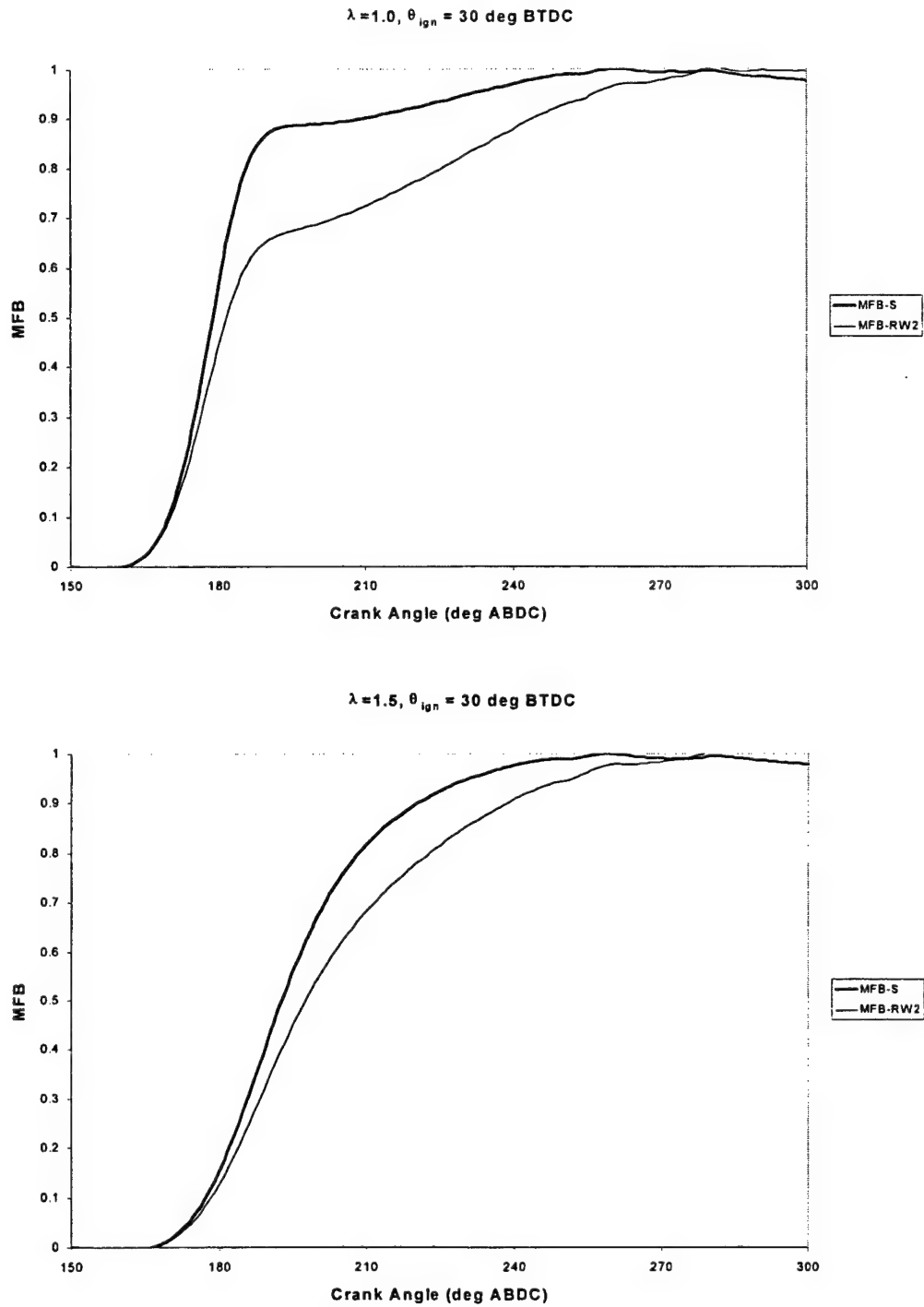


Figure 5.13. Mass fraction burned results using two different analysis methods for the mean cycles corresponding to Figure 5.12.

The proportion of the MFB which is participating in the slow burning phase in the stoichiometric case is approximately 35% according to the RW2 analysis. This is in good agreement with the amount that is estimated to be trapped in the crevices.

## 5.5 Summary

The purpose of this part of the work was to develop MFB analysis methods that would increase the accuracy of ISIS in performing cycle-by-cycle modelling. The first method examined was a two zone polytropic process model which calculated burn rate and combustion temperatures. This method assumed a constant value of polytropic index for the burned and unburned zones throughout combustion. As a result, the model was not able to either predict temperatures or calculate an accurate burn rate. Whilst it might be possible to improve the method, and so produce a workable model, it was decided to focus on the Rassweiler and Withrow method.

The Rassweiler and Withrow method was modified to allow for different compression and expansion indices throughout combustion. The method produced good results if, and only if, the calculated expansion index was correct. Accurate calculation of the expansion index is fraught with difficulty, primarily due to the uncertainty associated with the exact location of the end of combustion. Assuming the expansion index can be calculated with reasonable accuracy, the method does provide two advantages. First, the requirement to determine the end of combustion is less critical with this method. EVO can be used as the "end of combustion", and the MFB curve will rise to 1.0 at the actual end of combustion and will remain there until EVO. Some estimate of EOC is still required so that the expansion index can be calculated over an appropriate range. Several techniques for this are presented by Douglas et al. (1997). Second, the method does provide more accurate information about the later stages of combustion.

In the course of this investigation, it was discovered that the K4 engine has highly abnormal combustion characteristics that are caused by the slow burn up of its significant crevice mass. This phenomenon has impacted the remaining work in two ways. First, since combustion continued so late into the cycle, accurate expansion indices could not be calculated. In particular, with lean operation and retarded timing, combustion could continue up to EVO, with a resulting expansion index of less than 1.0 as calculated. Because of this, the RW2 method was not used in the work from this point on, and all MFB calculations were performed with the standard method.

Second, the non-standard burn rate curves could not be adequately modelled with a Wiebe function which was fitted to the 10% and 90% burn durations. When this was

attempted, it proved nearly impossible for ISIS to match the experimental performance parameters (IMEP and  $P_{max}$ ). Better results were obtained by fitting the Wiebe function to the 10% and 80% burn durations. Whilst this produced a poor match during the late stage of combustion, it provided a good fit for the main burn period. Since the late stages had little effect on the parameters being modelled, it was decided to modify ISIS and the Wiebe subroutine to accept 80% as the upper point for curve fitting.

## Chapter 6 Completeness of Combustion

### 6.1 Introduction

Due to the unusual combustion characteristics of the K4 engine, the modified Rassweiler and Withrow method (RW2) developed in Chapter 5 will not be used for further burn rate analysis. Instead, the standard Rassweiler and Withrow method will be used. As noted in Chapter 4, a key limitation of the Rassweiler and Withrow analysis is that mass fraction burned tends to unity, and this is the limit used to define the end of combustion by equation (4.7). It would seem, however, that the analysis method contains information about the combustion process that is not normally made use of. The objective of this portion of the work was to develop a completeness of combustion parameter based on the standard Rassweiler and Withrow method that could be calculated from experimental data on a cycle-by-cycle basis. The hypothesis is that this parameter, when used as an input to ISIS, will improve the accuracy of the cycle-by-cycle modelling.

### 6.2 Theoretical basis for calculating completeness of combustion

The denominator of the mass fraction burned expression of equation (4.7), i.e.

$$\sum_0^N \Delta p_c^* \quad (6.1)$$

(hereafter referred to as  $\Psi$ ) represents the pressure rise due to combustion normalised to a reference cylinder volume (either ignition timing, as originally suggested by Rassweiler and Withrow, or TDC as favoured by Stone and Green-Armytage (1987), Shayler (1990), and others). For the ideal conditions which are the basis of the Rassweiler and Withrow analysis, this would be expected to yield the adiabatic combustion pressure rise at the reference volume. The basis for making this statement can be explained with reference to Figure 6.1.

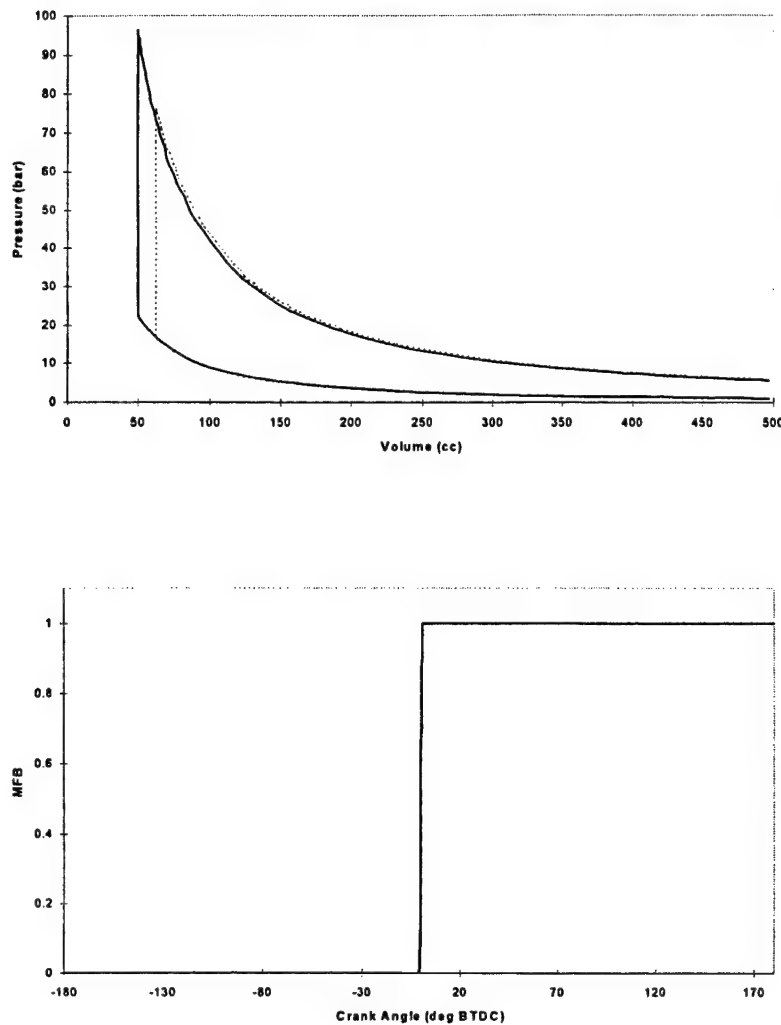


**Figure 6.1. ISIS generated Otto cycles.**

Figure 6.1 shows the pressure-volume and MFB curves for fuel-air standard cycles as simulated by ISIS. The two cycles have been contrived such that both cycles burn the same mass of fuel and air. The difference between the two cycles is the volume at which combustion occurs. In their discussion of the standard method, Rassweiler and Withrow (1938) make the assumption that the pressure rise due to combustion is inversely proportional to volume. They further state that the pressure rises must be normalised to a reference volume. Since the method accounts for the pressure rise due to piston motion, there is sometimes some confusion as to why the pressures must be normalised. This, too, can be explained with Figure 6.1.

For constant volume combustion, the heat input is given by Stone (1992) as

$$q_c = mc_v dT. \quad (6.2)$$

The equation of state may be differentiated and, noting that the volume is constant over the combustion period and assuming a constant value of specific heat capacity, becomes

$$V_c dP = mRdT, \quad (6.3)$$

from which follows

$$dT = \frac{V_c dP}{mR}. \quad (6.4)$$

Substituting equation (6.4) into equation (6.2) yields

$$dP = \frac{R}{c_v} q_c \frac{1}{V_c} = \frac{(\gamma - 1)q_c}{V_c}. \quad (6.5)$$

Hence it is seen that the pressure rise is inversely proportional to the volume. Since the heat input is also related to the product of the calorific value of the fuel and the mass, and since the two cycles above were generated using equivalent masses of fuel, the ratio of the two pressure rises is

$$\frac{dP_B}{dP_A} \approx \frac{V_{cA}}{V_{cB}}. \quad (6.6)$$

(If dissociation is neglected and the specific heat capacities, and hence gas constants, are assumed to be constant, then equation (6.6) is an equality.) This illustrates why the pressure rise due to combustion as calculated by Rassweiler and Withrow must be normalised to a common volume. In the standard method, it is assumed that the piston moves a small amount, and a portion of the fuel is burned. The piston then moves again, and more fuel is burned. At each "pause" in the piston motion, the combustion induces a pressure rise. In order to sum up the individual pressures, account must be made for the individual volumes at which combustion occurred.

The pressure data from Figure 6.1 was then analysed with the standard Rassweiler and Withrow method. The normalised pressure rise due to combustion ( $\Psi$ , or the

denominator of equation (4.7)) is compared to the actual pressure rise in these cases in Table 6.1.

**Table 6.1. Results of comparison of cycles presented in Figure 6.1.**

Case	$V_c$ (cc)	dP (bar)	$dP_B/dP_A$	$V_{cA}/V_{cB}$	$\Psi$ (bar)
A	50.00	73.50	0.807	0.806	74.97
B	62.00	59.34			60.80

Table 6.1 indeed shows that the pressure rise due to combustion can, and must, be referenced to a common volume. Furthermore, the denominator of the Rassweiler and Withrow method does correspond to the pressure rise due to combustion in this highly idealised case. However,  $\Psi$  does not exactly equal the pressure rise in these cases. Some error has been introduced since ISIS does require some piston motion in its cycle calculation. Hence, the cases presented have a combustion duration of 3 degrees crank angle, with an associated, but very small, volume change.

### 6.3 *Development of the completeness of combustion parameter*

On the basis of the preceding arguments, it is suggested that if  $\Psi$  is evaluated for any combustion cycle and compared with some 'maximum' which represents 'complete combustion', then an estimate of the completeness of combustion of the cycle compared with the maximum can be obtained. Completeness of combustion ( $\chi$ ) is defined as the fraction of the inducted fuel which is usefully burned during the cycle (Sztenderowicz and Heywood, 1990).

Initially, it is assumed that a large value of  $\Psi$  (referred to as  $\Psi_m$ ) corresponds to 'complete' combustion, and other values of  $\Psi$  are proportioned to this value with the assumption that completeness of combustion may be given by;

$$\chi = \frac{\Psi}{\Psi_m} . \quad (6.7)$$

Using the standard Rassweiler and Withrow method, the value of  $\Psi$  has been calculated. The results are presented in Figure 6.2 plotted against IMEP for each of



approximately 300 cycles at the experimental conditions noted (all conditions are with engine speed of 1000 rpm). Approximate MBT spark timing is 15 to 20° BTDC at these conditions.

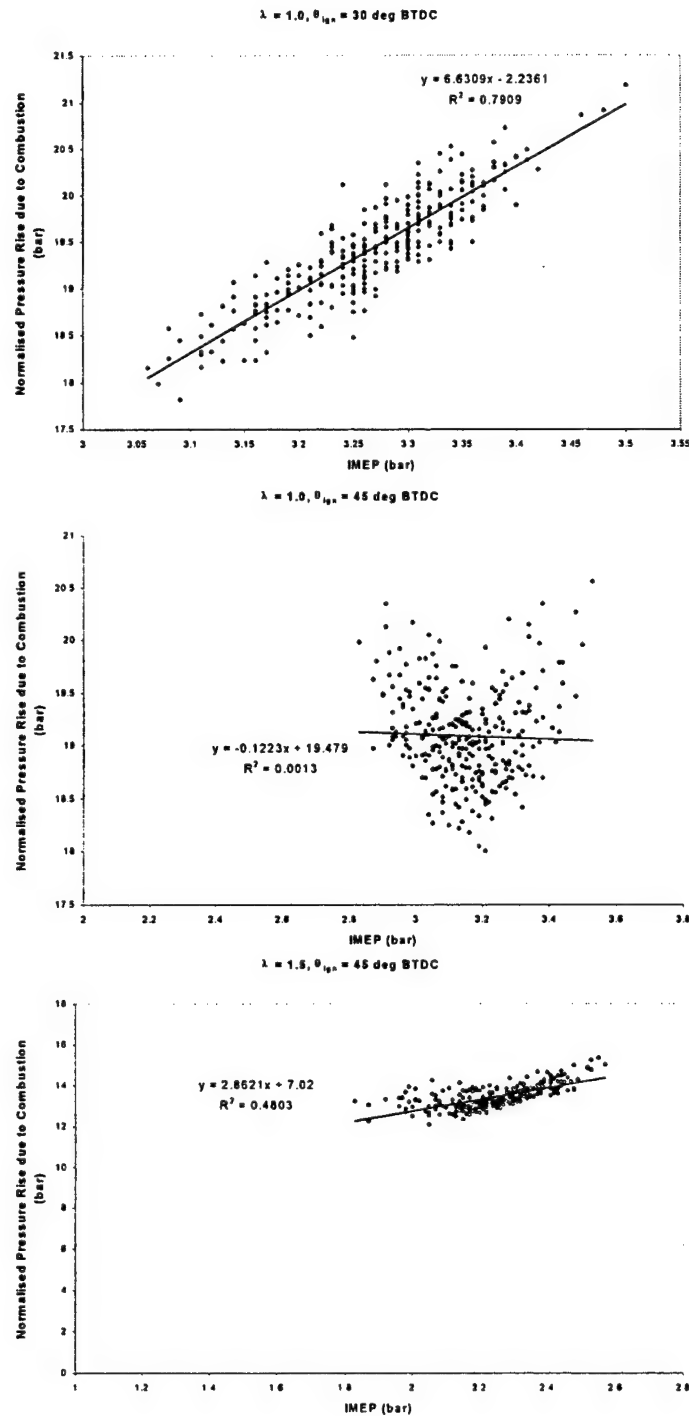


Figure 6.2. Normalised pressure rise due to combustion ( $\Psi$ ) vs. IMEP.

These results, and others which have been examined at wide open throttle operation and a range of non-dimensional air-fuel ratio ( $\lambda$ ) and spark timing, show that cycle-by-cycle variation in  $\Psi$  and IMEP is larger in the case of lean than for stoichiometric operation and that the variability is less for operating conditions closer to MBT. This is as anticipated, with the slower burning lean operation giving rise in general to larger cycle-by-cycle variability (reference Chapter 2). Tables 6.3 and 6.4 present summary data for these and other engine operating conditions, including the correlation coefficient ( $R$ ) between  $\Psi$  and IMEP (Table 6.3). Furthermore, the trend lines fitted to the data in Figure 6.2 also show values of  $R^2$ . In many cases, there is correlation between  $\Psi$  and IMEP. However, this cannot be stated in general. Since the pressure rise due to combustion is normalised to a reference volume in the Rassweiler and Withrow method, one expects a loss of phasing information. IMEP is strongly affected by the phasing of the burn whilst  $\Psi$  is less affected (the effects of spark timing on  $\Psi$  will be discussed later.) Hence, one would not expect much correlation between  $\Psi$  and IMEP. However, both  $\Psi$  and IMEP are affected by variations in the trapped mass and this may be one source of the strong correlation in some cases.

Figure 6.3 presents frequency distribution data for  $\Psi$  for the experimental conditions corresponding to Figure 6.2 and a number of other spark timing conditions. Significant points about these results include:

- a) the mean value of  $\Psi$  varies with engine operating conditions,
- b) the mean value of  $\Psi$  reduces as  $\lambda$  is increased, and
- c) the standard deviation of  $\Psi$  increases as  $\lambda$  is increased.

These trends are anticipated for the relation of adiabatic combustion pressure rise as it is influenced by  $\lambda$ , namely, that leaner mixtures induce a lower work output and higher cycle-to-cycle variation. The effect of spark timing on  $\Psi$  will be discussed later.

Table 6.2. Summary data for the experimental results presented in Figures 6.2 and 6.3.

Part Load						
ID:	P1015	P1030	P1045	P1515	P1530	P1545
$\lambda$	1.0	1.0	1.0	1.5	1.5	1.5
Ignition ( $^{\circ}$ BTC)	15	30	45	15	30	45
HC (ppm)	4015	5218	5542	9036	8299	9180
$\eta_{HC}^1$	95.78	94.51	94.17	86.19	87.32	85.97
NOx (ppm)	700	1550	1980	7	15	75
IMEP (bar)	3.84	3.27	3.15	1.46	2.33	2.25
mean $P_{max}$ (bar)	18.05	25.92	29.34	10.23	15.13	21.44
$\theta_{10}^2$	20	20	27	34	28	29
$\theta_{80}^2$	43	37	42	96	59	48
poly. Index $n_c^3$	1.31	1.33	1.32	1.28	1.31	1.30
poly. Index $n_e^3$	1.35	1.45	1.38	0.93 <sup>4</sup>	1.40	1.44

Wide open throttle (WOT)				
ID:	W1015	W1030	W1515	W1530
$\lambda$	1.0	1.0	1.5	1.5
ignition( $^{\circ}$ BTC)	15	30	15	30
HC (ppm)	4316	4348	6516	9354
$\eta_{HC}^1$	95.46	95.43	90.04	85.71
NOx (ppm)	1750	2560	10	110
IMEP (bar)	6.14	5.55	3.83	4.38
mean $P_{max}$ (bar)	33.02	45.68	17.33	29.20
$\theta_{10}^2$	18	19	26	27
$\theta_{80}^2$	36	33	61	52
poly. Index $n_c^3$	1.33	1.35	1.32	1.36
poly. Index $n_e^3$	1.43	1.44	1.37	1.37

Notes: 1.  $\eta_{HC}$  calculated by equation (6.8) described later.

2.  $\theta_{10}$  and  $\theta_{80}$  are the crank angle period for 10% and 80% MFB respectively.

3.  $n_c$  and  $n_e$  are the polytropic indices for compression and expansion.

4.  $n_e$  for case P1515 is too low due to the retarded ignition timing and lean operating condition. Combustion in many cycles continued up to exhaust valve opening in this case.

Table 6.3: Calculated results derived from the experimental data in Table 6.2.

Part Load						
ID:	P1015	P1030	P1045	P1515	P1530	P1545
$\Psi_{\max}$	24.92	21.26	20.66	16.43	16.33	15.35
$\Psi_{\text{mean}}$	23.69	19.45	19.11	13.15	14.1	13.47
$\sigma$	0.46	0.57	0.44	1.91	0.73	0.55
$sk$	-0.29	-0.073	0.532	-1.78	0.267	0.592
$kurt$	3.09	3.02	3.47	8.74	3.12	3.44
$\Psi_m$	24.52	20.54	20.08	15.43	15.61	14.69
$\Psi_{\text{mean}}/\Psi_m$ (%)	96.62	94.69	95.17	85.22	90.33	91.70
R of $\Psi$ vs. IMEP	0.314	0.889	0.036	0.844	0.550	0.693

Wide open throttle (WOT)				
ID:	W1015	W1030	W1515	W1530
$\Psi_{\max}$	39.67	35.5	30.83	29.98
$\Psi_{\text{mean}}$	37.42	33.44	27.29	27.03
$\sigma$	0.6529	0.7549	1.58	0.9458
$sk$	-0.108	-0.48	0.502	-0.097
$kurt$	3.35	4.19	2.11	4.00
$\Psi_m$	38.68	34.79	30.52	28.88
$\Psi_{\text{mean}}/\Psi_m$ (%)	96.74	96.12	89.42	93.59
R of $\Psi$ vs. IMEP	0.733	0.887	0.067	0.785

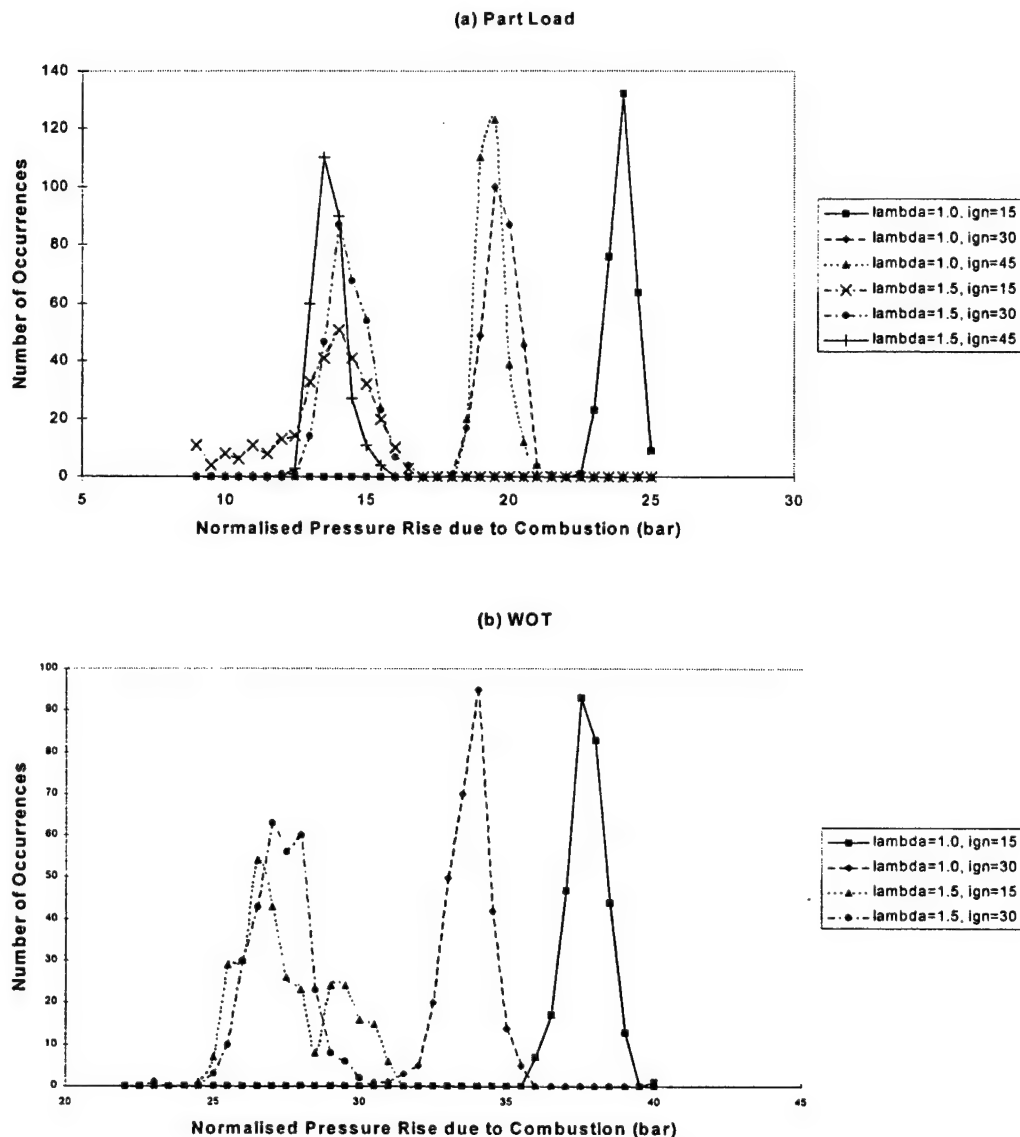


Figure 6.3. Frequency distribution of the normalised pressure rise due to combustion ( $\Psi$ ) determined from experimental data.

Unburned exhaust gas hydrocarbons are one result of incomplete combustion. Sztenderowicz and Heywood (1990) have attempted to use these as a measure of cycle-by-cycle variability in completeness of combustion. However, uncertainties in interpreting the results of the measurements left some doubt about the cycle-by-cycle variability in unburned hydrocarbons. Thus, mean hydrocarbon emission concentrations have been measured, and Table 6.2 shows the results for the operating conditions tested. Also presented is the value  $\eta_{HC}$ , which is the percentage of the intake fuel which has been burned, based on the mean

intake fuel concentration ( $[\text{HC}]_{\text{in}}$ ) and the measured mean exhaust HC concentration ( $[\text{HC}]_{\text{exh}}$ ):

$$\eta_{\text{HC}} = 1 - \frac{[\text{HC}]_{\text{exh}}}{[\text{HC}]_{\text{in}}} \quad (6.8)$$

It is anticipated that this is related to the average completeness of combustion ( $\chi$ ).

In order to relate  $\Psi$  to the completeness of combustion, the frequency distributions of  $\Psi$  (Figure 6.3) are examined, and require a 'large' value of  $\Psi$  to represent 'complete combustion'. Note that the form of these distributions differ depending on operating conditions. Thus, for part load,  $\lambda = 1.0$ , and a spark timing of  $30^\circ$  BTDC, the frequency distribution appears to be approximately normal. However, for  $\lambda = 1.5$  and a spark timing of  $15^\circ$  BTDC there is some skewness to the frequency distribution. Likewise, some of the distributions are more sharply peaked than others, a property which is characterised by the kurtosis. Table 6.3 presents the statistical data for  $\Psi$ , including the mean value ( $\Psi_{\text{mean}}$ ), the standard deviation ( $\sigma$ ), skewness ( $sk$ ), and kurtosis ( $kurt$ ).

In order to take account of the skewness and kurtosis, Pearson curves have been used to describe these non-normal distributions and to estimate the maximum value of  $\Psi$ . Karl Pearson (1895) first suggested that sample estimates of  $\sqrt{\beta_1}$  (skewness) and  $\beta_2$  (kurtosis) could be used to describe non-normal distributions in cases where the first four moments of the distribution could be calculated. For a sample of size  $n$ , these moments are defined as (D'Agostino, et al, 1990)

$$\begin{aligned} \sqrt{\beta_1} &= m_3 / m_2^{3/2} \\ \beta_2 &= m_4 / m_2^2, \end{aligned} \quad (6.9)$$

where

$$m_k = \sum_{i=1}^n (X_i - \bar{X})^k / n$$

and  $\bar{X}$  is the sample mean.

For a normal distribution, the skewness and kurtosis are 0 and 3, respectively. The calculated moments were input to a FORTRAN subroutine developed by Davis and Stephens (1983), and which was incorporated into COBRA. The subroutine calculates various significance points which relate to approximate percentage points in a normal distribution.

For the case at hand, a significance point of 97.5% was used to define  $\Psi_m$ . This corresponds to a value two standard deviations above the mean in a normal distribution, which is considered to be a satisfactory measure of complete combustion. The values in Table 6.3 show that in no case does this give a value of  $\Psi_m$  larger than the measured  $\Psi_{max}$ .

Values of  $\Psi_m$  calculated by the Pearson subroutine are presented in Table 6.3 and also values of  $\Psi_{mean}/\Psi_m$ . The values of  $\Psi_{mean}/\Psi_m$  can now be compared with the values of  $\eta_{HC}$  in Table 6.3, and Figure 6.4 shows the correlation.

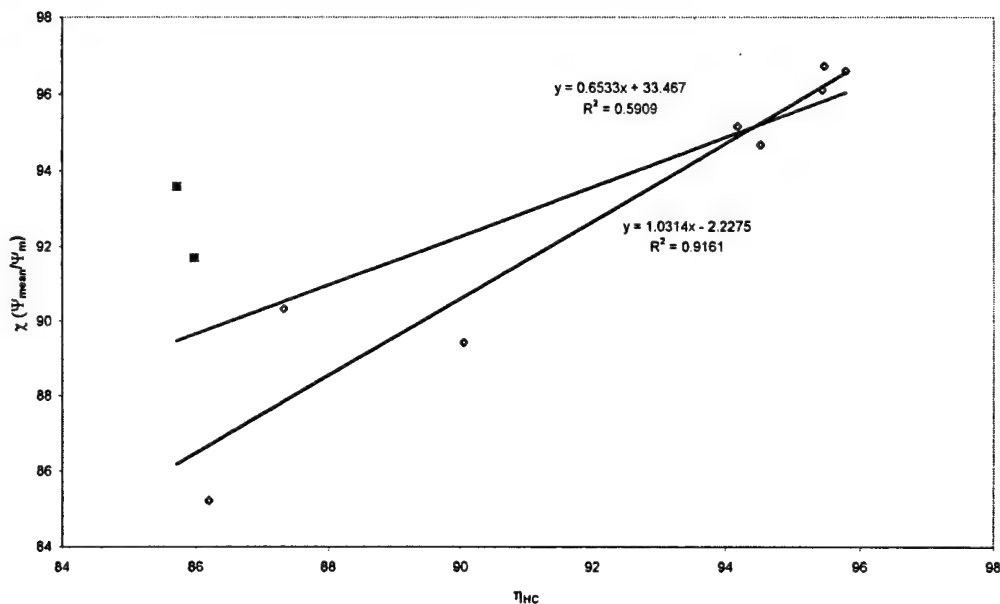


**Figure 6.4.** Mean value of completeness of combustion ( $\chi$ ) plotted against percentage of fuel burned ( $\eta_{HC}$ ).

Figure 6.4 presents all the data from Tables 6.2 and 6.3, but there are two points (marked with squares) that are considered anomalous. This corresponds to wide open throttle operation with  $\lambda = 1.5$  and spark timing of  $30^\circ$  BTDC, and part load with  $\lambda=1.5$  and spark timing of  $45^\circ$  BTDC. In examining the raw HC data, these two cases contained large spikes in the measured HC level. These excursions were large enough to cause the calculated average HC reading to be unreasonably high. The source of the excursions is unknown since no misfired cycles were indicated in the data. Since these cases do not represent a steady operating condition as far as HC measurement is concerned, trend lines have been fitted to the data both with and without these two points. The trend lines give a correlation coefficient ( $R$ ) of 0.769 for all data points and 0.957 with the dubious points removed. Furthermore, with these two points removed, the slope of the trend line is near unity with intercepts of (0.0,-

2.73) and (100.0, 100.91). This is taken to be a good fit to the data and support for the hypothesis that  $\chi$  is a good indicator of completeness of combustion.

In order to explore further the relationship between  $\Psi$  and engine operating conditions, ISIS (Raine, et al., 1995) has been run at the conditions specified in Table 6.4. As part of this work, ISIS was modified to allow for incomplete combustion (i.e.  $\chi \neq 1$ ). Details of this modification are contained in Appendix B. The cases with and without heat transfer and blow-by were investigated partly for the interest in the polytropic indices of these cases, and also to see how important these effects are on the parameter  $\Psi$ . Cases with heat transfer correspond to use of the Hohenberg (1979) relationship and cases with blow-by correspond to approximately 5% of the inlet charge escaping the cylinder before EVO. This corresponds to a relatively high value of blow-by (Heywood, 1988).

The model uses measured burn rate data for the mean cycle which is representative of each operating condition. The pressure-crank angle data from the simulation have been analysed by the same process that was used for the experimental data, in order to determine  $\Psi$ . A summary of key results from this process is presented in Table 6.4.



**Table 6.4. Calculated results from the engine simulation model ISIS for the conditions of the experiments as shown.**

Case	$\lambda$	IGN ANGLE	$\chi$	ht. trans.	Blow-by	$n_c$	$n_e$	$\Psi$	IMEP	$\Psi/\Psi_{\chi=1}$	$\Psi/\Psi_i$
1001	1.0	30	1.0	0	0	1.326	1.218	24.50	4.05		
1002	1.0	30	0.8	0	0	1.326	1.230	19.72	3.26	0.805	0.805
2001	1.0	30	1.0	1	0	1.296	1.379	17.72	3.12		
2002	1.0	30	0.8	1	0	1.296	1.378	14.04	2.45	0.792	0.573
3001	1.0	30	1.0	1	1	1.283	1.395	17.17	2.98		
3002	1.0	30	0.8	1	1	1.283	1.399	13.62	2.32	0.793	0.556
4001	1.5	30	1.0	0	0	1.333	1.266	18.21	2.83		
4002	1.5	30	0.8	0	0	1.333	1.270	14.64	2.27	0.804	0.804
5001	1.5	30	1.0	1	0	1.288	1.448	13.03	2.16		
5002	1.5	30	0.8	1	0	1.288	1.450	10.19	1.67	0.782	0.560
6001	1.5	30	1.0	1	1	1.274	1.479	12.33	2.04		
6002	1.5	30	0.8	1	1	1.274	1.479	9.62	1.57	0.780	0.528
7001	1.0	15	1.0	0	0	1.319	1.221	23.68	3.68		
7002	1.0	30	1.0	0	0	1.326	1.220	24.50	4.05		
7003	1.0	45	1.0	0	0	1.338	1.203	25.02	3.97		
8001	1.5	15	1.0	0	0	1.327	1.245	17.27	1.77		
8002	1.5	30	1.0	0	0	1.333	1.266	18.21	2.83		
8003	1.5	45	1.0	0	0	1.346	1.253	18.97	3.06		

Notes: 1. For heat transfer, 0 indicates adiabatic. For blow-by, 0 indicates no blow-by.

Table 6.4 gives calculated data for the compression and expansion polytropic index ( $n_c$  and  $n_e$ ),  $\Psi$ , and the ratio of  $\Psi/\Psi_{\chi=1}$ . For the cases of adiabatic combustion (cases 1002 and 4002), this ratio is very close to the modelled completeness of combustion (i.e. 0.8). In the cases with heat transfer and blow-by, the agreement is not so close (approximately 0.78 to 0.79), but is none the less acceptable.

The last column contains the ratio  $\Psi/\Psi_i$ , where  $\Psi_i$  is for the 'ideal' case with  $\chi = 1$  and no heat transfer or blow-by. It can be seen from this ratio that in the cases with heat transfer and blow-by,  $\Psi$  is reduced from the 'ideal' cases (i.e. 1001 and 4001). This indicates that in practice,  $\Psi$  could be used as a guide to the magnitude of these effects as well as completeness of combustion. However, it is anticipated that at a fixed engine operating

condition, the cycle-by-cycle variability in heat transfer and blow-by are small compared with variability in completeness of combustion. This is an assumption which has some support from the work of Sztenderowicz and Heywood (1990). The model results show that, based on the mean cycle data:

- a) the value of  $\Psi$  reduces as  $\lambda$  increases,
- b) spark timing has little effect on  $\Psi$ , and
- c)  $\Psi$  is closely related to completeness of combustion,  $\chi$ .

In particular, over the range of spark timing investigated here ( $15^\circ$  to  $45^\circ$ ), there was little change in  $\Psi$  for the adiabatic simulations. This is in contrast to the experimental data in which the stoichiometric cases with a spark timing of  $15^\circ$  BTDC, for both throttle settings, gave higher  $\Psi$  than at other spark timing conditions. The result confirmed by the model, i.e. that  $\Psi$  should not vary much with spark timing, is anticipated on theoretical grounds. It is suggested that this anomaly may be due to the fact that  $\Psi$  is affected by variations in trapped mass. In tuning ISIS to reproduce the part throttle experimental data, in the stoichiometric case with ignition timing of  $15^\circ$  BTDC, the trapped mass required for IMEP matching was 10% higher than the other timing conditions. This was traced to an imprecise throttle setting which produced a higher airflow in this case. In the stoichiometric wide open throttle case, airflow was not constant as spark timing was varied. This would indicate changes in the trapped mass which would in turn affect the value of  $\Psi$ .

The conclusions from the above are that the ratio  $\Psi/\Psi_m$  is a useful parameter in determining the completeness of combustion at a fixed engine operating condition. Analysis of the cycle-by-cycle pressure data allow the value of  $\Psi_m$  to be determined which corresponds to 'complete combustion', and then the cycle-by-cycle values of the ratio can be determined. This ratio ( $\chi$ ) is a parameter related to cycle-by-cycle variability in the combustion process and can be used in engine simulation calculations, avoiding the essential drawback of the standard Rassweiler and Withrow analysis which assumes complete combustion.

#### ***6.4 Implementation of completeness of combustion into cycle-by-cycle modelling***

Cycle-by-cycle modelling was repeated on the same set of experimental data presented in Chapter 4. This time, ISIS was modified to incorporate completeness of combustion ( $\chi$ ) for each cycle. The “maximum” value of the normalised pressure rise due to combustion ( $\Psi_m$ ) was calculated by COBRA as outlined previously for the 305 cycles in each case. This value was used to calculate a completeness of combustion for each cycle as shown by equation (6.7). This value ( $\chi$ ) was added to the COBRA output files containing air fuel ratio, ignition timing, and burn rate data for each cycle (see Appendix B). In implementing  $\chi$  within ISIS, the modelled burn rate was allowed to proceed normally until  $MFB=\chi_i$ . At that point combustion ended, and the unburned fuel was carried through the rest of the cycle calculations as a burned gas component. Details of the ISIS modifications are contained in Appendix B.

For each case of experimental data, ISIS was re-tuned to the mean cycle utilising the mean completeness of combustion for that data set. This involved some modification to the inducted airflow (or the trapped mass) to produce an equivalent IMEP despite less than 100% of the fuel being burned. The results of this modelling are shown in Table 6.5.

**Table 6.5. ISIS results for mean cycle and cycle-by-cycle modelling including completeness of combustion ( $\chi$ ).**

Part Load (1 litre/sec air flow) 1000 RPM								
$\lambda$	$\theta_{ign}$ (DBTDC)		IMEP- gross	IMEP- net	Pmax (bar)	CaPmax (DABDC)	NO (ppm)	Torque (N-m)
1.0	15	EXP (COV)	3.84 0.78	3.49 0.96	18.05 6.22	200	700	1.8
		ISIS-mcm	3.84	3.43	16.61	203	714	2.0
		ISIS-cbc (COV)	3.82 1.45	3.41 1.62	16.35 7.72	203	689	1.98
	30	EXP (COV)	3.27 2.31	2.90 2.71	25.92 3.58	187	1550	0.2
		ISIS-mcm	3.278	2.84	24.67	189	1530	0.0
		ISIS-cbc (COV)	3.27 3.46	2.84 3.98	24.63 4.63	189	1513	-0.02
	45	EXP (COV)	3.15 4.13	2.79 4.72	29.34 3.23	182	1980	-1.0
		ISIS-mcm	3.15	2.73	28.47	183	1994	-1.0
		ISIS-cbc (COV)	3.14 3.35	2.72 3.86	28.47 2.77	183	2012	-1.14
1.5	15	EXP (COV)	1.46 23.69	1.08 31.88	10.23 1.48	180	7	-4.7
		ISIS-mcm	1.46	1.06	10.70	180	3.0	-5.0
		ISIS-cbc (COV)	1.49 27.05	1.09 36.41	10.74 0.91	180	4.07	-4.99
	30	EXP (COV)	2.33 5.59	1.98 6.55	15.13 10.24	192	15	-2.1
		ISIS-mcm	2.35	1.94	13.81	192	15	-2.0
		ISIS-cbc (COV)	2.33 6.87	1.92 8.30	14.34 11.97	192	19.33	-2.05
	45	EXP (COV)	2.25 5.92	1.90 7.19	21.44 8.98	186	75	-2.4
		ISIS-mcm	2.26	1.84	21.87	187	76	-2.0
		ISIS-cbc (COV)	2.26 5.84	1.84 7.17	21.56 10.10	187	86.15	-2.33

WOT 1000 RPM								
$\lambda$	$\theta_{ign}$ (DBTDC)		IMEP- gross	IMEP- net	Pmax (bar)	CaPmax (DABDC)	NO (ppm)	Torque (N-m)
1.0	15	EXP	6.14	6.06	33.02	198	1750	10.8
		(COV)	0.85	0.89	6.68			
		ISIS-mcm	6.15	6.02	30.19	200	1751	11.0
	30	ISIS-cbc	6.16	6.03	30.24	200	1778	11.21
		(COV)	1.19	1.22	7.47			
		EXP	5.55	5.48	45.68	185	2560	8.5
1.5	15	(COV)	2.11	2.20	2.70			
		ISIS-mcm	5.56	5.45	43.67	187	2569	9.0
		ISIS-cbc	5.56	5.45	43.49	187	2553	9.00
	30	(COV)	2.81	2.82	3.44			
		EXP	3.83	3.73	17.33	190	10	3.3
		(COV)	8.77	8.99	11.35			
1.5	15	ISIS-mcm	3.84	3.75	17.39	183	10	3.0
		ISIS-cbc	3.78	3.68	17.88	188	12.39	2.74
		(COV)	9.38	9.54	8.26			
	30	EXP	4.38	4.27	29.20	192	110	4.5
		(COV)	2.10	2.23	8.80			
		ISIS-mcm	4.38	4.30	25.95	196	112	5.0
1.5	15	ISIS-cbc	4.36	4.28	26.39	195	128.5	4.82
		(COV)	2.65	2.69	11.01			
		EXP	3.83	3.73	17.33	190	10	3.3
	30	(COV)	8.77	8.99	11.35			
		ISIS-mcm	3.84	3.75	17.39	183	10	3.0
		ISIS-cbc	3.78	3.68	17.88	188	12.39	2.74

The results in Table 6.5 indicate that the incorporation of  $\chi$  had no detrimental effect on the mean values of the primary target parameters (IMEP,  $P_{max}$ ,  $CaP_{max}$ , NO). However, the predicted COV of IMEP showed improvement in all cases but one, including the cases where ISIS previously had over predicted the COV. A comparison of the COV of IMEP for both cases of ISIS modelling to the experimental COV is shown in Figure 6.5.

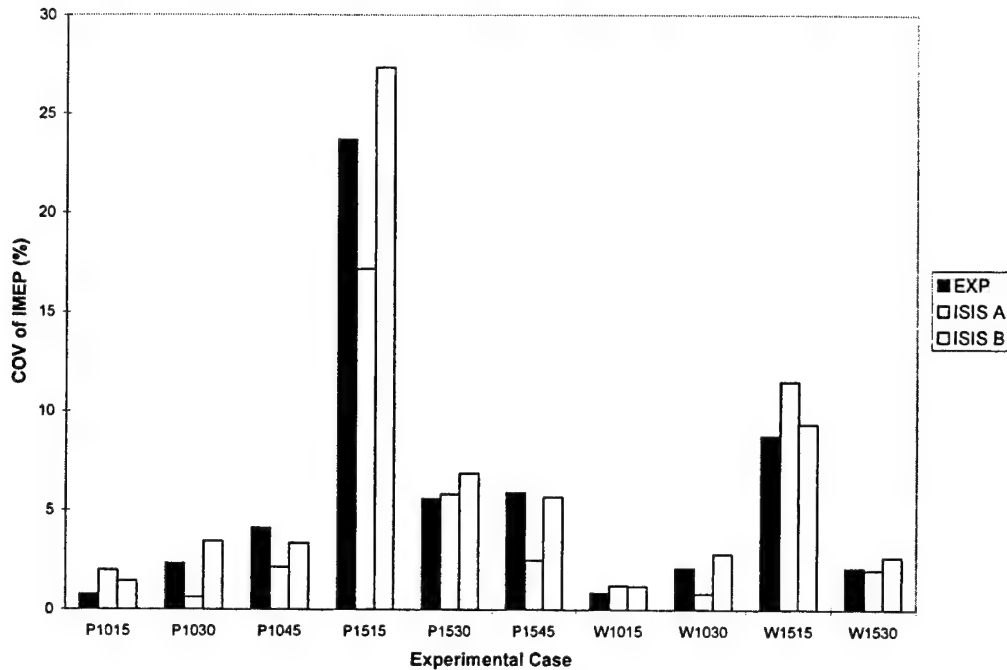


**Figure 6.5. Comparison of COV of IMEP: Experimental, ISIS with  $\chi=1$  (ISIS A), and ISIS allowing for incomplete combustion (ISIS B).**

Figure 6.5 indicates that a combination of burn rate and completeness of combustion better accounts for the effects of the various sources of cycle-by-cycle variation. There was one case in which the inclusion of  $\chi$  did not improve the COV modelling, and that was the lean, part load case with an ignition timing of 30 degrees BTDC (P1530). Although there was a slight degradation in this case, the modelled COV of IMEP is still within approximately one percentage point of the experimental COV, and this anomaly is not deemed significant in detracting from the overall performance of the second modelling case.

Several of the modelling techniques reviewed in Chapter 2 used frequency distributions to compare model results to experimental data (Brehob and Newman (1992), Shen et al. (1996)). The COV of IMEP provides a single, numeric basis on which to compare the two modelling cases. However, it is somewhat more informative to examine the experimental distribution of IMEP in comparison to the two modelling attempts. The frequency distributions of IMEP for three cases are presented in Figure 6.6. These three cases were selected to provide a representative cross section of the various operating conditions tested (WOT versus part load, lean versus stoichiometric operation, etc.). In addition, Figure 6.6 contains the one case in which addition of the completeness of combustion parameter degraded the COV of IMEP. The distributions for the remaining cases are contained in Appendix C.

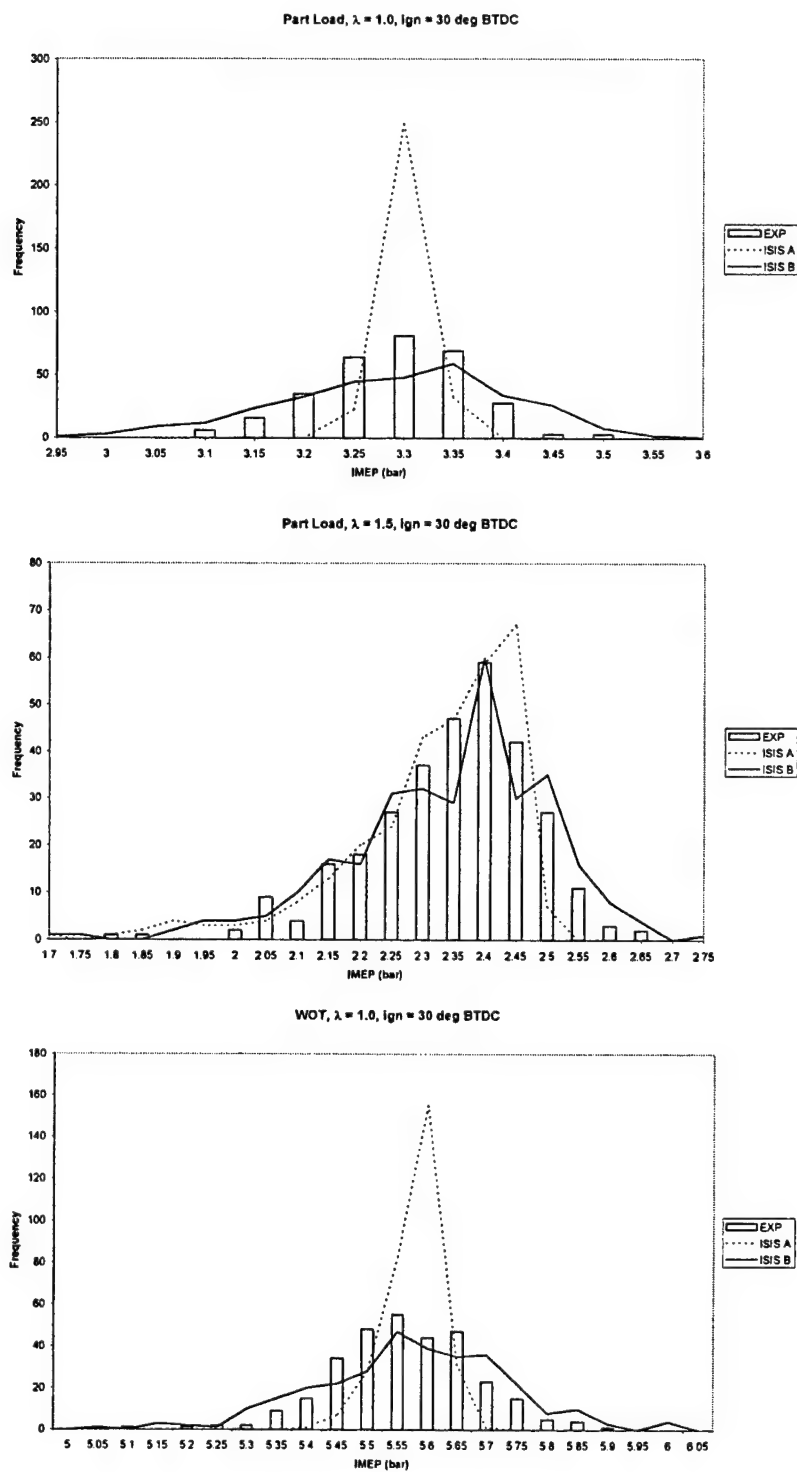


Figure 6.6. Frequency distributions of IMEP: Experimental, ISIS with  $\chi=1$  (ISIS A), and ISIS allowing for incomplete combustion (ISIS B).

Figure 6.6 gives a better indication of the improvements to be gained by including the completeness of combustion in the cycle-by-cycle modelling. The top and bottom cases graphically show the lack of scatter induced by allowing only the burn rate to vary. The centre case in Figure 6.6 is the case in which the COV of IMEP showed some degradation by including the completeness of combustion. In this case, the original modelling attempt (using only burn rate variations) modelled the distribution of IMEP quite well. Hence, there was very little room for improvement. Nonetheless, these statistical comparisons argue for the inclusion of the completeness of combustion. However, it is also true that whilst the statistical comparisons show good agreement, it is worth investigating whether the modelled IMEP does, in fact, bear any resemblance to the experimental IMEP on a cycle-by-cycle basis. Given that this examination is really an attempt to reproduce experimental data, the modelled results should correlate well with the experiment on a cyclic basis if completeness of combustion is an improvement to the model. Figure 6.7 is a comparison of the experimental IMEP to the modelled IMEP from both versions of ISIS: in the first instance, the “standard” ISIS model, and in the second, the ISIS model which incorporated completeness of combustion. The cases presented in Figure 6.7 are the same cases shown in Figure 6.6, and for the purpose of clarity, only the first 30 cycles in each case are presented.



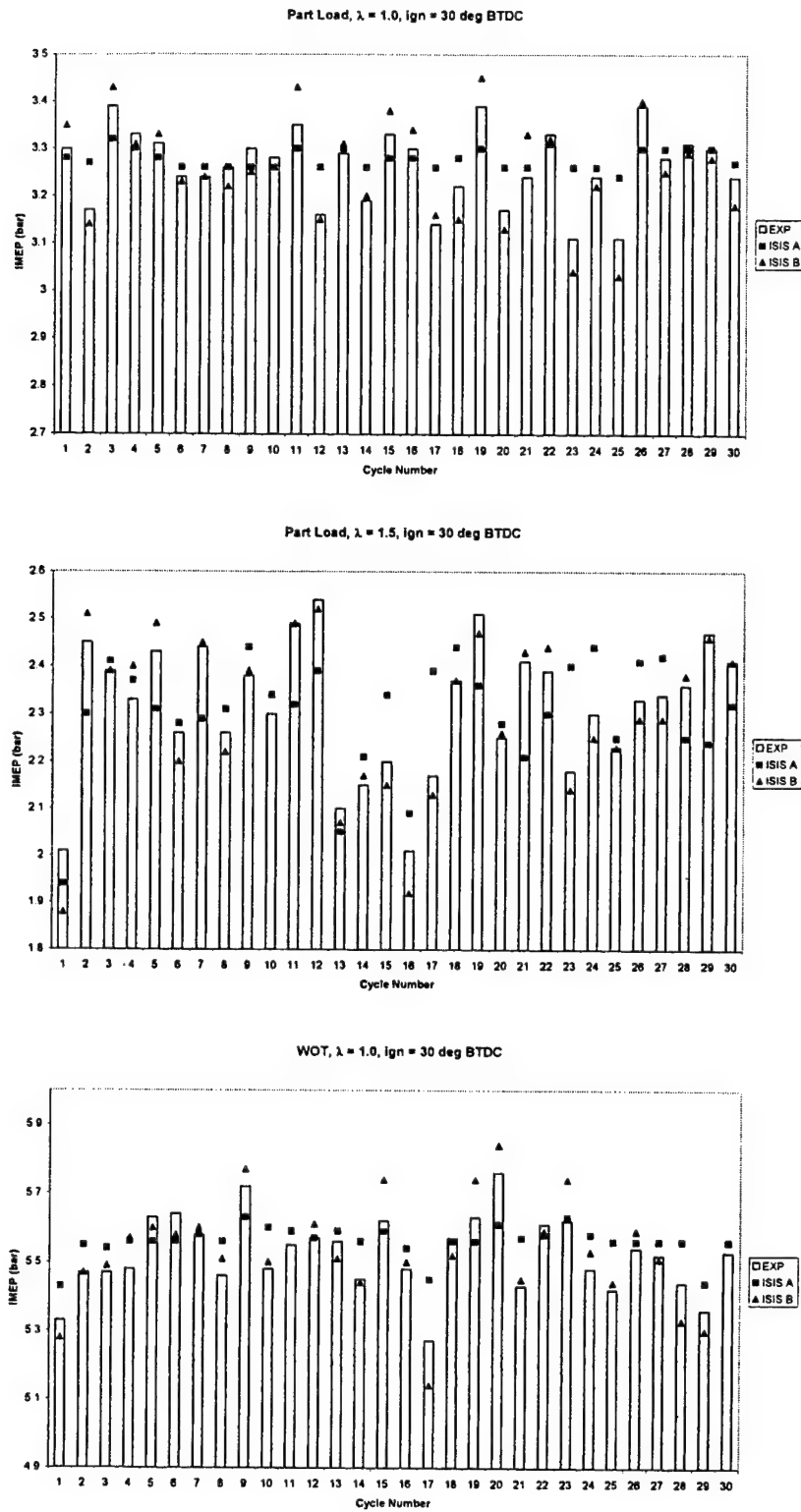


Figure 6.7. Cycle-by-cycle Comparison of IMEP: Experimental, ISIS with  $\chi=1$  (ISIS A), ISIS allowing for incomplete combustion (ISIS B).

Figures 6.5-6.7 and those contained in Appendix C indicate that incorporating completeness of combustion into the model improves the ability of ISIS to model the trends in IMEP. Despite the fact that in the second case in Figures 6.6 and 6.7, the COV of IMEP for the entire sample was slightly degraded, the model which incorporates completeness of combustion still models the trends in IMEP very well on a cycle-by-cycle basis. This confirms the conclusion that burn rate alone is not capable of capturing the effects of the majority of causes of cycle-by-cycle variation, and indicates that any attempt at cycle-by-cycle modelling would be improved by the inclusion of the completeness of combustion parameter.

Whether one chooses to implement a mean cycle model or a cycle-by-cycle model is primarily governed by the parameters of interest to the user. If one is interested in "overall" engine performance, the mean cycle model would be the method of choice due to its speed of implementation, as long as the limitations of accurately modelling the maximum pressure were kept firmly in mind. However, if the cycle by cycle variability of the engine is of paramount interest, one must use cycle-by-cycle modelling, and the results here indicate that its accuracy in predicting "overall" engine performance is not degraded over the mean cycle model. Furthermore, these results indicate that the cycle-by-cycle modelling is improved by including the completeness of combustion.

## 6.5 *Summary and introduction to next stage of work*

This chapter has focussed on the development of a completeness of combustion parameter ( $\chi$ ) derived from information contained in the standard Rassweiler and Withrow method of combustion analysis. This parameter was calculated for the experimental data on a cycle-by-cycle basis, and was then used as an input to ISIS. Incorporation of  $\chi$  had no detrimental effect on the mean values of the target parameters, and resulted in an improvement in the cycle-by-cycle modelling of IMEP in terms of the modelled COV.

This chapter has taken experimental data, fed it into a cycle simulation, and reproduced the engine performance parameters. At this point, it is well to ask what significance this exercise has in the context of predictive modelling. The significance is that it has demonstrated that a combination of burn rate and completeness of combustion are sufficient for modelling the cycle-by-cycle variations in the work output of an engine. In order to use these methods for predictive modelling, work needs to be done on developing a rigorous means of perturbing the burn rates and combustion completeness in order to provide

a statistically valid prediction of engine parameters. This question will be addressed more fully in Chapter 9.

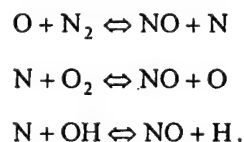
The one parameter which could not be compared to experimental data on a cycle-by-cycle basis was the NO. Given current emphasis on emissions from petrol engines, this is an important parameter, the modelling of which would be very useful to any engine development programme. An opportunity arose to use a fast response chemiluminescent detector (CLD), and thus attempt to validate ISIS cycle-by-cycle modelling of NO. The results of this experiment are discussed in Chapter 7.

## Chapter 7 Cycle-by-Cycle Modelling of NO

### 7.1 Introduction

Chapter 6 developed a cyclic completeness of combustion parameter ( $\chi$ ) which was used to perturb ISIS along with cyclic variations in burn rate. This approach allowed a cycle-by-cycle comparison between the model and the experiment to be made. The results of this approach indicated that variations in these two parameters (burn rate and completeness of combustion) produced good cyclic agreement in IMEP,  $P_{max}$ , and phasing of  $P_{max}$ . The model (ISIS) also produces cyclic values of NO, and whilst the mean value corresponded well to measured NO levels, no data existed to validate the approach taken. With the availability of a fast NO analyser, the opportunity arose to examine the validity of the model in predicting cyclic NO formation.

The oxides of nitrogen (NO,  $N_2O$ , and  $NO_2$ ) are all present in the exhaust of a spark ignition engine. However, nitrous oxide ( $N_2O$ ) and nitrogen dioxide ( $NO_2$ ) are present at much lower levels than NO, typically on the order of 20 ppm and 70 ppm respectively, compared to NO concentrations of 2000 ppm (Raine et al., 1995). Because of this, ISIS only models NO formation, and uses the extended Zeldovich mechanism (Heywood, 1988):



This is called the “thermal” route of NO formation (Raine et al., 1995). Since these reactions involve the O and OH radicals, it is usually necessary to couple them to the oxidation of the fuel. However, since the rate of NO formation by the thermal mechanism is usually slow compared to the rate of combustion, the NO reactions are decoupled from the fuel oxidation for modelling within ISIS. Rate constants for the forward and reverse reactions ( $k_i^+$  and  $k_i^-$ ) have been calculated in numerous studies. The rate of formation of NO can thus be written as

$$\frac{d[NO]}{dt} = k_1^+ [O][N_2] + k_2^+ [N][O_2] + k_3^+ [N][OH] - k_1^- [NO][N] - k_2^- [NO][O] - k_3^- [NO][H]$$

where  $[ ]$  denotes the concentration of the species in the units corresponding to those of the rate constants. At equilibrium the forward and reverse reaction rates are equal, so the extended Zeldovich reactions may be expressed as

$$R_1 = k_1^+ [O]_e [N_2]_e = k_1^- [NO]_e [N]_e$$

$$R_2 = k_2^+ [N]_e [O_2]_e = k_2^- [NO]_e [O]_e$$

$$R_3 = k_3^+ [N]_e [OH]_e = k_3^- [NO]_e [H]_e$$

where the subscript 'e' indicates equilibrium values. Since the concentration of nitrogen is much less than the concentrations of the other species (Heywood, 1988), the nitrogen is assumed to be in a steady state condition, i.e.,

$$\frac{d[N]}{dt} = 0.$$

By combining the equilibrium expressions with the assumption of steady state nitrogen, the rate of NO formation is given by (Heywood, 1988)

$$\frac{d[NO]}{dt} = \frac{2R_1 \left( 1 - \left( \frac{[NO]}{[NO]_e} \right)^2 \right)}{1 + \left( \frac{[NO]}{[NO]_e} \right) \frac{R_1}{(R_2 + R_3)}}.$$

ISIS integrates this expression to calculate the NO concentration at time  $t$ .

There is also a "prompt" mechanism in which NO is formed rapidly in the regions near the flame. The most important of these reactions are (Miller and Bowman, 1989)



The molecular nitrogen then reacts rapidly with hydrocarbon radicals to form amines or cyano compounds that then react to form NO (Miller and Bowman, 1989). The combustion modelling in ISIS is not detailed enough to incorporate prompt NO formation. However, thermal NO formation is considered to be the primary contributor to total NO formation in a

spark ignition engine (Raine et al., 1995). Thus, ISIS modelling of NO formation is limited to the thermal mechanism.

## 7.2 *Experimental facility*

Once again, the K4 engine test bed, as described in Chapter 3, was used for the following work. However, in this case a fast response chemiluminescent detector (CLD) was made available for the work. The operation of a fast CLD has recently been described by Reavell et al. (1997) and Baltisberger and Ruhm (1994). However, the fast CLD used in this study has a radically different sampling system which is similar to that used on the fast response flame ionisation detector (FID) described by Finlay, et al., (1990) and Cheng, et al., (1991). The sampling system delivers the sample to the chemiluminescence chamber where it is mixed with a flow of ozonised air. The resulting chemiluminescent reaction produces photons in the 700-1500 nm wavelength range, which are detected with a photomultiplier tube.

The fast response CLD's gas reaction chamber is housed in a remote sampling head so that sampling may be performed close to the exhaust system. The light from the chamber is transferred to the photomultiplier by a fibre-optic bundle. The main control unit also houses the power supply, electronics, ozone generator, and vacuum regulators.

It should be noted that the fast response CLD only measures NO. In order to measure NO<sub>2</sub>, a pre-reaction is required to convert the NO<sub>2</sub> in the sample to NO prior to detection. This would have a detrimental effect on the response time of the instrument. However, NO typically accounts for more than 95% of the total NO<sub>x</sub> emissions in SI engines (Heywood, 1988).

Calibration of the fast CLD was accomplished by flooding the sampling chamber with nitrogen to set the zero. The chamber was then flooded with a span gas of known NO concentration (2390 ppm) to set the span. Once the instrument was completely warmed up, it exhibited little drift for the duration of the experiments.

The engine was operated at 24 different operating points as summarised in Table 7.1.

**Table 7.1. Experimental operating points.**

Test ID	Speed (RPM)	Air Flow (litres/sec)	Nominal Load	Ignition (DBTDC)	Air-fuel ratio ( $\lambda$ )	Fuel
P0915	1000	1.0	1/3	15	0.9	methane
P0930	1000	1.0	1/3	30	0.9	methane
P1015	1000	1.0	1/3	15	1.0	methane
P1030	1000	1.0	1/3	30	1.0	methane
P1115	1000	1.0	1/3	15	1.1	methane
P1130	1000	1.0	1/3	30	1.1	methane
F0915	1000	2.0	2/3	15	0.9	methane
F0930	1000	2.0	2/3	30	0.9	methane
F1015	1000	2.0	2/3	15	1.0	methane
F1030	1000	2.0	2/3	30	1.0	methane
F1115	1000	2.0	2/3	15	1.1	methane
F1130	1000	2.0	2/3	30	1.1	methane
20915	2000	2.0	1/3	15	0.9	methane
20930	2000	2.0	1/3	30	0.9	methane
21015	2000	2.0	1/3	15	1.0	methane
21030	2000	2.0	1/3	30	1.0	methane
21115	2000	2.0	1/3	15	1.1	methane
21130	2000	2.0	1/3	30	1.1	methane
T0915	1000	1.0	1/3	15	0.9	toluene
T0930	1000	1.0	1/3	30	0.9	toluene
T1015	1000	1.0	1/3	15	1.0	toluene
T1030	1000	1.0	1/3	30	1.0	toluene
T1115	1000	1.0	1/3	15	1.1	toluene
T1130	1000	1.0	1/3	30	1.1	toluene

The probe for the fast response CLD was inserted into the exhaust pipe at a point 50 mm from the exhaust port outlet, and the exhaust pipe diameter was 40 mm. The data acquisition system recorded the cylinder pressure, crank flag, barrel pressure, and NO reading at 1 degree crank angle intervals, and 360 consecutive cycles were recorded at each operating point. The pressure data was analysed by COBRA, and the cyclic values of IMEP,  $P_{max}$ , phasing of  $P_{max}$ , and 10% and 80% burn rate were calculated.

### 7.3 Fast NO measurements

Reavell, et al., (1997) noted that cyclic measurements obtained with a fast response analyser must be handled with caution. The mass flow is highly unsteady during the exhaust event, and the portion of the trace obtained while the exhaust valve is closed must be ignored. This is due to the fact that there is no gas flow during that time. Hence, the following calculations were performed on the NO trace during the period when the exhaust valve was open.

In order to obtain a sensible value for cyclic NO, the measured trace must be mass averaged. This involves predicting two phenomena:

- a) the mass flow rate past the probe must be calculated on a crank angle basis, and
- b) the total response time must be calculated. This includes the time for the exhaust gas to flow from the cylinder to the sampling chamber plus the inherent response time of the instrument.

Whilst calculating the instantaneous mass flow through the exhaust valves would be possible (utilising experimental pressure measurements, thermodynamic properties calculated by ISIS, and the valve effective flow area), it was decided instead to calculate the instantaneous mass in the cylinder at each crank angle. Then, the difference in mass between successive crank angles was assumed to be equal to the instantaneous mass flow out of the cylinder and into the sampling probe (blow-by during blow-down and exhaust was assumed to be negligible). The results of the mean cycle simulation from ISIS were used to calculate the pressure, volume, temperature, and trapped mass at EVO. These quantities were used to calculate the specific gas constant ( $R_{\text{ISIS}}$ ) for the mixture. Exhaust blow-down was assumed to occur polytropically, with the polytropic index ( $n$ ) calculated between the end of combustion and EVO by a linear least squares fit to the experimental LogP-logV data. Hence, the in-cylinder temperature from EVO until BDC could be calculated by:

$$T_{i+1} = T_i \left( \frac{P_{i+1}}{P_i} \right)^{\frac{n-1}{n}}. \quad (7.1)$$

The in-cylinder mass was then calculated from



$$m_{i+1} = \frac{P_{i+1} V_{i+1}}{T_{i+1} R_{\text{ISIS}}} \quad (7.2)$$

During the exhaust stroke (from BDC to EVC), the in-cylinder heat transfer was estimated using the Woschni (1967) correlation of the form

$$h = 129.8 P^{0.8} u^{0.8} B^{-0.2} T^{-0.55} \text{ (W / m}^2 \text{ K)} \quad (7.3)$$

where  $P$  = instantaneous cylinder pressure (bar)

$B$  = bore diameter (m)

$T$  = instantaneous gas temperature (K)

$u = 6.18 v_p$ , where  $v_p$  is the mean piston speed (m/s).

The temperature at the next step was then calculated by

$$\Delta T = F \frac{hA(T - T_w)}{mc_p} \Delta t \quad (7.4)$$

where  $F$  was a weighting factor and  $\Delta t$  was the time between successive crank angles. The in-cylinder mass was calculated as before (equation 7.2). Since the temperature change during the exhaust stroke was assumed to be small, it was assumed the fluid had a constant specific heat capacity. The heat transfer weighting was adjusted so that the in-cylinder mass at EVC was equal to the estimated residual mass fraction used in ISIS.

Modelling the transit time from the exhaust valve to the instrument reading proved more difficult due to uncertainties in the actual instrument response time and the time delay associated with the exhaust gas sample travelling from the port to the analyser chamber. The solution to this is best explained with reference to Figure 7.1.

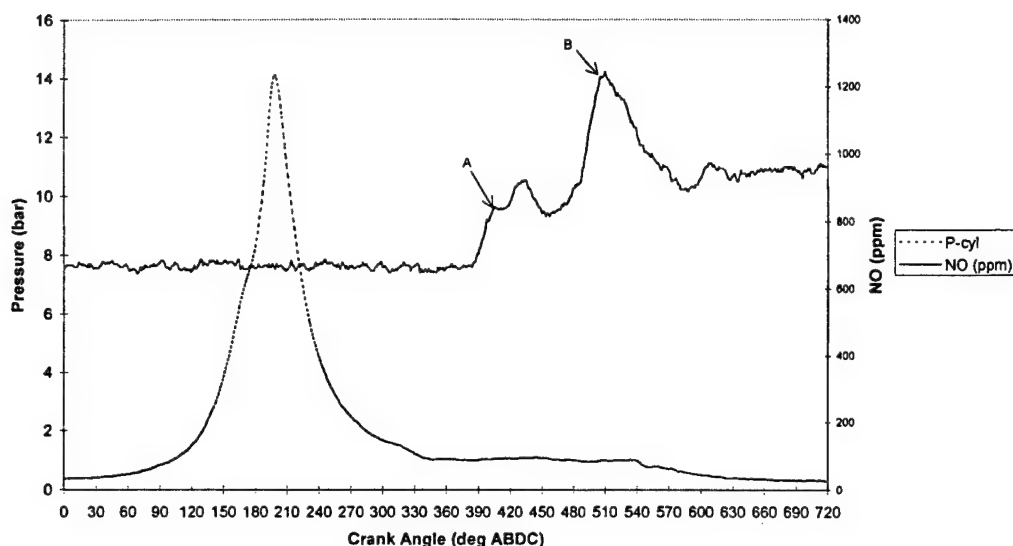
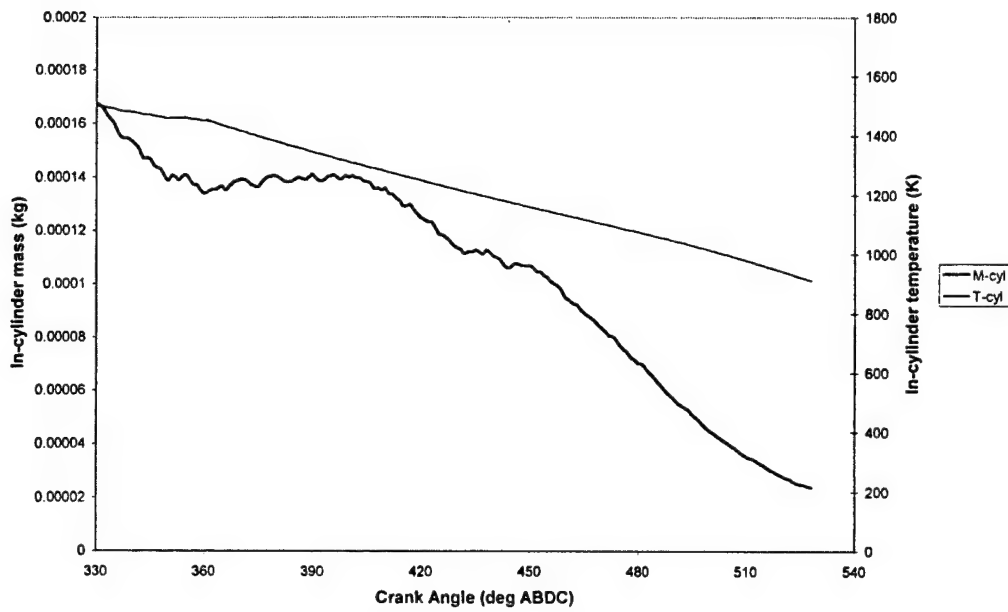


Figure 7.1. Sample NO trace.

Reavell et al. (1997) noted that the NO traces they obtained had a similar “signature”. They deduced that the initial peak in the signal, labelled point A in Figure 7.1, corresponds to the first gas passing through the exhaust valve clearing the old exhaust port gas from the previous cycle. After examining a large number of cycles, it was found that the occurrence of point A was nearly constant for a given operating condition. The time from EVO to point A was assumed to be the total transit time of the exhaust gas plus instrument response time for the experimental data, and this value (in degrees crank angle from EVO) was used to calculate the mass averaged NO value for each cycle.

A typical result of these calculations is shown in Figure 7.2 as a plot of calculated in-cylinder temperature and mass versus crank angle.



**Figure 7.2.** In-cylinder mass and temperature as a function of crank angle.

#### 7.4 Model results

The initial ISIS NO calculations were compared to a cyclic average of the NO signal. The average was performed on each cycle from the point of first instrument response (point A in Figure 7.1) until EVC. This was done to allow ISIS to calculate an initial estimate for the temperature at EVO. It was expected that the process would have to be iterated as the mass averaged NO values were computed. However, as Table 7.2 shows, the difference between the time average and the mass average was very small in the majority of cases.

Table 7.2. Comparison of time average to mass average for NO measurements.

Test ID	NO (ppm) time avg.	NO (ppm) mass avg.	% Difference
P0915	146	150	2.74
P0930	180	187	3.89
P1015	180	192	6.67
P1030	631	675	6.97
P1115	205	222	8.29
P1130	595	638	7.23
F0915	258	252	-2.33
F0930	417	397	-4.80
F1015	1315	1288	-2.05
F1030	2445	2419	-1.06
F1115	908	886	-2.42
F1130	1841	1817	-1.30
20915	120	126	5.00
20930	142	144	1.41
21015	169	175	3.55
21030	127	135	6.30
21115	148	149	0.68
21130	554	548	-1.08
T0915	418	406	-2.87
T0930	478	464	-2.93
T1015	807	762	-5.58
T1030	1005	1019	1.39
T1115	867	866	-0.12
T1130	1612	1606	-0.37

In fact, in two-thirds of the cases, the difference between the two averages was less than 5%, and the worst case was slightly over 8%. The agreement in the two averages can be attributed to the fact that the NO signature does not exhibit a characteristic “spike” during the exhaust as does a fast response flame ionisation detector (FID). This seems to indicate that mass averaging a fast NO signal is less critical than mass averaging a fast response FID signal. Nonetheless, the mass averaged NO value was used as the target parameter for ISIS

Once ISIS had been tuned to the mean cycle, the cycle-by-cycle burn rates and combustion completeness (calculated by COBRA) were used as inputs. A summary of ISIS inputs for each case is presented in Appendix D in order to facilitate reproduction of the modelled cases. The results of ISIS modelling for the target parameters (IMEP,  $P_{\max}$ ,  $\theta_{P_{\max}}$ , and NO) are shown in Table 7.3. These mean values were calculated by averaging the cyclic results for both the experimental data and the ISIS modelling.

**Table 7.3. Results of ISIS modelling.**

Test ID		IMEP (COV) (bar)	$P_{\max}$ (COV) (bar)	$\theta_{P_{\max}}$ (DABDC)	NO (ppm)
P0915	EXP	2.49 8.54	9.69 21.07	195	150
	ISIS	2.46 8.99	9.28 21.40	196	194
P0930	EXP	2.51 2.65	14.30 14.33	196	187
	ISIS	2.48 4.25	14.02 17.00	198	212
P1015	EXP	2.52 2.43	9.32 8.98	205	192
	ISIS	2.50 2.58	8.88 9.29	206	184
P1030	EXP	2.38 2.55	16.54 6.12	192	675
	ISIS	2.36 3.97	15.74 7.41	193	632
P1115	EXP	2.39 1.76	9.25 7.40	202	222
	ISIS	2.38 1.92	8.98 7.76	205	236
P1130	EXP	2.21 2.40	15.32 5.21	192	638
	ISIS	2.20 4.28	15.09 6.62	193	673
F0915	EXP	4.51 1.88	20.79 10.94	204	252
	ISIS	4.47 2.20	20.57 11.11	204	273
F0930	EXP	4.24 3.00	32.96 6.96	190	397
	ISIS	4.23 3.38	33.13 6.77	190	448
F1015	EXP	4.58 0.95	25.08 5.07	199	1288
	ISIS	4.60 1.43	24.37 5.03	199	1322
F1030	EXP	4.04 1.96	36.44 2.60	186	2419
	ISIS	4.06 1.99	35.57 2.42	186	2405
F1115	EXP	4.35 0.98	22.26 5.33	200	886
	ISIS	4.35 1.57	21.58 5.78	200	916
F1130	EXP	3.61 3.11	31.96 3.70	188	1817
	ISIS	3.62 3.31	31.66 3.63	188	1960

Test ID		IMEP (COV) (bar)	$P_{max}$ (COV) (bar)	$\theta_{P_{max}}$ (DABDC)	NO (ppm)
20915	EXP	1.29 41.02	7.71 0.92	179	126
	ISIS	1.35 40.79	7.53 0.61	180	76
20930	EXP	2.40 11.23	9.21 13.60	191	144
	ISIS	2.38 11.95	8.59 10.11	189	161
21015	EXP	1.86 19.26	8.12 2.08	181	135
	ISIS	1.87 20.35	8.85 1.08	180	154
21030	EXP	2.62 4.50	11.08 15.70	197	175
	ISIS	2.58 5.80	10.85 14.35	193	193
21115	EXP	2.34 8.28	8.28 6.36	185	149
	ISIS	2.33 8.52	9.00 2.57	182	149
21130	EXP	2.77 2.89	16.08 7.02	192	548
	ISIS	2.75 3.64	15.44 10.39	194	570
T0915	EXP	2.86 1.23	16.58 6.14	197	406
	ISIS	2.85 1.90	17.31 5.99	197	418
T0930	EXP	2.46 3.22	21.36 3.35	186	464
	ISIS	2.46 2.89	21.70 3.79	186	481
T1015	EXP	2.80 3.12	15.35 8.31	198	762
	ISIS	2.79 4.14	15.87 7.98	198	827
T1030	EXP	2.45 3.24	19.19 5.74	188	1019
	ISIS	2.44 3.68	18.86 5.48	188	995
T1115	EXP	2.59 8.44	12.08 15.07	202	866
	ISIS	2.57 11.32	12.68 15.01	203	945
T1130	EXP	2.41 2.61	17.72 5.46	190	1606
	ISIS	2.41 4.08	18.44 5.54	190	1658

As Table 7.3 indicates, the mean values of the target parameters as well as the COV of IMEP and  $P_{max}$  were adequately modelled by ISIS. Usual practice is to plot NO versus maximum cylinder pressure on a scatter plot. Figures 7.3-7.6 show these results for the stoichiometric cases. All other cases are shown in Appendix E.

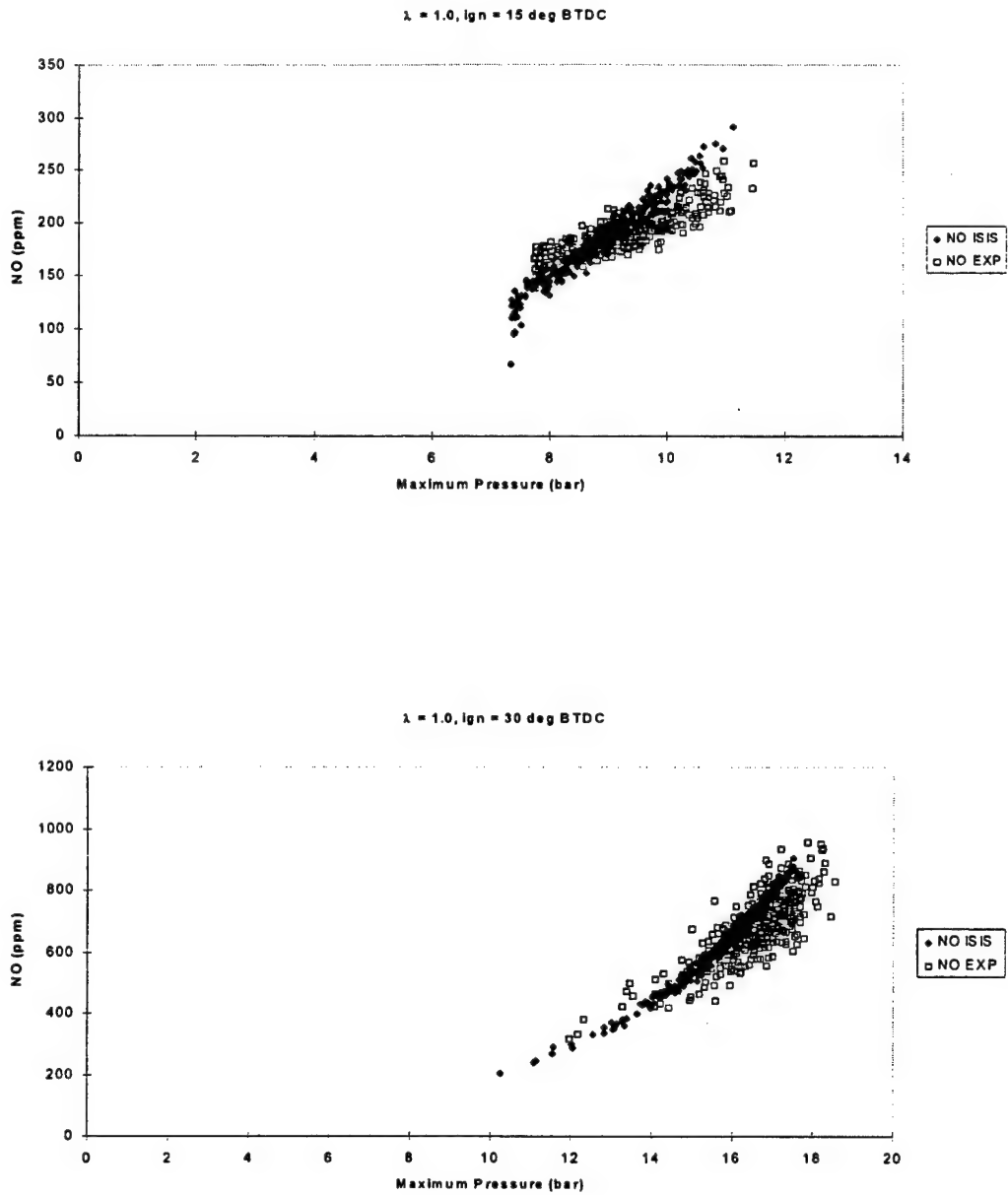


Figure 7.3. Maximum pressure versus NO for K4 at 1000 RPM, 1/3 load, running on methane.

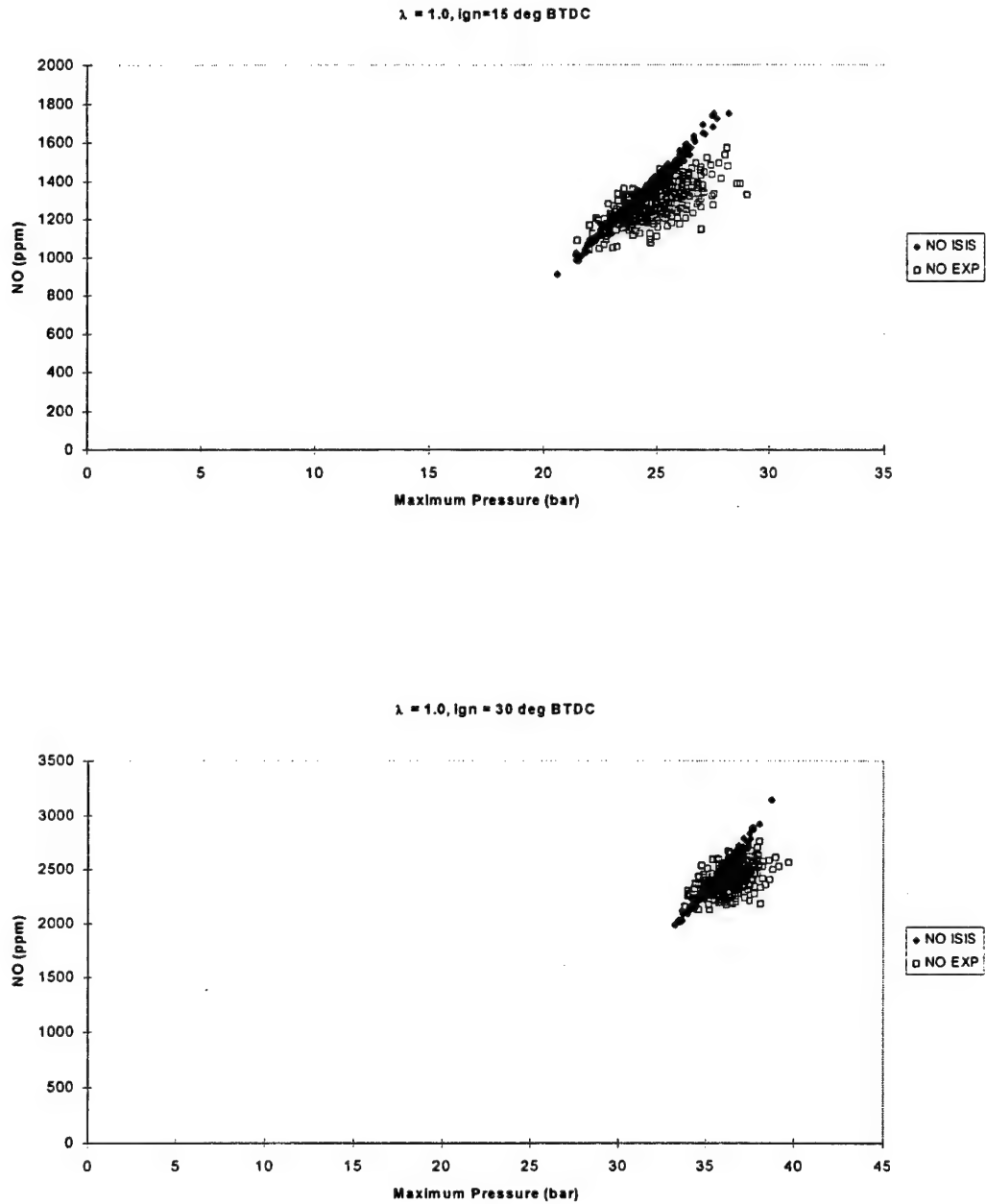


Figure 7.4. Maximum pressure versus NO for K4 at 1000 RPM, 2/3 load, running on methane.



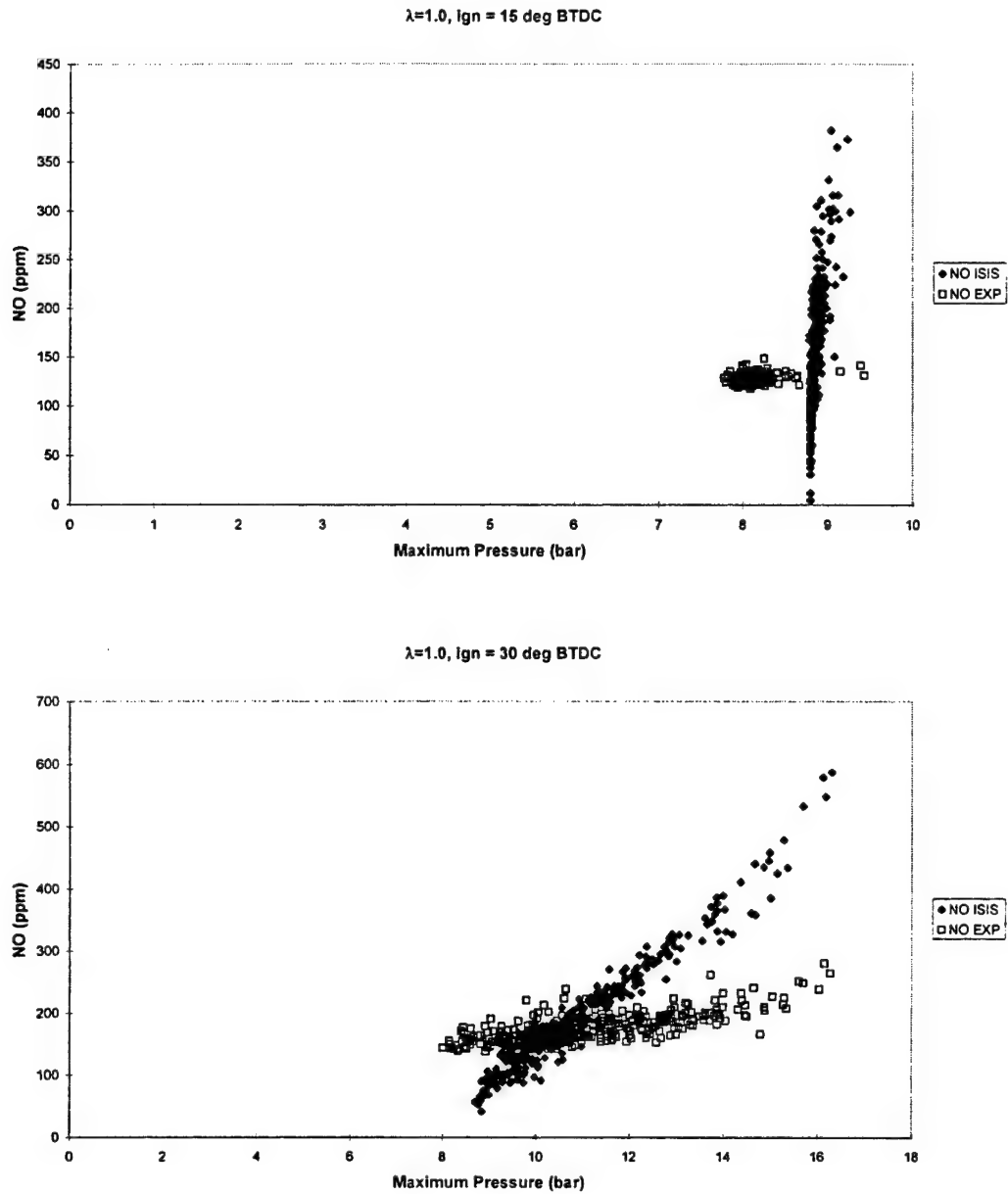
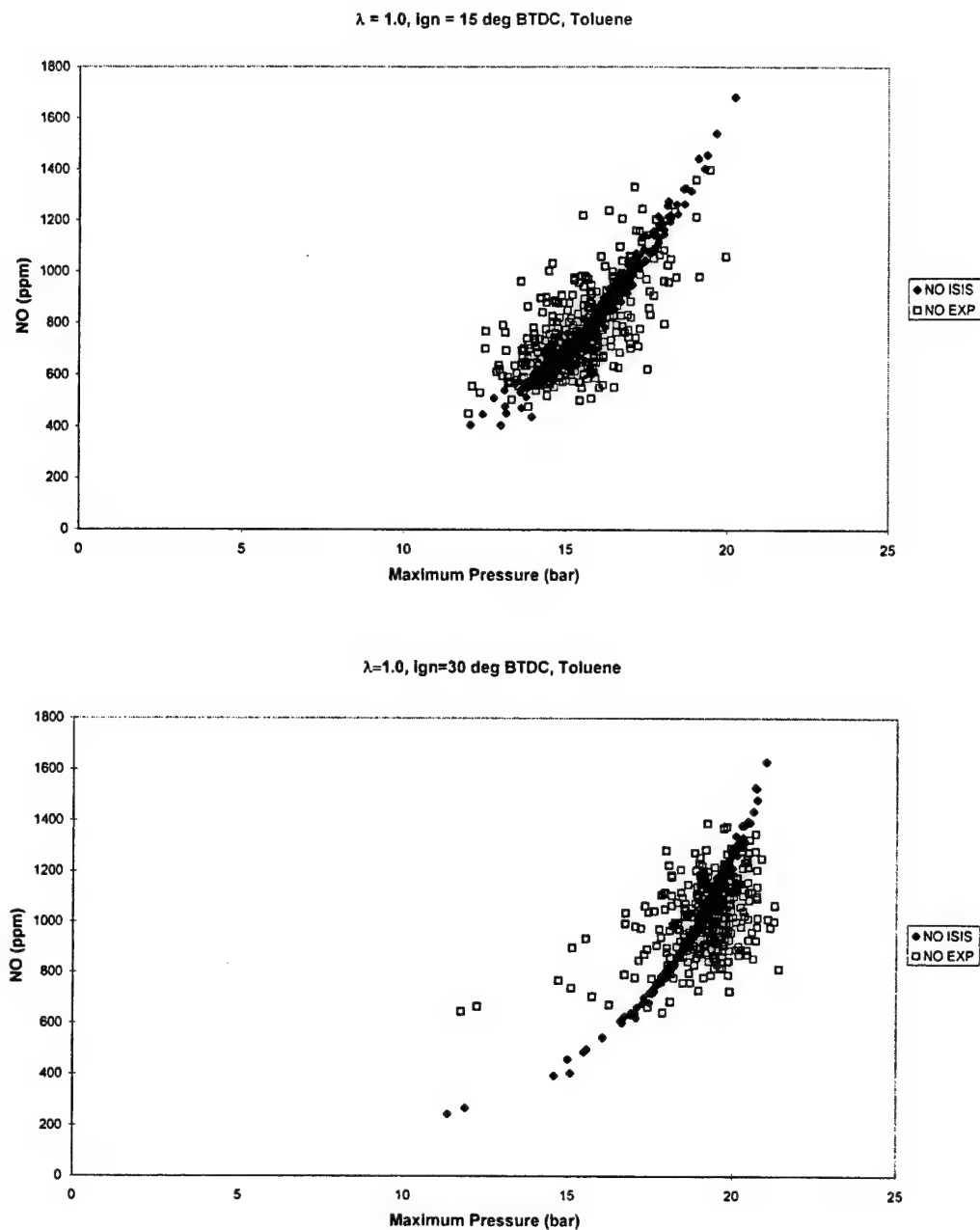


Figure 7.5. Maximum pressure versus NO for K4 at 2000 RPM, 1/3 load, running on methane.



**Figure 7.6. Maximum pressure versus NO for K4 at 1000 RPM, 1/3 load, running on toluene.**

These plots show good agreement with the mean NO level and with the general slope of the pressure-NO curve. The plots in Appendix E are similar, although the slope of the ISIS  $P_{\max}$ -NO plots for rich mixture cases had less agreement with the experimental data. Initially, questions were raised regarding the accuracy of the ISIS calculations during rich combustion. Hence, ISIS was set up to model constant volume combustion (i.e., a combustion bomb) and

the predicted combustion products were compared to those calculated by STANJAN (Reynolds, 1992), an interactive program for chemical equilibrium analysis. The results were in good agreement, and it was concluded that ISIS was performing accurate calculations during rich combustion.

Furthermore, the plot for 2000 RPM with retarded timing (Figure 7.5) requires some explanation. The throttle setting was not changed between 1000 and 2000 RPM in this experiment. Hence, at 2000 RPM the engine was highly throttled. With the retarded timing in this case, even with good combustion, the maximum pressure barely rose above the motoring pressure. ISIS shows virtually no variation in  $P_{\max}$ , and even in the experiment the variation was very small. This trend was also evident in the other cases with retarded timing at 2000 RPM. Since this was a rather dubious operating condition for the engine, it was decided to show the results whilst not concentrating on their analysis as this would necessitate the modification of COBRA and ISIS to cope with this condition.

Overall, the model results do not show as much scatter in NO as the experimental data. The differences could arise from deficiencies in the model (ISIS) or from the manner in which the mass averaged NO reading was calculated. To address these questions, a sensitivity analysis was performed both on the mass averaging calculations and on ISIS.

The mass averaged NO calculation requires a user input of total transit time, heat transfer weighting, and wall temperature, as well as a temperature at EVO calculated by ISIS. Each of these inputs was varied by  $\pm 10\%$  for the case of a stoichiometric mixture of toluene at an ignition timing of 15 degrees BTDC (case T1015). The results of this analysis are shown in Table 7.4 in comparison to the mass averaged NO level of 762 ppm.

**Table 7.4. Results of mass averaging calculations showing the sensitivity of computed NO to changes in input parameters by  $\pm 10\%$ .**

Reference input parameter	Effect on mass averaged NO	
	Computed NO	Percent change
transit time = 82 deg CA	752/771	-1.3%/+1.18%
heat transfer weighting = 1.0	760/764	-0.26%/-0.26%
$T_{\text{wall}} = 450 \text{ K}$	764/760	+0.26%/-0.26%
$T_{\text{EVO}} = 1317 \text{ K}$	759/765	-0.39%/+0.39%

As can be seen, the computed NO is fairly insensitive to variations in the input parameters. Again, this is most likely due to the nature of the NO "signature" and its lack of a large spike during the exhaust event. The primary ISIS inputs that were examined are shown in Table 7.5. Of these, the first 3 (pressure and temperature at IVC, and residual fraction) are

assumed constant for all cycles whilst the final three are computed from the experimental data on a cycle-by-cycle basis. Table 7.5 generally corresponds to the same experimental case as Table 7.4. However, the combustion completeness was lowered to 0.9 for the mean cycle in order to allow for a  $\pm 10\%$  deviation. Hence, the modelled performance parameters have slightly different values than those shown in Table 7.3.

**Table 7.5. Results of ISIS showing the sensitivity of output values to changes in input parameters by  $\pm 10\%$ .**

Reference input parameter	Effect on calculated output values		
	$P_{\max}$ (15.2 bar)	IMEP (2.68 bar)	NO (686 ppm)
$P_{\text{ivc}} = 0.51$ bar	+10.1%/-10.1%	+10.1%/-10.5%	+7.87%/-8.31%
$T_{\text{ivc}} = 433$ K	-7.76%/+10.1%	-11.6%/+14.2%	+24.2%/-18.5%
$r_f = 0.194$	-1.18%/+1.25%	-2.61%/+2.24%	-30.3%/+39.7%
10% burn = 17 deg CA	+0.86%/-0.59%	+0.00%/-0.75%	+2.19%/-2.62%
80% burn = 33 deg CA	-8.29%/+10.39%	-1.49%/+1.12%	-21.7%/+35.1%
$\chi = 0.9$	+6.91%/-6.32%	+10.8%/-10.8%	+33.4%/-25.4%

These calculations confirm the sensitivity of the NO model to variables that do not strongly affect the other target parameters. Whilst the burn rates and the combustion completeness are calculated from experimental data and are then used as inputs for the ISIS cycle-by-cycle modelling, the pressure at inlet valve closure, residual fraction, and the temperature at IVC are calculated for the mean cycle and are not varied cycle-by-cycle. It is assumed that the compression process varies very little cycle-to-cycle, and assuming a constant pressure at IVC for each cycle is reasonable. Assuming constant values for residual fraction and temperature at IVC is not so reasonable. Given the sensitivity of the NO to these two factors, it becomes clearer why the modelled results show less scatter than the experimental data.

### 7.5 *Concluding remarks*

The work presented here has compared modelled NO formation to experimental data on a cycle-by-cycle basis. The experimental data consisted of mass averaged cycle readings obtained with a fast CLD, whilst the modelled data were calculated using the extended Zeldovich mechanism within ISIS.

The results of the NO modelling show good agreement with experimental data in terms of the mean NO level and the slope of the maximum pressure-NO curve. However, the modelled data showed less scatter in the plots than the experimental data. This is attributed to the fact that the NO is particularly sensitive to the residual fraction and temperature at IVC, neither of which was allowed to vary on a cyclic basis within the model.

Since ISIS currently calculates a residual mass composition and temperature, it may improve its performance in modelling NO formation if the calculated residual properties were fed forward into the subsequent cycle in order to calculate a new residual fraction. Future work at Oxford will involve laser diagnostics to determine in-cylinder temperatures during combustion, and this may prove helpful in incorporating a variable temperature at IVC within the model.

## Chapter 8 Torque Estimation and Misfire Detection using Block Angular Acceleration

### 8.1 Introduction

The main body of this work has examined cycle-by-cycle variation and methods of modelling it within an established engine simulation. This chapter continues the theme of cyclic variation in the sense that the most extreme case of cycle-by-cycle variation is actual cylinder misfire. Over the past several years, much effort has been placed into systems capable of detecting misfires in a spark-ignition engine. This interest was spawned by the California Air Resources Board (CARB) on-board diagnostic regulations for 1994 model year vehicles (OBD-II). According to the CARB regulations (1991) engine misfire means, "lack of combustion in the cylinder due to absence of spark, poor fuel metering, poor compression, or any other cause". The regulations require that the vehicle's engine diagnostic system monitor misfire continuously. This concern is due to the fact that, even with a small number of misfiring cycles, engine performance degrades, hydrocarbon emissions increase, and driveability will suffer (Lee and Rizzoni, 1995). Furthermore, a misfired cycle results in a large quantity of unburned fuel being sent through the catalytic converter, which causes a reduction in its service life due to high temperature excursions (Klenk, et al., 1993). Several methods of misfire detection have been proposed (Klenk, et al., 1993):

- a) Monitoring catalyst temperature. This method is unacceptable since the catalyst temperature does not rise significantly in the case of low frequency misfire.
- b) Monitoring the oxygen sensor signal. This method also fails because a single misfire does not significantly alter the sensor output voltage.
- c) In-cylinder pressure monitoring. This method is the most accurate as individual cylinder IMEP could be calculated in real time. However, the cost of fitting each cylinder with a pressure transducer is prohibitive.
- d) Evaluation of crankshaft angular velocity fluctuations. This method has been the subject of much current work and appears to be very promising.

Since method d) above is currently the most favoured method of misfire detection, this chapter will focus on that area. Whilst flywheel angular velocity fluctuations do provide good indices of misfire detection under certain engine operating conditions, one of the primary difficulties in implementing this method is the fluctuating load torque applied to the

crankshaft through the drivetrain. The hypothesis in this chapter is that misfires can be detected by measuring the angular acceleration of the engine block, and that this measurement is relatively unaffected by the load applied at the opposite end of the drivetrain.

Examination of this hypothesis will begin with a review of the relevant literature pertaining to misfire detection by flywheel angular velocity measurements. This will be done in order to establish the current state of the art in misfire detection. A brief description of the experimental facilities used will be presented, followed by the development of the model used to reconstruct the torque applied by the cylinders in the engine. Next, various parameters will be derived for misfire detection, and the results of their use on a production 4-cylinder engine will be presented. The chapter will finally draw conclusions as to the advantages and disadvantages of using block angular acceleration as a method of misfire detection.

## **8.2 Literature review**

Before launching into a review of individual studies, it is helpful to examine, in general terms, the different methods of using flywheel velocity measurements. A classification system similar to that used by Williams (1996) will be used here, and the various methods will be distinguished by the following characteristics:

- a) Complexity of system model.
- b) Metric of misfire detection.
- c) Methods of analysis.
- d) Assumptions.

### **8.2.1 Complexity of system model**

The system models used range in complexity from the use of no model at all, to the use of a full dynamic model, which includes crankshaft torsional vibration, and the dynamics of the drivetrain. If no model is used at all, the analysis is performed on the measured velocity signal. This has the advantage of simplicity, but is limited to identifying misfires through pre-computed threshold levels or pattern recognition (discussed in Section 8.2.2) since without a model, cylinder torque cannot be reconstructed.

Next in order of complexity are models which use a single “lumped” inertia for the engine and drivetrain, and assume a rigid crankshaft. These models allow a composite cylinder torque to be calculated. If the engine in question does not have overlapping firing

intervals, the torque signal can be temporally divided and the individual cylinder torques can be estimated. Such methods do not work well under conditions where either crankshaft torsional vibration or the fluctuating inertial properties of the engine are significant.

Finally, complex models have been used which incorporate a flexible crankshaft and include the dynamics of the drivetrain and engine. These models do allow the calculation of individual cylinder torque contributions in engines where the firing pulses do not overlap.

### 8.2.2 Metrics of misfire detection

The parameter used to indicate a misfire is to a large degree dependant on the system model used in the analysis. In the case where no system model is used, one is forced into using either threshold criteria or pattern recognition to identify misfire. This requires the thresholds to be pre-computed for various speed and load combinations. Furthermore, threshold techniques can usually detect a misfire within an engine cycle, but may not be able to identify which cylinder misfired during that cycle. Pattern recognition techniques can allow identification of the specific misfiring cylinder, but at the added cost of collecting and computing reference patterns at various speed and load combinations.

For cases where a system model is employed, the reconstructed torque profile can be analysed to identify misfire. The option still exists for using threshold criteria or pattern recognition in this case. However, if the crankshaft is assumed to be rigid and the firing pulses do not overlap, the torque signal can be separated in the time (or crank angle) domain and the contribution of each individual cylinder can be calculated. Thus, the misfiring cylinder is immediately identified by a reduced contribution to the torque profile.

Several researchers have attempted to reconstruct cylinder pressure profiles from the flywheel angular velocity measurements. The major difficulty with this method is that the cylinder pressure has no effect on crankshaft torque (and hence flywheel angular velocity) at TDC. Hence, cylinder pressure cannot be reconstructed from the crankshaft torque at that point. Since the cylinder pressure at this point is critical to misfire detection, this limitation is a significant problem.

### 8.2.3 Methods of analysis

With the use of a system model, account must be made for the system response in calculating the torque applied to the crankshaft. This implies some sort of deconvolution in order to remove the effects of the reciprocating mass and to account for the system dynamics.



Deconvolution in the frequency domain becomes an algebraic operation, hence, most of the researchers reviewed here perform their analysis in the frequency domain.

There are further advantages to analysing the torque profile in the frequency domain. If the crankshaft is rigid and the firing pulses are uniform, the torsional excitation for all frequencies sums to zero except for multiples of the firing frequency (assuming each cylinder produces identical work on each firing pulse). In the case of a misfire, energy is transferred into sub-harmonics of the firing frequency, and this energy can be used to identify the misfire, normally through threshold values as outlined in section 8.2.2.

#### 8.2.4 Common assumptions

Most researchers have assumed that the dynamics of the system are known and remain constant. At low engine speeds, this assumption is generally valid. However, the inertial properties of an engine are time-varying (Shiao and Moskwa, 1994). At higher engine speeds, the variation in inertial properties becomes more significant, with a resulting degradation in the accuracy of the model.

When analysing the loads applied to the crankshaft, the load contributed by the drivetrain cannot be neglected. Normal procedure is to assume the drivetrain load is constant, and induces a DC torque to the crankshaft. This assumption should be valid in the case of an engine sitting in a test cell. However, for vehicular applications, significant dynamic loads can be induced in the drivetrain from the road.

The assumption of a torsionally rigid crankshaft has been mentioned numerous times in the preceding sections. The assumption is valid in cases where crankshaft torsional vibration is not significant, which means it is usually valid for low engine speeds. The torsional vibration characteristics of the crankshaft can be modelled, and taken into account in the system model. However, complete elimination of the effects of crankshaft vibration requires independent velocity measurements at each crank throw, which at this time is not a feasible option.

Finally, most researchers assume non-overlapping firing pulses. This is required since only one measurement is taken. Hence, only a composite torque profile can be calculated. With this assumption, the composite torque can be temporally filtered in order to deduce each cylinder's contribution to the torque profile. This assumption is generally valid for engines with fewer than 8 cylinders (Williams, 1996).

### 8.2.5 Review of relevant literature

Citron et al. (1989) developed a system for calculating engine torque and cylinder pressure from flywheel angular velocity measurements. They constructed a four degree of freedom model, which includes the crank and connecting rods, the flywheel, the vibration damper, and the vehicle loads (simulated by the dynamometer load). Each inertia is connected by torsional springs, and damping is included. The crankshaft was assumed to be rigid. The flywheel velocity was measured from the 142 tooth starter ring with a magnetic pick up. The velocity measurements were used as inputs to the model, and a crankshaft torque profile was calculated. This torque profile was assumed to be composed of a mean value plus a fluctuating component. They then subtracted the torque due to reciprocating components from this profile, and assumed that at TDC, the fluctuating component must be equal to the negative of the mean value (since cylinder torque at TDC is zero). The torque contribution for each cylinder was calculated by assuming that during the firing pulse, the firing cylinder was the only contributor to the torque profile. They also reconstructed cylinder pressure during the firing stroke for each cylinder, with the expected gaps in the calculations around TDC.

Plapp et al. (1990) developed an engine roughness parameter based on the difference between successive angular accelerations of the flywheel; the angular acceleration calculated by differentiating the velocity measurements. Since the difference in angular acceleration is zero for constant speed or constant acceleration conditions, they conclude that the method is valid for steady-state and transient operation. They also used pattern recognition to discriminate between angular acceleration fluctuations produced by misfire and those produced by load inputs. Their method does not require a system model, although pre-calculations are required to establish pattern libraries.

Klenk et al. (1993) also use the engine roughness parameter proposed by Plapp et al. (1990) and a misfire threshold is pre-computed for various engine speed and load combinations. They accounted for road or driver induced transients by noting that a misfire would induce short term reductions in angular acceleration (and hence rotational energy) whilst transient operation (such as throttle lift-off) would induce a long term reduction in energy. The long term transients were then used to modify the threshold values or even, under extreme conditions, to disable the misfire detection system. It was found that the system worked best at low engine speeds where the rigid crankshaft assumption was most valid.

Iida et al. (1990) developed a system model from which the IMEP for each cylinder is estimated. The IMEP as used by them is the integral of the torque profile over the firing

interval for each cylinder. Their model incorporated estimations of the torque applied by the valve train, accessories, and internal friction. It was found that at higher engine speeds, the model results were degraded due to crankshaft torsional vibration.

Brown and Neill (1992) estimate cylinder pressure from flywheel angular velocity measurements by using reference patterns contained in a knowledge database. The method was employed on a Detroit Diesel V-6 engine. They recorded data at an operating speed of 1200 RPM, and varied the fuelling level in each cylinder. The crankshaft velocity fluctuations were recorded as each cylinder was under-fuelled to establish the reference pattern. These reference patterns were then used to predict maximum cylinder pressure in later tests with a claimed accuracy of  $\pm 6\%$ .

Several researchers have focused on calculating the indicated torque waveform in the frequency domain (Rizzoni, 1986, Connolly, 1994, Connolly and Rizzoni, 1994, Lee and Rizzoni, 1995). The method employed uses a rigid crankshaft, lumped inertial model for the system, and the load torque and friction torque are assumed constant. The applied torque on a crankshaft is thus given by (Connolly, 1994)

$$T_c = T_p + T_m + T_f + T_L \quad (8.1)$$

where

$T_c$  = composite torque applied to crankshaft,

$T_p$  = torque due to gas pressure,

$T_m$  = torque due to reciprocating mass,

$T_f$  = torque due to friction load and pumping, and

$T_L$  = load torque through drivetrain.

Furthermore, the composite torque can be calculated through state-space deconvolution if the impulse response of the system is known. The angular velocity is related to the composite torque by (Connolly, 1994)

$$\Omega(\theta) = \int_{-\infty}^{\theta} T_c(\gamma) h(\theta - \gamma) d\gamma \quad (8.2)$$

where  $h(\theta)$  represents the impulse response of the system in the crank angle domain. When deconvolution is performed in the frequency domain, it becomes an algebraic operation, and the relationship between angular velocity and composite torque may be expressed by

(8.3)

where  $T_c(\lambda_f)$ ,  $\Omega(\lambda_f)$ , and  $H^{-1}(\lambda_f)$  are the Fourier Transforms of the composite torque, angular velocity signal, and impulse response at the frequencies  $n\lambda_f$ , (or the harmonics of the firing frequency,  $\lambda_f$ ). The reciprocating components also contribute energy to the harmonics of the firing frequency, and their contribution can be subtracted from the Fourier Transform of the composite torque to produce an indicated torque spectrum

(8.4)

where  $T_r(\lambda_f)$  is the Fourier Transform of the torque due to the reciprocating mass at the engine firing frequencies. The torque due to reciprocating mass is entirely defined by engine geometry and speed, hence it can be pre-computed for various engine speeds. The contribution of the load and friction torque is neglected since they are assumed to be insignificant at the frequencies of interest. The advantage of the method outlined is that in the  $\lambda$  domain, the engine firing frequency is constant for a given engine regardless of engine speed (Connolly, 1994). The corresponding time-based frequencies are not. Furthermore, due to the periodic nature of engine combustion, harmonics of the firing frequency provide a better signal-to-noise ratio (Lee and Rizzoni, 1995).

From equation (8.4), the resulting indicated torque waveform ( $T_i(\lambda)$ ) represents the fluctuating torque component of the measured signal. This component is then used with various metrics to identify misfire. Rizzoni (1989) calculates a torque vector for each engine cycle (one vector component for each cylinder). The torque vector components are defined as the rms value of the fluctuating torque in the harmonics deemed to be significant. These values are compared to the mean torque in order to identify a misfire. Connolly and Rizzoni (1994) calculate an rms torque value for each cylinder in a cycle based on the energy contained in the first 3 harmonics of firing frequency, and develop probability density functions to define misfires.

Lee and Rizzoni (1995) examine several different metrics for identifying misfire from the indicated torque waveform of equation (8.4). The first metric was a torque non-uniformity metric (TNM) and was based on the rms torque of each cylinder (incorporating an unspecified number of harmonics). The rms torque was subtracted from the mean torque to compute the TNM. The energy from torque non-uniformity (ETN) was based on the indicated torque waveform for an entire engine cycle. This had the effect of providing more data points for the Fourier Transform, with the result that the components of the torque signal below firing frequency could be analysed. Since the energy contained in the sub-harmonics

would theoretically be zero for identical cylinder combustion, a high level of energy at these frequencies would indicate a misfire. They also calculated a velocity non-uniformity metric (VNM) and an energy from velocity non-uniformity metric (EVN). These metrics were deduced from the measured velocity signal directly, and were then computed in the same manner as the TNM and ETN metrics. The advantage here is in bypassing the requirement for a model and any inherent inaccuracies therein. Their results indicated that the energy based metrics (ETN and EVN) provided better indications of misfire than the non-uniformity metrics (TNM and VNM). The disadvantage with the energy metrics, although not stated in the paper, is that by analysing the data over an engine cycle, one can only determine that a misfire occurred but cannot establish which cylinder in the cycle actually misfired.

### 8.2.6 Summary

This review has highlighted the significant features in work on detecting misfires via flywheel angular velocity fluctuations. The primary difficulties with this method are the assumptions of a rigid crankshaft and constant load torque. Thus, the hypothesis in this chapter is that measurements of the angular acceleration of the engine block could be used in a manner similar to the methods reviewed here in order to detect misfires. It is assumed that the engine block can be more realistically considered to be rigid. Also, the load torque from the opposite end of the drivetrain should have little effect on the response of the block at the frequencies of interest. Hence, it is hoped this method will overcome some of the disadvantages associated with crankshaft-based analysis.

The examination is presented in two stages. First, a model of the engine block is developed to include the requisite torque components and the stiffness and damping of the engine mounts. From this model, a torque waveform is calculated and compared to the torque produced by the cylinder gas pressure. Next, the torque and acceleration signals are analysed in the spatial frequency domain. Metrics are developed from the information contained in the frequency analysis, and are then used to detect misfires. Finally, conclusions regarding the feasibility of the method in question will be discussed.

### 8.3 System model

The engine block was assumed to be rigid, and as a result was modelled as a single degree of freedom, damped torsional oscillator. A schematic of the engine model and axis system used is shown in Figure 8.1.

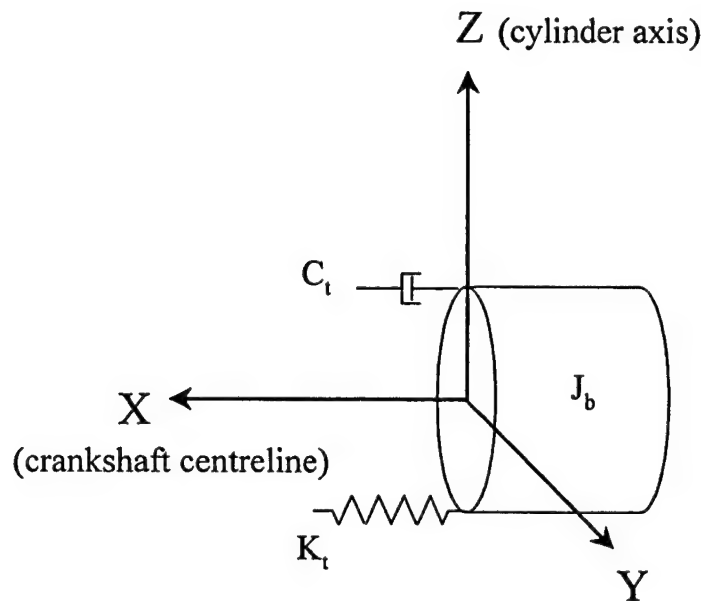


Figure 8.1. Single degree of freedom model.

The torsional stiffness and damping were provided by the engine mounts, and estimation of their properties will be discussed in the next section. Under these assumptions, the equation of motion for the engine block is

$$J_b \alpha_b + C_t \omega_b + K_t \theta_b = T_c(\theta) \quad (8.5)$$

where  $T_c$  is the composite torque applied to the block, and  $\alpha_b$ ,  $\omega_b$ , and  $\theta_b$  are the angular acceleration, velocity, and displacement of the engine block respectively. It must also be noted that there are two angular measurements involved in the model, namely crankshaft rotation and engine block rotation. The two measurements are distinguished by the subscript "b" which denotes rotation of the engine block. One would expect that the torque applied to the engine frame would be equal and opposite to that applied to the crankshaft. However, this

is not the case for two reasons. First, the engine frame is coupled to the crankshaft by gas pressure and piston friction (assuming frictionless bearings). Hence, the torque applied to the engine frame is not a function of the load applied at the other end of the drivetrain. For example, assume an engine existed which had massless pistons and conrods, and was operated with the spark plugs removed (no cylinder pressure). If this engine were being motored on a dynamometer, the only torque applied to the frame would be the (assumed) constant torque due to friction. Changing the load at the far end of the crank would cause the crank speed to change, but would not generate any motion of the engine frame. The second reason is that the angular momentum of the conrod changes as the crank turns, and this induces a different torque on the crank than it does on the frame (See Appendix F). The composite torque acting on the engine frame thus becomes

$$T_c(\theta) = -T_p(\theta) - T_m(\theta) - T_f(\theta) + T'_m(\theta) \quad (8.6)$$

where

$T_p(\theta)$  = torque due to gas pressure,

$T_m(\theta)$  = torque due to reciprocating mass,

$T_f(\theta)$  = torque due to friction load and pumping, and

$T'_m(\theta)$  = correction to torque due to angular motion of the conrod.

Each of these terms are calculated as a function of *crankshaft* position. The derivation of each term in equation (8.6) is extensively covered by Taylor (1985). The details of this derivation are contained in Appendix F, and only the final expressions will be given here. The terms on the right hand side of equation (8.6) are given by

$$T_p(\theta) = P_{cyl} A_p \frac{\dot{Z}(\theta)}{\Omega} \quad (8.7)$$

$$T_m(\theta) = -M_p \ddot{Z}(\theta) \left( \frac{\dot{Z}(\theta)}{\Omega} \right) \quad (8.8)$$

$$T_f(\theta) = \frac{\text{FMEP} * V_d}{4\pi} \quad (8.9)$$

$$T'_m(\theta) = (J_{cr} - M_{cr} r_1 r_2) \Omega^2 \sum_{n=1}^{\infty} S_n \sin 2n\theta \quad (8.10)$$

where

$P_{cyl}$  = measured cylinder pressure (N/m<sup>2</sup>),

$A_p$  = piston area (m<sup>2</sup>),

$\Omega$  = engine angular velocity (rad/sec),

$\dot{Z}(\theta), \ddot{Z}(\theta)$  = instantaneous piston velocity and acceleration (m/sec, m/sec<sup>2</sup>),

FMEP = friction mean effective pressure (N/m<sup>2</sup>),

$V_d$  = engine displacement (m<sup>3</sup>),

$J_{cr}$  = moment of inertia of the conrod about its c.g. (kg-m<sup>2</sup>),

$M_{cr}$  = mass of the conrod (kg),

$r_1, r_2$  = distances from conrod c.g. to centres of big and little ends (m), and

$S_n$  = Fourier coefficients.

By combining equations (8.5) and (8.6), the torque due to gas pressure can be calculated by

$$-T_p(\theta) = J_b \alpha_b + C_t \omega_b + K_t \theta_b + T_m(\theta) + T_f(\theta) - T'_m(\theta). \quad (8.11)$$

The inertial properties of the engine were known, and the angular acceleration was measured. The angular velocity and displacement of the block were calculated by integrating the angular acceleration signal. The constants of integration were determined by assuming that the mean angular velocity and displacement must be zero over an engine cycle since the block did not wind up. The stiffness and damping coefficients were determined experimentally as described in the next section. Thus, the only "unknown" term in equation (8.11) was the torque due to gas pressure. However, the #4 cylinder contained a piezoelectric pressure transducer. Hence the torque due to gas pressure could be calculated for that cylinder. If all cylinders were assumed to have the same pressure-time histories, a composite gas pressure torque curve could be constructed to compare with the torque estimated by the angular acceleration measurements. Results of this comparison will be given later.



#### 8.4 Experimental apparatus

The experimental work for this chapter was performed on a Rover K series 4-cylinder petrol engine. The engine characteristics, including the mass properties, are shown in Table 8.1.

**Table 8.1. Rover K16 specifications**

Bore (mm)	75
Stroke (mm)	79
Displacement (litres)	1.4
Firing order	1, 3, 4, 2
Mass (kg)	100
$I_x^1$ (kg-m <sup>2</sup> )	4.75
Conrod length (mm)	121.3
$I_{cr}^2$ (kg-m <sup>2</sup> )	0.477
$r_1^3$ (mm)	29.0
$r_2^4$ (mm)	92.3
Piston mass <sup>5</sup>	.373
Reciprocating mass <sup>6</sup>	.487

Notes:

1. Moment of inertia of the block about crankshaft centreline (see Figure 8.1).
2. Moment of inertia of conrod about centre of gravity.
3. Distance from centre of big end to centre of gravity of conrod.
4. Distance from centre of little end to centre of gravity of conrod.
5. Piston mass includes mass of gudgeon pin.
6. Reciprocating mass assumes portion of conrod mass moves with piston (see Appendix F for derivation).

The K16 was instrumented with a Kistler type 6123 piezo-electric pressure transducer in the #4 cylinder connected to a Kistler 5007 charge amplifier. Two Bruel and Kjaer type 4382 piezo-electric accelerometers were mounted to the engine back plate as shown in Figure 8.2,

with a spacing between accelerometers of 355 mm. The accelerometers were also connected to Kistler type 5001 charge amplifiers.

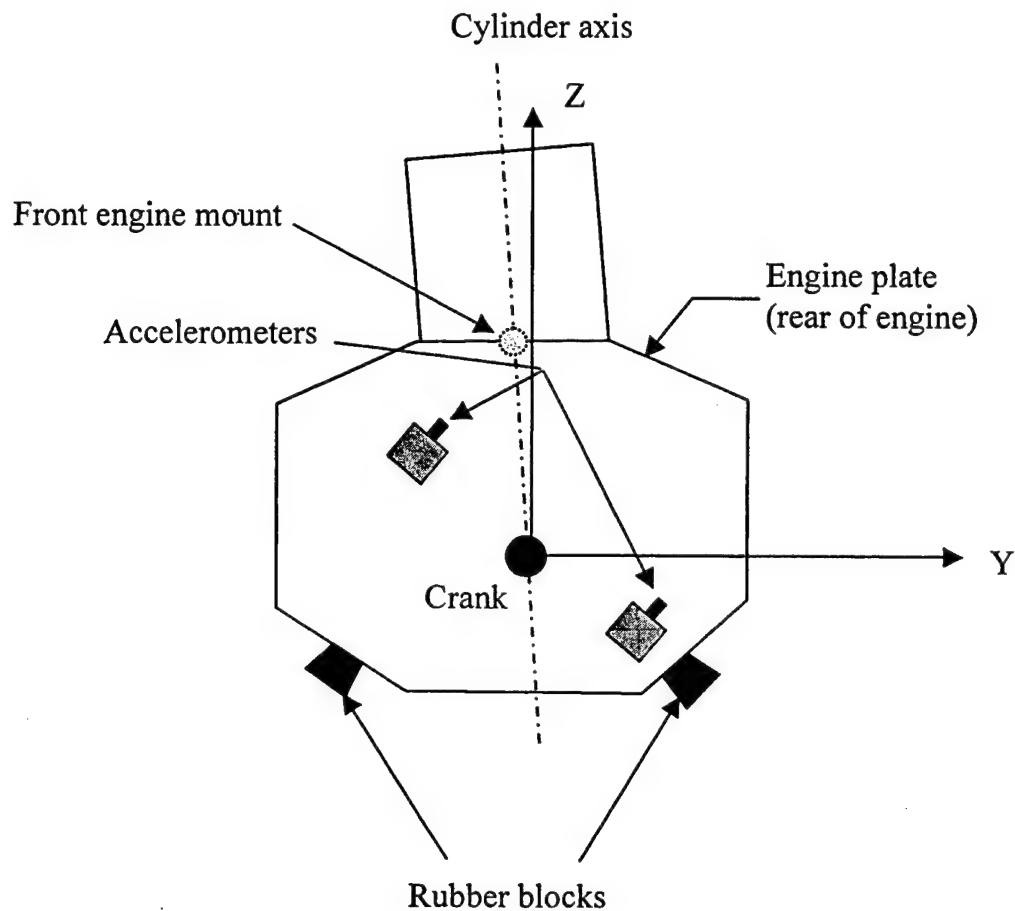


**Figure 8.2. K16 engine mounts and accelerometer location.**

The signals from the pressure transducer, accelerometers, and shaft encoder (TDC marker) were collected on the ComputerScope data acquisition system as described in Chapter 3. The accelerometer signals were calibrated in units of  $\text{m/sec}^2$ , and the two signals were subtracted to remove any translational displacement component. The difference between the accelerometer signals was divided by the distance between the two accelerometers to calculate the angular acceleration of the block.

The engine mount stiffness was estimated by applying a couple of known magnitude to the engine frame (via weights and a spring scale) and measuring the angular displacement with a clinometer as shown in Figure 8.3. The results of this experiment are shown in Table 8.2.

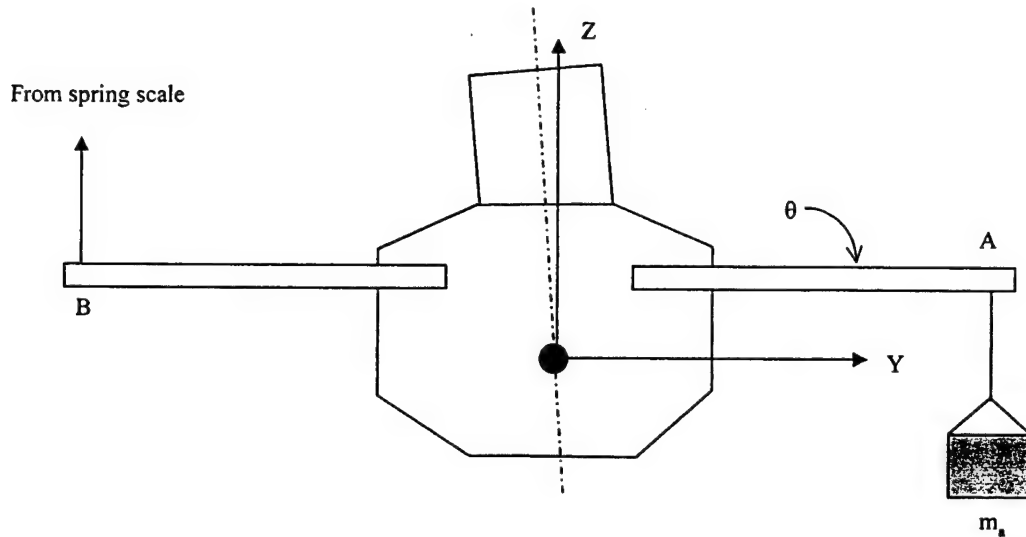


Figure 8.3. Experimental apparatus used to calculate mount stiffness.

Table 8.2. Engine mount stiffness measurements.

$m_A$ (kg)	$F_A$ (N)	$F_B$ (N)	$\Delta T$ (N-m)	$\Delta \theta$ (minutes)
0.0	0.0	0.0	0.0	0.0
2.5	24.52	24.52	49.4	11
5.0	49.03	49.03	49.4	9
7.5	73.55	73.55	49.4	10
10.0	98.07	98.07	49.4	8
7.5	73.55	73.55	49.4	10
5.0	49.03	49.03	49.4	7
2.5	24.52	24.52	49.4	9
0.0	0.0	0.0	49.4	11
Average			49.4	9.4

The results of this experiment yielded an average torsional stiffness of 18,100 N-m/rad for the engine mounts. The damping coefficient was estimated by subjecting the engine frame to an impulse and recording the angular acceleration, the results of which are shown in Figure 8.4.

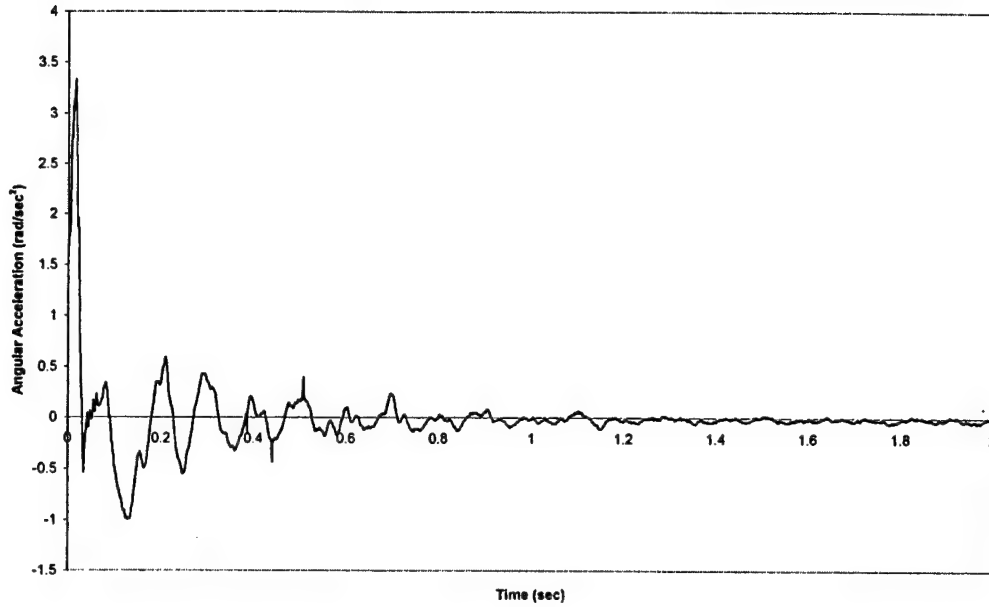


Figure 8.4. Impulse response of engine block.

The logarithmic decrement method of estimating the damping ratio is outlined in Thomson (1988). The analysis produced a damping ratio of  $\zeta = 0.170$ , and a torsional damping coefficient of  $C_t = 99.7 \text{ kg-m}^2/\text{sec}$ .

As a check on the calculated engine mount properties, a Discrete Fourier Transform (DFT) was performed on the impulse response shown in Figure 8.4. Furthermore, since the engine was modelled as a single degree of freedom oscillator, the non-dimensional magnitude of the impulse response in the frequency domain can be calculated by (Thomson, 1988)

$$|H(f)| = \frac{1}{\sqrt{\left(1 - \left(\frac{f}{f_n}\right)^2\right)^2 + \left(2\zeta\left(\frac{f}{f_n}\right)\right)^2}} \quad (8.12)$$

where  $f_n$  is the undamped natural frequency of the oscillator, and is given by

$$f_n = \frac{1}{2\pi} \sqrt{\frac{K_t}{J_b}} \quad (8.13)$$

The frequency response calculated by equation (8.12) is compared to the experimental frequency response in Figure 8.5.

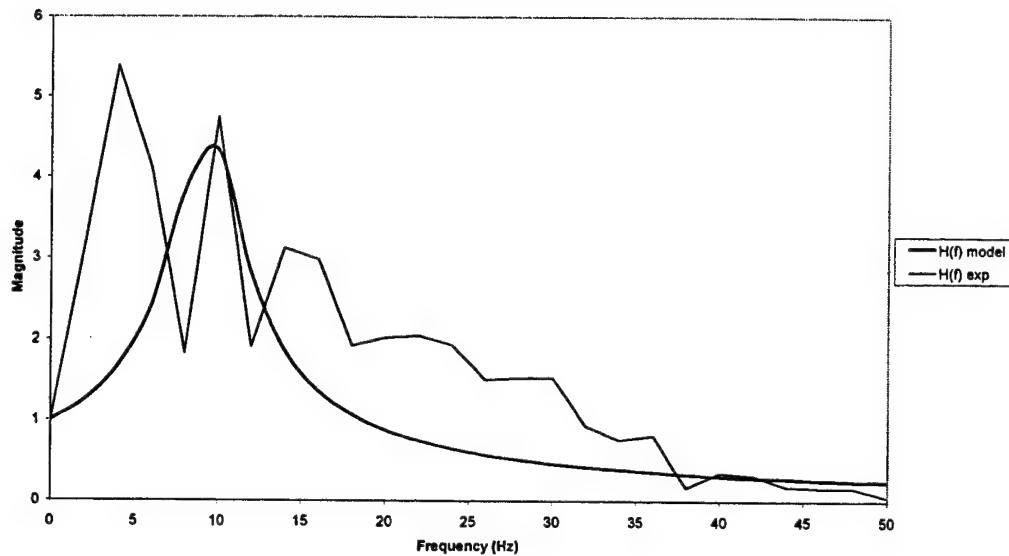


**Figure 8.5. Comparison of experimental frequency response to model frequency response.**

Several points must be brought out from Figure 8.5. First, the calculated stiffness properties predict a resonant torsional frequency of 9.83 Hz. This matches well with the experimental frequency response which shows a resonance peak at 10 Hz. However, the experiment also shows a resonance peak at 4 Hz. It is postulated that this resonance is due to a coupling between the torsional motion of the engine and the “pitching” motion (rotation about the Y axis). There are two qualitative arguments for this. First, as the engine is run up on the dynamometer, a large resonance is experienced passing 240 RPM (a rotational frequency of 4 Hz). If the engine speed is held at 240 Hz, the engine can be seen to be visibly rocking about the Y axis. Second, during the measurements of torsional stiffness, it was noted that at very large values of applied torque, the engine rotation was not purely about the X axis. As the torque was applied purely in the Y-Z plane, the off-axis rotation (again about the Y axis) can be attributed to the location of the engine mounts. If the mounts were located in such a way that the suspension forces produced by them acted through the engine centre of gravity, and the suspension couples produced by them acted about the principal axes of the engine, then the system would be decoupled (Taylor, 1985). This means that a force applied along an engine axis would only induce motion along that axis. Likewise, any torque applied around an axis would excite motion only about that axis. The current mounts on the K16 do not act through the c.g. or about any principal axis. What this implies is that the “rolling” and



### 8.5 Experimental results – torque estimation

The model described in Section 8.3 and Appendix F was used to calculate the torque produced by the cylinders. Since only cylinder #4 had a pressure transducer, it was assumed that the other three cylinders had identical pressure histories to cylinder #4. This allowed a composite torque to be calculated from the gas pressure measurements, and was then used as a basis of comparison for the modelled torque. Data was collected for 360 consecutive cycles at the operating conditions shown in Table 8.3.

**Table 8.3. Experimental operating points for Rover K16 engine.**

Case ID	Mot1	W1010	P1020	Mot2	25115	25130
Engine speed (RPM)	1200	1200	1200	2500	2500	2500
BMEP (bar)	-1.36	8.53	5.74	-1.75	9.76	4.85
$\lambda$	N/A	1.0	1.0	N/A	1.0	1.0
Ignition timing (deg BTDC)	N/A	10	20	N/A	15	30

Two short sets of data (44 consecutive cycles) were taken whilst motoring the engine at each speed (Mot1 and Mot2) in order to investigate the assumption that drivetrain load did not effect the angular acceleration of the block. All firing tests were performed with gasoline as the fuel. The results are presented in the following figures, one figure for each engine speed. The figures show the engine torque as calculated by the angular acceleration model (denoted “Block measurements”) as a dotted line, and the engine torque calculated from the pressure measurements from cylinder #4 (denoted “Gas pressure”) as a heavy line. The composite gas torque curves were generated by assuming that the pressures in all cylinders were identical. Hence, the pressure in cylinder #4 was phased appropriately to calculate the torque produced by each cylinder.

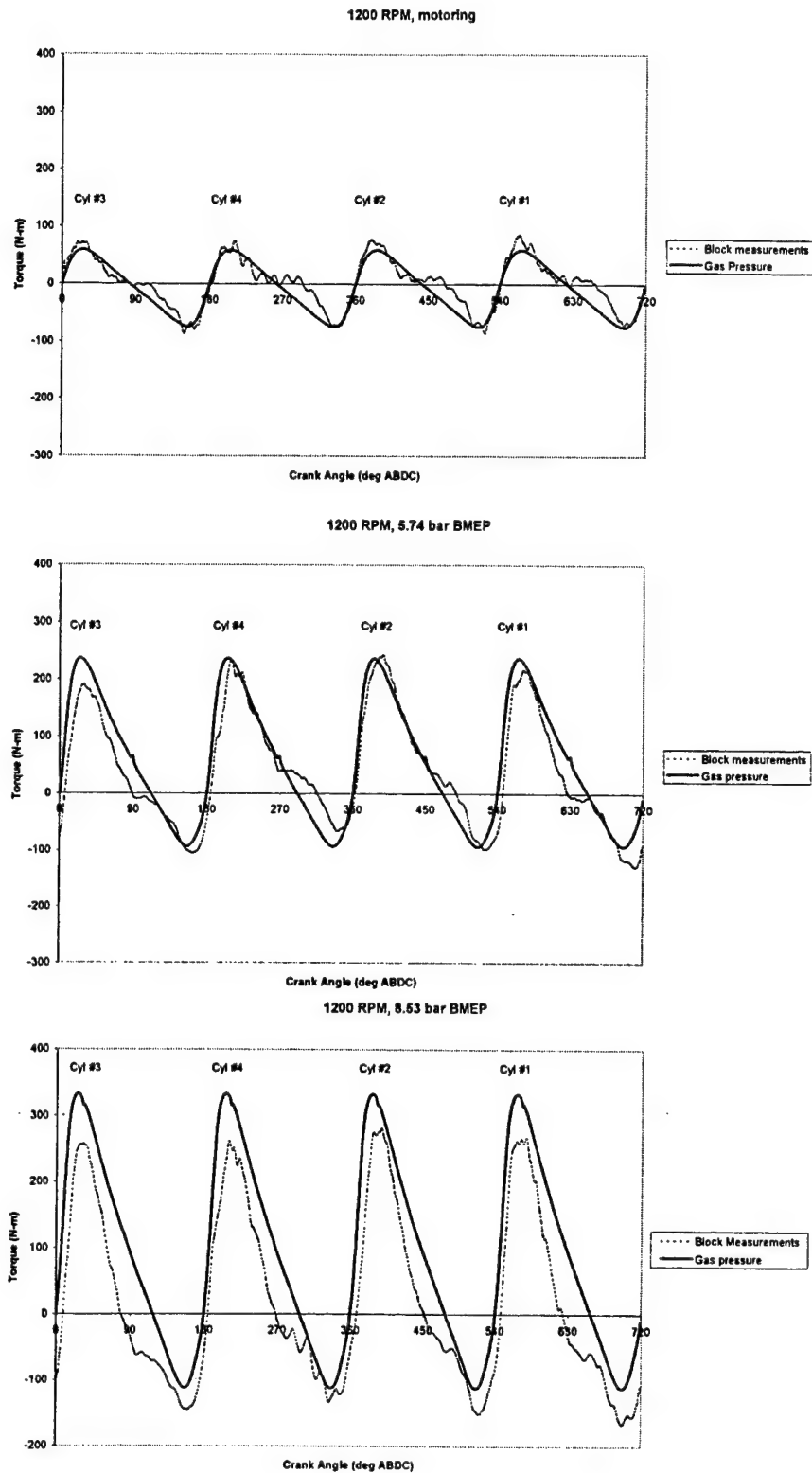
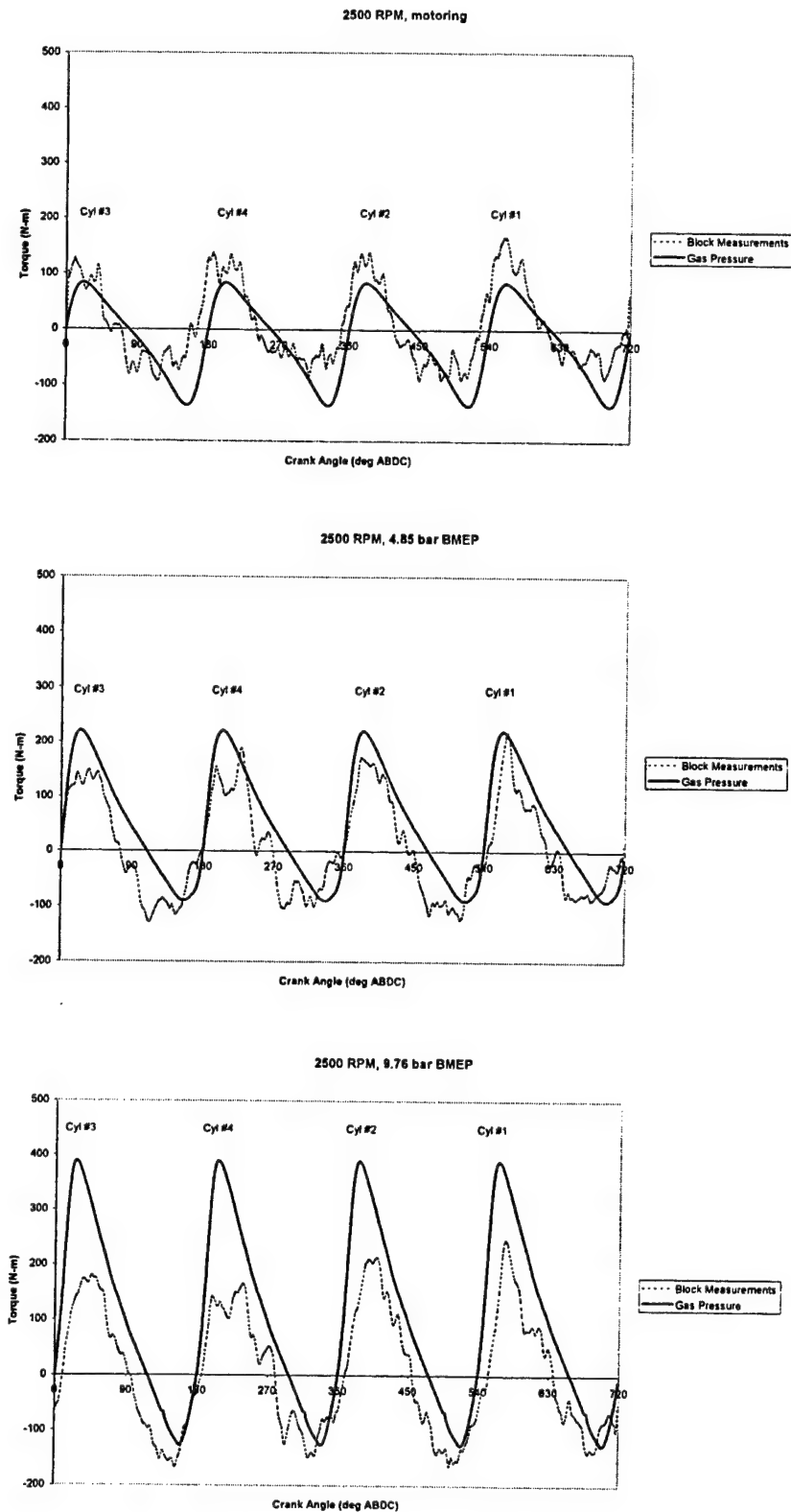


Figure 8.7. Comparison of torque calculated from angular acceleration of engine block to torque calculated from cylinder pressure measurements, 1200 RPM.



Figure 8.7 indicates that at this engine speed (1200 RPM), the model does a reasonable job of estimating the cylinder torque. It should be noted that in the cases shown in Figure 8.7, the load at the opposite end of the drivetrain (as measured by the dynamometer) is significantly different for each case. Hence, the assumption that drivetrain load does not affect the angular acceleration of the block is validated. The model's accuracy suffers somewhat at the WOT condition, where there appears to be a slight DC offset. This is most likely due to the friction correlation used in the model. The correlation given by the Rover Advanced Power Train Group (RAPT) is a function of engine speed only (see Appendix F), and this technique is supported by several others (Barnes-Moss, 1975, Heywood, 1988). However, these correlations were derived from motored engines, and both the pumping and frictional losses tend to be under-estimated (Stone, 1992). This indicates that friction correlations which account for the pressure load may give better results in this model, and such correlations have been proposed by Chen and Flynn (1965) and Winterbone (1986).

Another possible explanation for the decreased accuracy is the coupling between the rolling and pitching motion of the engine. Since the engine is of an in-line configuration, the effective moment arm for each cylinder about the Y axis is different. It is expected that the pitching motion would be exacerbated at high load conditions (e.g., at wide open throttle), and the model is not able to account for this effect. The results for 2500 RPM are shown in Figure 8.8.



**Figure 8.8.** Comparison of torque calculated from angular acceleration of engine block to torque calculated from cylinder pressure measurements, 2500 RPM.

Again, the figure indicates that drivetrain load has no effect on the block acceleration. However, the model's accuracy is considerably less at this engine speed. Once again, the effect of the coupled rolling and pitching motion is seen at WOT. Furthermore, the accuracy is reduced even at part throttle operation. In this case, the cause is postulated to be the assumed inertial properties of the engine. The inertia of the engine varies during each rotation, but it is also a function of engine speed (Shiao and Moskwa, 1994). As a result, one would expect a model with constant inertial properties to perform better at low engine speeds, since normally the given inertial properties of an engine are calculated on a non-running engine. One would also expect that the effective moment of inertia at high engine speeds would be larger than that at low speeds. Thus, at high engine speeds, the inertial effects would be underestimated.

Another possible source of error is in the damping. It was assumed that the system contained viscous damping. However, rubber blocks do not in fact provide this type of damping. A better estimate may be given by assuming the mounts provide structural damping (Meirovitch, 1975). This type of damping is produced by the hysteresis effect shown by elastic materials undergoing cyclic loading. As such, it is roughly proportional to the square of the vibration amplitude, and is independent of frequency (Meirovitch, 1975). Overestimation of the damping would again lead to an underestimation of the torque.

Despite the limitations outlined, the current model will be examined as a means of misfire detection. The effective work done by the torque over one cycle is related to the mean effective pressure (MEP) by

$$\frac{4\pi T}{V_s} = \text{MEP} \quad (8.12)$$

This calculation can be performed over an entire engine cycle. However, this would not be of great value in detecting misfires. First, if only one misfire occurred during the cycle, the reduction in MEP would be very small since the other three cylinders would still be producing work (hence the value of multi-cylinder engines). Second, even if the reduction in MEP could be identified, it would only indicate a misfire had occurred, it would not identify the misfiring cylinder. However, the torque curve can be temporally divided in order to calculate the work done on the firing stroke of each individual cylinder (assuming non-overlapping firing intervals), and will be called the cylinder mean effective pressure (CMEP). Each cylinder's CMEP can be calculated and compared to the others within an engine cycle. If one of the cylinders had a low CMEP, it would be identified as the misfiring cylinder. Figure 8.9 shows a plot of CMEP for cylinder #4 versus the "IMEP" for that cylinder calculated over the

firing stroke. Since the IMEP is negative for a misfired cycle, it gives a good indication of the ability of the CMEP to identify misfires.

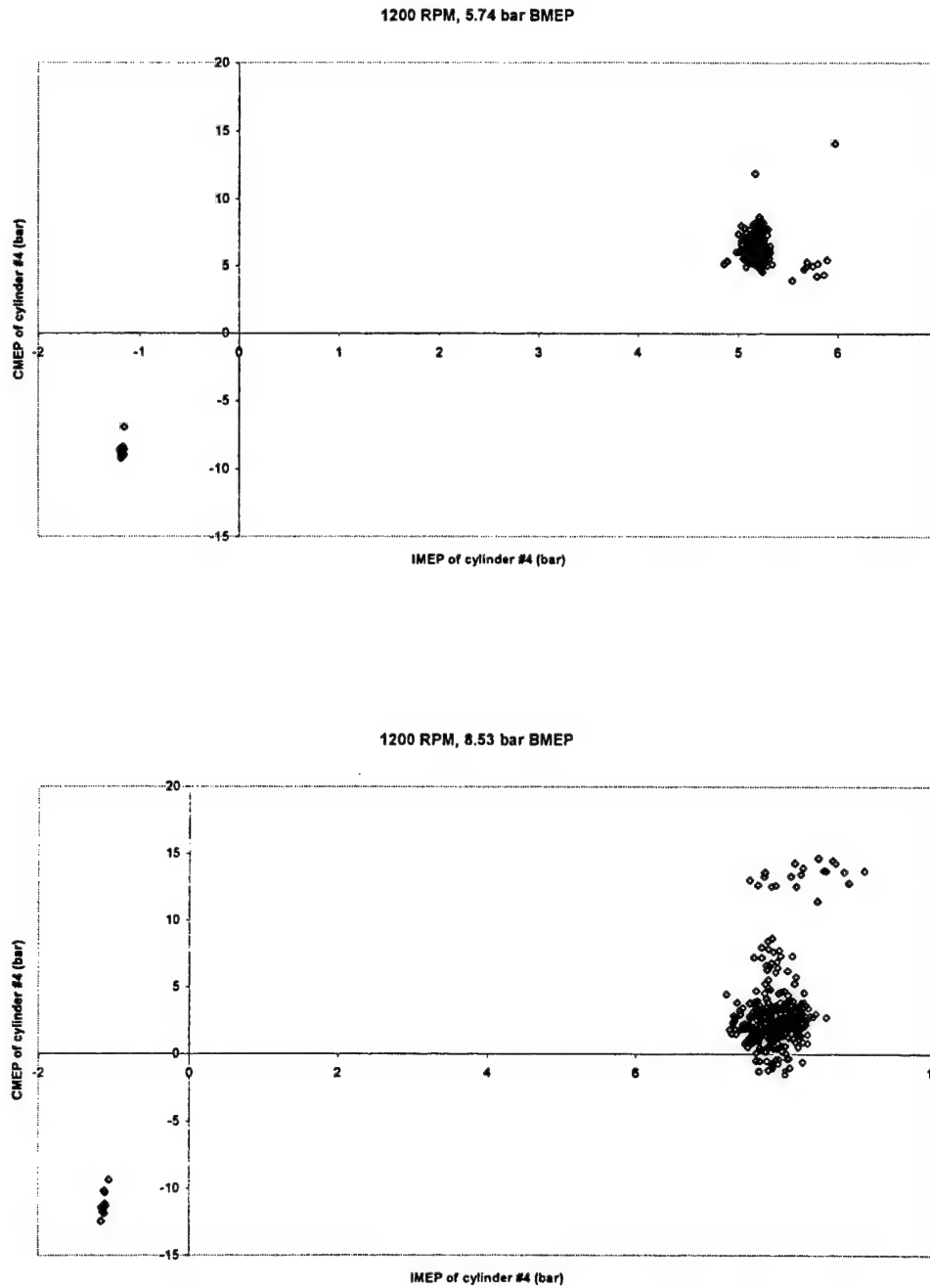


**Figure 8.9. CMEP versus IMEP for cylinder #4, 1200 RPM.**

Since the modelled torque curve at 1200 RPM was reasonable, one would expect good performance in misfire detection. The misfired cycles are clearly identified in Figure

8.9 by the fact that their IMEP is negative. The part load case in Figure 8.9 is ideal in that the CMEP is only negative for misfired cycles. Hence, in this case the misfires could be identified solely by cycles with a negative CMEP. In the WOT case, the misfired cycles could still be identified. However, the CEMP was negative for several cycles that had not actually misfired. This would require the use of some sort of threshold criteria to identify the misfired cycles, but the misfires could still be reliably detected. The cases at 2500 RPM are presented in Figure 8.10.

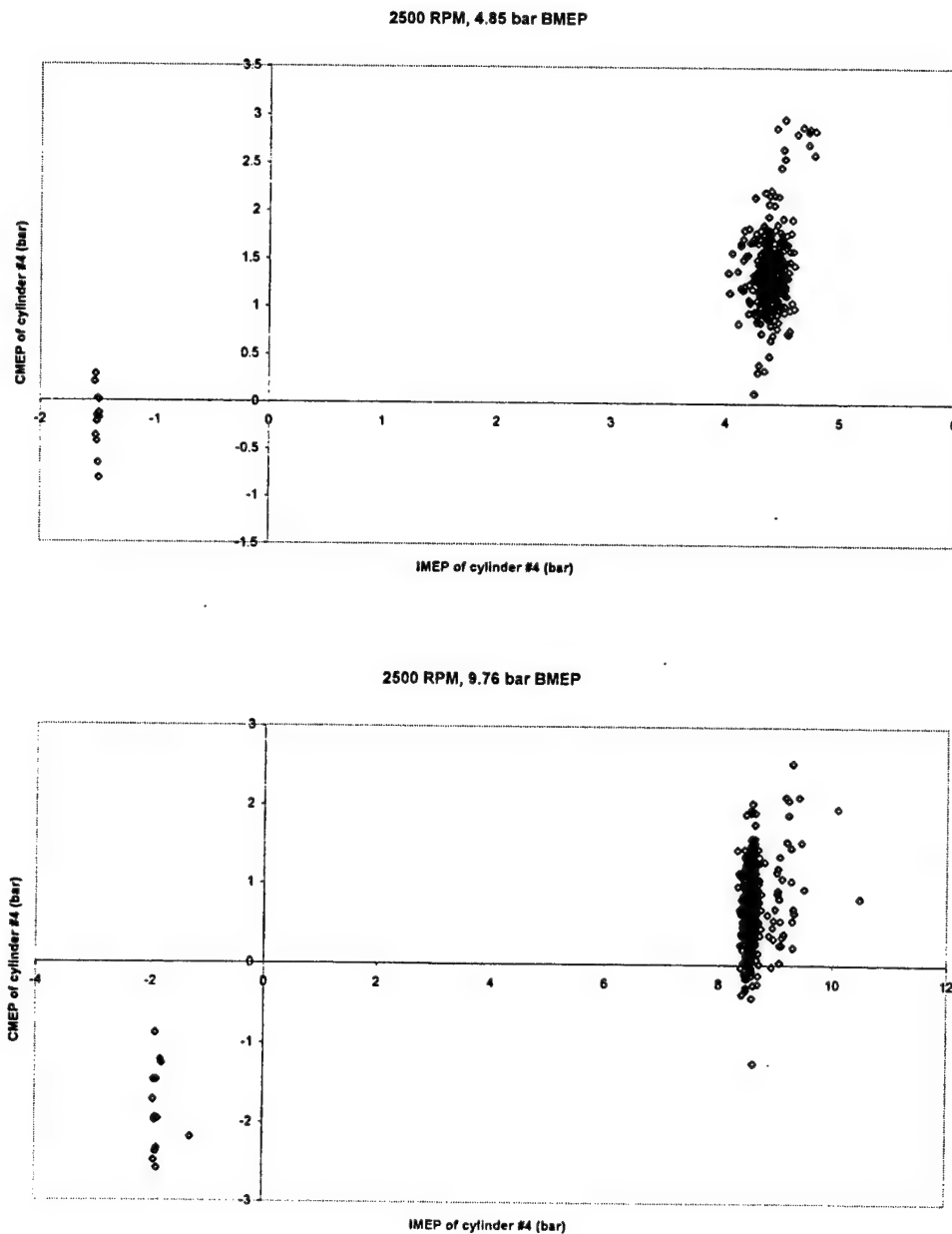


Figure 8.10. CMEP versus IMEP for cylinder #4, 2500 RPM.

Given the inaccuracies in the calculated torque at this engine speed, the model would not be expected to provide a good misfire metric at this speed. There is no clear threshold value which could be selected that would enable the metric to detect the misfires in either case presented in Figure 8.10. The sources of error in this model were discussed previously, and further work should be done to examine whether the suggested model improvements might increase the accuracy of misfire detection at high speeds.

Of course it is one matter to apply such a model to an engine sitting on a test bed, but quite another to apply it to an engine in an actual vehicle. The vehicle motion would significantly affect the angular acceleration measurements. Thus, the current metric (CMEP) might be of little value in a production vehicle. However, vehicle motion occurs at a frequency well below the firing frequency of the engine (ignoring for the moment any vibratory motion induced in the structure due to vehicular motion). Thus, the next portion of the work will attempt to analyse the calculated torque signal in the frequency domain, and to establish further metrics for misfire detection.

## 8.6 *Experimental results – frequency domain analysis*

The frequency analysis will proceed in a manner similar to that outlined by Connolly and Rizzoni (1994) and Lee and Rizzoni (1995). They have noted that frequency analysis of firing engine signals is best accomplished in the spatial frequency domain, where spatial frequency is defined as the Fourier Transform of the signal in the crankshaft angle domain. The advantage of this method is that in the crank-angle domain, the engine firing frequency (denoted  $\lambda_f$ ) is independent of engine speed. Specifically, the K16 fires four times per engine cycle (one engine cycle being two revolutions) regardless of engine speed. This allows the analysis to be based on harmonics and sub-harmonics of the firing frequency, which should lead to a better signal-to-noise ratio (Lee and Rizzoni, 1995).

The first step in the investigation was to perform Discrete Fourier Transforms (DFT's) on the experimental data. The results of the DFT's for the 1200 RPM, 5.74 bar BMEP case are presented in Figures 8.11 and 8.12. The DFT shown in Figure 8.11 was performed on blocks of data corresponding to one engine cycle, whilst the DFT of Figure 8.12 was performed on blocks of data corresponding to each cylinder's firing cycle. The former case provided a longer sample length and, since the sampling frequency was fixed at 180 samples/firing cycle, results in a finer frequency resolution on the plot. The DFT's in both figures were performed on cycles 18 and 19 of the data, cycle 19 being the first misfire in the data set.

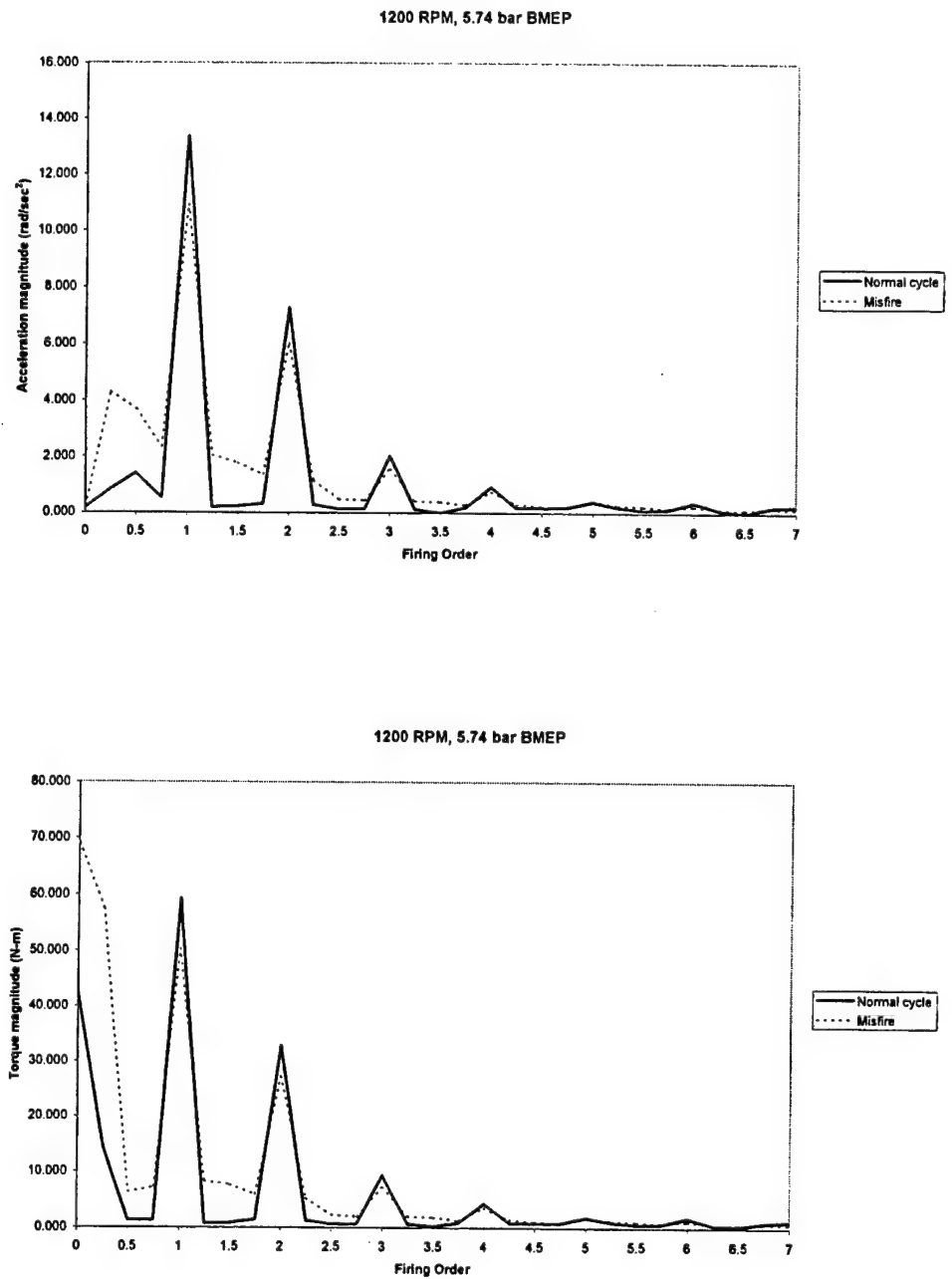


**Figure 8.11. DFT of acceleration and torque waveforms, computed over entire engine cycle and comparing normal cycle to misfired cycle.**

The DFT in the top portion of Figure 8.11 was performed on the measured angular acceleration signal, whilst the lower figure was performed on the torque curve modelled as outlined in Section 8.3. Both cases indicate that a misfire tends to excite low orders in the engine block/mount system. The torque results show a large DC offset due to the misfire.

This can be observed whilst the engine is running since a misfire causes the engine block to rotate significantly about its X axis. The engine then requires 2-3 cycles to return to its equilibrium position. The acceleration results do not show an increase in DC offset. This would imply that the misfire acts as an impulse load, and whilst it does excite lower orders of acceleration, its duration relative to the engine cycle is too short to affect the mean acceleration value. Figure 8.12 repeats the analysis of Figure 8.11, except that the DFT was performed over blocks of data corresponding to each cylinder's firing cycle (180 data points). The same cycles were analysed, and the results are for cylinder #4.

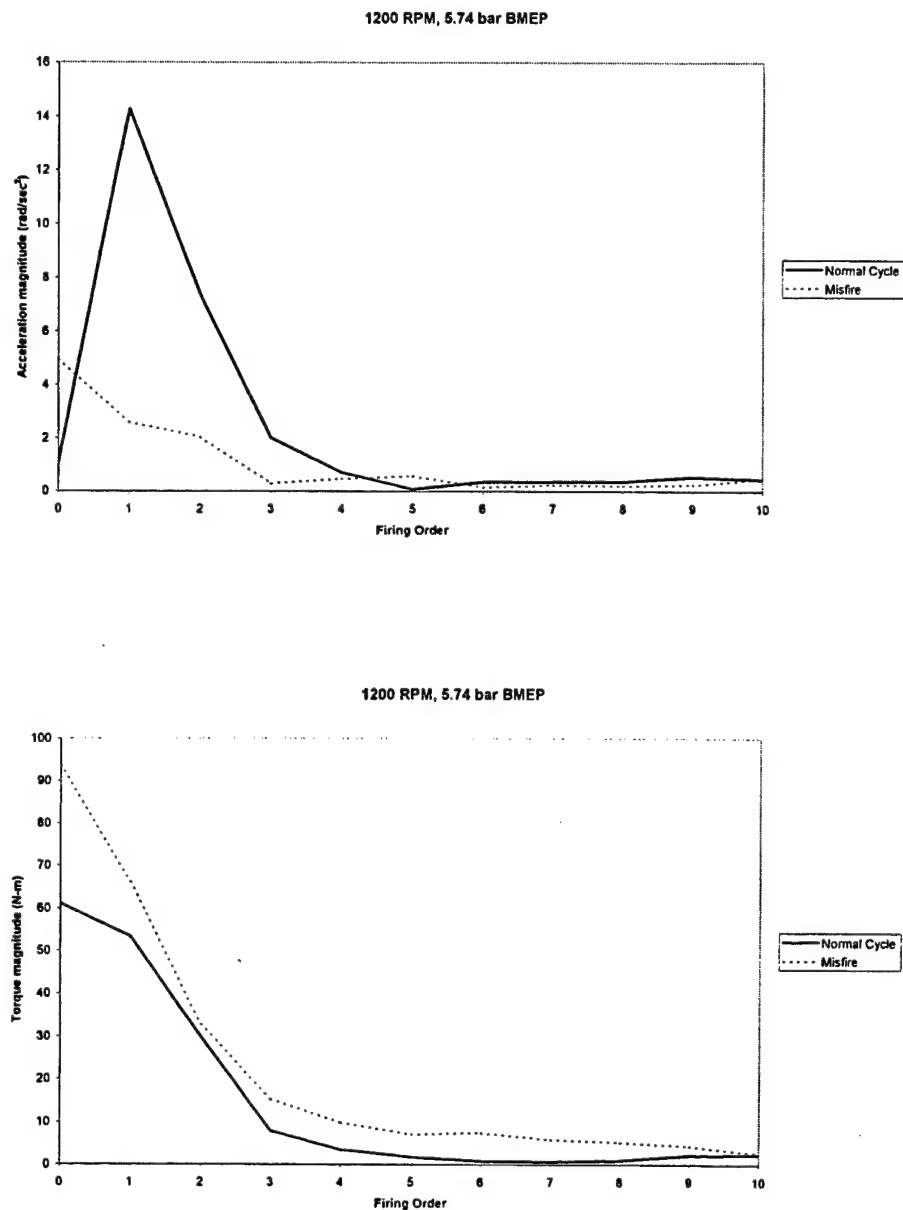


Figure 8.12. DFT of acceleration and torque waveforms, computed over firing cycle and comparing normal cycle to misfired cycle.



Figure 8.12 clearly illustrates the disadvantage of using a short sample length, namely, that some information is lost due to the decreased resolution of the frequency calculations. Nonetheless, there is still an increase in DC offset on the torque curve. There is also an increase in the DC offset on the acceleration curve. Again, it is postulated that this is due to the impulsive nature of the load imparted by the misfire. In the case presented in Figure 8.12, the DFT is performed over a shorter interval. Hence, the effect of the impulse is shown in the acceleration signal. This also has the effect of decreasing the magnitude in orders equal to and greater than the firing frequency.

Based on the aforementioned observations of the DFT results, four metrics of misfire detection were developed. The first two are based on the DFT's of each engine cycle. Theoretically, if combustion were uniform, the frequency content in the range below firing frequency would contribute no energy to the overall spectrum. Since the frequency resolution in this case allows a closer examination of the magnitudes of the lower engine orders, the metric will be the energy contained in the orders below the firing order. The metric will be calculated on both the acceleration and torque signals. Thus, the Low Frequency Torque Metric (LFTM) is defined as

$$\text{LFTM} = \sqrt{\sum_{n=1}^{N-1} |T(n\lambda_o)|^2} \quad (8.14)$$

where  $T(n\lambda_o)$  are the Fourier Transforms of the torque signal at frequencies below the firing order. Likewise, the Low Frequency Acceleration Metric (LFAM) is defined as

$$\text{LFAM} = \sqrt{\sum_{n=1}^{N-1} |A(n\lambda_o)|^2} \quad (8.15)$$

where  $A(n\lambda_o)$  are the Fourier Transforms of the angular acceleration signal at frequencies below the firing order. These metrics are plotted against the IMEP of cylinder #4 in Figures 8.13 and 8.14 for the low speed, low load case and the high speed, high load case. Results for the other two cases are presented in Appendix G.

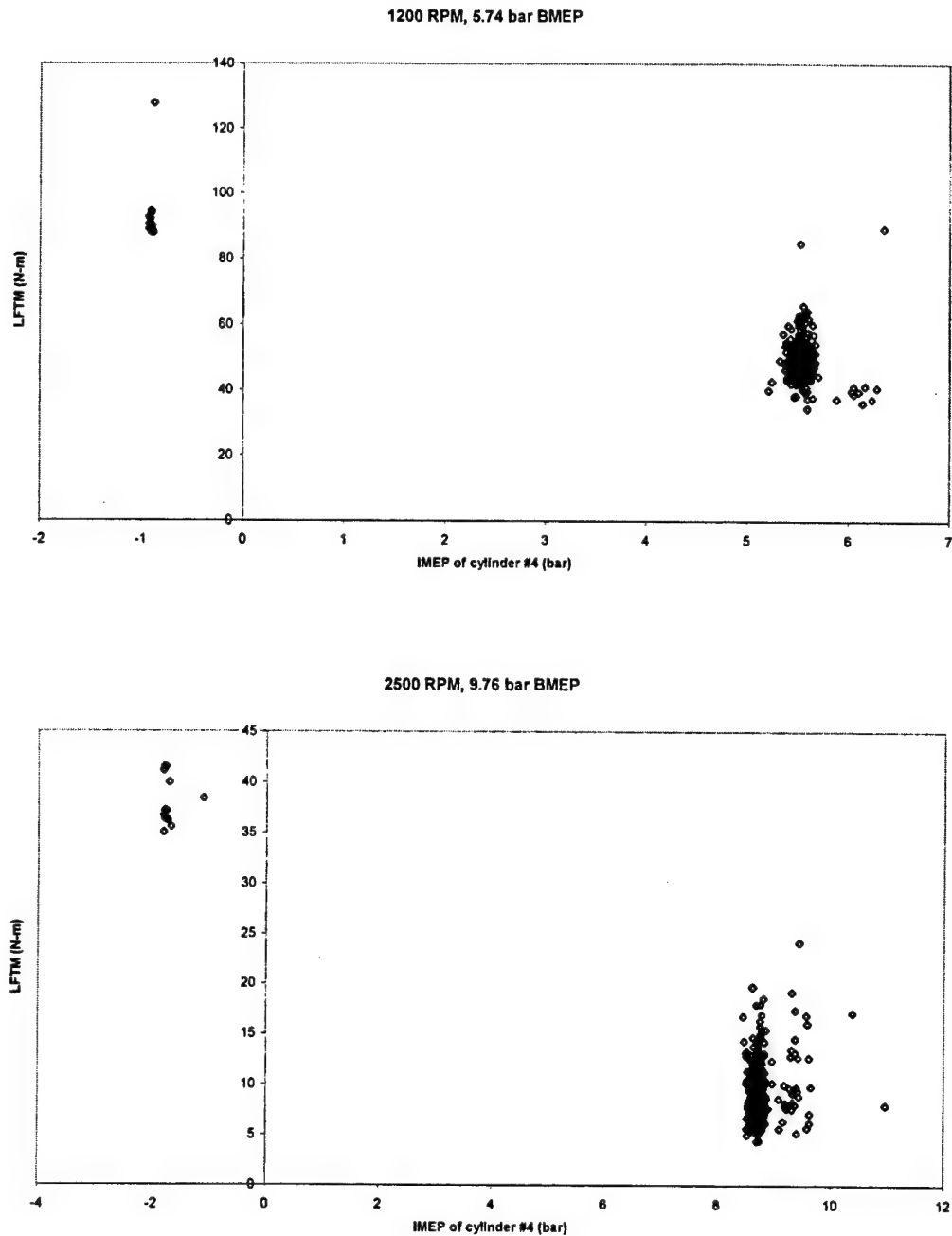


**Figure 8.13. Low Frequency Torque Metric versus IMEP of cylinder #4.**

Figure 8.13 indicates that the LFTM could be used to identify misfires, although the high speed, low load case shown in Appendix G would result in a number of misidentified misfires (i.e., cycles identified as misfires which are not). However, once again the technique would require a threshold value to be set for each speed and load combination. Also, since the metric was calculated over each engine cycle, it can only be used to indicate that a misfire

occurred on that cycle. It cannot distinguish which cylinder actually misfired. In the low speed, low load case presented in Figure 8.13, there are two points which stand out from the right hand cluster. These two points are from cycles 166 and 167. In this case, the misfire circuit induced a double misfire on cycles 164 and 165. Hence, these two points show that a double misfire induces a larger DC offset on the block, and it then requires more cycles for this offset to return to the equilibrium position. The figure for the low speed, low load case (see Appendix G) also shows a separate cluster of points which correspond to cycles which follow a misfire. This indicates that it takes longer for the engine block to regain its equilibrium position after a misfire when the load is high. Intuitively this makes sense since at high loads, a misfire causes a greater impulse to be applied to the block and mounts, with a corresponding greater deflection. Figure 8.14 shows the results for the LFAM.

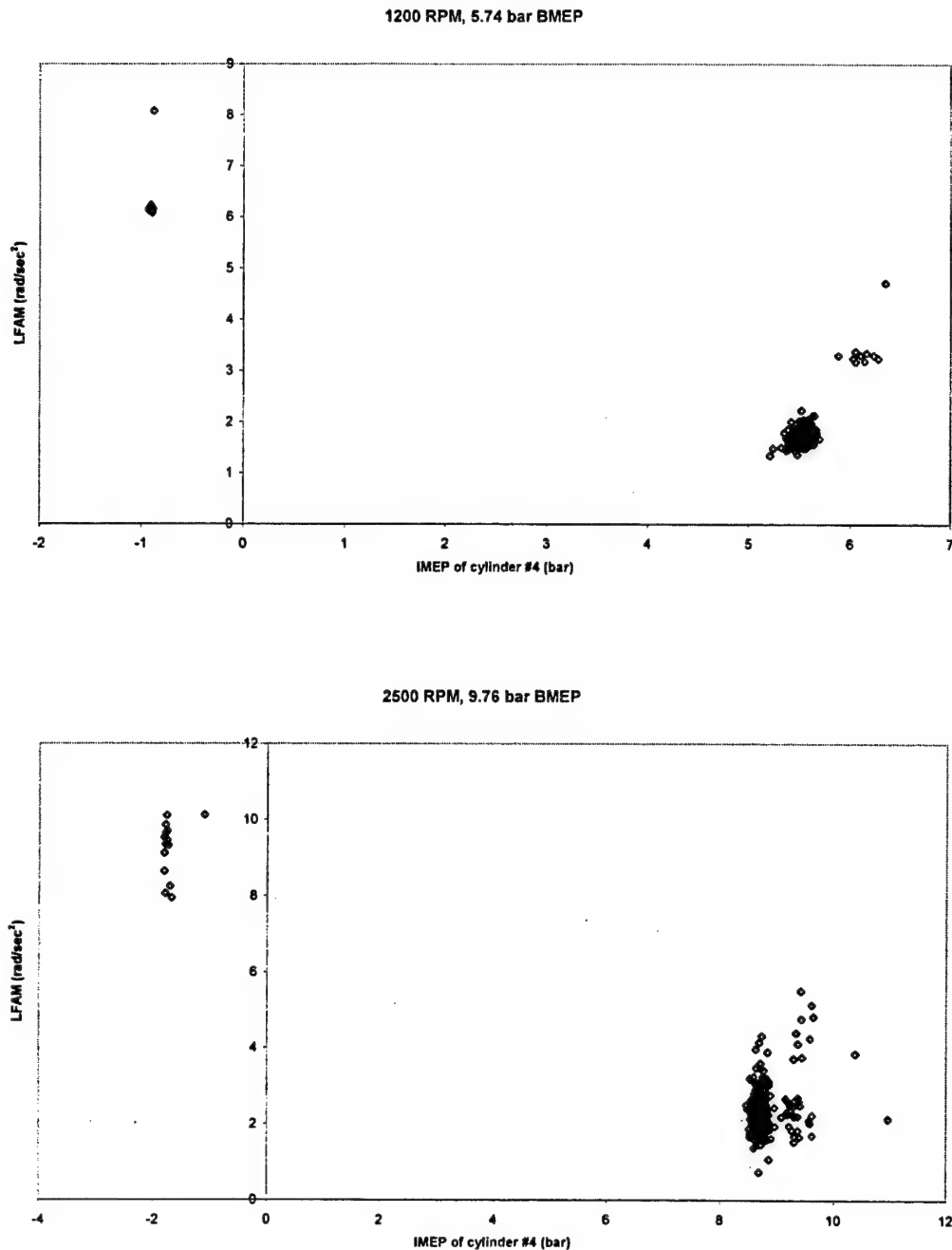


**Figure 8.14. Low Frequency Acceleration Metric versus IMEP of cylinder #4.**

Once again, this metric could be used to identify misfires if appropriate threshold values were pre-computed. The effects of the double misfire are again noted in Figure 8.14 in the low speed case, where there is a high value of the LFTM for the cycle following the double misfire. Also, Figure 2 of Appendix G shows the increased time required for the block to regain equilibrium after high load misfires.

The performance of the LFTM would tend to lead one to think the torque model used here was accurate at both high and low speeds. As explained in Section 8.5, there are significant inaccuracies in the model at high engine speeds. However, the LFTM is largely influenced by the DC offset induced in the engine block due to a misfire. Even though the model does not accurately model the torque at high engine speeds, it still predicts the increase in DC offset. Since the errors primarily dominate at higher frequencies, this metric is able to overcome some of the limitations of the model in predicting misfires.

Although the previous metrics indicate a possibility of success in identifying misfires, their primary disadvantage is that they require low frequency information. This presents severe problems for an engine mounted in a vehicle, since vehicle motion could be expected to fall into the low-frequency category (relative to firing frequency). Thus, two more metrics were defined based on higher firing orders, and used the results of the DFT's performed over the firing intervals for each cylinder. The metrics are estimates of the rms value of the individual cylinder torque and acceleration during one combustion period. Thus, the High Frequency Torque Metric (HFTM) is defined as

$$\text{HFTM} = \frac{1}{L} \sqrt{\sum_{n=1}^L |T(n\lambda_f)|^2} \quad (8.16)$$

where  $T(n\lambda_f)$  are the Fourier Transforms of the torque signal at harmonics of the firing frequency. For this analysis, the first three harmonics were used. Likewise, the High Frequency Acceleration Metric (HFAM) is defined as

$$\text{HFAM} = \frac{1}{L} \sqrt{\sum_{n=1}^L |A(n\lambda_f)|^2} \quad (8.17)$$

where  $A(n\lambda_f)$  are the Fourier Transforms of the angular acceleration signal at harmonics of the firing frequency. Results for the low speed, low load and high speed, high load cases are shown in Figures 8.15 and 8.16, the remaining cases are contained in Appendix G.

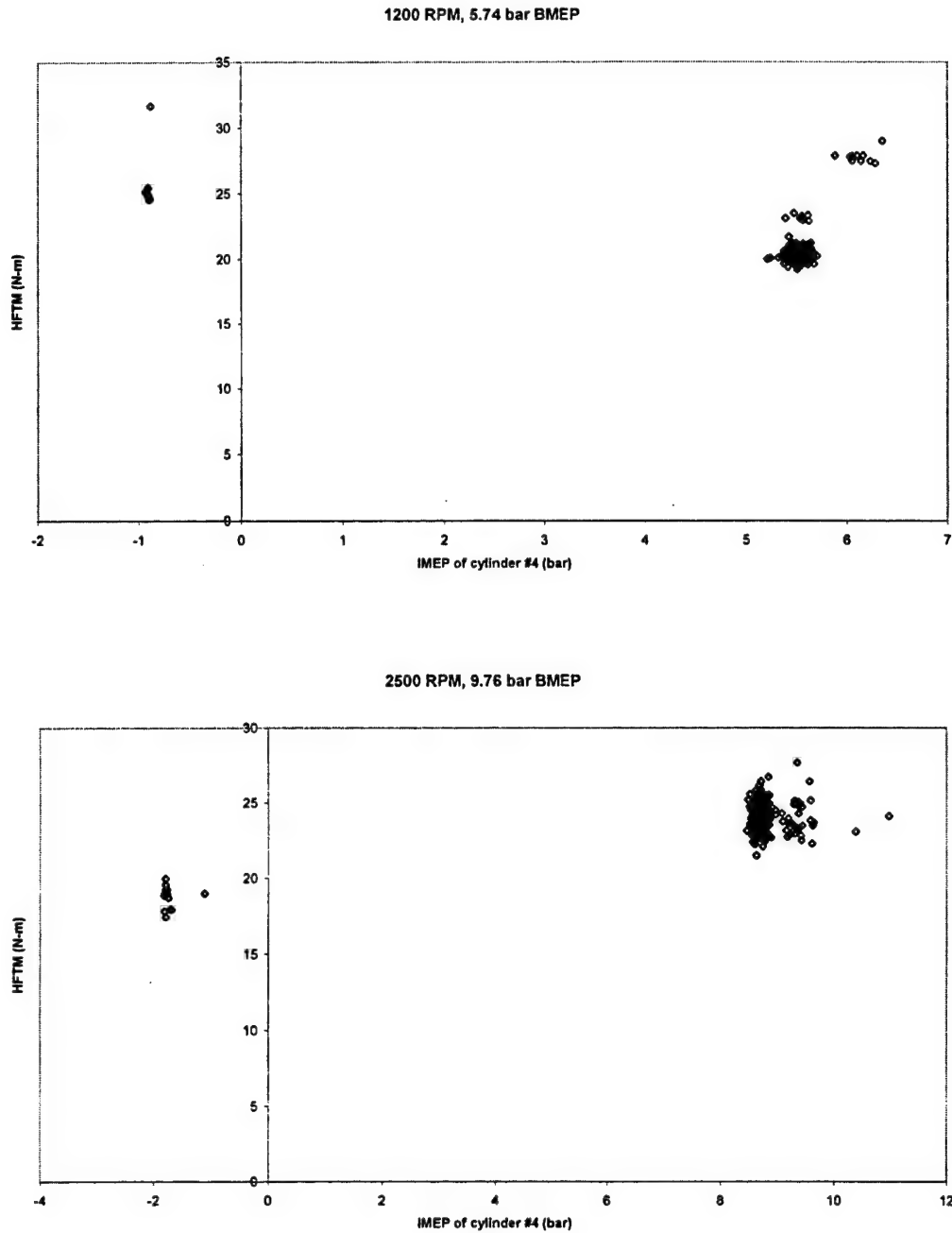


**Figure 8.15. High Frequency Torque Metric versus IMEP of cylinder #4.**

As might be expected after the discussion of the low frequency metrics, the HFTM would not be a reliable indicator of misfires. Some of the error in the HFTM is due to the previously discussed limitations of the model in calculating the torque. A further source of error is indicated by the work of Nakada and Tonosaki (1994). They investigated the vibrational characteristics of an in-line, 4-cylinder engine. They discovered that normal

torque fluctuations (induced by cycle-by-cycle variation in combustion and the mass of reciprocating components) excited torsional vibration of the block at all orders and half orders of the engine rotation speed. Particularly, the second and fourth orders of rotation speed were strongly excited. The second and fourth orders of engine rotation correspond to the first and second orders of firing frequency in a 4-cylinder engine. What this implies is that the assumption of a rigid block becomes less valid as engine speed increases. Thus, the rigid block assumption contains the same limitations as the rigid crankshaft assumption used by some of the work reviewed in Section 8.2. The limitations of assuming a rigid block are less apparent in the low frequency metrics due to the fact that misfires excite low orders very strongly. Hence, the errors associated with assuming a rigid block are overshadowed by the magnitude of the misfire-induced oscillations. Since the HFAM dispenses with the torque model altogether, it was hoped that it would be a more reliable indicator of misfire. The performance of the HFAM is shown in Figure 8.16.

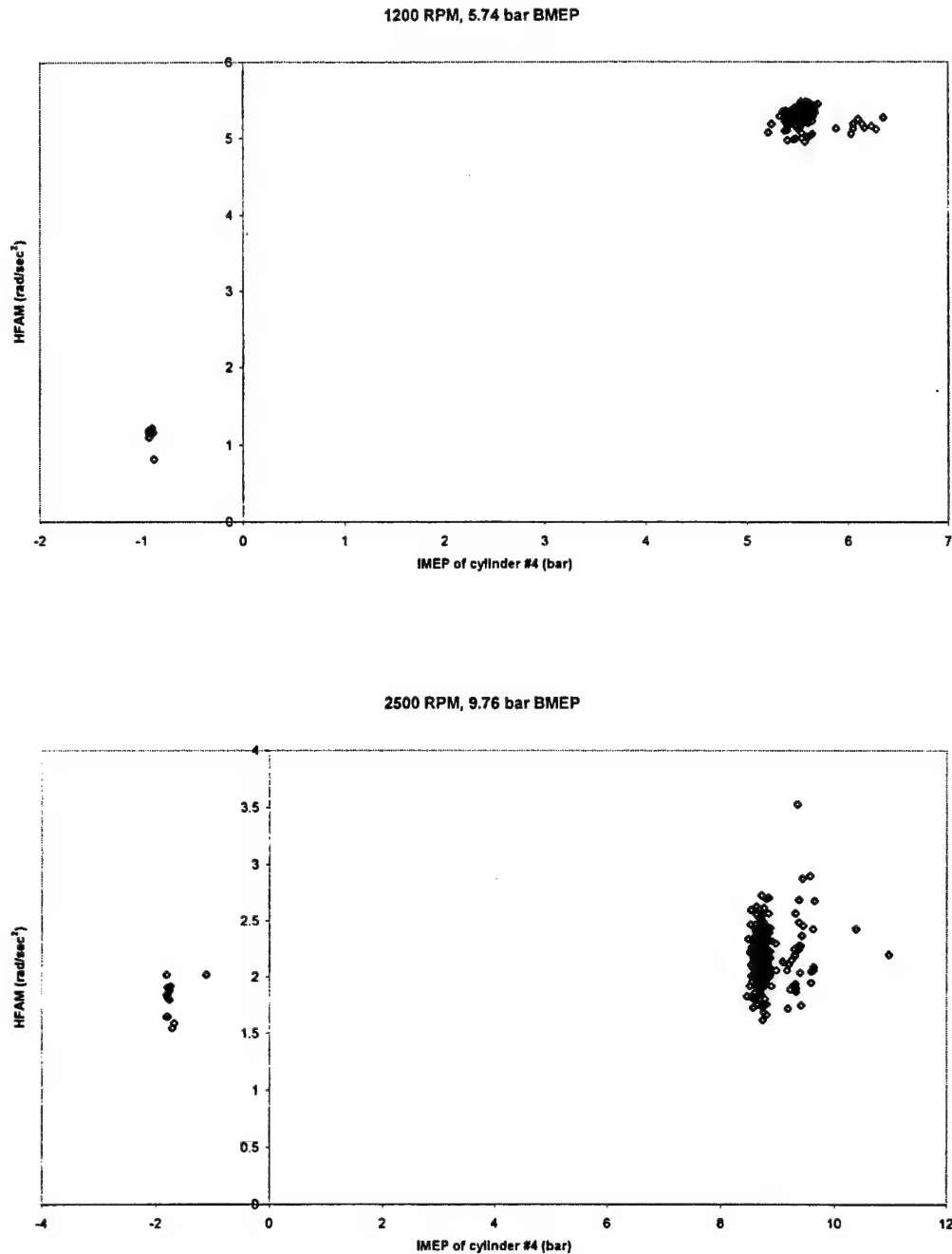


**Figure 8.16. High Frequency Acceleration Metric versus IMEP of cylinder #4.**

The performance of the HFAM is very good at the low engine speed, but again suffers at higher engine speeds. Again, this is postulated to be due to the rigid block assumption. The HFAM does not use a model, hence it does not “account” for structural vibration of the block. Nevertheless, the vibrations are real and are present in the acceleration signal. As engine speed increases, the magnitude of the structural vibration due to



reciprocating components increases. As a result, fluctuations in the acceleration signal due to cycle-by-cycle variation in combustion (or even complete misfires) are eventually reduced to the level of noise in relation to the acceleration induced by the reciprocating mass. Thus, the signal itself is not sensitive enough to indicate the presence of a misfire. The solution to this problem is to develop a model that incorporates the structural vibration modes of the block, and to eliminate those modes from the calculated torque signal. This would enable an analysis of the torque fluctuations due to combustion alone, and should in theory increase the ability of the misfire detection metrics to identify misfires.

### 8.7 *Concluding remarks*

This portion of the work has focused on misfire detection by analysing measurements of the angular acceleration of the engine block. Current practice is to use measurements of the flywheel angular velocity to detect misfires. This method is hampered by the load torque induced by the drivetrain, and torsional vibrations of the crankshaft. It is hypothesised that the method investigated here would overcome these limitations.

A model was constructed which assumed the block behaved as a single degree of freedom torsional oscillator. The calculated torque waveform confirmed that the angular acceleration of the block is not affected by the torque at the opposite end of the drivetrain. Furthermore, calculated torque was reasonably accurate at low engine speeds and loads, but was not so accurate at higher engine speeds or loads. This was postulated to be due to coupling between the rolling and pitching motion of the engine block within its mounts. Nevertheless, the model was not affected by the load torque provided by the dynamometer.

The calculated torque waveform was then used to calculate a cylinder effective pressure (CMEP) for cylinder #4. This was compared to the IMEP for that cylinder on a cycle-by-cycle basis as a means of identifying misfires. It was found that the CMEP was a reliable indicator at lower engine speeds and loads. The inaccuracies in the CMEP at higher speeds and loads were assumed to be the result of the previously discussed limitations to the one degree of freedom model.

Next, both the torque waveform and the measured angular acceleration signal were analysed in the spatial frequency domain. Four metrics for misfire identification were developed, based on either low or high frequency information. The results indicated that misfires tended to excite low orders in the engine block/mount system. Thus, metrics based on the energy contained in the low orders (below firing frequency) could be used to identify misfires.

The metrics based on the high frequency information were not generally reliable as misfire indicators. This is most likely to be due to the assumption of a rigid block. The block has been shown to undergo structural vibration at relatively low orders of firing frequency (Nakada and Tonosaki, 1994). In the case of the metric using the acceleration signal, it is postulated that the magnitude of the structural vibrations at high engine speeds becomes so large as to mask the effects of the torque fluctuations. The metric based on the calculated torque waveform does not account for structural vibration at all, with predictable results.

The final conclusion from this portion of the work is that the method of using block angular acceleration measurements is a viable means of both torque estimation and misfire identification. The accuracy of the torque estimation would be improved by:

- 1) Including the rigid body pitching motion of the block as a second degree of freedom. (The rear mounts on the production K16 are actually incorporated into the gearbox. The effects of this location on the pitching motion of the engine need to be examined, since it may eliminate the need to account for the pitching motion.)
- 2) Including structural vibration of the block (elimination of the rigid block assumption).
- 3) Incorporating variable inertial properties of the block based on engine speed.

Currently, the most reliable indicators of misfire are based on low order frequency information. This presents severe problems for identifying misfire in an engine mounted in a vehicle. With a model incorporating the changes suggested above, it is hoped that high frequency information would be available for misfire identification, thus making it more suitable for vehicular applications.

## Chapter 9 Conclusions and suggestions for further work

### 9.1 *Cycle-by-cycle modelling*

The objective of this portion of the work was to extend ISIS to enable it to model engine performance on a cycle-by-cycle basis. Since engine performance was the overall goal of the modelling, it was concluded that COV of IMEP would be the most appropriate metric to quantify the cycle-by-cycle variation. The initial modelling attempt used variations in burn rate to perturb the model. The results tended to under-predict the level of cyclic variation, and showed that burn rate information alone was insufficient. Thus, the work tested two hypotheses.

First, two methods of burn rate were examined under the hypothesis that the Rassweiler and Withrow method as used was not sufficiently robust. A two-zone polytropic process model was examined which calculated burn rate and the temperatures of the burned and unburned gases. This method proved to be unreliable in calculating either burn rate or temperatures. This was attributed to the assumption of a constant polytropic index throughout the combustion period.

Next, the Rassweiler and Withrow method was modified to include both the compression and expansion indices throughout the combustion period. The method was concluded to be a viable means of calculating mass fraction burned, provided that an accurate expansion index could be calculated. The Rover K4 exhibited non-standard combustion characteristics due to the slow burn up of a significant crevice volume. This made the calculation of an expansion index somewhat dubious, and the method was not used for mass fraction burned calculations on the K4.

The second hypothesis tested was that in addition to the variations in burn rate, variations in the completeness of combustion also existed, and needed to be incorporated into ISIS for cycle-by-cycle modelling. A completeness of combustion parameter ( $\chi$ ) was developed based on information contained in the Rassweiler and Withrow analysis. This parameter was incorporated into ISIS for each cycle modelled, and resulted in improvements to the cycle-by-cycle modelling of IMEP, maximum pressure, and the phasing of maximum pressure. Thus, it was concluded that for zero-dimensional thermodynamic models such as ISIS, burn rate and completeness of combustion perturbations were sufficient for accurate cycle-by-cycle modelling of engine performance parameters.

ISIS had been previously extended (Raine et al., 1995) to include nitric oxide kinetics. With the availability of a fast response chemiluminescent detector (CLD), cycle-by-

cycle measurements of NO could be compared to ISIS modelled values. It was found that ISIS under-predicted the cyclic variation in NO. NO formation was found to be particularly sensitive to the residual fraction and temperature at inlet valve closure, neither of which was allowed to vary cycle-by-cycle within ISIS. Thus, it was concluded that for cycle-by-cycle modelling of NO formation, variations in burn rate and combustion completeness were not sufficient, and that account must be made of cyclic variations in residual level and temperature in order to accurately model NO formation.

## 9.2 *Torque estimation and misfire detection*

The secondary objective of this work was to examine the feasibility of using measurements of the engine block angular acceleration to estimate the torque produced by the cylinders, and to identify misfired cycles. A model was constructed which assumed that the engine block behaved as a single degree of freedom torsional oscillator, and experimental data were taken from a Rover K16, in-line four cylinder engine. This model assumed that the block was rigid, and that the load torque had no effect on the calculated torque. The torque estimation showed good agreement with the torque calculated from cylinder pressure measurements taken from cylinder #4 at low engine speeds (1200 RPM) and loads, but less agreement at higher engine speeds (2500 RPM) and loads. This was attributed to two factors. First, due to the location of the engine mounts, the rolling and pitching motion of the engine was coupled both elastically and inertially. No account for this can be taken in a single degree of freedom model. Second, the inertial properties of the engine are a function of engine speed. Again, the engine model assumed constant inertial properties for the engine, and this resulted in an under-prediction of the gas torque at high engine speeds. The results also validated the assumption that load torque through the drivetrain had no effect on the torque calculations. This is a significant advantage over the current technique which uses measurements of flywheel angular velocity to detect misfires.

Metrics for misfire detection were developed in both the temporal and spatial frequency domains. In the temporal domain, the calculated torque waveform was used to calculate a mean effective pressure for each cylinder over its firing stroke (termed the cylinder mean effective pressure or CMEP). The CMEP for cylinder #4 was compared to the firing IMEP, and was found to be a reliable indicator of misfire at low engine speeds. At higher speeds, its accuracy declined due to the previously discussed limitations with the model in use.

In the spatial frequency domain, metrics were developed based on both high and low frequency information contained in the torque waveform and the measured angular

acceleration signal. The low frequency metrics proved to be the most reliable misfire indicators. However, their use in vehicular applications is considered doubtful since vehicle body motion would induce block motion at low frequencies, thus rendering the metrics incapable of detecting misfires. The high frequency metrics were not reliable misfire indicators. This was postulated to be due to structural vibrations in the block. Thus, the assumption of a rigid block was invalidated, particularly at high engine speeds.

### **9.3 *Suggestions for further work***

#### **9.3.1 Cycle-by-cycle modelling**

Whilst this work demonstrated that cyclic variations in burn rate and combustion completeness were sufficient to model cycle-by-cycle variations in IMEP, using this information to recreate experimental data is of limited value. The variations in burn rate and combustion completeness need to be used to predict engine performance. Most of the studies reviewed in Chapter 2 assumed the parameters to be perturbed exhibited a Gaussian distribution. Whilst this technique produced good results in the studies reviewed, Chapter 6 of this work has shown that the distribution of combustion completeness (as evidenced by the normalised pressure rise due to combustion) can be significantly non-Gaussian. Thus, work needs to be done on developing distributions for burn rate and combustion completeness. It is expected that these distributions would be different for each operating point (speed, load, air-fuel ratio, ignition timing, etc.). Although this seems to imply that an engine needs to be built before it can be modelled, this may not be the case. A recent paper by Ball et al. (1998) attempted to use ISIS to model NO measurements taken with a fast response CLD by Reavell et al. (1997). Reavell et al. performed their experiments on a Ricardo Hydra engine. Whilst the geometry of the Hydra was known, Ball et al. did not have burn rate information from the experiments described by Reavell et al. Thus, burn rate and combustion completeness data derived from the K4 engine was used to model the performance of the Hydra. The results were in good agreement with the experimental values. The two engines do have similar combustion chambers, and this may be the key to the good agreement. Nonetheless, these results indicate that it may not be necessary to build an engine before one can model it.

ISIS requires some modification if it is to be used for cycle-by-cycle modelling of NO. First, some account must be made for cyclic variations in residual level. ISIS currently calculates the composition and temperature of the residuals. As a first step, this information could be fed forward to the next cycle within ISIS. This would only account for the

temperature variations of the residuals. However, work by Sztenderowicz and Heywood (1990) concluded that fresh charge displacement due to variations of residual temperature had a greater effect on cyclic variations in IMEP than variations in the actual residual level. The relationship between residual temperature and fresh charge displacement would also have to be quantified in order to incorporate this into ISIS. Furthermore, the residual temperature information and assumed residual level could be used to perturb the temperature at IVC on a cyclic basis.

On the other hand, more recent work by Berckmuller et al. (1997) and Knapp et al. (1997) indicates that the effect of residuals on cyclic variation is due primarily to the residuals being inhomogeneously mixed with the fresh charge. The inhomogeneities tend to affect the early flame growth. Since ISIS is a zero-dimensional model, this effect cannot be modelled explicitly. Thus, the variations in burn rate would have to be relied upon to account for this effect. Work is currently being done on the K4 using laser diagnostics to measure in-cylinder temperature and species concentration. It is hoped that these techniques will be of use in determining the cyclic variations in residual temperature and their effects on conditions at IVC.

### 9.3.2 Torque estimation and misfire detection

Two avenues of approach are envisioned for improving the torque model used on the K16 engine. In the temporal domain, the model could be extended to include the rigid body pitching motion of the engine block. This would require a second set of accelerometers to measure rotation about the engine block Y axis. The result would be a set of coupled matrix equations which could be solved for the torque induced about the X axis by the cylinder pressure. The model would also be improved by including the structural vibration modes of the block itself. The work done by Nakada and Tonosaki (1994) and Dixon et al. (1994) would provide a good starting point as they both develop structural vibration models for in-line 4-cylinder engines. Further refinements could be pursued in determining the damping provided by the engine mounts. The model would also be improved by incorporating variable inertial properties for the block.

It may prove more profitable to perform the entire analysis in the frequency domain as outlined by Connolly and Rizzoni (1994), Connolly (1994), and Lee and Rizzoni (1995). The measured acceleration signal could then be deconvoluted by dividing it by the impulse response in a straightforward algebraic operation. The effects of the reciprocating mass would also have to be subtracted from this result, although this effect is completely determined by engine geometry and speed and can be calculated off-line for each desired

operating point. The advantage of this method is that it would incorporate the effects of the coupled motion, the variable inertial properties, and the structural vibration of the block. The difficulty lies in the fact that the impulse response would have to be experimentally determined at each desired engine speed. Lee and Rizzoni (1995) mention the determination of the impulse response. However, they do not give any indication as to how this is accomplished on a running engine. By performing the analysis in the frequency domain, it is hoped that more information would be contained in the higher frequencies, thus avoiding the complications of detecting a misfire through low frequency information in a vehicular application.

---

## References

Al-Himyary, T.J., and Karim, G. A. (1988), *A diagnostic two-zone combustion model for spark-ignition engines based on pressure-time data*, SAE paper 880199.

Alkidas, A.C., Drews, R.J., and Miller, W.F. (1995), *Effects of piston crevice geometry on the steady-state engine-out hydrocarbon emissions of a SI engine*, SAE paper 952537.

Amann, C.A. (1985), *Cylinder-pressure measurement and its use in engine research*, SAE paper 852067.

Ball, J.K., Raine, R.R., and Stone, C.R. (1998), *Combustion analysis and cycle-by-cycle variations in spark ignition engine combustion, part II: A new parameter for completeness of combustion and its use in modelling cycle-by-cycle variations in combustion*, Proceedings of the ImechE, Part D: Journal of Automobile Engineering.

Baltisberger, S., and Ruhm, R.H. (1994), *Fast NO measuring device for internal combustion engines*, SAE paper 940962.

Barnes-Moss, H.W. (1975), *A designer's viewpoint*, in Passenger Car Engines, ImechE Conf. Proc., pp.133-147, MEP, London.

Belmont, M.R., Hacothen, J., and Carpenter, P.W. (1994), *Tumble and Swirl: Are they a Mixed Blessing?*, Proceedings of the ImechE, Part D: Journal of Automobile Engineering, Vol. 208, pp. 223-226.

Belmont, M.R., Hancock, M.S., and Buckingham, D.J. (1986), *Statistical Aspects of Cyclic Variability*, SAE Paper 860324.

Berckmuller, M., Tait, N.P., and Greenhalgh, D.A. (1997), *The Influence of Local Fuel Concentration on Cyclic Variability of a Lean Burn Stratified Charge Engine*, SAE Paper 970826.

Beretta, G.P., Rashidi, M., and Keck, J.C. (1983), *Turbulent Flame Propagation and Combustion in Spark Ignition Engines*, *Combustion and Flame*, Vol. 52, pp. 217-245.



Blizard, N.C., and Keck, J.C. (1974), *Experimental and Theoretical Investigation of Turbulent Burning Model for Internal Combustion Engines*, SAE Paper 740191.

Bowman, C.T. (1975), *Kinetics of pollutant formation and destruction in combustion*, Prog. Energy and Combustion Science, Vol. 1, pp. 33-45.

Bradley, D., Lau, A.K.C., and Lawes, M. (1992), *Flame Stretch Rate as a Determinant of Turbulent Burning Velocity*, Phil. Trans. R. Soc. London, Vol. 338, pp.359-387.

Brandstatter, W., Johns, R.J.R., and Wigley, G. (1985), *The Effect of Inlet Port Geometry on In-Cylinder Flow Structure*, SAE Paper 850499.

Brehob, D.B., and Newman, C.E. (1992), *Monte Carlo Simulation of Cycle by Cycle Variability*, SAE paper 922165.

Brown, A.G. (1991), *Measurement and Modelling of Combustion in a Spark Ignition Engine*, PhD Thesis, Brunel University.

Brown, A.G., Stone, C.R., and Beckwith, P. (1996), *Cycle-by-Cycle Variations in Spark Ignition Ignition, Part I: Flame Speed and Combustion Measurements and a Simplified Turbulent Combustion Model*, SAE Paper 960612.

Brown, T.S., and Neill, W.S. (1992), *Determination of Engine Cylinder Pressures from Crankshaft Speed Fluctuations*, SAE Paper 920463.

Brunt, M.F.J. and Emtage, A.L. (1997), *Evaluation of burn rate routines and analysis errors*, SAE paper 970037.

Brunt, M.F.J., and Pond, C.R. (1997), *Evaluation of techniques for absolute cylinder pressure correction*, SAE paper 970036.

California Air Resources Board (1991), *Technical status Update and Proposed Revisions to Malfunction and Diagnostic System Requirements Applicable to 1994 and Subsequent California Passenger Cars, Light-Duty Trucks, and Medium-Duty Vehicles – (OBDII)*, CARB staff report.

Chanchaona, S., McFeaters, J.S., and Raine, R.R. (1990), *Effects of High Compression Ratio and Combustion Chamber Shape on Cycle-to-Cycle Variability*, SAE Paper 900385.

Chen, S.K., and Flynn, P. (1965), *Development of a compression ignition research engine*, SAE Paper 650733.

Cheng, C-O, Cheng, W.K., Heywood, J.B., Maroteaux, D., and Collings, N. (1991), *Intake port phenomena in a spark-ignition engine at part load*, SAE paper 912401.

Cheung, H.M., and Heywood, J.B. (1993), *Evaluation of a one-zone burn-rate analysis procedure using production SI engine pressure data*, SAE paper 932749.

Citron, S.J., O'Higgins, J.E., and Chen, L. (1989), *Cylinder by Cylinder Engine Pressure and Pressure Torque Waveform Determination Utilizing Speed Fluctuations*, SAE Paper 890486.

Cole, D.E., and Mirsky, W. (1968), *Mixture Motion – Its Effect on Pressure Rise in a Combustion Bomb: A New Look at Cyclic Variation*, SAE Paper 680766.

Connolly, F.T. (1994), *Direct Estimation of Cyclic Combustion Pressure Variability using Engine Speed Fluctuations in an Internal Combustion Engine*, SAE Paper 940143.

Connolly, F.T., and Rizzoni, G. (1994), *Real Time Estimation of Engine Torque for the Detection of Engine Misfires*, Transactions of the ASME, Journal of Dynamic Systems, Measurement, and Control, Vol. 116, pp. 675-686.

D'Agostino, R.B., Belanger, A., and D'Agostino, R.B., Jr. (1990), *A Suggestion for Using Powerful and Informative Tests of Normality*, The American Statistician, Vol. 44, No. 4, November, 1990.

Davis, C.S., and Stephens, M.A. (1983), *Approximate Percentage Points using Pearson Curves*, Applied Statistics, Royal Statistical Society, 1983.

Daw, C.S., Finney, C.E.A., Green, J.B., Kennel, M.B., Thomas, J.F., and Connolly, F.T. (1996), *A Simple Model for Cyclic Variations in a Spark Ignition Engine*, SAE Paper 962086.

Dixon, J., Rhodes, D.M., and Phillips, A.V. (1994), *The generation of engine half orders by structural deformation*, Paper C487/032, Proceedings of the ImechE.

- Douglas, R., Kee, R.J., and Carberry, B.P. (1997), *Analysis of In-Cylinder Pressure Data in Two-Stroke Engines*, SAE Paper 972792.
- Ellison, R.J., Harrow, G.A., and Hayward, B.M. (1968), *The Effect of Tetraethyl-Lead on Flame Propagation and Cyclic Dispersion in Spark-Ignition Engines*, *Journal of the Institute of Petroleum*, Vol. 54, No. 537, pp. 243-250.
- Erjavec, J., and Scharff, R. (1992), *Automotive Technology, A Systems Approach*, Delmar Publishers, Inc., New York.
- Ferguson, C. R. (1986), *Internal Combustion Engines*, Applied Thermosciences, John Wiley and Sons, Inc., New York.
- Finlay, I.C., Boam, D.J., Bingham, J.F., and Clark, T.A. (1990), *Fast response FID measurement of unburned hydrocarbons in the exhaust port of a firing gasoline engine*, SAE paper 902165.
- Fox, J.W., Cheng, W.K., and Heywood, J.B. (1993), *A model for predicting residual gas fraction in spark-ignition engines*, SAE paper 931025.
- Grunefeld, G., Beushausen, V., Andresen, P., and Hentschel, W. (1994), *A Major Origin of Cyclic Energy CONversion Variations in SI Engines: Cycle-by-Cycle Variations of the Equivalence Ratio and Residual Gas of the Initial Charge*, SAE Paper 941880.
- Hacohen, J., Belmont, M.R., Thurley, R.W.F., Thomas, J.C., Morris, E.L., and Buckingham, D.J. (1992), *Experimental and Theoretical Analysis of Flame Development and Misfire Phenomena in a Spark-Ignition Engine*, SAE Paper 920415.
- Hamai, K., Kawajiri, H., Ishizuka, T., and Nakai, M. (1986), *Combustion Fluctuation Mechanism Involving Cycle-to-Cycle Spark Ignition Variation due to Gas Flow Motion in S.I. Engines*, 21st International Symposium on Combustion.
- Heywood, J.B. (1988), *Internal Combustion Engine Fundamentals*, McGraw-Hill Book Company, New York.

Hoard, J., and Rehagen, L. (1997), *Relating Subjective Idle Quality to Engine Combustion*, SAE Paper 970035,

Hohenberg, G.F. (1979), *Advanced approaches for heat transfer calculations*, SAE paper 790825, SAE Trans. Vol.88.

Holmstrom, K., and Denbratt, I. (1996), *Cyclic Variation in an SI Engine Due to the Random Motion of the Flame Kernel*, SAE Paper 961152.

Iida, K., Akishino, K., and Kido, K. (1990), *IMEP Estimation from Instantaneous Crankshaft Torque Variation*, SAE Paper 900617.

Kistler Instrument Corporation (1981), *Type 5006 Charge Amplifier with Galvo Output Operating Instructions*, Kistler Instrument Corp., Amherst, New York.

Klenk, M., Moser, W., Mueller, W., and Wimmer, W. (1993), *Misfire Detection by Evaluating Crankshaft Speed – A Means to Comply with OBDII*, SAE Paper 93099.

Kuo, T.W. (1990), *What Causes Slower Flame Propagation in the Lean-Combustion Engine?*, Transactions of the ASME, Journal of Engineering for Gas Turbines and Power, Vol. 112, pp. 348-356.

Lancaster, D.R., Kreiger, R.B., Sorenson, S.C., and Hull, W.L. (1976), *Effects of Turbulence on Spark-Ignition Engine Combustion*, SAE Paper 760160.

LeCoz, J.F. (1992), *Cycle-to-Cycle Correlations Between Flow Field and Combustion Initiation in an S.I. Engine*, SAE Paper 920517.

Lee, d., and Rizzoni, G. (1995), *Detection of Partial Misfire in IC Engines Using Measurement of Crankshaft Angular Velocity*, SAE Paper 951070.

Lee, K.H., and Foster, D.E. (1995), *Cycle-by-Cycle Variations in Combustion and Mixture Concentration in the Vicinity of Spark Plug Gap*, SAE Paper 950814.

Lucas, G.G., and Brunt, M.F.J. (1982), *The Effect of Combustion Chamber Shape on the Rate of Combustion in a Spark Ignition Engine*, SAE Paper 820165.

Lucas Logic, Ltd. (1982), *Dial-A-Time MK II Manual*.

Lyon, D., *Knock and cyclic dispersion in a spark ignition engine*, Proceedings of ImechE, International Conference on Petroleum Based Fuels and Automotive Applications, 25-26 November, 1986, pp. 105-116.

Martin, J.K., Plee, S.L., and Remboski, D.J. (1988), *Burn Modes and Prior-Cycle Effects on Cyclic Variations in Lean-Burn Spark-Ignition Engine Combustion*, SAE Paper 880201.

Matekunas, F.A. (1983), *Modes and Measures of Cyclic Combustion Variability*, SAE Paper 830337.

Matsuoka, S., Yamaguchi, T., and Umemura, Y. (1971), *Factors Influencing the Cyclic Variation of Combustion of Spark Ignition Engine*, SAE Paper 710586.

Meirovitch, L. (1975), *Elements of Vibration Analysis*, McGraw-Hill, Inc., New York.

Mendis, K.J.S., Stone, C.R., Ladommatos, N., and Weller, G., *Modelling and Measurements from a Natural Gas Fuelled Engine*, SAE Paper 930927.

Nakada, T., and Tonosaki, H. (1994), *Excitation Mechanism of Half Order Engine Vibrations*, Paper C487/017, Proceedings of the ImechE.

Ozdor, N., Dulger, M., and Sher, E. (1994), *Cyclic Variability in Spark Ignition Engines A Literature Survey*, SAE Paper 940987.

Pashley, N.C. (1997), *Ignition Systems for Lean-Burn Gas Engines*, PhD Thesis, University of Oxford.

Patterson, D.J. (1966), *Cylinder Pressure Variations, A Fundamental Combustion Problem*, SAE Paper 660129.

Pearson, K. (1895), Philos. Trans. R. Soc. London, A186, pp. 343-414.

Peyton Jones, J.C., Landsborough, K.J., and Roberts, J.B. (1997a), *Identification of Stochastic Models for Cyclic Variations from Measured Pressure Data*, SAE Paper 970060.

Peyton Jones, J.C., Roberts, J.B., and Landsborough, K.J. (1997b), *Stochastic Simulation of Cycle-by-Cycle Cylinder Pressure Variations in a Spark Ignition Petrol Engine*, Paper No. 257-121, IASTED International Conference on Modelling and Simulation, Pittsburgh, USA.

Pischinger, S., and Heywood, J.B. (1988), *A Study of Flame Development and Engine Performance with Breakdown Ignition Systems in a Visualization Engine*, SAE Paper 880518.

Plapp, G., Klenk, M., and Moser, W. (1990), *Methods of On-Board Misfire Detection*, SAE Paper 900232.

Raine, R.R., Stone, C.R., and Gould, J. (1995), *Modelling of nitric oxide formation in spark ignition engines with a multizone burned gas*, Combustion and Flame, 102: 241-255, 1995.

Rassweiler, G.M., and Withrow, L. (1980), Motion pictures of engine flames correlated with pressure cards, SAE paper 800131 (originally presented in January 1938).

RC Electronics, Inc. (1987), *ComputerScope Reference Manual*, RC Electronics, Inc., Goleta, California.

Reavell, K. St J., Collings, N., Peckman, M., and Hands, T. (1997), *Simultaneous fast response NO and HC measurements from a spark ignition engine*, SAE paper 971610.

Reynolds, W.C., *STANJAN User Manual*, Stanford University, 1992.

Rizzoni, G. (1986), *A Dynamic Model for the Internal Combustion Engine*, PhD dissertation, University of Michigan, Ann Arbor, Mich.

Roberts, J.B., Peyton Jones, J.C., and Landsborough, K.J. (1997a), *Cylinder Pressure Variations as a Stochastic Process*, SAE Paper 970059.

Roberts, J.B., Peyton Jones, J.C., and Landsborough, K.J. (1997b), *Estimation of a Stochastic Model for Cycle-by-Cycle Variations in Cylinder Pressure Measurements from a Spark Ignition Engine*, 16<sup>th</sup> IASTED International Conference on Modelling, Identification, and Control, Innsbruck, Austria.

Rogers, G. F. C. and Mayhew, Y. R. (1988), *Thermodynamic and Transport Properties of Fluids*, 4th Edn., Blackwell.

Shayler, P.J., Wiseman, M.W., and Ma, T. (1990), *Improving the Determination of Mass Fraction Burnt*, SAE paper 900351.

Shen, H., and Jiang, D. (1992), *Investigation on the Flame Initiation and Early Development in a Spark Ignition Engine*, SAE Paper 922239.

Shen, H., Hinze, P.C., and Heywood, J.B. (1994), *A Model for Flame Initiation and early Development in SI Engine and its Application to Cycle-to-Cycle Variations*, SAE paper 942049.

Shen, H., Hinze, P.C., and Heywood, J.B. (1996), *A Study of Cycle-to-Cycle Variations in SI Engines Using a Modified Quasi-Dimensional Model*, SAE paper 961187.

Shiao, Y., and Moskwa, J.J. (1994), *Misfire Detection and Cylinder Pressure Reconstruction for SI Engines*, SAE Paper 940144.

Soltau, J.P. (1960) *Cylinder Pressure Variations in Petrol Engines*, ImechE Conference Proceedings, July, 1960, pp. 96-116.

Stevens, S.P., Shayler, P.J., and Ma, T. (1992), *A basis for the predictive control of cyclic dispersion in a spark ignition engine*, Proceedings of the ImechE, International Conference on Combustion in Engines, 1-3 December, 1992, pp. 175-182.

Stone, C.R. (1992), *Introduction to Internal Combustion Engines*, 2<sup>nd</sup> Edn. Macmillan.

Stone, C.R., and Green-Armytage, D.I. (1987), *Comparison of methods for the calculation of mass fraction burnt from engine pressure-time diagrams*, Proc IMechE, Part D, 201(D1), 61-67.

Stone, C.R., Brown, A.G., and Beckwith, P. (1992), *A turbulent combustion model used to give insights into cycle-by-cycle variations in spark ignition engine combustion*, Proceedings of the ImechE, International Conference on Combustion in Engines, 1-3 December, 1992, pp. 47-53.

Stone, C.R., Brown, A.G., and Beckwith, P. (1996), *Cycle-by-Cycle Variations in Spark Ignition Ignition, Part II: Modelling of Flame Kernel Displacements as a Cause of Cycle-by-Cycle Variations*, SAE Paper 960613.

Stone, C.R., Carden, T.R., and Podmore, I. (1993), *Analysis of the effect of inlet valve disablement on swirl, combustion, and emissions in a spark ignition engine*, Proc. Instn Mech. Engrs, Part D, 207, 295-305.

Sztenderowicz, M.L., and Heywood, J.B. (1990a), *Mixture Nonuniformity Effects on S.I. Engine Combustion Variability*, SAE Paper 902142.

Sztenderowicz, M.L., and Heywood, J.B. (1990b), *Cycle-to-cycle IMEP fluctuations in a stoichiometrically-fueled SI engine at low speed and load*, SAE paper 902143.

Tabaczynski, R.J., Trinker, F.H., and Shannon, B.A.S. (1980), *Further Refinement and Validation of a Turbulent Flame Propagation Model for Spark-Ignition Engines*, Combustion and Flame, Vol. 39, pp. 111-121.

Taylor, C.F. (1985), *The Internal Combustion Engine in Theory and Practice*, Volume 2, MIT Press, Cambridge, Massachusetts.

Thomson, W.T. (1988), *Theory of Vibration with Applications*, Prentice Hall, New Jersey.

Turns, S. R. (1996), *An Introduction to Combustion - Concepts and Applications*, Int. Edn, McGraw-Hill.

Williams, J. (1996), *An Overview of Misfiring Cylinder Engine Diagnostic Techniques Based on Crankshaft Angular Velocity Measurements*, SAE Paper 960039.

Winterbone, D.E. (1986), 'Transient performance', in Horlock, J.H. and Winterbone, D.E. (eds), *The Thermodynamics and Gas Dynamics of Internal Combustion Engines*, Vol. II, Oxford University Press.

Woschni, G. (1967), *A universally applicable equation for the instantaneous heat transfer coefficient in the internal combustion engine*, SAE paper 670931, SAE Trans., Vol. 76, p. 3065.



Young, M.B. (1980), *Cyclic Dispersion – Some Qualitative Cause-and-Effect Relationships*, SAE Paper 800459.

Young, M.B. (1981), *Cyclic Dispersion in the Homogeneous-Charge Spark-Ignition Engine-A Literature Survey*, SAE Paper 810020.

## Appendix A Derivation of Rassweiler and Withrow relationship with variable polytropic indices

In the following derivations, the equation numbering and notation of Rassweiler and Withrow have been retained for ease of reference to their original publication. The notation used by Rassweiler and Withrow is:

$n'$	polytropic exponent for the non-inflamed (unburned) portion of the charge (determined from the compression P-V diagram)
$n''$	polytropic exponent for the inflamed (burned) portion of the charge (determined from the expansion P-V diagram)
$V_t$	total volume of combustion chamber during combustion
$V_{tr}$	total volume of combustion chamber at end of combustion
$V_{ti}$	total volume of combustion chamber at ignition
$V_t''$	total volume of inflamed portion during combustion
$V_t'$	total volume of unburned portion during combustion
$V_{ti}''$	'extrapolated' volume of inflamed portion at ignition conditions
$V_{ti}'$	'extrapolated' volume of unburned portion at ignition conditions
$P_t$	observed pressure during combustion
$P_{ti}$	observed pressure at ignition
$P_{tr}$	observed pressure at end of combustion

Rassweiler and Withrow present two methods to determine the mass fraction burnt. Method 1 is based upon the compression index  $n'$  (for unburned mixture)

$$mfb = 1 - \left( \frac{V_t - V_t''}{V_{ti}} \right) \left( \frac{P_t}{P_{ti}} \right)^{\frac{1}{n'}} \quad (4)$$

and Method 2 is based on the expansion index  $n''$  (for burned mixture)

$$mfb = \left( \frac{V_t''}{V_{tr}} \right) \left( \frac{P_t}{P_{tr}} \right)^{\frac{1}{n''}} \quad (7)$$

In order to use these relations, measurements are needed for the cylinder pressure ( $P_t$ ) and for the burned gas volume at time  $t$  ( $V_t''$ ) which was obtained from film.

Rassweiler and Withrow then extend the analysis by assuming that  $n' = n'' = n$ , and derive an expression (eqn. (23)) which avoids the need for measurements of burnt gas volume.

$$mfb = \frac{(V_t P_t^{1/n} - V_{ti} P_{ti}^{1/n})}{(V_{tf} P_{tf}^{1/n} - V_{ti} P_{ti}^{1/n})} \quad (23)$$

The analysis is repeated with  $n' \neq n''$  starting with equations (4) and (7).

Rearranging equation (4) gives

$$mfb = 1 - \left( \frac{V_t}{V_{ti}} \right) \left( \frac{P_t}{P_{ti}} \right)^{\frac{1}{n'}} + \left( \frac{V_t''}{V_{ti}} \right) \left( \frac{P_t}{P_{ti}} \right)^{\frac{1}{n'}}$$

and further rearranging gives

$$mfb - 1 + \left( \frac{V_t}{V_{ti}} \right) \left( \frac{P_t}{P_{ti}} \right)^{\frac{1}{n'}} = \left( \frac{V_t''}{V_{ti}} \right) \left( \frac{P_t}{P_{ti}} \right)^{\frac{1}{n'}}$$

and hence

$$V_t'' P_t^{1/n'} = V_{ti} P_{ti}^{1/n'} \left( mfb - 1 + \left( \frac{V_t}{V_{ti}} \right) \left( \frac{P_t}{P_{ti}} \right)^{\frac{1}{n'}} \right)$$

Now substituting for  $V_t''$  into equation (7) gives

$$mfb = \frac{V_{ti} P_{ti}^{1/n'} P_t^{1/n''}}{V_{tf} P_{tf}^{1/n''} P_t^{1/n'}} \left( mfb - 1 + \left( \frac{V_t}{V_{ti}} \right) \left( \frac{P_t}{P_{ti}} \right)^{\frac{1}{n'}} \right)$$

and rearranging gives

$$\text{mfb} \left( \frac{V_{\text{tf}} P_{\text{tf}}^{1/n''} P_{\text{t}}^{1/n'}}{V_{\text{ti}} P_{\text{ti}}^{1/n'} P_{\text{t}}^{1/n''}} - 1 \right) = \left( \left( \frac{V_{\text{t}}}{V_{\text{ti}}} \right) \left( \frac{P_{\text{t}}}{P_{\text{ti}}} \right)^{\frac{1}{n'}} - 1 \right)$$

and therefore

$$\text{mfb} = \frac{\left( \frac{V_{\text{t}} P_{\text{t}}^{1/n'}}{V_{\text{ti}} P_{\text{ti}}^{1/n'}} - 1 \right)}{\left( \frac{V_{\text{tf}} P_{\text{tf}}^{1/n''} P_{\text{t}}^{1/n'}}{V_{\text{ti}} P_{\text{ti}}^{1/n'} P_{\text{t}}^{1/n''}} - 1 \right)} = \frac{V_{\text{ti}} P_{\text{ti}}^{1/n'} P_{\text{t}}^{1/n''}}{V_{\text{ti}} P_{\text{ti}}^{1/n'}} \frac{\left( V_{\text{t}} P_{\text{t}}^{1/n'} - V_{\text{ti}} P_{\text{ti}}^{1/n'} \right)}{\left( V_{\text{tf}} P_{\text{tf}}^{1/n''} P_{\text{t}}^{1/n'} - V_{\text{ti}} P_{\text{ti}}^{1/n'} P_{\text{t}}^{1/n''} \right)}$$

So that finally

$$\text{mfb} = \frac{P_{\text{t}}^{1/n''} \left( V_{\text{t}} P_{\text{t}}^{1/n'} - V_{\text{ti}} P_{\text{ti}}^{1/n'} \right)}{\left( V_{\text{tf}} P_{\text{tf}}^{1/n''} P_{\text{t}}^{1/n'} - V_{\text{ti}} P_{\text{ti}}^{1/n'} P_{\text{t}}^{1/n''} \right)} \quad \text{Expression (a)}$$

This has been transferred to the text replacing the notation of Rassweiler and Withrow with the standard notation used in this work.

To check the 'limits' of this expression:

For  $n' = n'' = n$  expression (a) reduces to

$$\text{mfb} = \frac{P_{\text{t}}^{1/n} \left( V_{\text{t}} P_{\text{t}}^{1/n} - V_{\text{ti}} P_{\text{ti}}^{1/n} \right)}{\left( V_{\text{tf}} P_{\text{tf}}^{1/n} P_{\text{t}}^{1/n} - V_{\text{ti}} P_{\text{ti}}^{1/n} P_{\text{t}}^{1/n} \right)} = \frac{\left( V_{\text{t}} P_{\text{t}}^{1/n} - V_{\text{ti}} P_{\text{ti}}^{1/n} \right)}{\left( V_{\text{tf}} P_{\text{tf}}^{1/n} - V_{\text{ti}} P_{\text{ti}}^{1/n} \right)}$$

which is identical to Rassweiler and Withrow eqn.(23).

Or in Expression (a) for  $P_{\text{t}} = P_{\text{tf}}$

$$\text{mfb} = \frac{P_{\text{tf}}^{1/n''} \left( V_{\text{tf}} P_{\text{tf}}^{1/n'} - V_{\text{ti}} P_{\text{ti}}^{1/n'} \right)}{\left( V_{\text{tf}} P_{\text{tf}}^{1/n''} P_{\text{tf}}^{1/n'} - V_{\text{ti}} P_{\text{ti}}^{1/n'} P_{\text{tf}}^{1/n''} \right)} = \frac{\left( V_{\text{tf}} P_{\text{tf}}^{1/n'} - V_{\text{ti}} P_{\text{ti}}^{1/n'} \right)}{\left( V_{\text{tf}} P_{\text{tf}}^{1/n'} - V_{\text{ti}} P_{\text{ti}}^{1/n'} \right)} = 1$$

which is the correct limit.

And in Expression (a) for  $P_t = P_{ti}$

$$mfb = \frac{P_{ti}^{1/n''} (V_{ti} P_{ti}^{1/n'} - V_{ti} P_{ti}^{1/n'})}{(V_{ti} P_{ti}^{1/n''} P_{ti}^{1/n'} - V_{ti} P_{ti}^{1/n'} P_{ti}^{1/n''})} = \frac{P_{ti}^{1/n''} P_{ti}^{1/n'} (V_{ti} - V_{ti})}{P_{ti}^{1/n'} (V_{ti} P_{ti}^{1/n''} - V_{ti} P_{ti}^{1/n''})}$$

therefore

$$mfb = \frac{(P_{ti}^{1/n''} V_{ti} - P_{ti}^{1/n''} V_{ti})}{(V_{ti} P_{ti}^{1/n''} - V_{ti} P_{ti}^{1/n''})} = 0$$

which is also the correct limit.

## Appendix B Modification of the Wiebe mass fraction burned relation to allow for incomplete combustion.

The original routine developed by Ferguson (1986) is based on the differential form of the first law of thermodynamics, and the relevant equations are derived therein. Within this formulation, the differential heat release is defined as

$$dQ = Q_{in} dx$$

where  $x$  is the mass fraction burned, and is defined by a cosine function in the original routine. The differential equation of the first law is integrated along with differential equations for work, heat transfer, NO formation, and mass loss. ISIS has been modified (Raine et al., 1995) to allow different formulations of the burn rate. For the current work, a Wiebe function has been used, as described in Chapter 4. Thus, within ISIS it is the derivative of the Wiebe function which is incorporated into the differential equations, and thus must be determined here.

The "completeness of combustion" parameter,  $\chi$ , has been defined in this work such that at the end of the combustion period ( $\theta_b$ ), mass fraction burned =  $\chi$ .

Thus, a modified Wiebe function may be defined as

$$x = \chi \left[ 1 - \exp \left\{ -a \left( \frac{\theta - \theta_s}{\theta_b} \right)^{m+1} \right\} \right] \quad (B.1)$$

Now to determine  $\frac{dx}{d\theta}$ , let  $z = \left( \frac{\theta - \theta_s}{\theta_b} \right)^{m+1}$  so that  $x = \chi [1 - \exp\{-az\}]$ .

$$\text{Hence } \frac{dz}{d\theta} = \frac{m+1}{\theta_b^{m+1}} (\theta - \theta_s)^m \text{ and } \frac{dx}{dz} = a\chi \exp\{-az\}$$

$$\text{so that } \frac{dx}{d\theta} = \frac{dx}{dz} \frac{dz}{d\theta} = a\chi \exp\{-az\} \frac{m+1}{\theta_b^{m+1}} (\theta - \theta_s)^m, \text{ or}$$

$$\frac{dx}{d\theta} = a\chi \exp\left\{-a\left(\frac{\theta - \theta_s}{\theta_b}\right)^{m+1}\right\} \frac{m+1}{\theta_b^{m+1}} (\theta - \theta_s)^m. \quad (\text{B.2})$$

From equation (B.1),  $\exp\left\{-a\left(\frac{\theta - \theta_s}{\theta_b}\right)^{m+1}\right\} = 1 - \frac{x}{\chi}$ . Substituting this into equation (B.2) yields

$$\frac{dx}{d\theta} = \chi a \frac{m+1}{\theta_b^{m+1}} (\theta - \theta_s)^m \left(1 - \frac{x}{\chi}\right). \quad (\text{B.3})$$

ISIS was also modified to allow for incomplete combustion in the calculation of UCHEM (the chemical internal energy of the species present at the end of expansion) and then in the calculation of ETACOM (combustion efficiency). This required modifications mainly in the subroutine PROC\_OUT, but also in places where it was necessary to account for fuel in the unburned zone at the end of expansion. Previous versions of ISIS assumed that there was no fuel left at the end of expansion, so UCHEM did not include the value of fuel internal energy. Data for the chemical internal energies of species are taken from Turns (1996) and have been confirmed against data from Mayhew and Rogers (1988).

The burn rate files output by COBRA for input into ISIS were modified as shown below. Line 1 of the file contains the lower MFB value and higher MFB value specified by the user for Wiebe function fitting. Subsequent lines contain (in order): spark timing, relative air-fuel ratio ( $\lambda$ ), degrees crank angle to the lower MFB value, degrees crank angle to the higher MFB value, and completeness of combustion ( $\chi$ ).

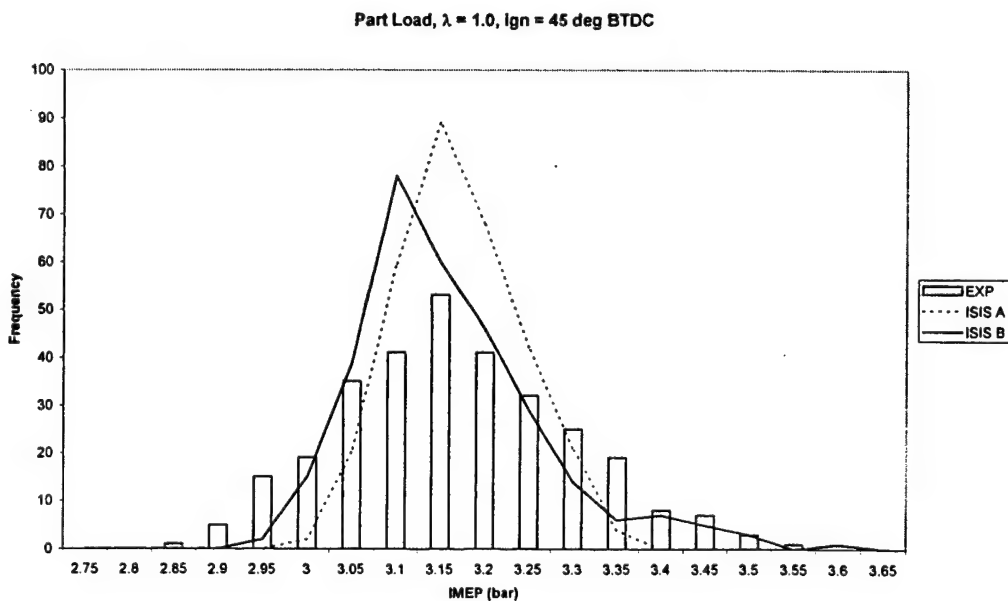
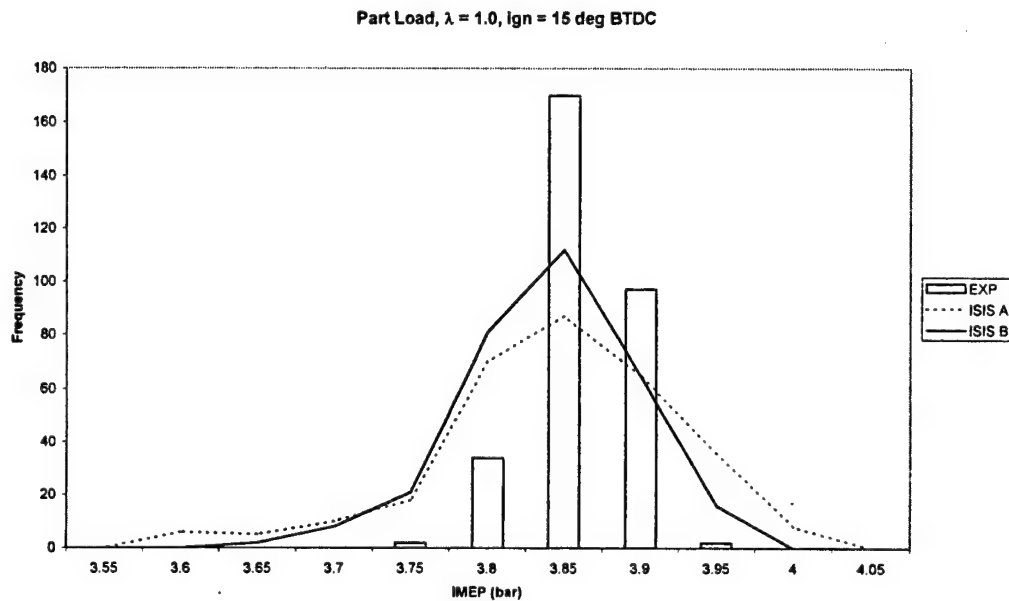
0.1	0.8			
25.0	1.0	19.0	37.0	1.0
25.0	1.0	19.0	37.0	0.95
25.0	1.0	19.0	37.0	0.9
25.0	1.0	19.0	37.0	0.85
25.0	1.0	19.0	37.0	0.8
25.0	1.5	29.0	77.0	1.0
25.0	1.5	29.0	77.0	0.95
25.0	1.5	29.0	77.0	0.9
25.0	1.5	29.0	77.0	0.85

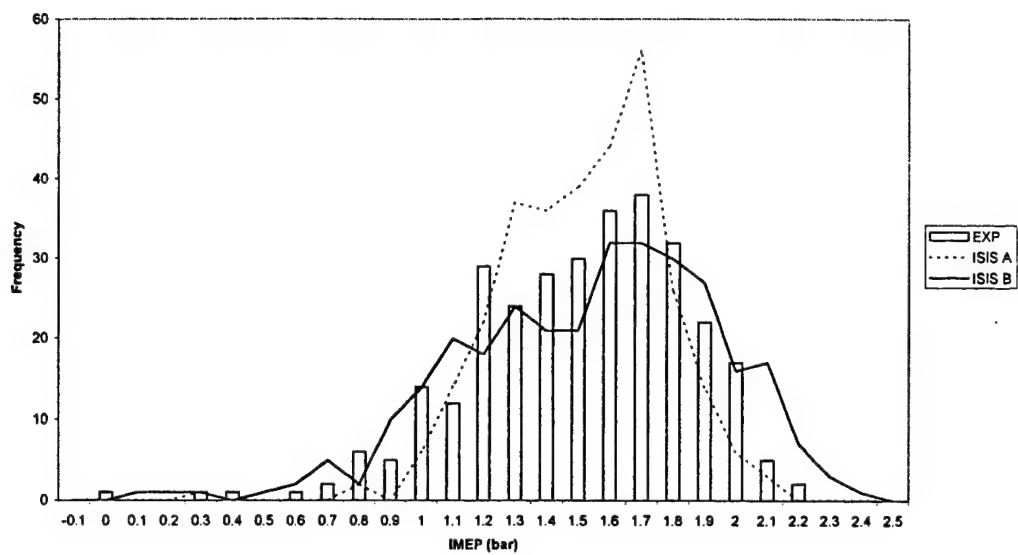
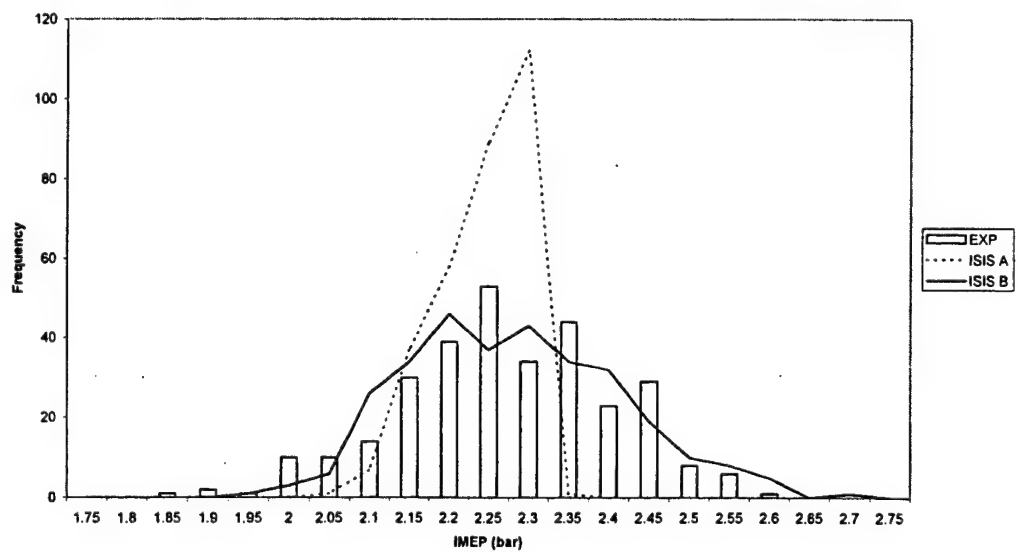
It should also be noted that, due to the manner in which  $\chi$  was calculated, a few cycles in each case had a combustion completeness of over 100% ( $\chi > 1.0$ ). This is due to the fact that the normalised pressure rise due to combustion, which is the basis of calculating  $\chi$ , is sensitive to variations in the trapped mass. Hence, the few cycles in which  $\chi$  exceeded 1.0 were assumed to be due to higher trapped masses (for example, such as might result from the residuals of a weak cycle). In these cases, ISIS used a combustion completeness of 1.0.

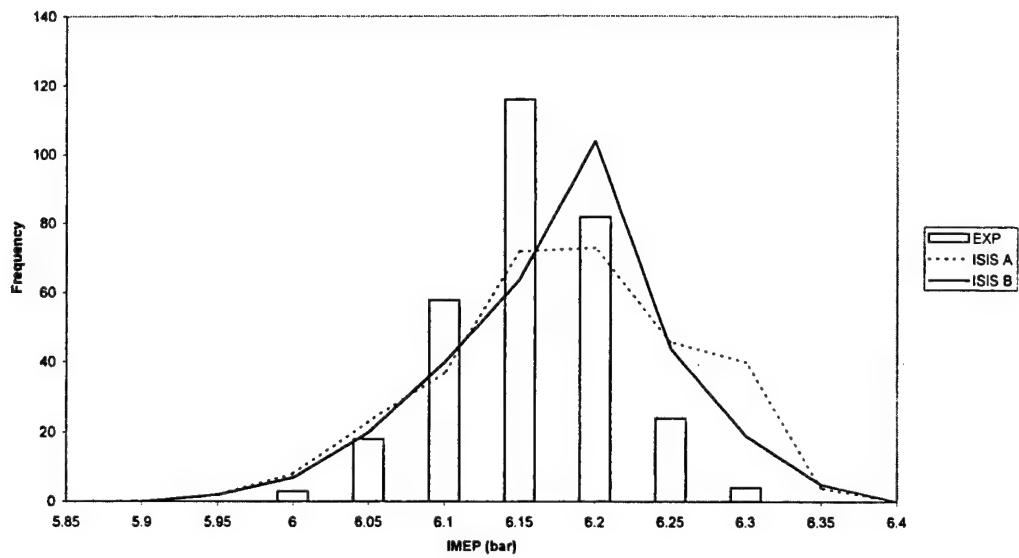
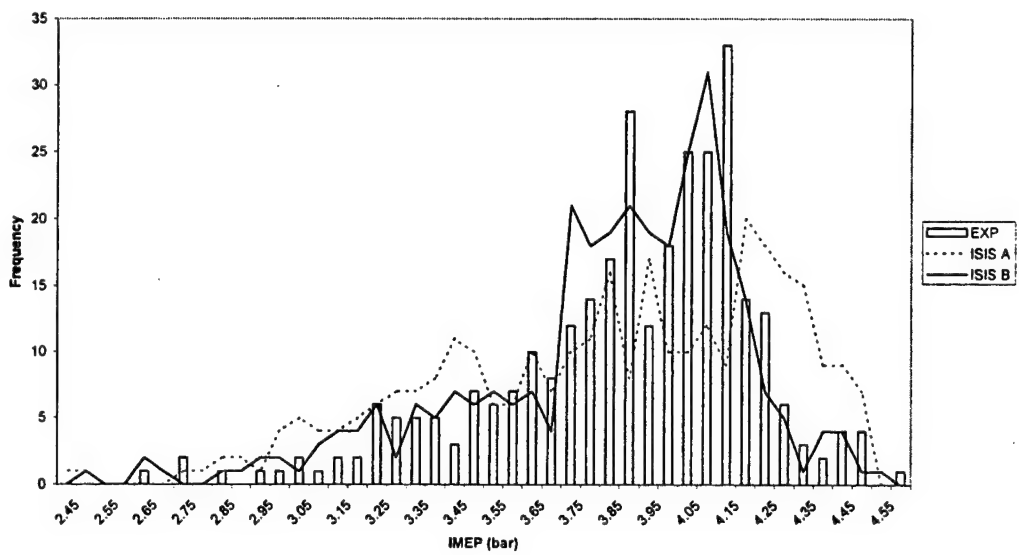


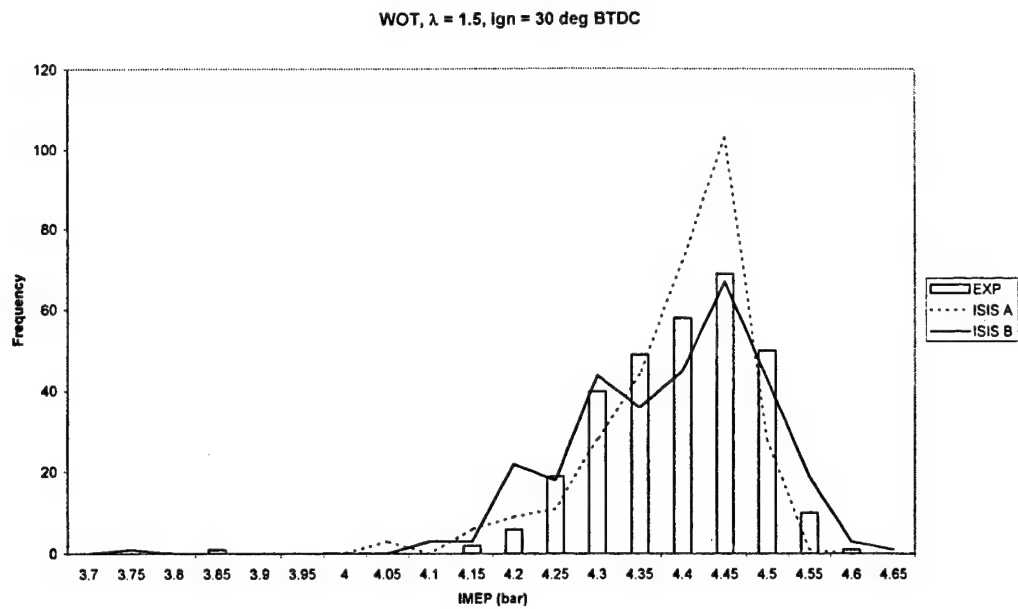
## Appendix C Experimental and Modelled IMEP distribution plots.

This appendix contains frequency plots of IMEP for the cases modelled but not included in Chapter 6. The operating point for each case is shown on the respective plot. In each case, the distributions labelled "ISIS A" are the results of ISIS modelling with only burn rate variations. The distributions labelled "ISIS B" are the results of modelling which included completeness of combustion.



Part Load,  $\lambda = 1.5$ , Ign = 15 deg BTDCPart Load,  $\lambda = 1.5$ , Ign = 45 deg BTDC

WOT,  $\lambda = 1.0$ , Ign = 15 deg BTDCWOT,  $\lambda = 1.5$ , Ign = 15 deg BTDC



## Appendix D Summary of ISIS inputs for cycle-by-cycle modelling of NO.

This appendix contains a summary of the ISIS inputs used in the NO modelling described in Chapter 7. Obviously, many of the inputs are determined by the engine and operating point and will not be restated here. Several input parameters were held constant for all cases modelled. These include:

Heat transfer correlation – Hohenberg (1979)

Heat transfer weighting – 1.0 for both burned and unburned regions

Number of burned zones – 10

Reaction rates and tolerances – Heywood (1988)

Furthermore, it was discovered that the blow-by from the K4 had increased substantially since the experimental data for combustion completeness had been taken. The K4 was run at 1000 RPM on a stoichiometric mixture of methane. The blow-by was measured by sealing the mirror ports in the lower cylinder barrel, and measuring the blow-by flow with a positive displacement airflow meter. Table D.1 summarises the experimental measurements taken. Cases A, B, and C used an ignition timing of 15 degrees BTDC, whilst cases D and E used an ignition timing of 30 degrees BTDC.

**Table D.1. K4 blow-by test measurements.**

$\Delta t$ (sec)	Case A V (ft <sup>3</sup> )	Case B V (ft <sup>3</sup> )	Case C V (ft <sup>3</sup> )	Case D V (ft <sup>3</sup> )	Case E V (ft <sup>3</sup> )
0	7.46	8.40	9.30	0.70	2.00
30	7.52	8.55	9.43	0.89	2.18
60	7.63	8.70	9.57	1.07	2.36
90	7.72	8.86	9.72	1.26	2.54
120	7.81	8.99		1.45	2.75
150	7.93	9.11		1.67	2.94
180	8.07	9.24		1.89	3.12
$\Delta V/\Delta t$	0.00339	0.00467	0.00467	0.00661	0.00622

The mean volumetric blow-by flow rate was

$$\frac{\Delta V}{\Delta T_{\text{mean}}} = \dot{V}_b = 0.00511 \text{ ft}^3 / \text{sec} (28.317 \text{ litres} / \text{ft}^3) = 0.14476 \text{ litres} / \text{sec}$$

The following assumptions were made regarding the blow-by gas:

- a) it had the same composition as the intake mixture ( $R=300.1$ ),
- b) the pressure was equal to the ambient pressure (1.019 bar), and
- c) the gas was at the ambient temperature (30 C).

Following from these assumptions, the mass flow rate of the blow-by gas was

$$\dot{m}_b = \frac{P \dot{V}_b}{RT} = \frac{(1.019 \text{E}^5)(0.14476)}{(300.98)(303.15)} = 0.16164 \text{ g} / \text{sec}.$$

The blow-by mass per cycle is then given by

$$m_b = 0.16164 \text{ g} / \text{sec} \left( \frac{120}{1000} \right) = 0.0194 \text{ g} / \text{cycle}.$$

For methane, the stoichimetric gravimetric air-fuel ratio is 17.13. Assuming an average residual level of 0.13, and noting that the intake flow rate was measured to be 1.0 litre/sec:

$$\dot{m}_{\text{air}} = \frac{(1.019 \text{E}^5)(1.00)}{(300.98)(303.15)} = 1.171 \text{ g} / \text{sec}.$$

And the intake mass per cycle is given by

$$m_{\text{air}} = 1.171 \text{ g} / \text{sec} \left( \frac{120}{1000} \right) = 0.1405 \text{ g} / \text{cycle}$$

The trapped mass is then given by

$$m_{\text{in}} = \frac{m_{\text{air}} + \frac{m_{\text{air}}}{\text{AFR}_g}}{1 - r_f} = \frac{0.1405 + \frac{0.1405}{17.13}}{1 - 0.13} = 0.171 \text{ g} / \text{cycle}.$$

Hence, the average blow-by is

$$\frac{m_b}{m_{in}} = \frac{0.0194}{0.171} = 0.1134 = 11.34\%$$

Within ISIS, blow-by is modelled as an exponential mass loss:

$$\frac{m_i}{m_o} = \exp \left[ -C \left( \frac{\theta_i - \theta_{IVC}}{\omega} \right) \right] \quad (D.1)$$

where  $\omega$  is the angular speed of the engine in rad/sec, and  $m_o$  is the calculated mass at IVC. Since the K4 was losing 11.34% of its mass over each cycle, the ratio of the mass at the end of the cycle to the mass at IVC is

$$\frac{m}{m_o} = 0.8866 .$$

Thus, the only unknown in equation (D.1) is the blow-by constant,  $C$ . This was calculated to be 2.34, and was used for all cases modelled in Chapter 7.

Table D.2 summarises the other inputs required by ISIS. The first four parameters (wall temperature, pressure and temperature at IVC, and residual fraction) did not vary cycle-by-cycle. The last three parameters (10% burn duration, 80% burn duration, and combustion completeness) are shown for the mean cycle for each case. For the cycle-by-cycle modelling, these three parameters were perturbed by inputting the cyclic values computed from the experimental data.

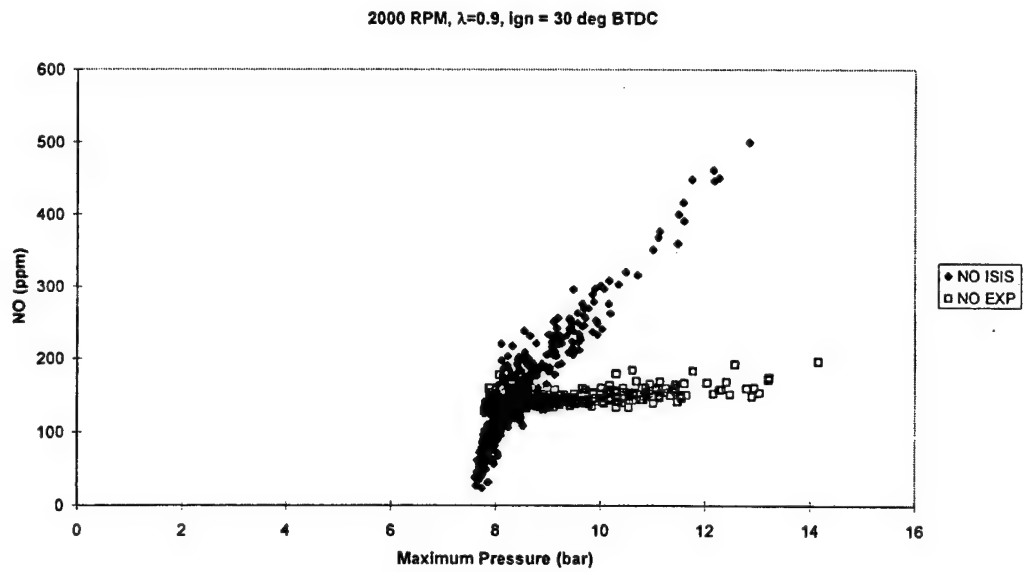
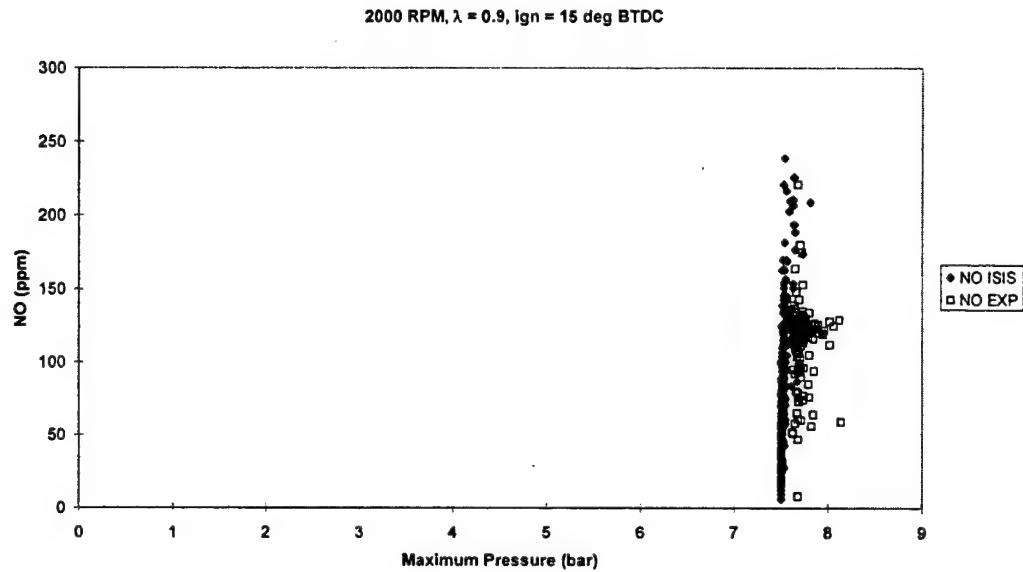
Table D.2. ISIS input parameters for cases modelled in Chapter 7.

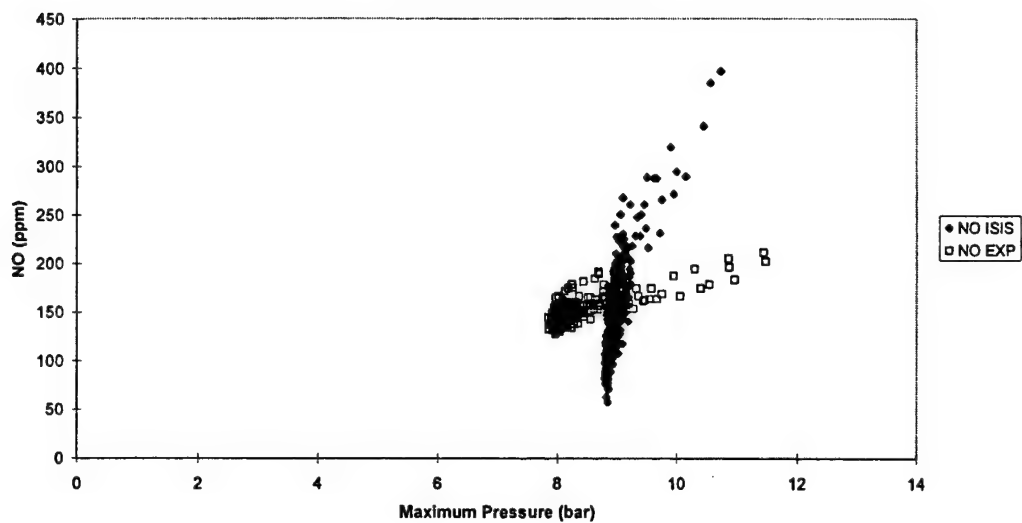
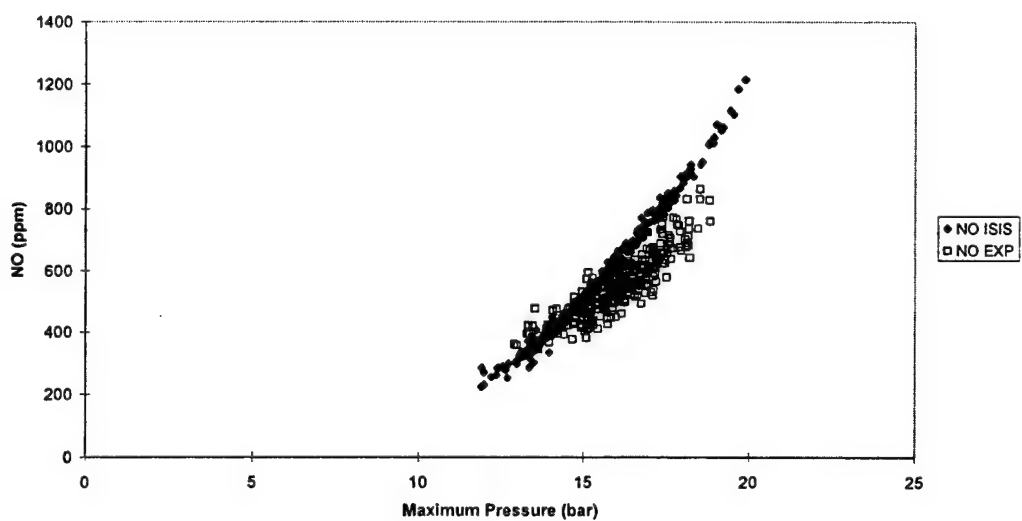
Test ID	$T_{\text{wall}}$ (K)	$P_{\text{ivc}}$ (bar)	$T_{\text{ivc}}$ (K)	Residual fraction	10% burn (degrees CA)	80% burn (degrees CA)	$\chi$
P0915	450	0.50	423	0.033	28	57	0.932
P0930	450	0.51	434	0.092	29	51	0.886
P1015	450	0.46	393	0.110	25	52	0.953
P1030	450	0.46	422	0.149	24	42	0.918
P1115	435	0.46	401	0.091	24	52	0.962
P1130	435	0.46	428	0.138	24	44	0.926
F0915	450	0.87	445	0.073	22	42	0.944
F0930	450	0.88	458	0.148	22	38	0.949
F1015	450	0.87	451	0.111	17	36	0.967
F1030	450	0.89	478	0.169	17	32	0.968
F1115	435	0.85	430	0.101	18	40	0.961
F1130	435	0.86	470	0.172	19	35	0.949
20915	450	0.47	436	0.010	50	107	0.878
20930	450	0.47	417	0.030	40	84	0.947
21015	450	0.56	466	0.050	40	89	0.916
21030	450	0.54	453	0.121	34	68	0.932
21115	435	0.55	446	0.067	31	74	0.988
21130	435	0.59	471	0.118	25	53	0.937
T0915	450	0.52	442	0.191	17	31	0.965
T0930	450	0.51	447	0.248	19	32	0.959
T1015	450	0.51	433	0.194	17	33	0.936
T1030	450	0.45	417	0.230	22	35	0.931
T1115	450	0.51	430	0.140	20	40	0.903
T1130	450	0.48	435	0.191	23	38	0.935

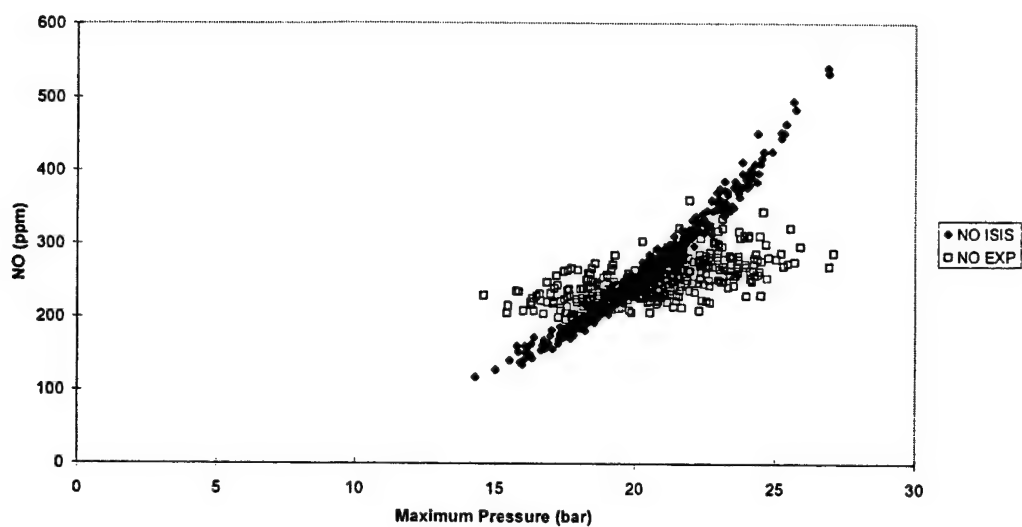
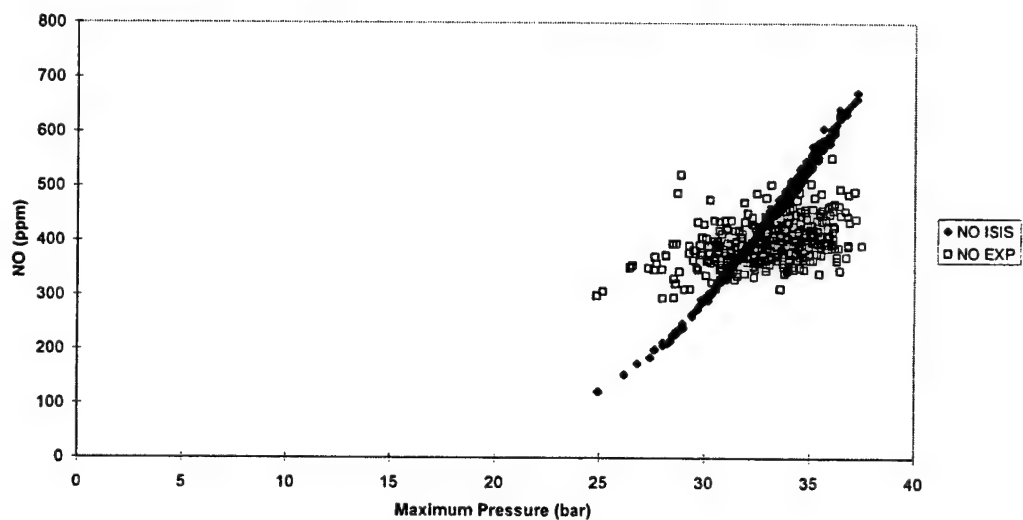


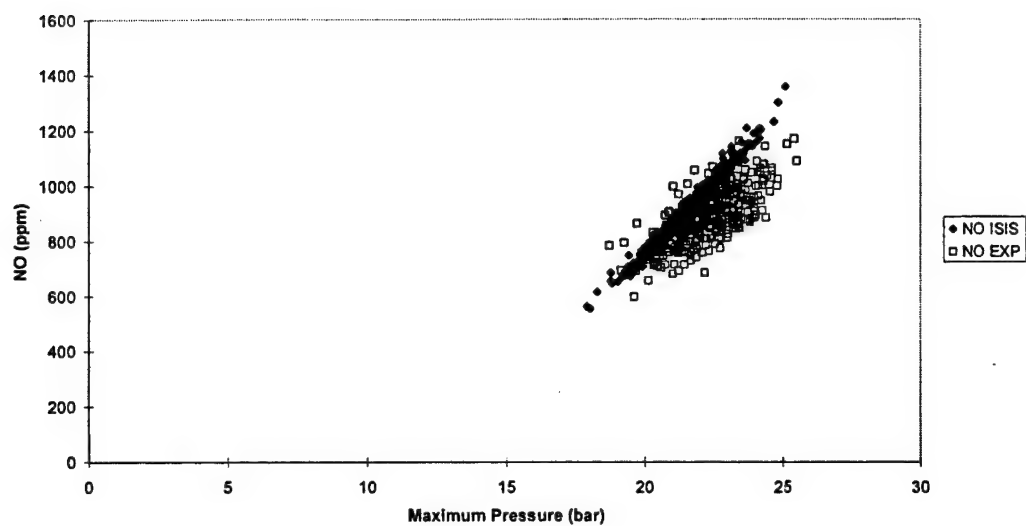
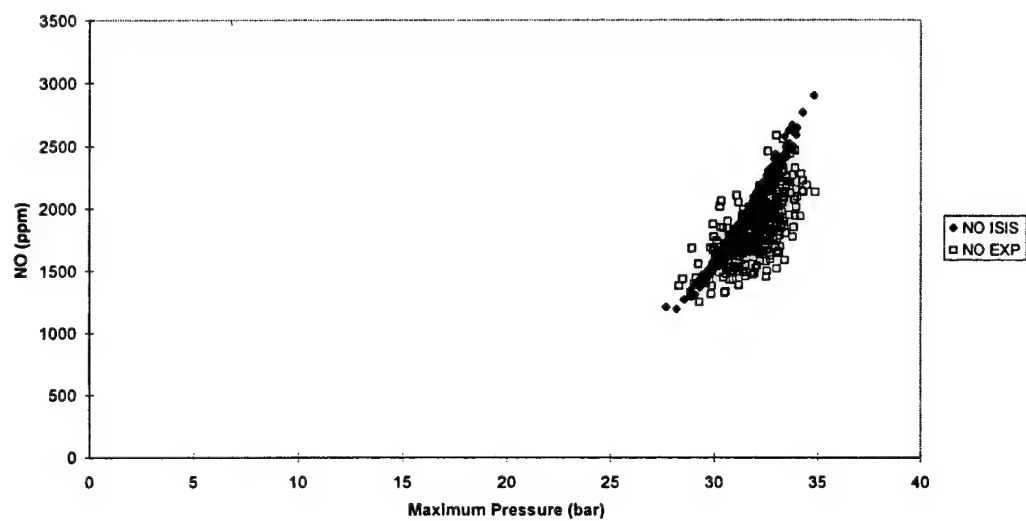
## Appendix E Results of NO modelling

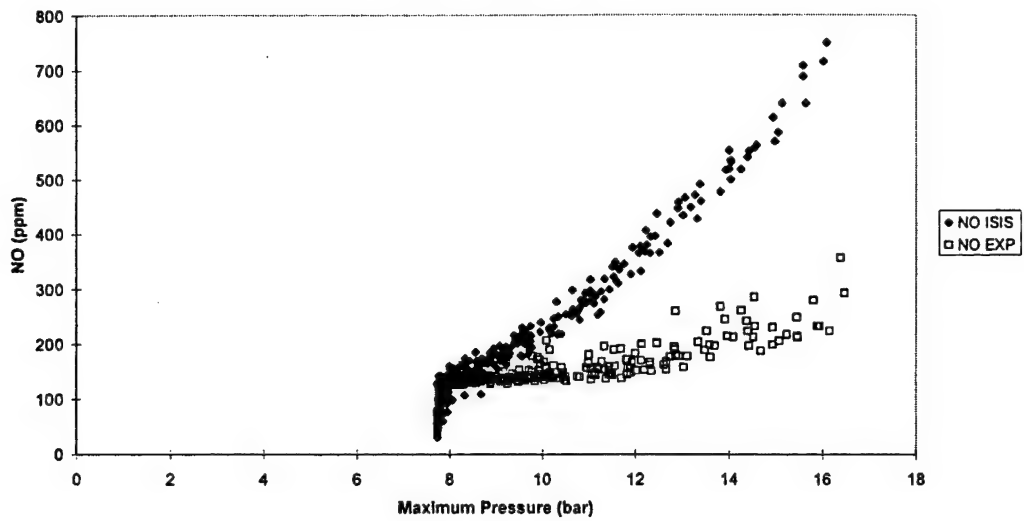
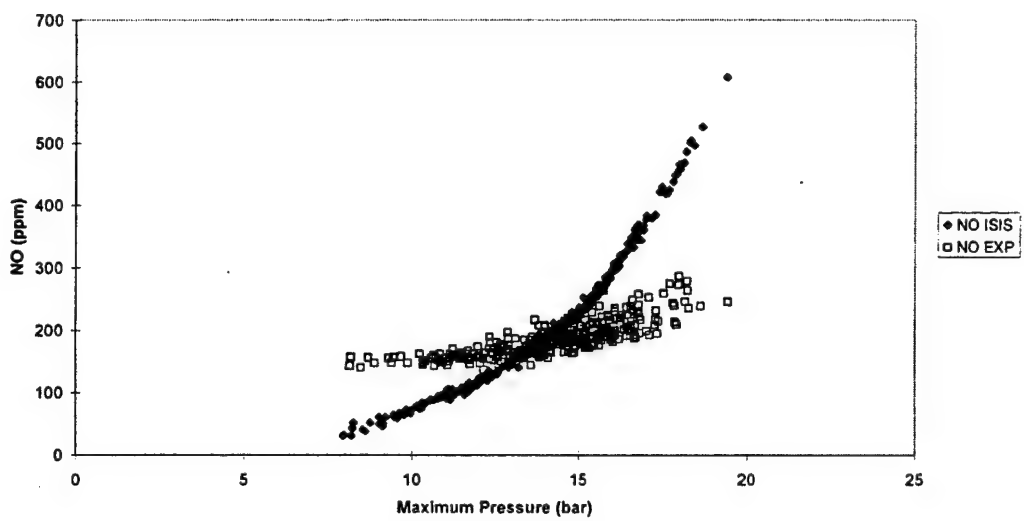
This figure contains plots of NO versus maximum pressure for the cases not shown in Chapter 7. The operating points for each case are annotated on the figures.

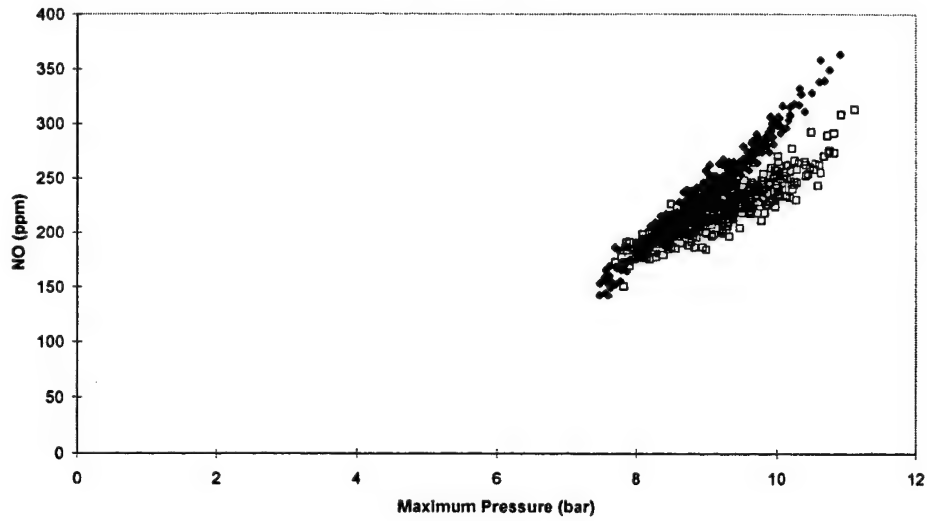
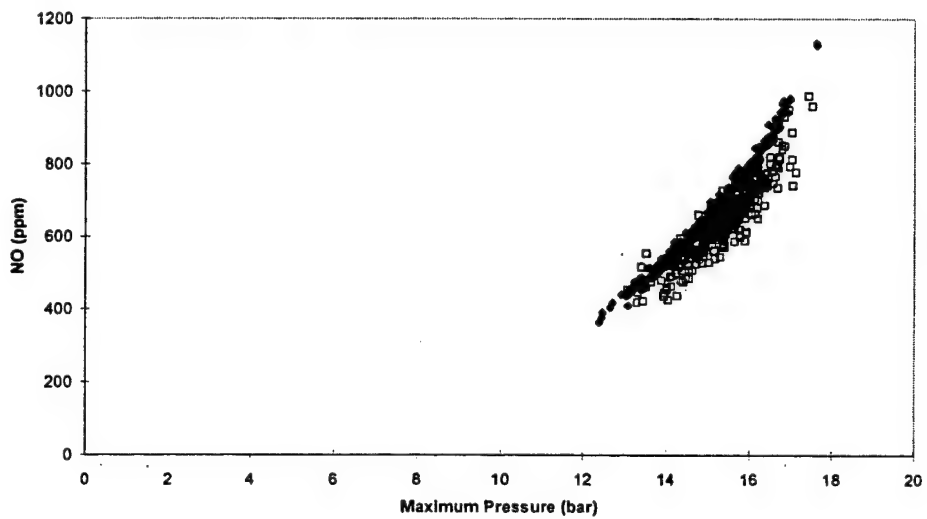


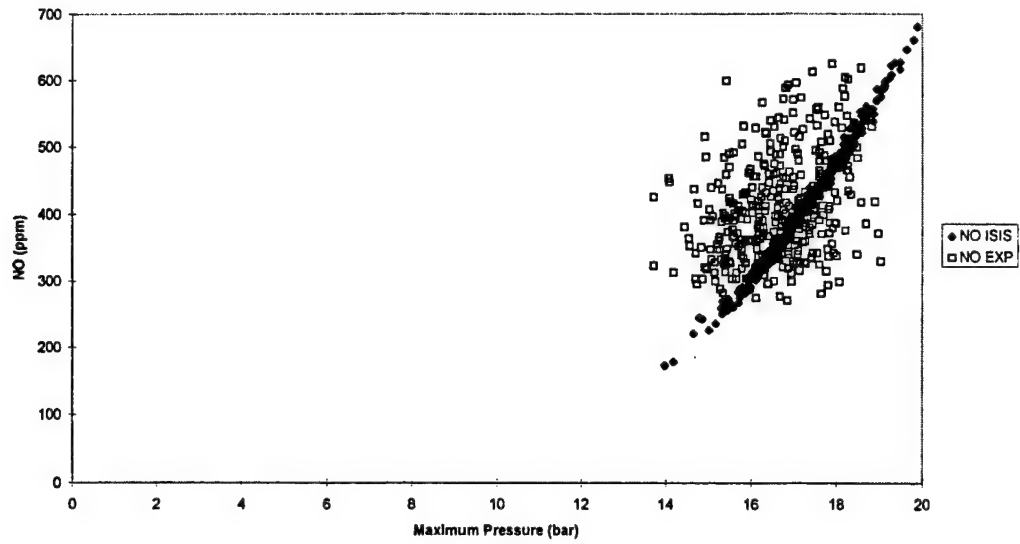
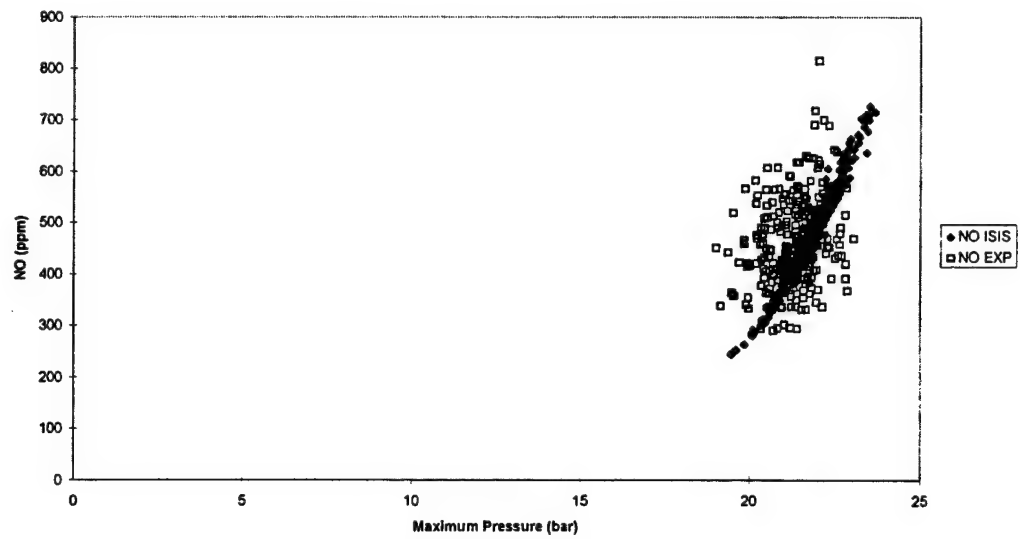
2000 RPM,  $\lambda=1.1$ , ign = 15 deg BTDC2000 RPM,  $\lambda=1.1$ , ign = 30 deg BTDC

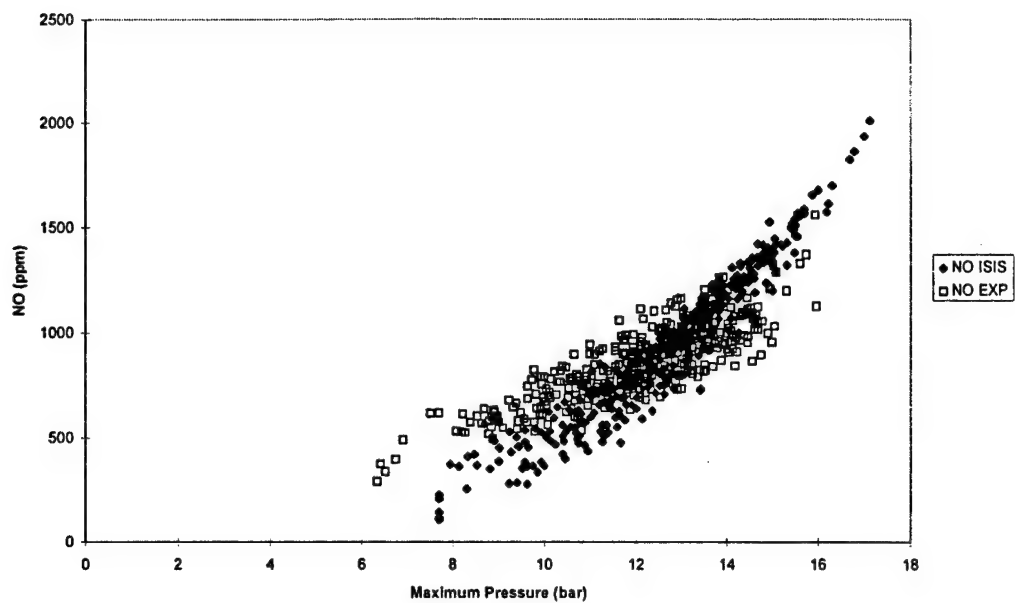
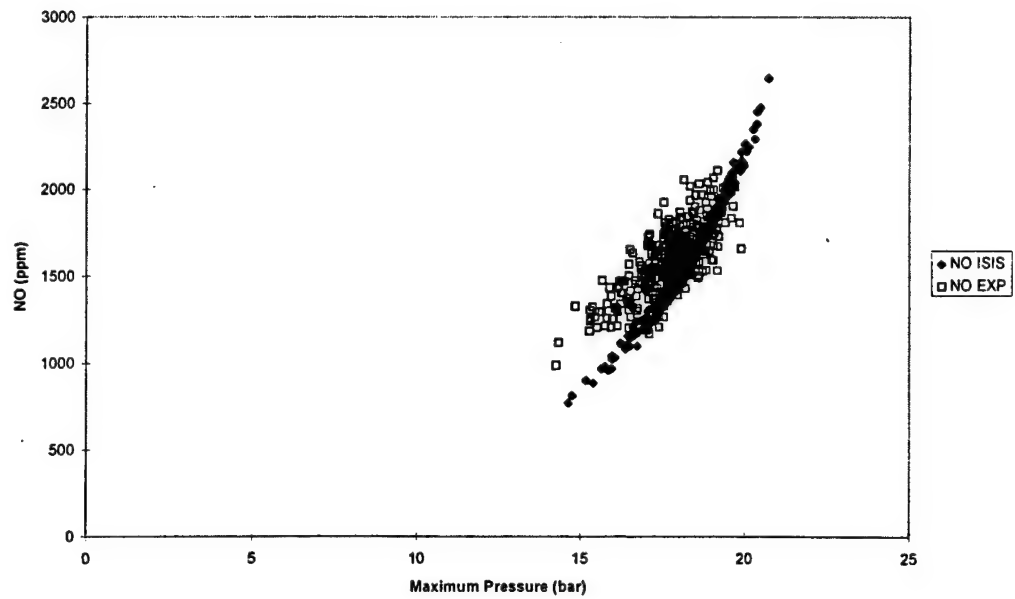
2/3 Load,  $\lambda = 0.9$ , Ign = 15 deg BTDC2/3 Load,  $\lambda = 0.9$ , Ign = 30 deg BTDC

2/3 Load,  $\lambda = 1.1$ , Ign=15 deg BTDC2/3 Load,  $\lambda = 1.1$ , Ign=30 deg BTDC

1/3 Load,  $\lambda = 0.9$ , Ign = 15 deg BTDC1/3 Load,  $\lambda = 0.9$ , Ign = 30 deg BTDC

1/3 Load,  $\lambda = 1.1$ , Ign = 15 deg BTDC1/3 Load,  $\lambda = 1.1$ , Ign = 30 deg BTDC

Toluene,  $\lambda = 0.9$ ,  $\text{ign}=15$  deg BTDCToluene,  $\lambda=0.9$ ,  $\text{ign}=30$ deg BTDC

Toluene,  $\lambda=1.1$ , Ign=15 deg BTDCToluene,  $\lambda=1.1$ , Ign=30 deg BTDC



## Appendix F Derivation of composite torque using engine block angular acceleration

The following derivation is contained in detail in Taylor (1985). Taylor develops expressions for the torque applied to the crankshaft, as this method is physically more intuitive. The signs may then be adjusted appropriately to apply the torque to the block, or engine frame to use Taylor's terminology. To begin, the composite torque acting on the crankshaft is

$$T_c = T_p + T_m + T_f + T'_m \quad (F.1)$$

where

$T_c$  = composite torque applied to the crankshaft,

$T_p$  = torque due to gas pressure,

$T_m$  = torque due to reciprocating mass,

$T_f$  = torque due to friction load and pumping, and

$T'_m$  = correction to torque due to angular motion of the conrod.

The axis system used for this derivation is shown in Figure F.1 below, and follows normal automotive practice.

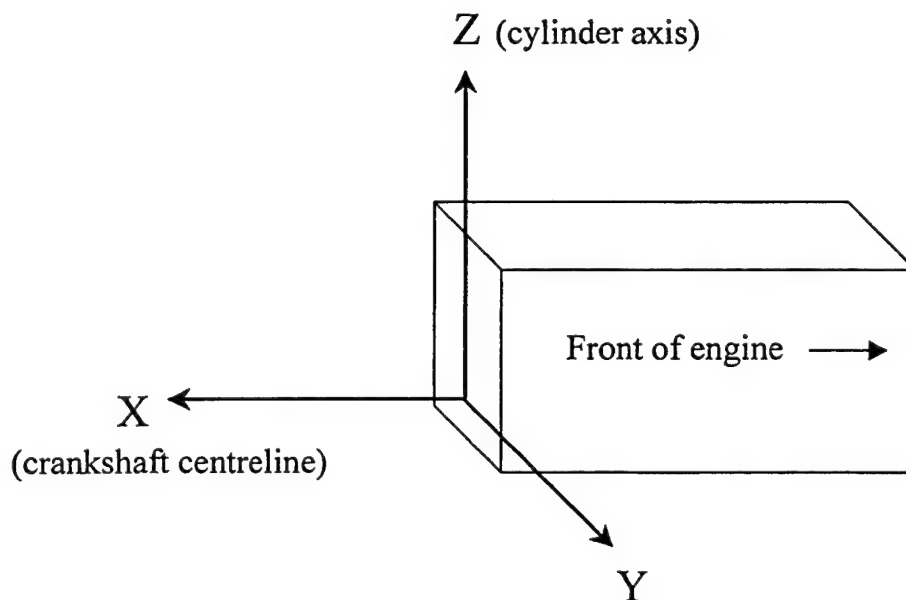
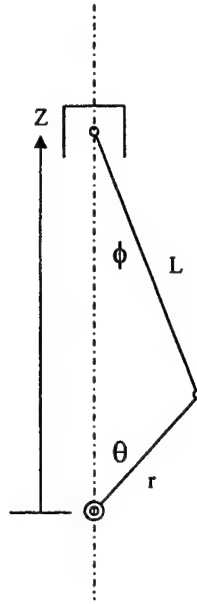


Figure F.1. Engine axis system.

With this axis system, a positive torque is in the direction of crankshaft rotation (clockwise as viewed from the front of the engine). The derivation starts by defining the position and motion of the piston as defined in Figure F.2.



**Figure F.2. Piston position.**

The position of the little end with respect to the crankshaft centre is

$$Z = L \cos \phi + r \cos \theta. \quad (\text{F.2})$$

Since  $L \sin \phi = r \sin \theta$ , and  $\cos^2 \phi + \sin^2 \phi = 1$ , the position of the little end becomes

$$Z = r \left( \cos \theta + \frac{L}{r} \sqrt{1 - \left( \frac{r}{L} \right)^2 \sin^2 \theta} \right). \quad (\text{F.3})$$

The binomial theorem may be used to expand the radical

$$Z = r \left\{ \cos \theta + \frac{L}{r} \left[ 1 - \frac{1}{2} \left( \frac{r}{L} \right)^2 \sin^2 \theta - \frac{1}{8} \left( \frac{r}{L} \right)^4 \sin^4 \theta + \dots \right] \right\}. \quad (\text{F.4})$$

The powers of  $\sin \theta$  can be expressed as equivalent multiple angles which produces

$$Z = r \left\{ \cos \theta + \frac{L}{r} \left[ 1 - \frac{1}{2} \left( \frac{r}{L} \right)^2 (1/2 - 1/2 \cos 2\theta) - \frac{1}{8} \left( \frac{r}{L} \right)^4 (3/8 - 1/2 \cos 2\theta + 1/8 \cos 4\theta) + \dots \right] \right\} \quad (\text{F.5})$$

Normally,  $(r/L)^2$  is less than 0.1, and the  $(r/L)^4$  terms can be neglected. Thus

$$Z \approx r \left\{ \cos \theta + \frac{L}{r} \left[ 1 - \frac{1}{2} \left( \frac{r}{L} \right)^2 (1/2 - 1/2 \cos 2\theta) \right] \right\}. \quad (\text{F.6})$$

This expression can be differentiated twice to give the piston velocity and acceleration (assuming constant angular velocity of the crankshaft):

$$\dot{Z} \approx -r\Omega \left( \sin \theta + \frac{1}{2} \frac{r}{L} \sin 2\theta \right) \quad (\text{F.7})$$

$$\ddot{Z} \approx -r\Omega^2 \left( \cos \theta + \frac{r}{L} \cos 2\theta \right) \quad (\text{F.8})$$

The reciprocating mass contains the mass of the piston and gudgeon pin, plus some portion of the conrod mass. This is usually accomplished by treating the conrod as two masses as shown in Figure F.3.

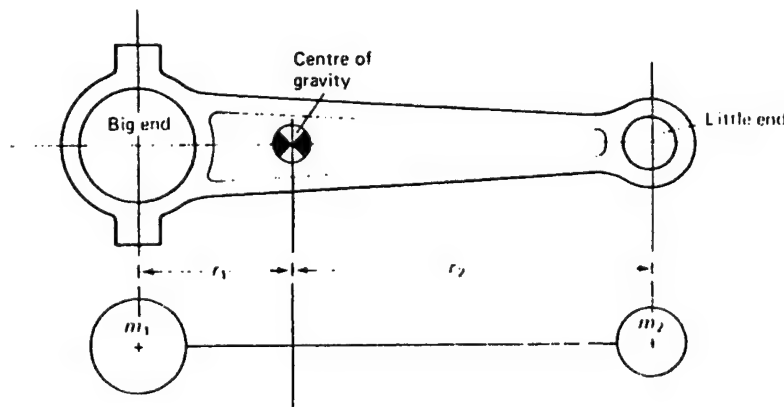


Figure F.3. Equivalent conrod mass (from Stone, 1992).

For equivalence

$$m_{cr} = m_1 + m_2$$

$$m_1 r_1 = m_2 r_2.$$

The mass  $m_2$  is considered to be part of the piston assembly, and is assumed to undergo reciprocating motion only. The mass  $m_1$  is assumed to undergo pure rotation with the crankshaft, and is normally countered with balance weights incorporated into the crankshaft.

### **Torque applied to crankshaft due to gas pressure**

The torque due to gas pressure may be found by noting that the work done by the gas must be equal to the work done on the crankshaft

$$PdV = T_p d\theta. \quad (F.9)$$

Since  $dV = A_p dZ$ , where  $A_p$  is the piston area,

$$T_p = PA_p \frac{dZ}{d\theta}. \quad (F.10)$$

However,

$$\frac{dZ}{d\theta} = \frac{dZ/dt}{d\theta/dt} = \frac{\dot{Z}}{\Omega}. \quad (F.11)$$

Therefore

$$T_p = PA_p \frac{\dot{Z}}{\Omega}. \quad (F.12)$$

### **Torque applied to crankshaft due to reciprocating mass**

The torque applied to the crankshaft by the reciprocating mass is found by noting that the change in kinetic energy of the piston is equal to the work done by the crankshaft on the conrod

$$d\left(\frac{M_p}{2}\dot{Z}^2\right) = -T_m d\theta. \quad (F.13)$$

Differentiating equation (F.13) with respect to time gives

$$\frac{d}{dt}\left(\frac{M_p}{2}\dot{Z}^2\right) = M_p\dot{Z}\ddot{Z} = -T_m \frac{d\theta}{dt} = -T_m \Omega. \quad (F.14)$$

Finally

$$T_m = -M_p \ddot{Z} \left(\frac{\dot{Z}}{\Omega}\right). \quad (F.15)$$

#### Correction to torque due to angular momentum of the conrod

The torque required to rotate the conrod may be determined by reference to Figure F.4.

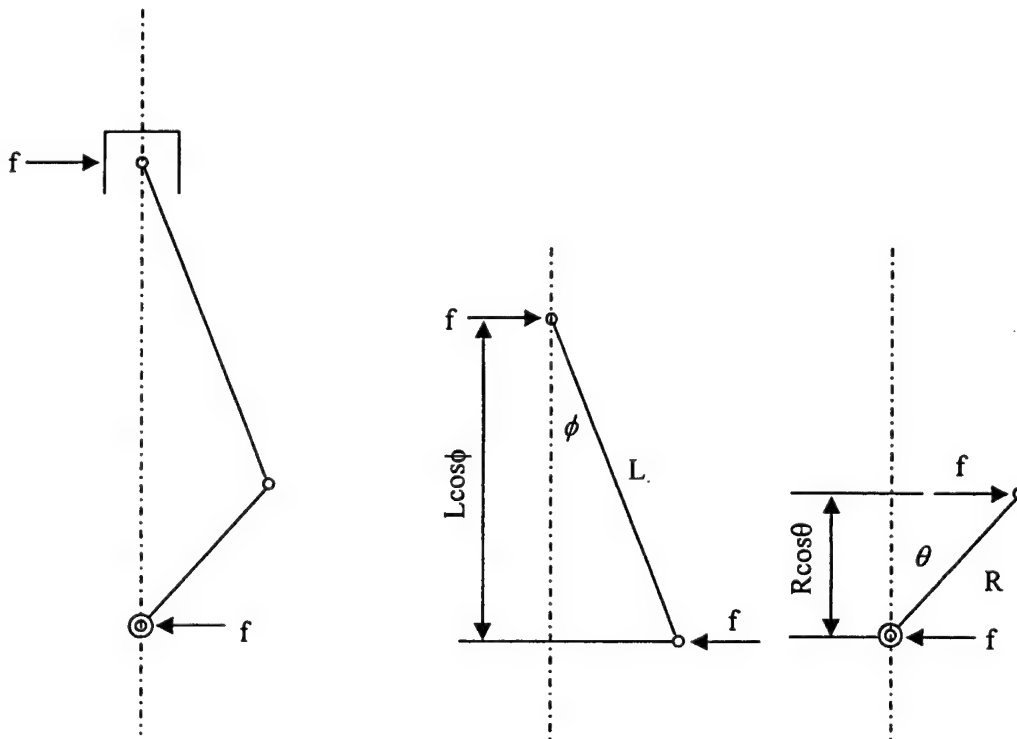


Figure F.4. Inertia torques acting on conrod and engine block (from Taylor, 1985).

The required torque is given by Newton's Law, and is

$$I_{cr} \ddot{\phi} = fL \cos \phi, \text{ hence}$$

$$f = \frac{I_{cr} \ddot{\phi}}{L \cos \phi} \quad (F.16)$$

The torque acting on the crankshaft will thus be

$$T = fr \cos \theta = \frac{I_{cr} \ddot{\phi} r \cos \theta}{L \cos \phi}. \quad (F.17)$$

The torque due to the reciprocating mass of the conrod has been accounted for in the derivation of  $T_m$ . However, the fictitious conrod used in this derivation has a different moment of inertia than the actual conrod, thus a correction must be applied to equation (F.1). The moment of inertia of the fictitious conrod is

$$I'_{cr} = (m_1 r_1^2 + m_2 r_2^2). \quad (F.18)$$

From the equations used to establish the equivalency of the fictitious rod,  $m_1 = m_2 r_2 / r_1$  and  $m_2 = m_1 r_1 / r_2$ . Making this substitution into equation (F.18) gives

$$I'_{cr} = M_{cr} r_1 r_2. \quad (F.19)$$

In considering the torque required to rotate the conrod, the difference between the torque acting on the actual rod and that acting on the fictitious rod is

$$(I_{cr} - M_{cr} r_1 r_2) \ddot{\phi}. \quad (F.20)$$

Combining equations (F.19) and (F.20) thus gives the correction to the inertia torque for the true moment of inertia of the conrod

$$T'_m = (I_{cr} - M_{cr} r_1 r_2) \ddot{\phi} \frac{r \cos \theta}{L \cos \phi}. \quad (F.21)$$

With reference to Figure F.4, it can be seen that the correction to the inertia torque applied to the block is not equal and opposite to equation (F.21). In this case, the torque applied to the block is  $f(r\cos\theta + L\cos\phi)$ , and equation (F.21) becomes

$$T'_m = (I_{cr} - M_{cr}r_1r_2)\ddot{\phi}\left(\frac{r\cos\theta}{L\cos\phi} + 1\right). \quad (F.22)$$

Equation (F.22) may be reduced to a trigonometric series (Taylor, 1985)

$$T'_m = (I_{cr} - M_{cr}r_1r_2)\Omega^2 \sum_{n=1}^{\infty} S_n \sin 2n\theta \quad (F.23)$$

where  $S_n$  are coefficients given by Taylor (1985) to be  $-0.35$  and  $-0.055$  for the first two terms of the series.

#### Torque applied to crankshaft due to friction

Determining the friction level in an engine is a notoriously difficult task (Stone, 1992). Often, a motoring test is performed with the assumption that the torque required to motor the engine is equal to the friction torque. However, the friction level will change under firing conditions due to the increased temperature of operation and the greater gas pressure loads within each cylinder. The engine used for this work is a four-cylinder Rover K16 1.4 litre MPI engine. The Rover Advanced Power Train division has developed an expression for the friction mean effective pressure (FMEP) for this engine, and this correlation has shown good agreement with experiment. The FMEP (in bar) may be estimated by

$$\text{FMEP} = 0.697 + N(2.995 \times 10^{-8} N - 1.487 \times 10^{-5}) \quad (F.24)$$

where  $N$  is the engine speed in revolutions per minute. The torque due to friction is related to the FMEP by noting that the work done by the torque in two revolutions is equal to the MEP times the engine displacement (Taylor, 1985)

$$T_f(4\pi) = \text{FMEP} * V_d. \quad (F.25)$$

Hence, the torque due to friction is

$$T_f = \frac{\text{FMEP} * V_d}{4\pi} \quad (\text{F.26})$$

and this is assumed to be constant over the entire cycle.

The foregoing equations were derived for a single cylinder. Since all the torques act about the same axis, the torques produced by each cylinder may be added directly. This is accomplished by varying the phasing of each cylinder's torque input on the basis of engine firing order.

The composite torque acting on the engine frame is not equal and opposite to the torque acting on the crankshaft due to the correction torque from the rotation of the conrod. However, a separate correction factor has been derived. Hence, the composite torque acting on the engine frame is given by

$$T_c = -T_p - T_m - T_f + T'_m. \quad (\text{F.27})$$



## Appendix G Misfire metric results

The figures in this appendix plot the misfire identification metrics versus the IMEP of cylinder #4. The four metrics were defined as:

$$\text{Low Frequency Torque Metric - LFTM} = \sqrt{\sum_{n=1}^{N-1} |T(n\lambda_o)|^2}$$

$$\text{Low Frequency Acceleration Metric - LFAM} = \sqrt{\sum_{n=1}^{N-1} |A(n\lambda_o)|^2}$$

$$\text{High Frequency Torque Metric - HFTM} = \frac{1}{L} \sqrt{\sum_{n=1}^L |T(n\lambda_f)|^2}$$

$$\text{High Frequency Acceleration Metric - HFAM} = \frac{1}{L} \sqrt{\sum_{n=1}^L |A(n\lambda_f)|^2} .$$

The cases presented are the low speed, high load case and the high speed, low load case.

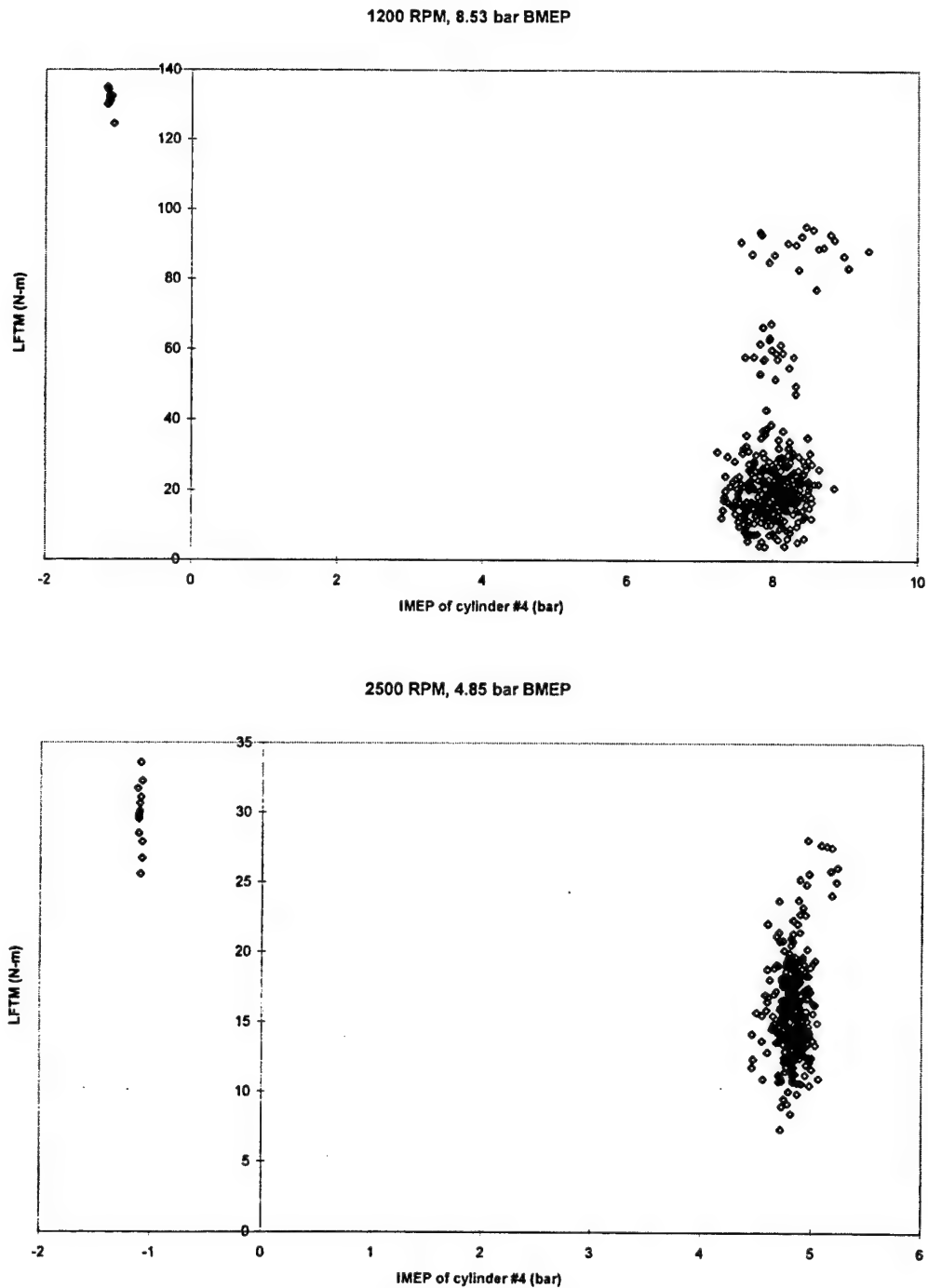


Figure G.1. LFTM versus IMEP of cylinder #4.

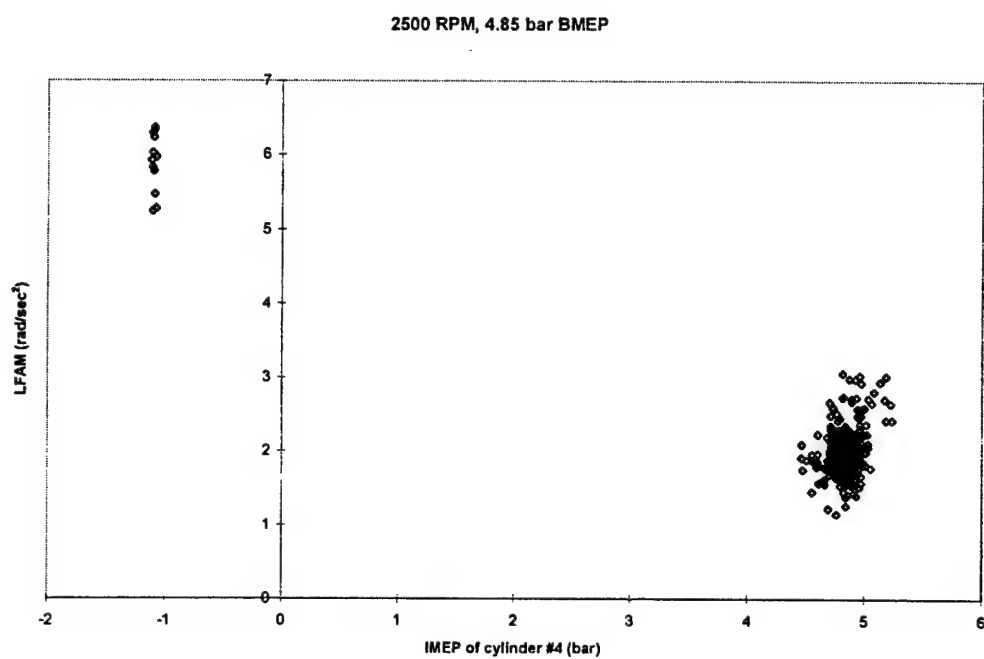
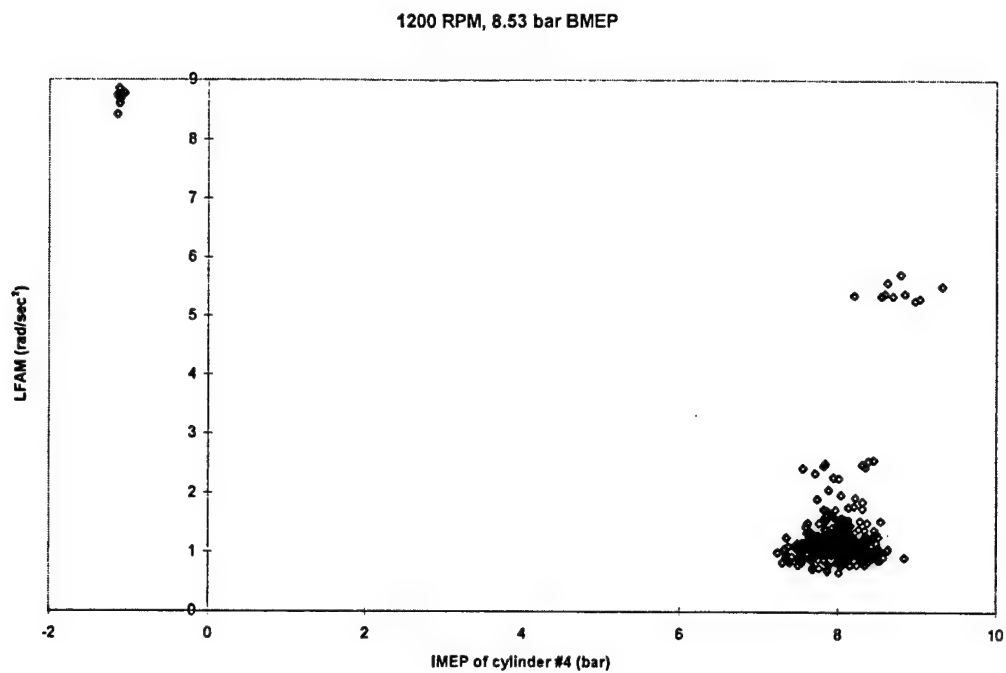


Figure G.2. LFAM versus IMEP of cylinder #4.

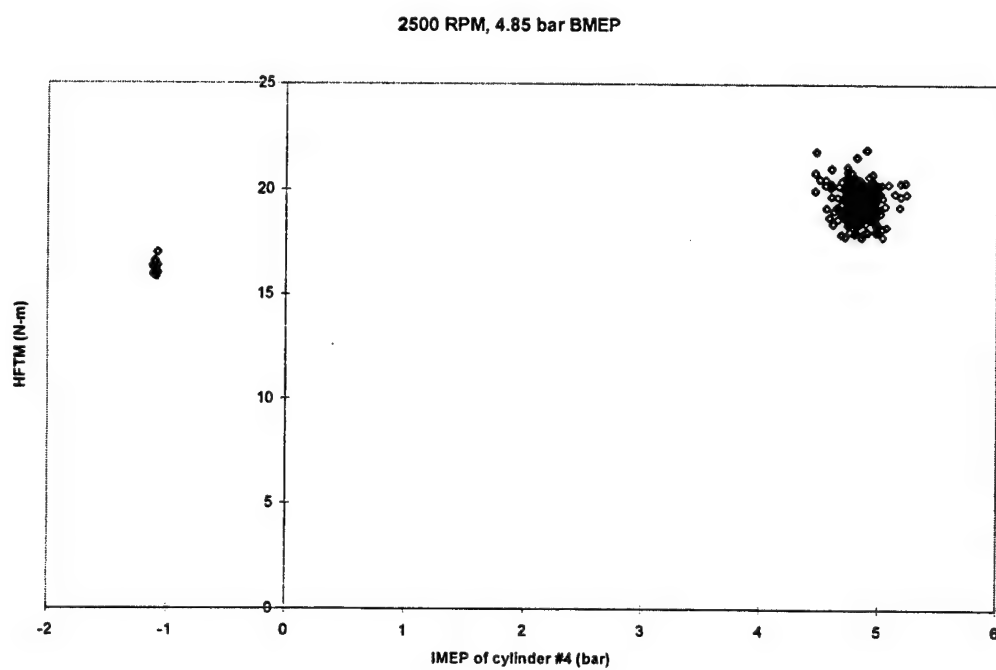
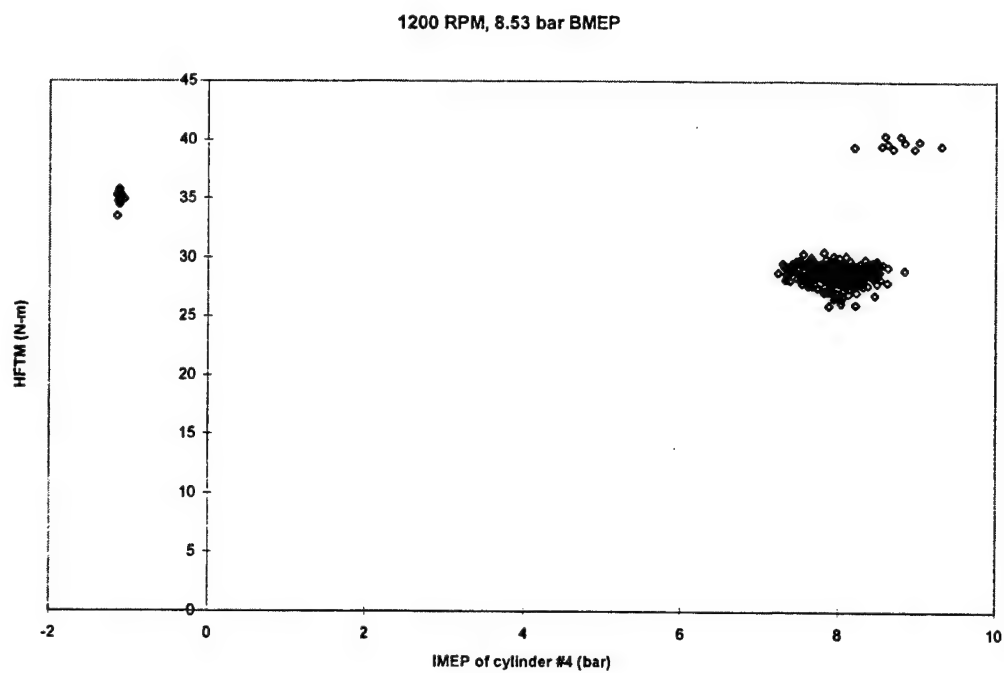
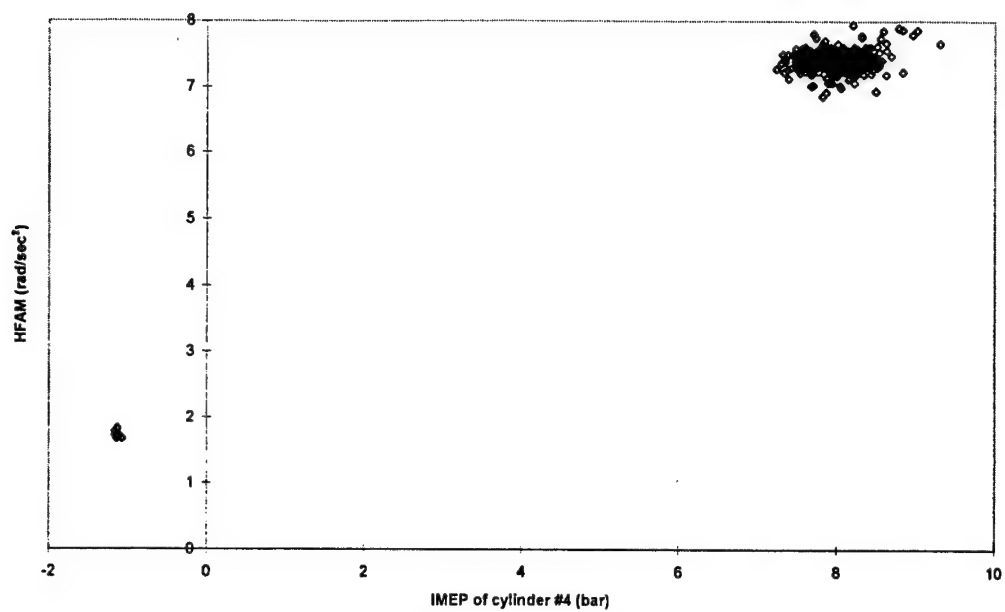
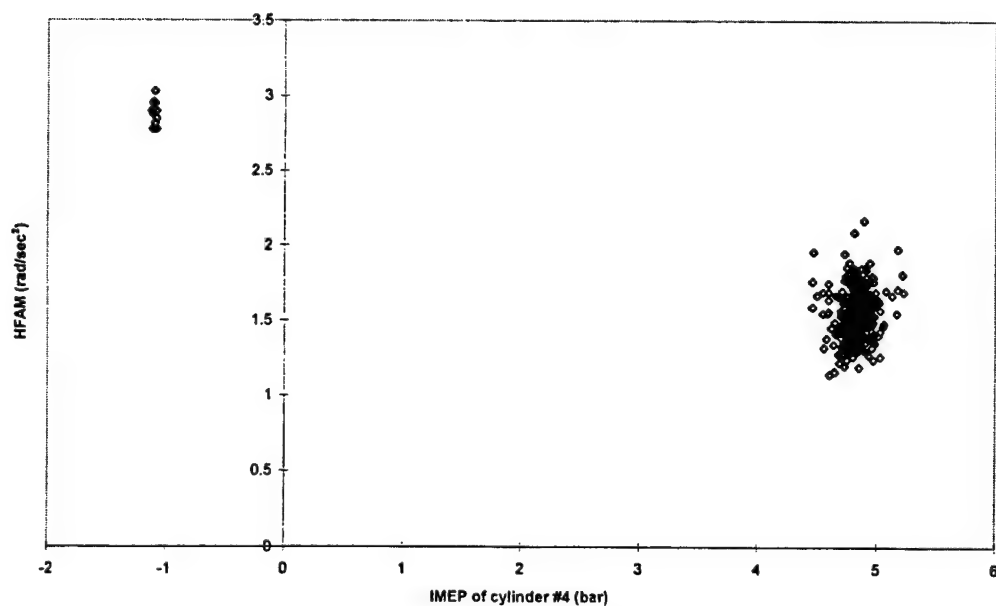


Figure G.3. HFTM versus IMEP of cylinder #4.

1200 RPM, 8.53 bar BMEP



2500 RPM, 4.85 bar BMEP



**Cycle-by-cycle variation in spark ignition internal combustion engines**

**Jeffrey K. Ball, Major, USAF**

**248 pages, 1998**

**Doctor of Philosophy**

**Oxford University**

**Abstract**

The primary objective of this work was to extend the engine cycle simulation used by the Oxford Internal Combustion Engine Group to enable it to perform cycle-by-cycle modelling. Modelling attempts using burn rate information alone resulted in an under-prediction of the cyclic variability exhibited by the engine. This under-prediction was postulated to be due to incomplete combustion, which is not detected by the burn rate model. A completeness of combustion parameter was derived from information contained in the Rassweiler and Withrow analysis. This parameter was used along with burn rate variations to perturb the cycle simulation and resulted in good cycle-by-cycle agreement between the experimental data and the modelled data. Cyclic measurements of NO showed that the technique did not predict the cyclic variability in NO formation, and this was attributed to the sensitivity of NO formation to parameters that were not allowed to vary on a cyclic basis within the model.

The second objective of this work was to examine the feasibility of using measurements of the angular acceleration of the engine block as a means of detecting misfires. Torque estimation was good under low speed conditions, but was less accurate at high speed and load due to a coupling of the block rolling and pitching motion. Misfire metrics were developed in both the temporal and spatial frequency domains. The metrics based on low frequency information were most reliable. However, their accuracy was degraded at high engine speeds due to structural vibration of the block and the variable inertial properties of the engine, neither of which were incorporated into the model. It was concluded that the measurements of the angular acceleration of the block could be used to detect misfires, and that the most significant advantage of this method was the fact that the load torque through the drivetrain did not affect the calculations.

## Bibliography of key sources

Connolly, F.T. (1994), *Direct Estimation of Cyclic Combustion Pressure Variability using Engine Speed Fluctuations in an Internal Combustion Engine*, SAE Paper 940143.

Connolly, F.T., and Rizzoni, G. (1994), *Real Time Estimation of Engine Torque for the Detection of Engine Misfires*, Transactions of the ASME, Journal of Dynamic Systems, Measurement, and Control, Vol. 116, pp. 675-686.

Ferguson, C. R. (1986), *Internal Combustion Engines*, Applied Thermosciences, John Wiley and Sons, Inc., New York.

Heywood, J.B. (1988), *Internal Combustion Engine Fundamentals*, McGraw-Hill Book Company, New York.

Matekunas, F.A. (1983), *Modes and Measures of Cyclic Combustion Variability*, SAE Paper 830337.

Raine, R.R., Stone, C.R., and Gould, J. (1995), *Modelling of nitric oxide formation in spark ignition engines with a multizone burned gas*, Combustion and Flame, 102: 241-255, 1995.

Rassweiler, G.M., and Withrow, L. (1980), Motion pictures of engine flames correlated with pressure cards, SAE paper 800131 (originally presented in January 1938).

Stone, C.R. (1992), *Introduction to Internal Combustion Engines*, 2<sup>nd</sup> Edn. Macmillan.

Young, M.B. (1980), *Cyclic Dispersion – Some Qualitative Cause-and-Effect Relationships*, SAE Paper 800459.

Young, M.B. (1981), *Cyclic Dispersion in the Homogeneous-Charge Spark-Ignition Engine-A Literature Survey*, SAE Paper 810020.

**Cycle-by-cycle variation in spark ignition internal combustion engines**

**Jeffrey K. Ball, Major, USAF**

**248 pages, 1998**

**Doctor of Philosophy**

**Oxford University**

**Abstract**

The primary objective of this work was to extend the engine cycle simulation used by the Oxford Internal Combustion Engine Group to enable it to perform cycle-by-cycle modelling. Modelling attempts using burn rate information alone resulted in an under-prediction of the cyclic variability exhibited by the engine. This under-prediction was postulated to be due to incomplete combustion, which is not detected by the burn rate model. A completeness of combustion parameter was derived from information contained in the Rassweiler and Withrow analysis. This parameter was used along with burn rate variations to perturb the cycle simulation and resulted in good cycle-by-cycle agreement between the experimental data and the modelled data. Cyclic measurements of NO showed that the technique did not predict the cyclic variability in NO formation, and this was attributed to the sensitivity of NO formation to parameters that were not allowed to vary on a cyclic basis within the model.

The second objective of this work was to examine the feasibility of using measurements of the angular acceleration of the engine block as a means of detecting misfires. Torque estimation was good under low speed conditions, but was less accurate at high speed and load due to a coupling of the block rolling and pitching motion. Misfire metrics were developed in both the temporal and spatial frequency domains. The metrics based on low frequency information were most reliable. However, their accuracy was degraded at high engine speeds due to structural vibration of the block and the variable inertial properties of the engine, neither of which were incorporated into the model. It was concluded that the measurements of the angular acceleration of the block could be used to detect misfires, and that the most significant advantage of this method was the fact that the load torque through the drivetrain did not affect the calculations.



## Bibliography of key sources

Connolly, F.T. (1994), *Direct Estimation of Cyclic Combustion Pressure Variability using Engine Speed Fluctuations in an Internal Combustion Engine*, SAE Paper 940143.

Connolly, F.T., and Rizzoni, G. (1994), *Real Time Estimation of Engine Torque for the Detection of Engine Misfires*, Transactions of the ASME, Journal of Dynamic Systems, Measurement, and Control, Vol. 116, pp. 675-686.

Ferguson, C. R. (1986), *Internal Combustion Engines*, Applied Thermosciences, John Wiley and Sons, Inc., New York.

Heywood, J.B. (1988), *Internal Combustion Engine Fundamentals*, McGraw-Hill Book Company, New York.

Matekunas, F.A. (1983), *Modes and Measures of Cyclic Combustion Variability*, SAE Paper 830337.

Raine, R.R., Stone, C.R., and Gould, J. (1995), *Modelling of nitric oxide formation in spark ignition engines with a multizone burned gas*, Combustion and Flame, 102: 241-255, 1995.

Rassweiler, G.M., and Withrow, L. (1980), Motion pictures of engine flames correlated with pressure cards, SAE paper 800131 (originally presented in January 1938).

Stone, C.R. (1992), *Introduction to Internal Combustion Engines*, 2<sup>nd</sup> Edn. Macmillan.

Young, M.B. (1980), *Cyclic Dispersion – Some Qualitative Cause-and-Effect Relationships*, SAE Paper 800459.

Young, M.B. (1981), *Cyclic Dispersion in the Homogeneous-Charge Spark-Ignition Engine-A Literature Survey*, SAE Paper 810020.